

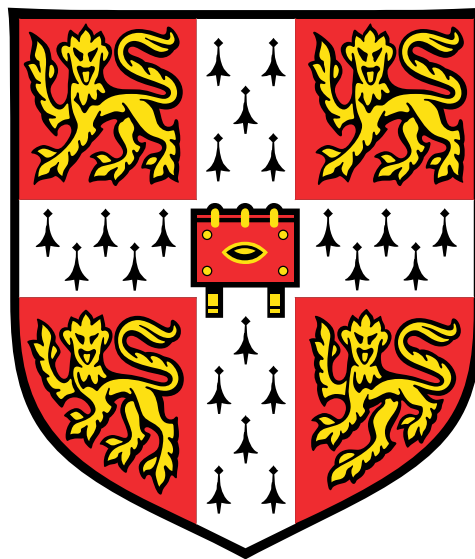
---

---

FABRICATION AND INORGANIC MODIFICATION  
OF 3D CARBON NANOTUBE STRUCTURES  
FOR APPLICATIONS IN ENERGY STORAGE

---

---



**Sarah Jessl, M. Sc.**

Department of Engineering  
University of Cambridge

This dissertation is submitted for the degree of  
*Doctor of Philosophy*

St. John's College

**June 2018**







*I would like to dedicate this thesis to  
my loving mum, Sylvia Jessl, who is always there for me,  
and my supportive friend and mentor, Daror Copic.*



# Declaration

I hereby declare that, except where specific reference is made to the work of others, the contents of this dissertation are original and have not been submitted in whole or in part for consideration for any other degree or qualification in this, or any other university. This dissertation is my own work and contains nothing which is the outcome of work done in collaboration with others, except as specified in the text and acknowledgements. This dissertation contains fewer than 65,000 words including appendices, bibliography, footnotes, tables and equations and has fewer than 150 figures.

Sarah Jessl  
June 2018



# Acknowledgements

A PhD is a challenge, a PhD is tough,  
Why else would you do it if not for the love,  
The love of science, the love of discovery,  
The love of development, the love of a journey.

And yes, what an exciting journey it was,  
Not always fun, not always a blast.  
Nevertheless, so worth the strain,  
So much personal development to gain.

I'm grateful for the wonderful people, always there  
When I needed them, to show me how much they care,  
They were patient, made sure I stayed on track,  
Answered questions, gave helpful feedback.

Two special people to point out from the team  
It is obviously Michael and Davor, I mean.  
Michael accepted me for my PhD,  
And has been an amazing supervisor to me.

A supervisor, very patient and encouraging,  
Never doubtful and always listening,  
With fruitful discussions at the weekly meeting slot,  
With great ideas and solutions a lot,  
No problem impossible, none too hard.  
What a great supervisor right from the start!

Davor started training me from day one,  
As my mentor always encouraging and so much fun,  
Challenging to enable personal growth,  
Pushing and supporting with balance always both.

He always made sure I got my work done,  
But also taught me many skills for the long run.  
He became a close and supportive friend,

I really appreciate all the time he spent.

Additionally supported by our Nanomanufacturing team,

Endless knowledge together - so it might seem.

Also social fun with BBQs, pub nights and lunch,

So grateful for this delightful bunch!

The IfM with its people is an awesome place,

To relax and discuss all the emotions we face,

Glad to be in such a nice environment,

With people that care without an equivalent.

Not many projects can be done alone,

Collaborators' expertise and insights were shown

To push research forward and contribute,

Making it possible to go down a novel route.

Prof. Seveno and Prof. Han, thanks to you,

For collaborating on important projects, too.

Simon and Jan, with your electrochemical expertise,

Thanks for measuring my samples with ease.

A big thanks to my College, St. John's,

Always social events and support tons,

Especially amazing my tutor Dr. Helen Watson there,

I don't know many who showed more care,

Always there for every issue and advice,

Having so much support is incredibly nice.

Finally I'd like to thank Ivana and all my friends,

my family, my six siblings and my parents,

Always encouraging, there for me around the clock,

Let me just say: YOU ROCK!

I'm grateful to have you all in my life,

To support me for whatever I strife,

To feel your love every minute, every day

This makes me strong and helps me go my way.

Another chapter of my life finishes with this submission,

So excited to see what's next, what kind of position.

Not much left to add, say or do,

except a huge **THANK YOU** to all of you!





## Abstract

Structured electrodes with tailored nanoscale morphology and chemistry are highly desirable for a range of applications. In particular, emerging energy storage applications such as thick Lithium-ion battery (LIB) electrodes and photoanodes for watersplitting require new electrode structures that simultaneously optimise electron, ion, and thermal transport. In this PhD thesis, advanced structured electrodes are fabricated by creating 3D carbon-inorganic hybrid architectures. In this process, patterned vertically aligned carbon nanotubes (CNT) were used as the structural scaffolds to shape the electrodes while inheriting the excellent thermal and electrical properties of CNTs.

First, UV and colloidal lithographic patterning processes were developed to create micro- and nanopores respectively within the CNT structures. Those structures provide high surface area and conductive backbone for the synthesis of hybrid CNT-inorganic structures. Specifically, the parameter space to create honeycomb shaped CNT structures with pores ranging from 300 nm to 30  $\mu\text{m}$  has been established.

Next, the micro-pore CNT structures have been chemically modified with iron oxide using microwave-assisted, hydrothermal synthesis for fabricating high areal loading LIB anodes. The areal loading was increased by 120% compared to a standard battery film while at the same time retaining a high capacity (900  $\text{mAhg}^{-1}$  at 0.2 C). Then thick electrodes with optimised diffusion pathways were created by coating the nanopatterned CNTs with silicon using physical vapour deposition. These electrode structures are up to 50% thicker than previously reported structures and still retain a stable capacity (650  $\text{mAhg}^{-1}$ ) and a good high-rate performance. Finally, the honeycomb shaped CNT structures have been coated with bismuth vanadate using a hotcasting process and the electrode architecture has been optimized for good conductivity by the addition of a Pd/Au layer between the CNTs and the  $\text{BiVO}_4$ . The photoelectrode performance was measured and shows a clear increase in current density when exposed to light.

Each of these novel electrodes illustrate how patterning vertically aligned carbon nanotube structures combined with inorganic surface modification enables the creation of advanced electrodes with new formfactors and improved performance in comparison to literature and to classic drop-casted battery films of the same materials.



# Table of contents

<b>List of figures</b>	<b>xv</b>
<b>List of tables</b>	<b>xxi</b>
<b>List of abbreviations</b>	<b>xxiii</b>
<b>I Introduction and Project Goals</b>	<b>1</b>
<b>II Introduction to Carbon Nanotubes: Structures and Modification</b>	<b>7</b>
<b>1 Carbon Nanotubes (CNT) Overview</b>	<b>9</b>
1.1 CNT structure and properties . . . . .	10
1.1.1 CNT structure . . . . .	10
1.1.2 CNT properties . . . . .	12
1.2 Fabrication methods for pristine CNT powders . . . . .	14
1.3 Vertically aligned CNT structures . . . . .	16
1.3.1 Fabrication of vertically aligned CNT structures . . . . .	16
1.3.2 CNT forest growth by chemical vapor deposition . . . . .	19
1.4 CNT forest patterning and shaping . . . . .	28
1.4.1 CNT forest patterning by UV- lithography . . . . .	28
1.4.2 CNT forest patterning by colloidal lithography . . . . .	31
1.4.3 CNT forest shaping by elastocapillary self-aggregation of CNTs . . . . .	37

<b>2</b>	<b>Chemical Modification of Carbon Nanotubes</b>	<b>41</b>
2.1	Nucleation theory . . . . .	42
2.2	CNT functionalization . . . . .	45
2.2.1	Gaseous phase modification . . . . .	45
2.2.2	Liquid phase modification . . . . .	48
<b>III</b>	<b>Results</b>	<b>55</b>
<b>3</b>	<b>Fabrication of 3D CNT Structures with pores</b>	<b>57</b>
3.1	Introduction . . . . .	58
3.2	CNT honeycomb fabrication . . . . .	58
3.2.1	CNT honeycomb fabrication process . . . . .	58
3.2.2	Influence of temperature on CNT honeycomb formation and the underlayer on growth height . . . . .	60
3.2.3	Influence of mask design parameters and growth time on CNT honeycomb formation . . . . .	63
3.2.4	Introduction of stress relief features to avoid cracking . . . . .	65
3.3	Fabrication of 3D CNT structures using colloidal lithography . . . . .	67
3.3.1	Fabrication of 3D CNT structures from colloidal templates . . . . .	68
3.3.2	Influence of change in initial particle size . . . . .	72
3.3.3	Densification of nanoscale 3D CNT structures . . . . .	73
3.4	Conclusion . . . . .	74
<b>4</b>	<b>Inorganic Modification of 3D CNT Structures for Lithium-Ion Batteries</b>	<b>77</b>
4.1	Introduction to lithium-ion batteries . . . . .	78
4.2	Coated 3D CNT structures as advanced electrode architectures . . . . .	83
4.2.1	Iron oxide as an anode material . . . . .	85
4.2.2	Silicon as an anode material . . . . .	86
4.3	Modification of 3D CNT structure with iron oxides ( $\alpha$ -Fe <sub>2</sub> O <sub>3</sub> ) . . . . .	89
4.3.1	Fabrication process of the 3D CNT structure with iron oxides . . . . .	89
4.3.2	Modification on Si-wafer before transfer onto polymer film . . . . .	90
4.3.3	Transfer of honeycomb structures onto polymeric films . . . . .	97

4.3.4	Low temperature modification on conductive polymer film . . . . .	99
4.3.5	Initial electrochemical characterization for Fe <sub>2</sub> O <sub>3</sub> . . . . .	110
4.3.6	Conclusion . . . . .	114
4.4	Modification of the nanoscale 3D CNT structure with silicon . . . . .	115
4.4.1	Fabrication process of the nanoscale 3D CNT structure with silicon . . . . .	115
4.4.2	Thermal CVD-process for Si-deposition . . . . .	116
4.4.3	PVD-process for Si-deposition . . . . .	120
4.4.4	Initial electrochemical characterization for silicon . . . . .	121
4.4.5	Conclusion . . . . .	123
<b>5</b>	<b>Inorganic Modification of CNT Honeycomb Structures for Watersplitting</b>	<b>125</b>
5.1	Introduction to solar watersplitting . . . . .	126
5.2	BiVO <sub>4</sub> -coated CNT honeycombs as photoelectrodes . . . . .	130
5.3	Modification with bismuth vanadate - BiVO <sub>4</sub> . . . . .	131
5.3.1	Microwave-assisted, hydrothermal growth of BiVO <sub>4</sub> on CNT structures . . . . .	131
5.3.2	Hotcasting of BiVO <sub>4</sub> on CNT structures . . . . .	138
5.4	BiVO <sub>4</sub> photoelectrode characterization . . . . .	142
5.5	Conclusion . . . . .	144
<b>6</b>	<b>Summary</b>	<b>145</b>
<b>7</b>	<b>Experimental Section</b>	<b>155</b>
7.1	3D CNT structure preparation . . . . .	156
7.2	Honeycomb transfer onto polymer films and copper tape . . . . .	158
7.3	Inorganic modification of 3D CNT structures . . . . .	159
7.4	Further modification of 3D CNT structures . . . . .	163
7.5	Electrochemical measurements . . . . .	164
7.6	Equipment . . . . .	165
	<b>Bibliography</b>	<b>167</b>
	<b>Appendix A Theoretical Background Carbon Nanotubes</b>	<b>187</b>

<b>Appendix B Results</b>	<b>189</b>
B1 Formation of 3D CNT Structures . . . . .	189
B2 Modification with Iron Oxide . . . . .	193
B3 Modification with Silicon . . . . .	196
B4 Modification with Bismuth Vanadate . . . . .	196

# List of figures

0.1	PhD project overview . . . . .	5
1.1	Random CVD-grown CNTs, scale bar 100 $\mu\text{m}$ . . . . .	9
1.2	Structure of a CNT . . . . .	10
1.3	SWNT and MWNT structure and TEM . . . . .	11
1.4	Elbow connections and Stone-Wales defect in CNTs . . . . .	12
1.5	Wet chemistry growth of chiral CNTs . . . . .	16
1.6	Ways of CNT arrangement . . . . .	17
1.7	Spinning of yarns from vertically aligned MWNTs . . . . .	18
1.8	Variety of knitted structures from MWNT . . . . .	18
1.9	Schematic setup of a CVD reactor and SEM of a CNT forest . . . . .	19
1.10	Mass and areal density evolution for a hot- and cold-wall reactor. . . . .	21
1.11	CNT-diameter and CNT-length evolution . . . . .	22
1.12	CNT micropillar growth . . . . .	23
1.13	CNT forest growth stages . . . . .	25
1.14	Gas preheating influence on forest height . . . . .	27
1.15	Overview of patterning process by UV-lithography . . . . .	28
1.16	Comparison of negative and positive photoresists . . . . .	31
1.17	Colloidal lithography process . . . . .	32
1.18	Creation of hcp collidal crystals . . . . .	33
1.19	DLVO potential curve . . . . .	34
1.20	Forces and interactions on interfaces . . . . .	34
1.21	Monolayer formation process by N. Vogel . . . . .	35
1.22	Schematic showing densification process . . . . .	37

1.23	Schematic images showing densification techniques . . . . .	38
1.24	CNT foam formation . . . . .	38
1.25	Surface designs by densification . . . . .	40
2.1	CNT strand coated with TiO <sub>2</sub> , scale bar 2 μm. . . . .	41
2.2	Gibbs free energy change with nucleus radius and LaMer theory . . . . .	44
2.3	CVD deposition mechanism . . . . .	47
2.4	CNT forest modification with silicon by CVD . . . . .	48
2.5	CNT forest modification with SnO <sub>2</sub> and MnO <sub>2</sub> particles . . . . .	49
2.6	CNT forest modification with Ni particles . . . . .	50
2.7	Growth of hollow α-Fe <sub>2</sub> O <sub>3</sub> nanohorns on CNTs . . . . .	52
2.8	Temperature profile of microwave vs. oil-bath heating . . . . .	53
3.1	Vertically aligned CNTs shaped into honeycombs, scale bar 100 μm. . . . .	57
3.2	CNT honeycomb formation . . . . .	59
3.3	Etching of the CNT forest crust . . . . .	59
3.4	Honeycomb densification process . . . . .	60
3.5	Influence of growth temperature on CNT honeycomb formation . . . . .	61
3.6	Underlayer influence on forest height . . . . .	62
3.7	Crack percentage in honeycombs with spacing, diameter and growth time . . . . .	64
3.8	Different heights with a stress relief pattern . . . . .	66
3.9	Different sizes of stress relief hexagons . . . . .	66
3.10	Collapsed area in stress relief hexagons . . . . .	67
3.11	Template creation using colloidal lithography . . . . .	68
3.12	Graph with influence of etching time on sphere diameter . . . . .	69
3.13	Influence of etching time on PS spheres and CNT forest structure . . . . .	70
3.14	Large area overview of colloidal growth and height . . . . .	71
3.15	Monolayer formation with 300 nm spheres . . . . .	73
3.16	Densification methods for nanoscale CNT structures . . . . .	74
4.1	Vertically aligned CNTs coated with Fe <sub>2</sub> O <sub>3</sub> , scale bar 1 μm. . . . .	77
4.2	Schematic overview of the most commonly used Li-ion battery . . . . .	79

4.3	Redox mechanisms for the three types of anode materials in Li-ion batteries . . . . .	80
4.4	Theoretical capacities of anode materials . . . . .	81
4.5	Diffusion parallel and perpendicular to vertically aligned CNTs . . . . .	83
4.6	Schematic overview of advanced architecture . . . . .	84
4.7	Iron oxide modification on CNTs . . . . .	86
4.8	Si-CNT composites with CVD reported in literature . . . . .	87
4.9	Process of iron oxide modification the 3D CNT structure . . . . .	89
4.10	Coating of the CNT honeycomb structure with a solvothermal method . . . . .	91
4.11	Coating of the colloidal CNT structure with a solvothermal method . . . . .	92
4.12	Coating of a high 3D CNT structure with Fe <sub>2</sub> O <sub>3</sub> . . . . .	94
4.13	Coating of a lower 3D CNT structure with Fe <sub>2</sub> O <sub>3</sub> . . . . .	95
4.14	Transfer process of 3D honeycomb structures onto a PVA film . . . . .	97
4.15	Re-growth from Si-wafer after transfer onto a PVA film . . . . .	98
4.16	Transfer process of 3D honeycomb structures onto a PCP film . . . . .	98
4.17	Temperature screen of Fe <sup>2+</sup> and Fe <sup>3+</sup> as a precursor-XRD . . . . .	102
4.18	Development of the Fe <sub>2</sub> O <sub>3</sub> nanoparticles over time . . . . .	103
4.19	Coating of ~500 μm 3D CNT structure with iron oxide from Fe <sup>2+</sup> on PCP film . . .	104
4.20	Coating of ~500 μm 3D CNT structure with iron oxide and height change . . . . .	105
4.21	Coating of a nanoscale CNT structure with iron oxide from Fe <sup>2+</sup> on a PCP film . . .	106
4.22	Synthesis data for Fe <sub>2</sub> O <sub>3</sub> in the microwave reactor . . . . .	107
4.23	Large area overview of coating on PCP film . . . . .	107
4.24	Coating of ~300 μm 3D CNT structure with iron oxide from Fe <sup>3+</sup> on PCP film . . .	108
4.25	Coating of nanoscale CNT structure with iron oxide from Fe <sup>3+</sup> on PCP film . . . . .	109
4.26	Electrochemical characterization of Fe <sub>2</sub> O <sub>3</sub> -CNT structure with Fe <sup>3+</sup> . . . . .	111
4.27	Coated 3D CNT structure opened after 40 cycles . . . . .	112
4.28	Electrochemical characterization of Fe <sub>2</sub> O <sub>3</sub> -CNT structure with Fe <sup>2+</sup> . . . . .	113
4.29	XRD-comparison of the two precursors used for the Fe-2O <sub>3</sub> formation . . . . .	113
4.30	Fabrication process Si-colloidal CNT structure . . . . .	115
4.31	Coating of the nanoscale CNT structure with thermal Si-CVD . . . . .	116
4.32	Height change during transfer and EDX of intial bottom after transfer . . . . .	117
4.33	Thicker Si-coating on nanoscale 3D CNT structure . . . . .	119

4.34	PVD Si-coating on microscale 3D CNT structure . . . . .	120
4.35	Electrochemical characterization of CVD-grown Si on nanoscale structures . . . . .	121
4.36	Electrochemical characterization of PVD-grown Si on microscale structures . . . . .	123
5.1	CNT honeycombs coated with BiVO <sub>4</sub> , scale bar 30 μm. . . . .	125
5.2	Comparison energy density of fuel cells and batteries . . . . .	126
5.3	Schematic of a PEC cell . . . . .	127
5.4	Overview of semiconductors in solar watersplitting . . . . .	128
5.5	Two examples for BiVO <sub>4</sub> with conductive materials . . . . .	130
5.6	Concept of suggested hybrid photoelectrode . . . . .	131
5.7	Transfer of CNT honeycomb structures onto film and coating . . . . .	132
5.8	Coating of 3D CNT structures following a hydrothermal, 1h protocol . . . . .	133
5.9	Coating of 3D CNT structures with olive-like BiVO <sub>4</sub> nanoparticles . . . . .	135
5.10	Coating of 3D CNT structures with olive-like BiVO <sub>4</sub> - soaking in precursor . . . . .	136
5.11	Coating of 3D CNT structures with BiVO <sub>4</sub> hydrothermally by Liu et al. . . . .	137
5.12	Coating of 3D CNT structures with BiVO <sub>4</sub> hydrothermally - stirred reactor . . . . .	138
5.13	Hotcasting with acetic acid and acetylacetone as solvents . . . . .	139
5.14	Hotcasting with ethylene glycol and water as solvents . . . . .	140
5.15	Hotcasting with nitric acid as a solvent . . . . .	141
5.16	Two configurations of the honeycomb-BiVO <sub>4</sub> photoelectrode . . . . .	141
5.17	Photocurrent measurement of BiVO <sub>4</sub> structure with Mo underlayer . . . . .	142
5.18	Photocurrent measurement of BiVO <sub>4</sub> structure with Au/Pd conductive coating . . . . .	143
6.1	Stress relief features connected by foamed CNT forest . . . . .	149
6.2	Stress relief features connected by serpentine structures . . . . .	149
6.3	CNT honeycombs for heavy metal sensing . . . . .	151
6.4	CNT honeycombs for bone tissue engineering . . . . .	153
7.1	Langmuir blodgett trough setup for monolayer formation . . . . .	157
7.2	Set-up for BiVO <sub>4</sub> photoelectrode measurements . . . . .	164
A1	Overview of microwave radiation and chemistry applications . . . . .	188
B1	Densification with and without crust . . . . .	189

B2	Cracking during honeycomb formation for increased forest height . . . . .	191
B3	Effect of RIE-ICP etching on PS spheres . . . . .	191
B4	Etched colloids with a tilted view . . . . .	192
B5	Shear effect after transfer of colloidal CNT structure . . . . .	193
B6	Synthesis of hollow Fe <sub>2</sub> O <sub>3</sub> nanospheres . . . . .	193
B7	Synthesis of Fe <sub>2</sub> O <sub>3</sub> cubes . . . . .	194
B8	Reference patterns for matched XRD patterns . . . . .	194
B9	Particle overview for different reaction times . . . . .	195
B10	Coating of the 3D CNT structures on PCP film . . . . .	195
B11	Cracking in a thick standard film . . . . .	196
B12	EDX mapping of bottom of sample after transfer . . . . .	196
B13	SEM and XRD of particles produced following Zhang et al.'s protocol . . . . .	196
B14	XRD of coating with BiVO <sub>4</sub> - using a recipe by Shang et al. . . . .	197
B15	Coating of 3D CNT structures with olive-like BiVO <sub>4</sub> - soaking in precursor 2 . . . . .	197
B16	Initial hotcasting results by J. Rongé . . . . .	197
B17	Serpentine structures for stress relief features . . . . .	198



# List of tables

4.1	Temperature screen of Fe <sup>2+</sup> and Fe <sup>3+</sup> as a precursor-SEM . . . . .	101
4.2	Si-O ratio measured with EDX on coated sample . . . . .	118
7.1	Growth times and temperatures and the resulting CNT structure heights . . . . .	158
7.2	Overview of further hotcasting experiments . . . . .	163
A1	Comparison between evaporation and sputtering PVD . . . . .	187
A2	Comparison of several powder synthesis methods . . . . .	188
B1	Comparison of negative and positive photoresist characteristics . . . . .	189
B2	Overview of experimental parameters using 'design of experiments' . . . . .	190
B3	Area change before and after densification for stress relief features . . . . .	191
B4	Etching rates for various parameters . . . . .	192



# List of abbreviations

## Greek Symbols

$\gamma$	Surface tension
$\theta$	Contact angle

## Acronyms / Abbreviations

AFM	Atomic force microscopy
ALD	Atomic layer deposition
CA	Chronoamperometry
CNTs	Carbon nanotubes
CV	Cyclic voltammetry
CVD	Chemical vapor deposition
DMF	Dimethylformamide
EC-DMC	Ethylene carbonate - dimethyl carbonate
EG	Ethylene glycol
HAp	Hydroxyapatite
hcp	Hexagonally-close packed
HRTEM	High resolution transmission electron microscopy
LIB	Lithium-ion battery
LiPF <sub>6</sub>	Lithium hexafluorophosphate
MWNTs	Multi-walled carbon nanotubes
Nd:YAG	Neodymium-doped yttrium aluminium garnet, Nd:Y <sub>3</sub> Al <sub>5</sub> O <sub>12</sub>
NMP	N-Methyl-2-pyrrolidone

PANI	Polyaniline
PCBM	Phenyl-C61-butyric acid methyl ester
PCP-film	PVDF/CNT/PCBM-film
PEC	Photoelectrochemical
PMMA	Poly(methylmethacrylate)
PNIPAM	Poly(N-isopropylacrylamide)
PS	Polystyrene
PVA	Polyvinyl alcohol
PVDF	Poly(vinylidene fluoride)
PVD	Physical vapor deposition
PV	Photovoltaics
RAFT	Reversible addition fragmentation chain transfer
RHE	Reversible hydrogen electrode
RIE	Reactive ion etching
rpm	Rotations per minute
SAXS	Small angle X-Ray scattering
SDS	Sodium dodecyl sulfate
SEI	Solid-electrolyte interface
SEM	Scanning electron microscopy
SWNTs	Single-walled carbon nanotubes
THF	Tetrahydrofuran
UCST/ LCST	Upper/ lower critical solution temperature
UV	Ultraviolet
VACNT	Vertically aligned carbon nanotubes
VLS	Vapor-liquid-solid
VSS	Vapor-solid-solid

## **Part I**

# **Introduction and Project Goals**



Carbon can appear in many different structures and hybridization states. The first all-carbon molecule found was the buckminsterfullerene, discovered by Kroto and Smalley in 1985.<sup>[1]</sup> Another all-carbon molecule is graphite with its planar structure with  $sp^2$  hybridized atoms and an electron cloud surrounding the planar layers due to the overlapping  $\pi$  orbitals. The layers are stacked in an ABAB sequence with a layer spacing of about 0.334 nm.<sup>[2]</sup> A single layer of graphite is called graphene and was discovered in 2004 by Novoselov et al.<sup>[3]</sup> This created as much scientific interest as the recognition of carbon nanotubes (CNTs) in 1991 by Iijima.<sup>[4]</sup> The structure of single-walled CNTs is that of a "rolled up" graphene sheet, which means it is a tube made out of a hexagonal lattice of  $sp^2$  carbon atoms with either open or closed tips and a void single internal channel. CNTs can be single-walled or multi-walled which have a structure with several concentric cylinders around each other.<sup>[5]</sup> Since 1991, CNTs have been under thorough scientific investigation for various applications due to their unique mechanical, thermal and electrical properties.<sup>[6]</sup> Low-defect single-walled CNTs show a Young's modulus of up to 1 TPa,<sup>[7]</sup> a current density that exceeds copper ( $4 \cdot 10^9 \text{ A cm}^{-2}$ )<sup>[8]</sup> and a thermal conductivity ( $3500 \text{ W m}^{-1} \text{ K}^{-1}$ )<sup>[9]</sup> that exceeds diamond. Due to those very interesting properties, CNTs have been considered as promising materials for applications in a range of domains, such as water purification and filtration,<sup>[10–15]</sup> CNT-polymer composites for advanced electrical and mechanical properties,<sup>[16–18]</sup> transistors,<sup>[19–23]</sup> MEMS-devices like resonators,<sup>[24–26]</sup> sensors and biosensors,<sup>[27–31]</sup> electrodes for supercapacitors and batteries<sup>[32–35]</sup> and flexible electronics.<sup>[36–39]</sup>

CNTs can be grown with high quality and at precisely determined locations to record lengths of half a meter.<sup>[40]</sup> A challenge, however, is to preserve their impressive properties in CNT assemblies, as these typically degrade by an order of magnitude when the assembly is random. To preserve the properties for the above mentioned applications, much work has focused on CNT alignment, horizontally, e.g. into films or sheets<sup>[41–44]</sup> or yarns,<sup>[45–48]</sup> or vertically into CNT "forests".<sup>[49–51]</sup> CNT forests are very promising due to additional, specific properties, such as anisotropy through alignment and high specific surface area.<sup>[52]</sup> Patterning of vertically aligned forests<sup>[53]</sup> offers opportunities for advanced electrode designs that are able to tackle challenges of diffusion limited processes, as they e.g. occur in Lithium-ion batteries. Vertically aligned CNT structures themselves have already been reported for a range of applications, such as supercapacitor electrodes,<sup>[54,55]</sup> microelectromechanical devices<sup>[56]</sup> and integrated nanoelectronic devices.<sup>[57]</sup> Depending on the application of these electrodes a different surface chemistry is needed. The focus in this thesis is on creating advanced CNT electrode structures with the corresponding active materials for Lithium-ion battery and watersplitting electrodes. These hybrids are synthesized and tested electrochemically to investigate their performance as advanced electrodes compared to the current standards in both areas.

**Advanced Li-ion battery anodes** Electrochemical advances in portable electronics and electric vehicles require Li-ion batteries with even higher energy and higher power density. One way to improve the energy density is to increase the amount of active material by increasing the thickness of the active material slurry film in comparison to the collector electrode. This increases the gravimetric battery performance as more material can be added without increasing other materials of the total cell mass, such as packaging, which can also lead to a 50% reduction in cost.<sup>[58]</sup> However to date, such thick

electrodes suffer from (i) poor Li-ion diffusion through the electrode (ii) poor electrical conductivity and thus ohmic losses, (iii) poor heat dissipation, and (iii) manufacturing challenges such as cracking and flaking of the electrode during drying.<sup>[58]</sup> This thesis is aiming to address those bottlenecks by an advanced electrode architecture combining a vertically aligned CNT structure with diffusion pathways and desired battery materials. Those advanced, thick electrode structures should enable a better high rate performance and increased stability compared to standard film electrodes with the same materials. While a range of three-dimensional hybrid structures, such as Fe<sub>2</sub>O<sub>3</sub>/C foams,<sup>[59]</sup> Nickel nanotube arrays with Fe<sub>3</sub>O<sub>4</sub>@MnO<sub>2</sub>,<sup>[60]</sup> porous wood<sup>[61]</sup> and CNT forests with electroplated Nickel particles<sup>[32]</sup> or Manganese oxide,<sup>[62]</sup> has been reported for energy storage, very limited literature can be found on CNT/inorganic hybrid structures with vertically aligned CNTs for Lithium-ion batteries which makes this an exciting gap in the literature to explore. A few records highlight the promise of those hybrid structures, e.g. Lu et al.<sup>[63]</sup> reported CNT forests with electrodeposited V<sub>2</sub>O<sub>5</sub>, Gohier et al.<sup>[64]</sup> showed a coating with silicon on CNT forests and Ahmad et al.<sup>[65]</sup> highlighted the advantage of a 3D CNT cone structure with Fe<sub>2</sub>O<sub>3</sub> for flexible batteries.

**Advanced photoelectrodes for solar watersplitting** With the current search for more sustainable energy sources, water as a feedstock for fuel is very promising as a cheap, abundant and non-toxic material. Clean energy can be gained by hydrolysis, resulting in H<sub>2</sub> as a fuel. This can be done through photoelectrochemical splitting of water.<sup>[66,67]</sup> Here the electrode surface area is directly linked to the amount of charge pairs created and thus crucial for the efficiency of the device. Additionally, it needs to be ensured that the charge separation is faster than the recombination time. A conductive 3D CNT backbone with a photoactive material coating is a promising architecture to address these points and achieve a higher conversion. Bismuth vanadate (BiVO<sub>4</sub>) is a widely used material in solar watersplitting and is thus combined with the new CNT structure.

**Approach for electrode fabrication** Patterned vertically aligned CNT forests of different heights and structure dimensions are prepared in this thesis using two types of lithographic methods, colloidal and UV-lithography, with subsequent CNT growth in a chemical vapor deposition (CVD) furnace. Those structures are then modified with the respective inorganic materials for the specific application, using a range of protocols. As strong inorganic-carbon coupling has been shown to increase the electrochemical performance of electrodes,<sup>[68–71]</sup> in-situ synthesis is used for the coatings. Hydrothermal, microwave-assisted synthesis is used for the first time on CNT forests. Previously reported coating methods for CNT forests utilize either gas phase deposition, electrodeposition or drop-casting of pre-synthesized particles to not destroy the delicate CNT hierarchical structure. This significantly limits the range of materials that can be used or often relies on physical adsorption of the active material onto the CNTs which can result in poor electrical contact over long term cycling. Thus the hydrothermal, microwave-assisted approach is a very promising route for further research and an increase in the material range for carbon-inorganic hybrid materials.

Figure 0.1 shows an overview of the approach followed in the PhD project.

- (I) **3D CNT structure synthesis:** The first objective is the fabrication of the growth template either on the microscale using UV-lithography or on the nanoscale using colloidal lithography. By adjusting the template masks, various pore sizes for the CNT structures, grown by CVD, can be achieved. This is reported in chapter 3.
- (II) **3D CNT structure modification:** The synthesized vertically aligned CNT structures on nano- and microscale are then functionalized with selected materials. Iron oxide and silicon are used as anode materials for Lithium-ion batteries (reported in chapter 4). Bismuth vanadate represents a material that is used in watersplitting applications (reported in chapter 5).
- (III) **Electrochemical testing:** The synthesized CNT/inorganic material hybrid electrodes are then tested for their electrochemical performance. This is done by Simon Engelke in the same group for the Lithium-ion battery anodes (results in chapter 4) and by Jan Rongé at KU Leuven, Belgium, as electrodes for solar watersplitting (results in chapter 5).

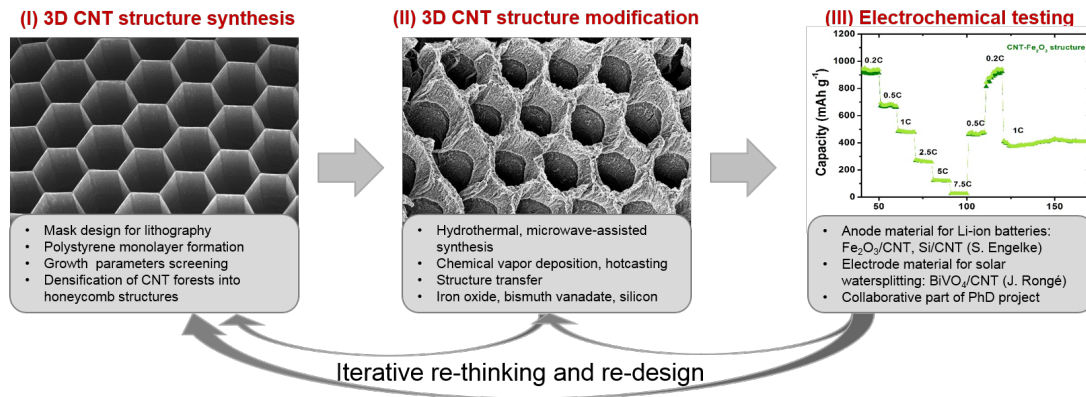


**Fig. 0.1** Overview of the steps of the project, from the synthesis of the 3D CNT structure to the modification to the final testing for the applications.



## **Part II**

# **Introduction to Carbon Nanotubes: Structures and Modification**



## Chapter 1

# Carbon Nanotubes (CNT) Overview



Random CVD-grown CNTs, scale bar 100  $\mu\text{m}$ .

## 1 Carbon Nanotubes (CNT) Overview

Carbon nanotubes (CNTs), first described in 1991 by Iijima,<sup>[4]</sup> are a very promising material for many applications due to their impressive mechanical, electronic and thermal properties. This chapter will discuss the CNT structure, their properties and the fabrication of CNT powders and aligned structures, as well as patterning methods for vertically aligned CNT and elastocapillary self-aggregation for different shapes in CNT structures.

### 1.1 CNT structure and properties

#### 1.1.1 CNT structure

A single-walled CNT can be imagined as a "rolled up" graphene sheet. This means the tubular structure is composed of a hexagonal lattice of  $sp^2$  hybridized carbon atoms with a strong  $\sigma$  bond of 0.142 nm and with the  $p_z$ , or  $\pi$ , orbitals providing an electron bond network.

As shown in figure 1.2, graphene sheets can theoretically be rolled up in different ways to form CNTs. This is described by the circumference vector, also called chiral vector  $C$ . It leads to different CNT structures that are chiral to each other. The chiral vector is defined by a pair  $(n,m)$  of integers.<sup>[72]</sup>

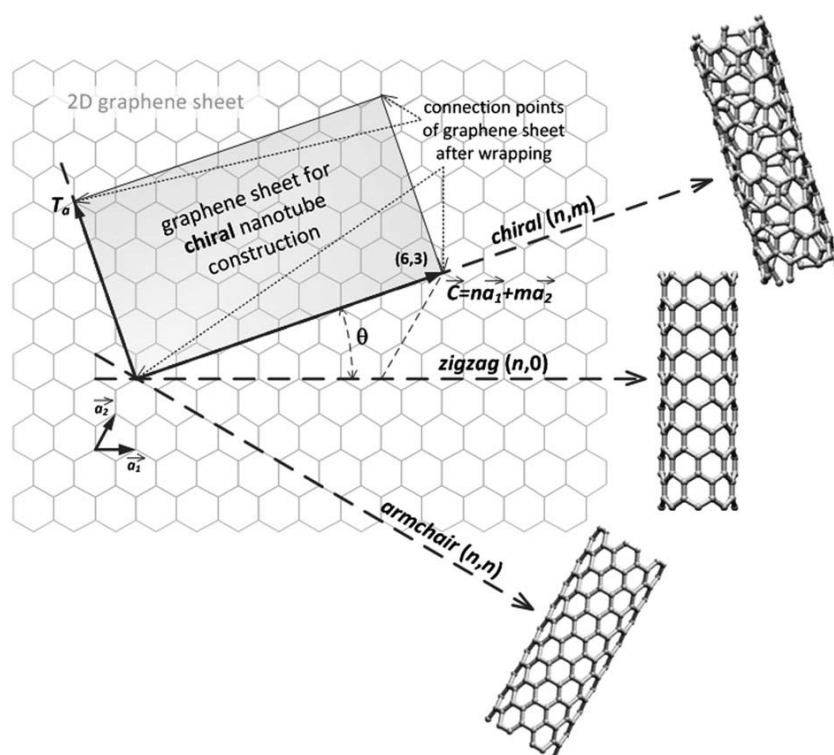


**Fig. 1.2** Schematic overview of the different structures of CNTs, as defined by the chiral vector and its integers  $(n,m)$ .<sup>[6]</sup>

We can distinguish three types of CNTs depending on their chirality: (1) the "zig-zag" configuration with  $m = 0$   $(n,0)$ , (2) the "armchair" configuration has an  $n$  equal to  $m$   $(n,n)$  and (3) general "chiral"

CNTs where  $n > m > 0$ .<sup>[2]</sup> As  $|a_1| = |a_2| = 0.246 \text{ nm}$ , the length of the chiral vector  $C$  is defined as  $0.246\sqrt{n^2 + nm + m^2}$ . Hence, the diameter  $d_t$  of specific configuration is given by<sup>[2]</sup>

$$d_t = 0.246\sqrt{n^2 + nm + m^2}/\pi. \quad (1.1)$$

And the chiral angle  $\theta$  is defined as

$$\theta = \sin^{-1} \frac{\sqrt{3}m}{2\sqrt{(n^2 + nm + m^2)}}. \quad (1.2)$$

This chirality determines the electrical properties of CNTs, as explained later. CNTs can occur as single-walled (SWNTs), double-walled and multi-walled CNTs (MWNTs). For MWNTs several concentric single-walled CNTs are wrapped around each other with a spacing of 0.340 nm. The typical diameters range between 0.8 to 2 nm for SWNTs and 5 to 20 nm for MWNTs.<sup>[5]</sup> The length is dependent on the synthesis method and ranges from less than 100 nm to the record of half a meter.<sup>[40]</sup>

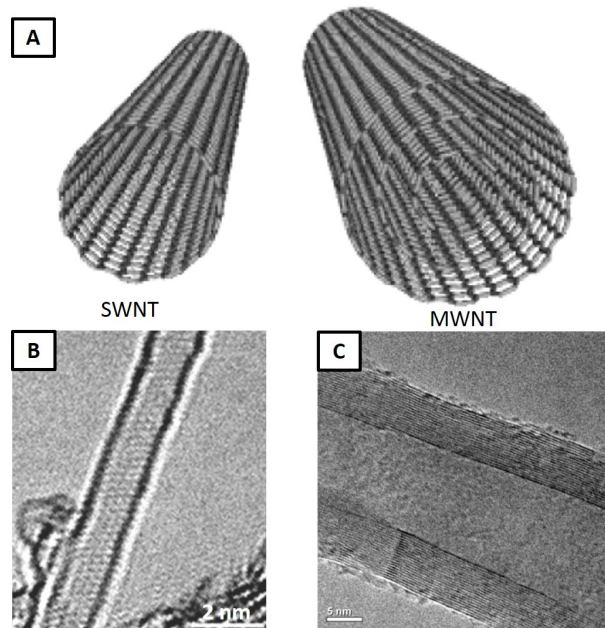


**Fig. 1.3** SWNTs and MWNTs are schematically shown in A.<sup>[73]</sup> An HRTEM image of a SWNT with enhanced contrast of the zig-zag structure<sup>[74]</sup> and a TEM image of a CVD-synthesized MWNT is shown in C.<sup>[73]</sup>

A schematic structure of an SWNT and an MWNT can be seen in figure 1.3(A). Then an high resolution transmission electron microscope (HRTEM) image of a SWNT is shown in (B) and a TEM image of an MWNT in figure 1.3(C).<sup>[73,74]</sup>

The shown hexagonal network is not always perfect - depending on the synthesis method it can contain defects. *Elbow connections* can occur when armchair tubes are joined to zig-zig tubes by a pentagonal ring on the outer side of the elbow and a heptagon on the inner side. Another type of defect is the Stone-Wales transformation, shown in figure 1.4. In this type of defect two hexagons turn

## 1 Carbon Nanotubes (CNT) Overview

into a pentagon and a heptagon, introducing a '5-7-7-5' rearrangement. While individual pentagons and hexagons can introduce a positive or negative curvature in the perfect linear tube structure, this one cancels itself out. Those defects can be seen in figure 1.4 with the elbow connection for a (5,5) armchair CNT in (A) and the Stone-Wales transformation in (B).

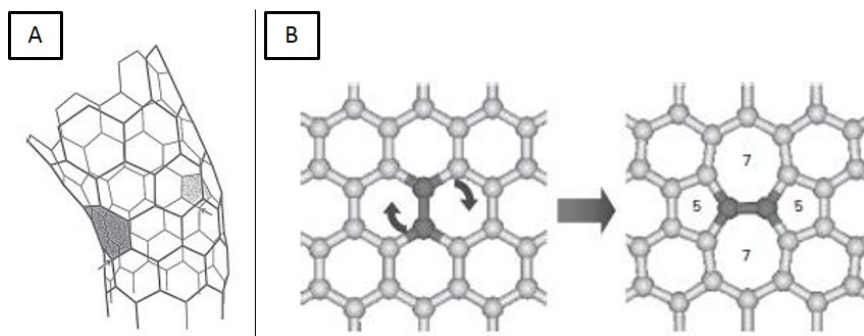


**Fig. 1.4** A perspective drawing with pentagon and heptagon shaded in (A) shows the *elbow connection* of a (5,5) armchair. In (B) the Stone-Wales transformation that leads to a '5,7,7,5' defect is shown.<sup>[2]</sup>

The structure can also be affected by defects through vacancies or adatoms.<sup>[2]</sup> The higher the concentration of defects, the lower their stiffness and tensile strength.<sup>[26]</sup>

### 1.1.2 CNT properties

As mentioned before, CNTs are highly attractive due to their impressive properties that can exceed those of existing materials. Those properties will be discussed in more detail in this chapter.

#### 1.1.2.1 Mechanical properties

Due to the strong  $sp^2$  bond between the carbon atoms, CNTs have a high Young's modulus and tensile strength. The Young's modulus of individual high-quality nanotubes exceeds 1 TPa. For MWNTs a tensile strength of 100 GPa has been measured.<sup>[18]</sup> This strength is over 10-fold higher than any industrial fibre.<sup>[5]</sup> One way to utilize this strength is to spin CNT yarns and fibres out of those CNTs.<sup>[75]</sup> However, those values vary depending on the synthesis method. The arc-grown CNTs have a Young's modulus of around 870 GPa whereas the catalytically grown ones only reach a modulus of 100-350 GPa. This clearly demonstrates that catalytically grown CNTs are inferior to arc-grown ones due to their high defect density.<sup>[2]</sup>

#### 1.1.2.2 Electrical properties

SWNTs are classified as metallic or semiconducting according to a simple ruleset depending on their chirality. Armchair CNTs all are metallic, zig-zag CNTs are metallic when  $n$  is divisible by three, but otherwise semiconducting. Chiral CNTs are metallic when  $n-m=3q$ , where  $q$  is an integer;

otherwise they are semiconducting. About one-third of chiral tubes are metallic and two-thirds are semiconducting.<sup>[2]</sup>

Electrical transport inside CNTs is affected by scattering, defects and lattice vibrations, which can lead to higher resistance. Defect-free metallic SWNTs show ballistic behaviour. Ballistic transport occurs when electrons pass along a conductor without experiencing any scattering from impurities or phonons. Then the electrons do not encounter any resistance. This is an important aspect of quantum wire behaviour and means that large amounts of current can be conducted without dissipating heat. It depends on structural perfection, temperature and the size of the driving electric field.<sup>[76]</sup> A metallic SWNT has a resistance around 6.5 k $\Omega$ . SWNT bundles exhibit current densities up to  $1,000 \cdot 10^6 \text{ Acm}^{-2}$ , which exceeds copper ( $\sim 10^6 \text{ Acm}^{-2}$ ).<sup>[77]</sup> Chen et al.<sup>[52]</sup> found that the electrical conductivity peaks (178 S/cm) around a wallnumber of 2.7 and a diameter of 5.4 nm.

Arc-discharge MWNTs have been found to have an average resistivity of several  $\text{k}\Omega\mu\text{m}^{-1}$ , a resulting electrical conductivity of approximately  $1\text{-}2 \cdot 10^3 \text{ Scm}^{-1}$  and very high current densities of about  $10^7 \text{ Acm}^{-2}$ .<sup>[78,79]</sup> MWNTs produced the same way were also tested for their current carrying capacity and reliability under high current densities ( $>10^2 \text{ Acm}^{-2}$ ) and no failure in the structure or change in resistance for temperatures of up to 250 °C has been found, making them very promising choices for nanoelectronic devices as they can avoid electromigration.<sup>[80]</sup>

### 1.1.2.3 Thermal properties

Thermal conductivity of CNTs is superior to even that of diamond due to the strength and toughness of the  $\text{sp}^2$  bonds and 1D character of the tubes which strongly limits the allowed scattering processes.<sup>[75]</sup> Individual SWNTs can have a thermal conductivity of  $3500 \text{ W m}^{-1}\text{K}^{-1}$  at room temperature,<sup>[5]</sup> exceeding that of pure diamond is around  $2000\text{-}3000 \text{ Wm}^{-1}\text{K}^{-1}$ .<sup>[2]</sup> Even for catalytically grown MWNTs the intrinsic thermal conductivity at room temperature was measured to be  $2586 \text{ Wm}^{-1}\text{K}^{-1}$ .<sup>[81]</sup> Looking at the heat transport, it is ballistic for SWNTs at low temperatures. At higher temperatures, the thermal conductivity decreases due to defects.<sup>[75]</sup>

### 1.2 Fabrication methods for pristine CNT powders

A lot of systematic research began with Iijima's observation of CNTs produced in an arc-discharge fullerene reactor.<sup>[82]</sup> Since then, several new methods to synthesize CNTs have been developed. The most important ones are shortly discussed here.

#### Arc discharge

In this fabrication method, a chamber is filled with He and a direct-current arc-discharge is used between two graphite electrodes to generate CNTs. Also H<sub>2</sub> or CH<sub>4</sub>, ethanol, acetone and hexane can be used as gases for the atmosphere. MWNTs can easily be generated in this high temperature process and by tuning the gas type and pressure a high yield and high purity/ crystallinity can be achieved.<sup>[6]</sup> While the throughput of the synthesis can be very high (20-100 mg min<sup>-1</sup>), the discharge only lasts for a few minutes.<sup>[2]</sup> There are several theories for the formation of nanotubes during the arc-discharge:<sup>[2]</sup> (1) A vapour phase growth was proposed where the nucleation and growth is assumed as a direct condensation from the vapour phase with the arc's electric field playing an essential role. (2) A liquid phase growth was suggested by De Heer et al.<sup>[83]</sup> in 2005 where they proposed that the arc-discharge caused the anode to locally liquify creating liquid carbon globules which act as nucleation points of CNTs and nanoparticles. (3) Harris et al.<sup>[84]</sup> proposed a solid state model in 1994 where the carbon condenses onto the cathode, experiences very high temperatures and then acts as seeds for the nanotube growth. (4) The other suggested model is the crystallization model where the authors suggested that the growth of the MWNTs doesn't occur from one end to another but rather in the form of a crystallization process from the surface to the center.<sup>[2]</sup>

With the addition of a metal catalyst, such as Ni, Fe or Co, also SWNTs can be produced.<sup>[85]</sup> In this process, unwanted species such as MWNTs or fullerenes are typical by-products. A high crystallinity and purity can be achieved by a modified process using a carbon anode with 1% Fe-catalyst in an H<sub>2</sub>-Ar atmosphere, combined with an oxidation purification process to remove the Fe catalyst nanoparticles.<sup>[6]</sup>

#### Laser vaporization

The pulsed laser deposition uses a high temperature technique similar to the arc discharge. A laser pulse is applied to a graphite pellet that also contains the catalyst material in a furnace that is heated to ~1200 °C with an inert gas at a constant pressure. Catalysts are usually Ni or Co and the lasers are Nd:YAG and CO<sub>2</sub>. The process is very dependent on the laser properties, the structural and chemical composition of the target material, the chamber pressure, the buffer gas and the temperature.<sup>[2]</sup> SWNTs of high-quality and high-purity can be grown. It has been reported that mostly metallic SWNTs can be grown with this method.<sup>[86]</sup> However, the equipment is very expensive and has a poor scalability.<sup>[6]</sup>

### Chemical vapor deposition

Chemical vapor deposition (CVD) can be used to produce large volumes of CNTs as it is easy to scale up, uses low cost feedstocks and has a high yield and little waste.<sup>[87]</sup> The produced CNTs have shorter lengths and a higher defect density that influences their properties.<sup>[44]</sup> In addition to low catalyst yields and short catalyst lifetimes as the disadvantages of this methodology,<sup>[6]</sup> it is believed to generate CNTs that are structurally inferior to the two previously mentioned methods. While this might be true for MWNTs, SWNTs with high structural perfection have been produced using CVD methods.<sup>[2]</sup> For SWNTs, several factors need to be controlled: the temperature, the feedstock and the size of the catalyst particles are most important. The temperatures in the furnace need to be increased to 900-1200 °C and the feedstock needs to be adjusted accordingly to the ones with a high thermal stability, such as CH<sub>4</sub> and CO. Addition of H<sub>2</sub> or benzene to the gas flow enhances the SWNTs yield.<sup>[2]</sup> Nanoparticles of less than 1.8 nm were observed to be the most active in SWNT growth, while above 7 nm did not lead to any SWNT growth.<sup>[88]</sup> By controlling the growth process very well, it is possible to direct the synthesis for specific electronic structures of SWNTs, metallic or semiconducting, control B- or N-doping, length and purity and produce large quantities.<sup>[5,6]</sup>

To produce high volumes of MWNTs, it was found that ferrocene or iron pentacarbonyl as the catalyst as well as the carbon source work very well. This also brings the advantage that there is no spare catalyst that needs to be removed afterwards.<sup>[2]</sup> Deck et al.<sup>[89]</sup> published a study looking at a variety of transition metal catalysts and their activity of MWNT growth. They found that of the tested catalysts, Fe, Co and Ni are the only catalysts producing MWNTs with the solubility of the carbon in the metal being the most important parameter. This solubility was found to be 0.5-1.5 wt% carbon for successful growth with lengths varying from 2 μm to 3 mm and diameters ranging from 20 nm to 60 nm. The mechanism suggested here is that the carbon-containing molecules decompose on one side of the metal particle and the tube grows on the opposite side.<sup>[2]</sup>

The good control of the growth process in this method enables growth of CNT arrays on substrates.<sup>[2]</sup> SWNTs as well as MWNTs can be grown this way. Dai et al.<sup>[90]</sup> have shown that vertically aligned SWNT arrays can be grown on Si/SiO<sub>2</sub> substrates and Fe catalysts with a plasma enhanced CVD method. Vertically aligned CNT growth using CVD is a crucial part of this thesis and will be discussed more in detail in chapter 1.3.

### Classical wet chemistry

Bottom-up organic syntheses have been reported where homogeneous CNTs with well defined structures can be formed. A CNT synthesis with control of chirality was prepared by utilizing hoop-shaped carbon macrocycles, that keep information regarding chirality and diameter, as templates.<sup>[91]</sup>

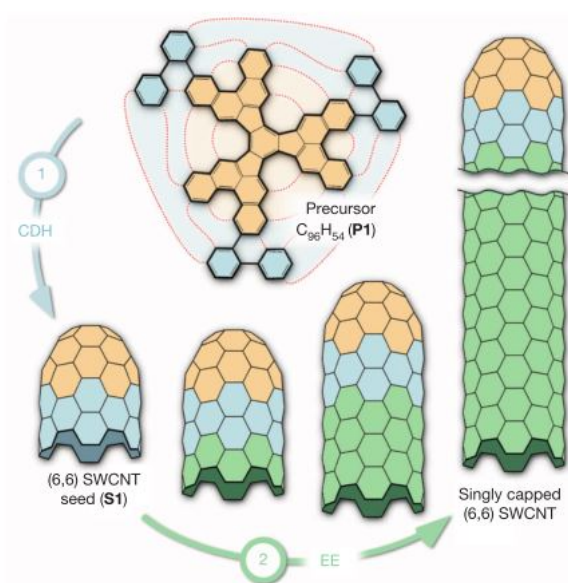


**Fig. 1.5** Schematic illustration of the two-step bottom-up synthesis of SWNTs with specific chirality.<sup>[92]</sup> In step 1 the polycyclic hydrocarbon precursor undergoes a cyclodehydrogenation, forming the seed for subsequent epitaxial elongation (step 2) into a singly capped (6,6) SWNT.

Also a solvent-free growth of armchair CNTs by a gas-phase Diels-Alder cycloaddition of benzyne to an aromatic hydrocarbon has been reported by Fort and Scott.<sup>[6,93]</sup> A controlled synthesis of single-chirality CNTs has been published by Sanchez-Valencia et al.<sup>[92]</sup> which uses a two-step synthesis starting with an organic precursor and then a CVD-type reactor. This process is schematically shown in figure 1.5. After the cyclodehydrogenation of a suitable polycyclic hydrocarbon precursor (step 1), seeds for the nanotube growth are generated. Those singly capped ultrashort (6,6) SWNTs are then grown via epitaxial elongation in a CVD furnace, forming singly capped (6,6) SWNTs.

### 1.3 Vertically aligned CNT structures

#### 1.3.1 Fabrication of vertically aligned CNT structures

Aligned CNTs are the most promising configuration to exploit the impressive properties of individual CNTs. The properties of CNTs are known to decrease by about an order of magnitude in random assemblies. Thus, for many applications the need for an alignment of the CNTs has arisen. CNTs can be assembled in a number of ways, each leading to specific structural properties for targeted CNT applications. Those ways of assembly can be seen in figure 1.6 in relation to the scale of alignment.<sup>[94]</sup>

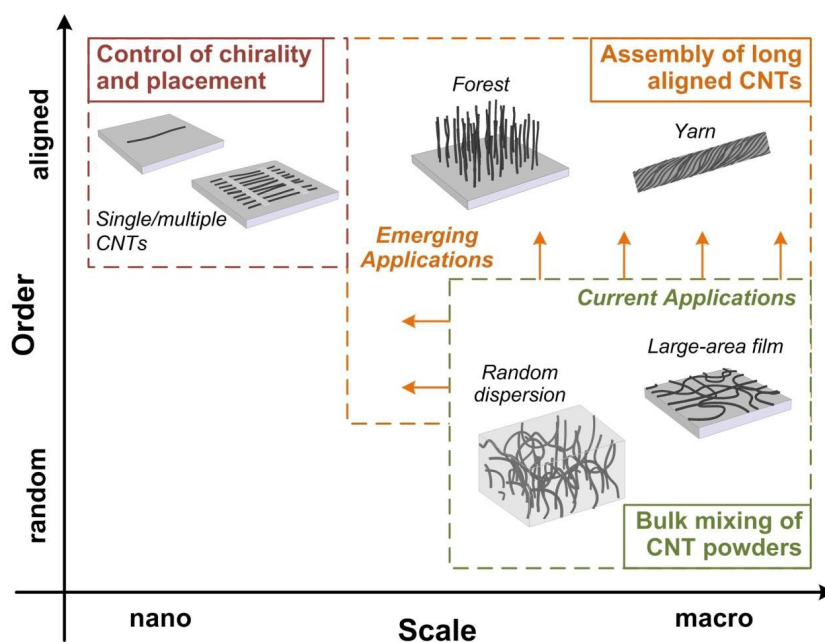
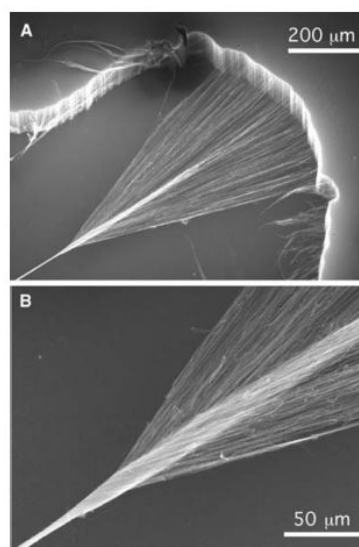


Fig. 1.6 Ways of CNT arrangement. [94]

Forests, yarns and sheets can be created to improve the properties and add new functionalities, like shape recovery, dry adhesion and high damping. [5] Ways to align CNTs and make assemblies are briefly listed here, including some examples:

- **CNT film creation:** Films can be created by post-processing or self assembly of dispersed CNTs as shown by various groups. [41–43,95] Fan's group synthesized super-aligned CNT arrays on 4" Si-wafers in low-pressure chemical vapor deposition (LP-CVD) systems, which can then be transformed into sheets. [96] Baughman's group described a process to obtain highly oriented CNT sheets by densifying an electronically conducting aerogel. [97] Lieber's group reported an alignment process using a 'bubble-blowing' method from a CNT suspension. [95]
- **CNT forest growth:** Self organizing, vertically aligned CNTs can be grown on a substrate with a catalyst in a chemical vapor deposition (CVD) process. [49–51] They show properties like high porosity, high specific surface area and flexibility. [52]

- **Alignment in fibres:** Windle's group employs "direct spinning" of CNTs where the CNTs are spun into fibres in a continuous process directly after gas phase synthesis in a CVD furnace.<sup>[45]</sup> Baughman's group developed an "array spinning" process where CNT fibres are spun from a forest of vertically aligned CNTs.<sup>[46]</sup> This spinning process can be seen in figure 1.7. Vigolo et al.<sup>[47]</sup> established the continuous spinning of fibres from a liquid crystal suspension, whereas Ericson et al.<sup>[48]</sup> use an acid spinning method that shows parallels to the Kevlar technology. Also electrospinning can be used to create yarns.<sup>[98]</sup> A range of MWNT yarns is shown in figure 1.8.<sup>[46]</sup>



**Fig. 1.7** SEM image of the spinning process of yarn from vertically aligned MWNTs forest.<sup>[46]</sup>

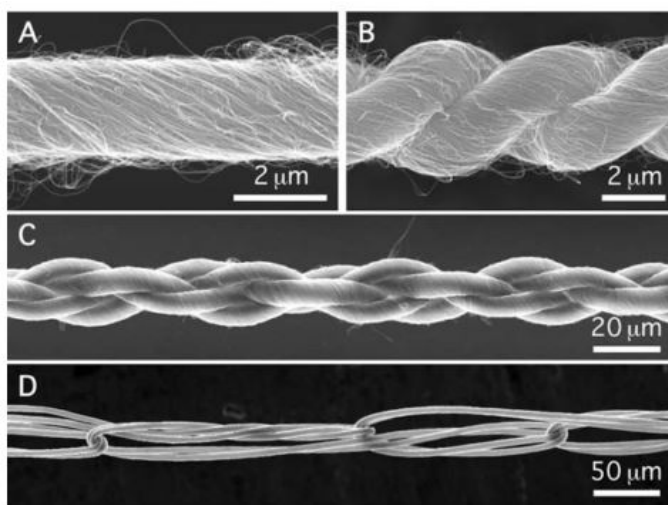


**Fig. 1.8** SEM images of MWNT yarns formed into more complicated knitted structures.<sup>[46]</sup>

CNT forest growth by CVD is one of the most versatile methods for creating structured CNT assemblies. It is usually done on Si-wafers as it allows to use UV-lithography and deposition techniques. CNT forest can also be grown in microscale arrangements of aligned CNTs using lithographic patterning of the catalyst, adding more functionality and flexibility to it. CNT forest growth was also demonstrated on A4 sized substrates<sup>[50]</sup> and commercial 300 mm wafer tools are available for this process, making this a potentially scalable method. For our applications a conductive structure with pores for the diffusion limited processes is needed. This can be achieved by CNT forests. Due to these advantages, this project focusses on CNT forests grown by CVD methods.

### 1.3.2 CNT forest growth by chemical vapor deposition

Li et al.<sup>[51]</sup> showed for the first time a large area alignment of CNTs on mesoporous silica with iron (Fe) particles as a catalyst when they used thermal decomposition of acetylene gas at temperatures above 700 °C. Following this, many reports have been published describing the growth of vertically aligned CNTs by CVD processes. A CVD process requires an activated carbon species. Methane, acetylene, carbon monoxide or liquid hydrocarbons are commonly used as carbon sources. CVD reactors can generate active carbon species either by thermal (thermal CVD) or by plasma activation (plasma-enhanced CVD).<sup>[99,100]</sup> Catalysts usually are first row transition metals like nickel, cobalt or Fe. The choice of catalyst significantly influences the growth process, growth rate and yield - and is thus an important parameter in the growth process. For forest growth, the catalyst is deposited on a substrate. This is done in various ways including physical vapour deposition, deposition from suspension as a thin metal-layer or nanoparticles on a substrate.<sup>[101]</sup>

In many thermal CVD processes, a quartz tube is inserted in a furnace either run at low or at atmospheric pressure. In figure 1.9(A) a schematic set-up of a CVD-furnace can be seen. This furnace has multiple mass flow controllers for different gases to be introduced into the flow reactor.<sup>[99]</sup> In the SEM in figure 1.9(B) a CVD grown forest can be seen. The vertically aligned CNTs are clearly visible in the higher magnification inset in (C). The forest was grown on an Si-wafer using Fe as a catalyst and an Al<sub>2</sub>O<sub>3</sub> underlayer.

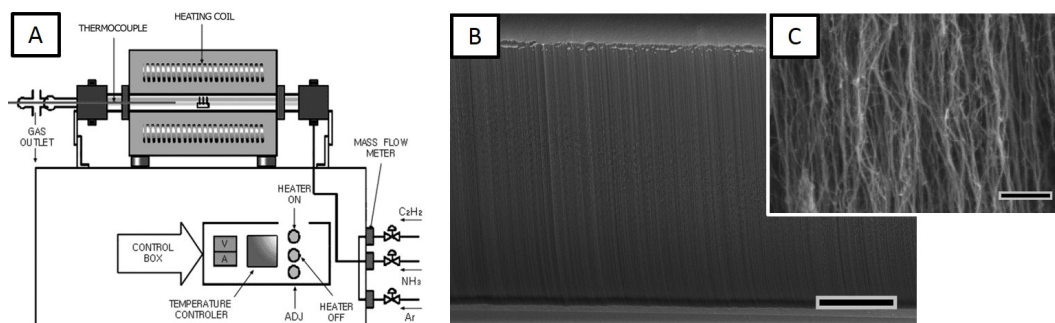


**Fig. 1.9** A schematic set-up of a CVD furnace is shown in (A). It has several mass flow controllers which enables the introduction of a range of gas mixtures into the flow reactor.<sup>[99]</sup> In (B) an SEM image of a CVD grown forest can be seen with a higher magnification in (C) where the alignment of the CNTs is clearly visible. Scalebar in (B) is 50  $\mu\text{m}$  and (C) is 300 nm.

The advantage of using a CVD process lies in the fact that it can easily be scaled up and is a cost-effective method to produce large area CNT arrays. A disadvantage, however, is their low density with the maximum density being about  $1 \cdot 10^{12}$  CNTs per  $\text{cm}^2$ .<sup>[102]</sup> Also the selection of the right feedstock and process parameters for a certain type of CNTs can be challenging.<sup>[103]</sup> It is well understood how to grow single-walled and multi-walled CNTs but the CNT growth of specific chiralities is just at the beginning of being understood, as shown by Yang et al.<sup>[104]</sup> where highly specific catalyst particles are used. Compared to CNT powders, CNT forests, especially lithographically patterned ones, can be very expensive and have a lower throughput. However, many

## 1 Carbon Nanotubes (CNT) Overview

---

application require a more specific arrangement of structures that cannot easily be provided by powders.

### CNT forest growth mechanism with CVD

CNT forest fabrication needs to be well understood to achieve the desired structures with the right density and height, thus the proposed growth mechanisms and dynamics will be discussed here.

**Growth mechanisms** When the catalyst is placed on a substrate, two possible growth mechanism have been observed, either *tip-growth* where the catalyst is lifted of the substrate by the growing CNT,<sup>[105]</sup> or *base-growth* or *root-growth* where the catalyst remains on the substrate while the CNT grows.<sup>[106]</sup> During the decomposition of the carbon species, CH or CCH and H radicals get formed which then dissociate into C and H atoms.<sup>[106]</sup> The interaction between the catalyst and substrate material is mainly responsible for the type of growth.<sup>[103]</sup> An example for a weak interaction between the catalyst and the substrate material resulting in tip-growth is Nickel as a catalyst on SiO<sub>2</sub>.<sup>[107]</sup> In contrast, using Fe or Co particles on a SiO<sub>2</sub> substrate or Fe on an alumina layer leads to base-growth.<sup>[2,108,109]</sup> For a thermal CVD growth a thin film of Fe was found to work very well, whereas for plasma-enhanced CVD growth Ni is preferred as a catalyst.<sup>[110]</sup>

For the growth of the CNT itself, initially the *scooter* mechanism was described for laser ablation and arc-discharge CNT growth.<sup>[111]</sup> It focusses on the importance of the isolated metal atom during growth absorbing onto open edges of a curving graphene sheet, and then scooting around at the edge to promote annealing of any carbon structure that is not the most energetically favored. Contrary to this mechanism, Yudasaka et al.<sup>[112]</sup> proposed a model where CNTs are produced through a separation of graphene from a molten carbon-metal mixtures.

For CVD-CNT synthesis, these models were adapted to explain the CVD-type growth. Dai et al.<sup>[113]</sup> described the mechanism for MWNTs as the following: The formation of a graphene cap, which they called *yarmulke*, lowers the surface energy of the particle. Newly arriving carbon atoms can either grow the shell around the carbon particle, form another cap below the initial one, forcing the out-most one to lift up and form a cylindrical tube, or add to the growing cylindrical section. The C atoms diffuse through the metal particle until supersaturation occurs, leading to segregation and graphitization.<sup>[114]</sup> This is similar to the vapor-liquid-solid (VLS) model suggested for the growth of silicon nanowires.<sup>[115]</sup> The yarmulke mechanism with the cap formation has been validated by in-situ TEM measurements.<sup>[116,117]</sup> Molecular dynamics simulations for the formation of that cap on an iron particle where shown by Ohta et al.,<sup>[118]</sup> giving further insights into the catalytic effects of the metal particle.

As this mechanism does not apply to all growth conditions, e.g. when using a non-metal catalyst, a vapor-solid-solid (VSS) model was proposed by Page et al.<sup>[119]</sup> for the growth of SWNTs from SiO<sub>2</sub>. In this model the SWNT nucleation occurred after the carbothermal reduction of the SiO<sub>2</sub> surface to SiC by CO and a subsequent carbon saturation. Another mechanism was proposed by Hofmann et al.<sup>[120]</sup> where they suggested a surface diffusion process rather than bulk diffusion for solid Ni and

Co. This model is supported by the fact that the activation energy of the MWNTs' growth rates corresponds clearly to the diffusion of carbon into solid metal particles. If the particles were liquid, the diffusion would be much faster.<sup>[2,121]</sup>

**Growth dynamics and stages** The morphology of a CNT forest has been shown to be spatially non-uniform and parameters like the alignment, diameter and packing density change dependent on the position in the forest. Bedewy et al.<sup>[109,122]</sup> have developed a method to understand more about those parameters and the associated growth dynamics. This method utilizes small angle X-ray scattering (SAXS) and real-time height kinetics. Using the X-ray to scan vertically through the forest, they study the mass and areal density of the forest dependent on the distance from the top. The results for a cold- and a hot-wall reactor are shown in figure 1.10. A cold-wall reactor has a heated substrate whereas the hot-wall reactor has a heated tube. As it can be seen in the graphs, process conditions like the rate of heating and annealing time (both shorter for the cold-wall reactor) significantly change the initial growth rate.

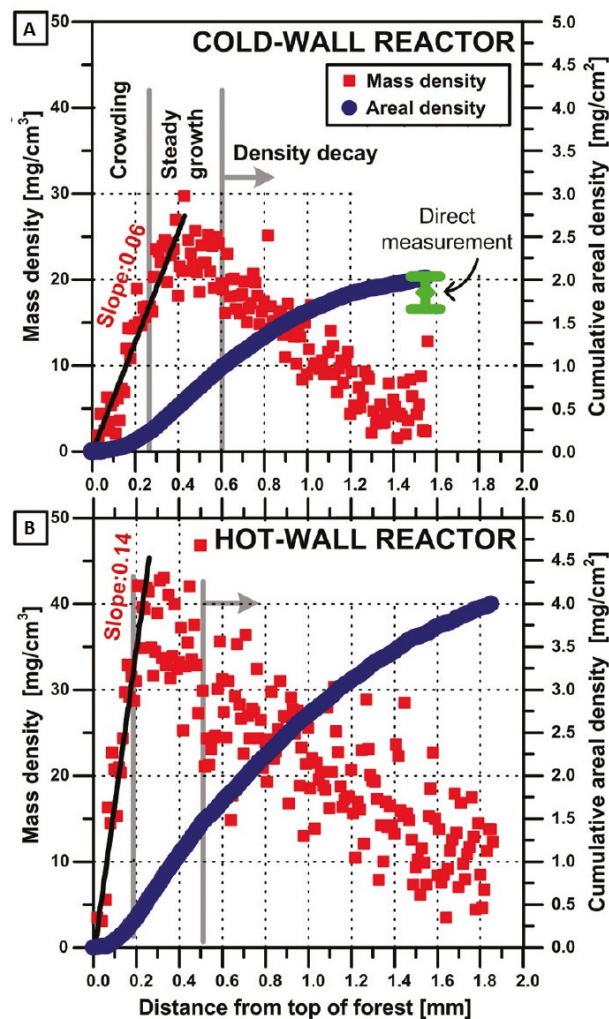


**Fig. 1.10** The graphs show the development in mass density and areal density in regards to the position measured in the forest (given in distance to the top of the forest) for a cold-wall reactor (A) and a hot-wall reactor (B).<sup>[109]</sup>

## 1 Carbon Nanotubes (CNT) Overview

The crowding phase in the cold-wall reactor is longer than for the hot-wall reactor. After the steady growth phase, the mass density starts decreasing for both reactors. The mass density curves also clearly show that the region of true uniformity of a forest is very small. The final cumulative areal density is twice as high for the hot-wall reactor which, as already mentioned, can be attributed to the process conditions. A longer annealing time might lead to more time for the reduction of the Fe particles and thus more active catalyst species.

In further analysis of the performed SAXS measurements it was found that the diametral ratio of the inner to outer CNT diameter is constant during the crowding phase in the beginning showing that there is no preferential nucleation of smaller or larger CNTs, as seen in figure 1.11A. During the steady growth stage and the density decay, however, the ratio increases and then starts dropping again in the termination stage. From this diametral ratio the number of walls can be calculated and it was found that it decreases from  $\sim 7$  to 5 after the crowding stage and then remains constant during the termination stage which can be linked to the catalyst activity, as smaller diameters lead to slow activation and long catalyst lifetimes. Not every catalyst particle contributes to the growth; in fact only maximum of 11% are activated. Additionally the CNT lengthening is compared to the forest height, as shown in figure 1.11B. It can be seen that a direct measurement of the forest height significantly underestimates the CNT length due to their tortuosity, making the mass density a better way to measure forest evolution.<sup>[109]</sup>

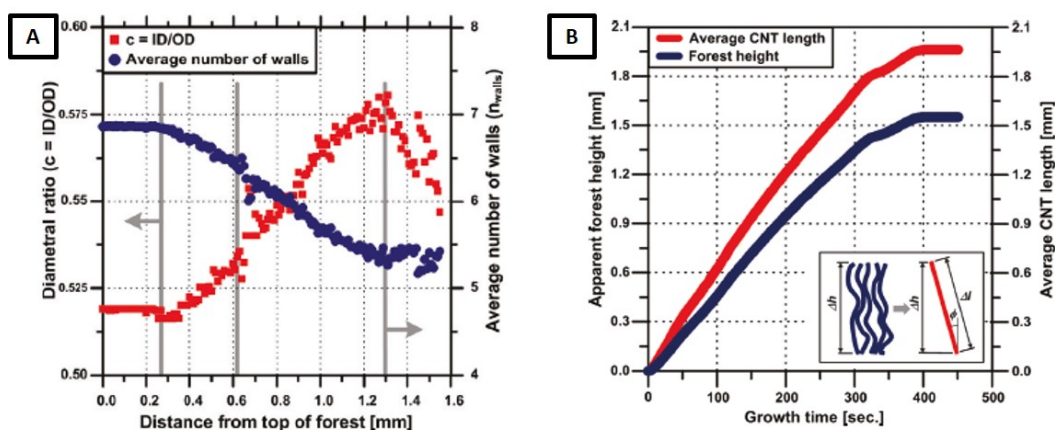


**Fig. 1.11** The development of the diametral ratio and the average number of walls with the distance from the top is shown in (A) and a comparison of the average CNT length and the forest height with the growth time is shown in (B), emphasizing the coupling and pinning aspect of the CNT forest growth.<sup>[109]</sup>

CNTs get pinned into contact by van der Waals forces which prevent slip during growth.<sup>[123]</sup> If the growth rates between CNTs in the forest are different, it leads to the observed tortuosity of the forests. Thus, the growth process is a combination of diameter dependent growth and mechanical coupling which enables the formation of a dense forest.<sup>[123]</sup> The mismatch in growth rates, however, can lead to mechanical stresses on the CNTs which might have an influence on the kinetics and perfection of individual CNTs and can create the observed defects in forests.<sup>[124]</sup>

The alignment of the CNTs in the structure is an important bulk parameter that was found to be linked to the density of the forest by Xu et al.<sup>[125]</sup> Using the Herman's Orientation Factor (calculated

from the fast Fourier transformation of the SEM images) they characterized the alignment of the CNTs and found a sigmoidal (“S-curve”) relation to the forest density which can be linked to the crowding effect during CNT growth. This means that neighboring CNTs physically interact with each other to form a common growth direction and was described by Fan et al.<sup>[126]</sup> for CNT arrays. The perfect alignment becomes increasingly difficult with higher CNT density due to limiting factors, such as imperfect spacing and nonuniform growth rates dominating the crowding process. Using environmental transmission electron microscopy Balakrishan et al.<sup>[127]</sup> similarly found that the CNT density is linked to the dynamics of the CNT self-organization. If the density is too low, a random horizontal network is formed due to the lack of crowding from neighboring CNTs. However, with a higher density vertically aligned growth can be observed. The CNT density can also be linked to the growth temperature, as a too low temperature can lead to incomplete reduction of the particles, whereas a too high temperature supports coarsening of larger particles. Both scenarios have a significant influence on the amount of active particles and thus the crowding of the nucleated CNTs. Hence, mechanical coupling plays a significant role in the self-organization. De Volder et al.<sup>[128]</sup> showed this phenomenon for the growth of vertically aligned CNT pillars. The growth time and the spacing between the pillars significantly influence whether vertically aligned growth can be observed or not (figure 1.12). The formation of a ‘crust’ made of horizontal CNTs in the initial growth stage was also reported here.

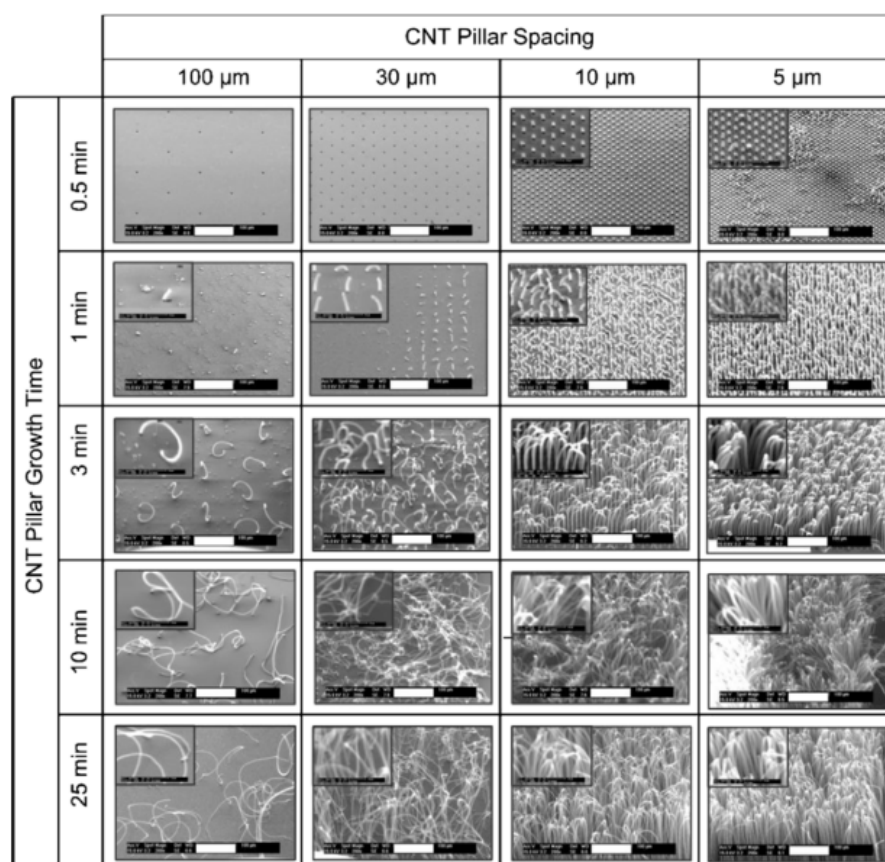


**Fig. 1.12** The vertically aligned growth of CNT micropillars is studied here, depending on growth time and spacing.<sup>[128]</sup>

## 1 Carbon Nanotubes (CNT) Overview

---

With all those insights, Bedewy et al.<sup>[109]</sup> suggest a multiple stage model that clearly describes the evolution in the forest morphology in each of the stages, as depicted in figure 1.13. It is important to keep in mind that depending on the CVD and catalyst system used, these stages may differ slightly. As this report uses a setup almost identical to ours, the characteristics of those stages are explained more in detail.<sup>[109]</sup>

- **Particle formation:** In the first step of the synthesis, the substrate is heated in a reducing atmosphere, resulting in the reduction of the iron film. Particles are formed by dewetting which then are stable during the addition of the hydrocarbon gas.
- **Self-organization:** Hydrocarbon precursor gas is introduced and CNTs randomly nucleate on the surface forming a tangled CNT mesh which is often referred to as "the crust". It is hypothesized that this crust forms a support for subsequent aligned forest nanotube growth.
- **Crowding:** The "crowding" stage is the high density region that is following the formation of the crust. The density increase (here up to 5-fold) is due to increasing population of active catalyst particles and a maximum density of approx.  $9 \cdot 10^9$  CNTs/cm<sup>2</sup> is reached. The nucleation kinetics are dependent on the hydrocarbon gas composition, surface carbonization and other process parameters as discussed later on.
- **Steady growth:** In the steady growth stage, the report observed a reduction in diameter of more than 10 % and the orientation parameter reaches a maximum, indicating that the straightest tubes can be found in this region. Also, an increase in catalyst activity from 1% to 11% was observed.
- **Density decay:** The orientation of the CNTs, the number of walls (from 7 to 5) and the diameter decreases. The catalyst shows diffusion into the alumina substrate layer. The decrease in CNT diameter is suggested to be caused by diffusion of Fe atoms into the substrate and thus an increase in catalyst particle size.
- **Termination:** The alignment is rapidly lost and the CNT diameter distribution is broadening. Termination happens due to catalyst deactivation, caused by mechanisms like catalyst poisoning, carbon overcoating, evaporation or diffusion. The deactivation rate eventually dominates until the structure is no longer self-supporting and stops growing. Amama et al.<sup>[129]</sup> investigated the role of water addition in the CNT growth and suggested that it is very likely that the formation of amorphous coating rather than the diffusion limitation through the rather low density forests is the reason for the growth termination. Due to the oxidizing properties of water, it can remove that amorphous carbon and thus support longer forest growth.

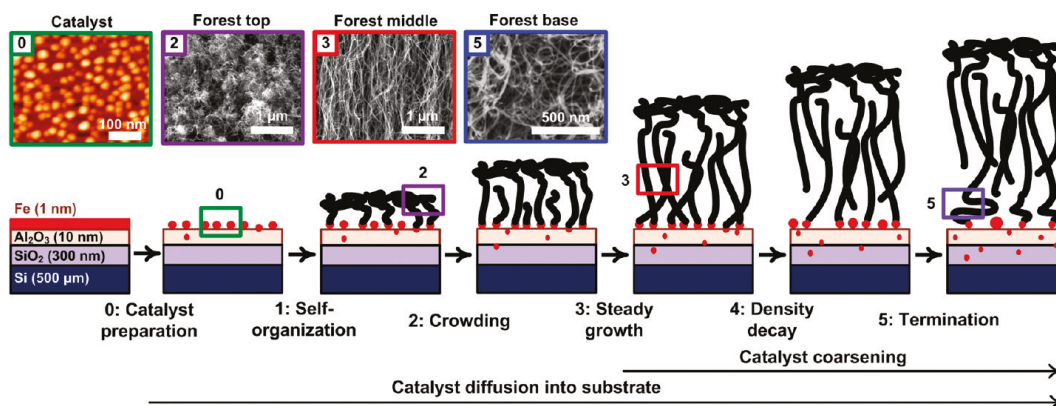


**Fig. 1.13** The different stages of CNT forest growth are shown schematically, including an AFM image of the catalyst particles after annealing and SEM images of relevant stages and parts of the forest. [109]

Looking more specific at the catalyst phase, a study suggested that the Fe-catalyst is crystalline during the CNT nucleation and the CNTs can be grown directly from the carbide ( $\text{Fe}_3\text{C}$ ) phase, indicating a complex dynamic motion of metal and carbon atoms in those nanoparticles for the CNT growth. [116] Using grazing-incidence X-ray diffraction and environmental TEM, Wirth et al. [130] studied the phase of the iron catalyst more in detail and found that the oxide supported Fe nanoparticle distributions are a mixture of  $\alpha$ - and  $\gamma$ -phases. For  $\gamma$ -rich phases they found the metallic Fe to be the main active catalyst phase for the CNT growth. This shows that carbide formation is not a requirement for active catalyst particles. For the  $\alpha$ -rich mixtures, however, carbide formation is dominant and part of the growth process.

Park et al. [131] developed a method of measuring the CNT forest density via optical attenuation which might help to establish a quality control concept for manufacturing. A new growth termination model speculates that lifted catalyst particles significantly affect the growth and growth termination of CNT forests (here grown in a hot-filament CVD) along with Ostwald ripening and sub-surface diffusion. [132]

### Parameters that influence CNT forest growth

In general, the forest synthesis is a complex process which is not fully understood to date and influenced by a range of parameters. Thus, careful tuning is necessary to obtain a particular forest height and morphology, and the reproducibility might be challenging. [109] It is crucial to increase our understanding of the process, as the properties of the forest and the CNTs in it are strongly influenced its growth conditions. A range of parameters important for the CNT growth will be discussed in the following paragraph.

**Catalyst influence** For the growth of CNTs, the catalyst is one of the most crucial parameters to be kept in mind. As the dimensions of the catalyst particles determine the type of CNT and its diameter, not only the catalyst material itself needs to be carefully selected, but also all parameters that influence the particle formation from the initial film, such as thickness and heating rate.

## 1 Carbon Nanotubes (CNT) Overview

---

- **Catalyst material:** The most common catalysts are Fe, Ni and Co but also other metals, alloys and oxides have been used. A more detailed overview can be found in a review by Nessim et al.<sup>[103]</sup>
- **Catalyst film thickness:** It was found that the diameter of the CNTs is closely linked to the size of the catalyst particles.<sup>[110,133]</sup> Thus the catalyst film thickness needs to be taken into account.<sup>[103]</sup> A metal film with a thickness of 13 nm leads to a CNT diameter distribution of 30-40 nm, whereas a film thickness of 27 nm leads to 100-200 nm CNT diameter due to the generation of larger catalyst particles.<sup>[103]</sup> Not only the catalyst diameter distribution is crucial for the CNT growth, but also the particle density is important. It was shown that it has to be at least  $5 \cdot 10^{11} \text{ m}^{-2}$  for forest growth.<sup>[134]</sup>
- **Heating rate:** The size and monodispersity of the catalyst are influenced by the heating rate, as it can be seen from the measurements by Meshot et al.<sup>[135]</sup> Using grazing incident SAXS they found that the annealing temperature and time influences the particle formation. A rapid heating rate in a  $\text{C}_2\text{H}_4$  atmosphere can lead faster to a higher forest, as the self-organization starts earlier in combination with an increased number density of CNTs.

**Catalyst underlayer** In addition to the catalyst, the type of substrate that the CNT forest is grown on and the type and thickness of the underlayer of the catalyst can significantly influence the growth since it influences properties like coarsening and dewetting due to the formation of alloys or different mobilities.<sup>[103]</sup> Delzeit et al.<sup>[136]</sup> showed that the thickness of the Al and the Fe-layer has a significant influence on the MWNT growth, e.g. without an Al underlayer they observed no growth. The most commonly used underlayer materials are silicon oxide, magnesium oxide and alumina due to the fact that they are cheap, commercially available and easy to handle.<sup>[134]</sup> The Al underlayer helps stabilize the catalyst clusters and thus prevents catalyst sintering.<sup>[137,138]</sup> De Volder et al. created CNT pillars that are partly grown on silicon oxide and partly on titanium nitride (TiN) surfaces. Those underlayers induce differences in the catalyst morphology. The catalyst particles on TiN are smaller. This way the growth speeds of the CNTs seem to change and bending pillars can be created which are interesting for advanced functional materials, e.g. due to their superhydrophobicity.<sup>[139]</sup>

**Gas influence** Composition of the gases and the feed rate also influences the diameter and number of walls of the resulting CNTs.<sup>[101]</sup> The catalyst lifetime and carbon deposition on the nanoparticle is influenced by variations in the gas composition, e.g. by introducing  $\text{O}_2$ ,  $\text{H}_2$  or  $\text{CO}_2$ . Growth enhancing agents like water or ethanol can be added which then enhance the catalyst activity and lifetime.<sup>[109]</sup> Water vapor can slow down Ostwald ripening of the catalyst, act as a mild oxidizer and etches the amorphous carbon coating on the catalyst that leads to catalyst poisoning or remove other by-products.<sup>[122,129]</sup> Thus, Hata et al. showed that they can grow ultra-high purity single-walled CNTs on a Al-underlayer with an Fe-catalyst and the addition of parts per million of water.<sup>[140]</sup> This catalyst-underlayer system has been frequently used afterwards. Li et al.<sup>[141]</sup> investigated the influence of moisture further and found a 30% improvement in the growth rate with increasing the moisture level. They developed a method that decreases the coupling between the annealing and the

growth phases and thus, were able to gain better control over the moisture levels and increased the process consistency. Nessim et al.<sup>[101,142]</sup> showed the growth of tall forest by preheating O<sub>2</sub> gas and generating water vapor in-situ by introducing the O<sub>2</sub> gas into the furnace. They also observed that the pretreatment time influences the growth height and crystallinity since it influences the generation of carbon species. Thus the preheating temperature for the gas can have a significant influence on the height of the forest (figure 1.14) and on the crystallinity of the CNTs. This shows that a control of the CNT crystallinity is possible by tuning the gas composition and introducing specific precursor molecules through different pretreatment temperatures.

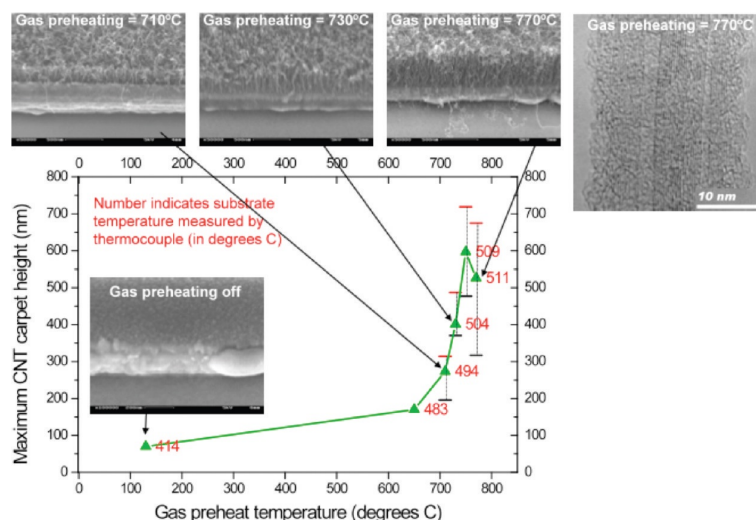


**Fig. 1.14** The correlation between gas preheating temperatures and the CNT forest height is shown in the graph. SEM images showing the forest heights for various temperatures can be found above the graph.<sup>[143]</sup>

Carbonaceous deposits on the walls from previous reactions can improve the CNT nucleation and growth and also alkynes accelerate the CNT growth.<sup>[109]</sup> The addition of oxygen can lead to single- or few-walled CNT forests as the addition of O<sub>2</sub> together with H<sub>2</sub> influences the catalyst evolution.<sup>[144]</sup> Magrez et al.<sup>[145]</sup> showed that the MWNTs can be grown at 400 °C if CO<sub>2</sub> and C<sub>2</sub>H<sub>2</sub> are added in stoichiometric amounts. Also they managed to induce CNT growth on many different surfaces, like coins and aluminium foil, using this gas-feedstock system.

Those are some of the many factors that influence the growth of forests and should be kept in mind. This is not a final list and other parameters such as growth temperature should also be considered. Also, the adhesion to the substrate is especially relevant when lift-off from the substrate is required or further processing steps are done. Su et al.<sup>[146]</sup> have reported an improvement in adhesion to the substrate by microwave treatment of CNTs grown at low temperatures due to a change in the location of the Ni-catalyst particles.

## 1.4 CNT forest patterning and shaping

To introduce various structures into the grown forests, the catalyst can either be patterned before CNT growth or modified after growth, e.g. by partial lift-off,<sup>[147]</sup> laser ablation<sup>[148,149]</sup> or water-assisted machining.<sup>[150]</sup> In this thesis, the focus is on catalyst patterning before the growth. Different lithographic methods are used to create the micro- or nanoscale patterns on an Si-wafer. The patterned wafer is then used as a mask during the deposition of the growth catalyst via a physical vapor deposition (PVD) process. Afterwards the grown structures can be shaped using an elastocapillary self-aggregation process called densification. Details on lithography and densification can be found in chapter 3.

### 1.4.1 CNT forest patterning by UV- lithography

UV-lithography is used to create patterns between 0.8  $\mu\text{m}$  to mm.<sup>[151]</sup> It uses the reaction of photoactive polymers with UV-light to create pattern on the substrate. Due to the small scale patterns, photolithography needs to be done in a clean room in a dust-free environment, as small dust particles can disturb the pattern. The process itself consists of multiple steps which are shown in figure 1.15<sup>[151]</sup> and are shortly described in the following points with regards to the process used to create the 3D CNT structures.

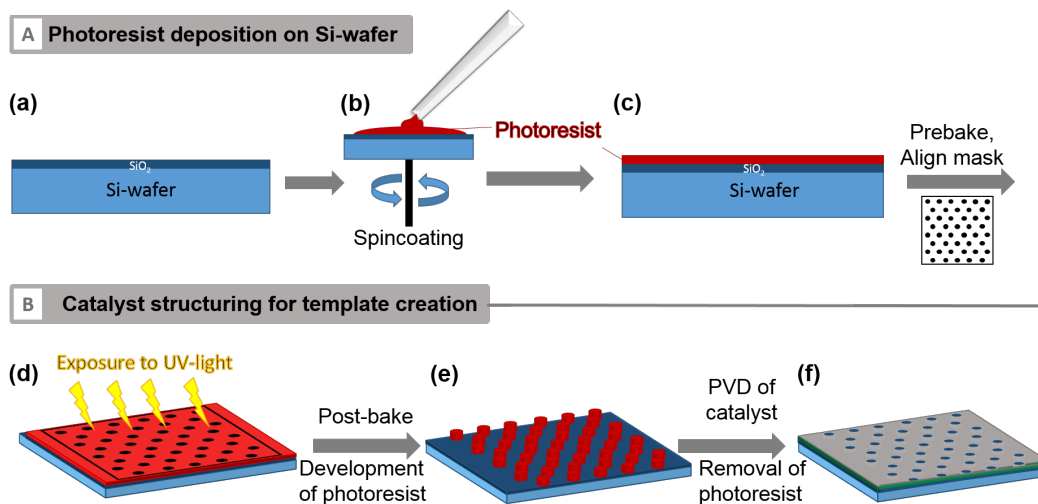


**Fig. 1.15** Schematic overview of the UV-Lithography process. The wafer after cleaning is shown in (a). Then the photoresist is deposited on it by spin-coating (b) to form a film of defined thickness (c). This film is then exposed to UV-light through a mask (d), followed by a post-bake and a development step (e). In our process, this template is then used for the catalyst layer deposition with subsequent lift-off (e).

- **Wafer cleaning and preparation (a):** Before any lithography, the wafer is cleaned thoroughly. This can e.g. be done by RCA cleaning (protocol that uses DI water:hydrogen peroxide: ammonia with a ratio of 5:1:1 at 80 °C) to remove organics and metal ions.<sup>[152]</sup> An additional etching step, e.g. in O<sub>2</sub>-plasma can be added to remove organic contaminants. A dehydration step at 200 °C removes all the remaining water molecules. After this, adhesion promoters can

be deposited onto the Si-wafer as an intermediate layer between substrate and photoresist to increase the adhesion between them. Here Ti-prime is used as an adhesion promoter, spin-coated onto the Si-wafer at 4000 rpm for 40s and then baked for 2 min at 115 °C.

- **Spincoating of photoresist (b):** A photosensitive organic polymer resin called a photoresist is spin-coated onto the substrate. Usually the wafer is spun at speeds between 1800 and 8000 rotations per minute (rpm), depending on the viscosity of the photoresist and the required thickness. The photoresist thickness,  $T$ , is a function of spin speed, concentration and viscosity of the solution; thus, data sheets exist for each photoresist to adjust the spin speed for the desired thickness. Typical thicknesses range from 0.5 to 2  $\mu\text{m}$ . A challenge here is making thicker photoresist layers for high aspect ratio structures, as well as thinner layers for feature sizes below 0.2  $\mu\text{m}$ . In our process, AZ5214E is used as a positive photoresist, spin-coated at 3000 rpm for 30s.
- **Prebake of photoresist (c):** After spin-coating, the photoresist is prebaked at around 100 °C (e.g. 115 °C for AZ5214E for 1 min). Prebaking the photoresist is necessary as the resist still contains up to 15% solvent after spin-coating as well as potentially built-in stresses.<sup>[151]</sup> Prebaking removes these and also helps promote adhesion to the substrate.
- **UV-light exposure and postexposure bake (d):** The photoresist coated substrate is then exposed to UV-light (350 - 500 nm) through a mask. The photon dose during the exposure (in  $\text{J}/\text{cm}^2$ ) needs to be adapted to the photoresist to avoid overexposure or underexposure. Upon exposure, a chemical reaction is introduced in the photoresist. This reaction changes the resin's solubility in the developer solvent. Photoresist bleaching (the exposed photoresist becomes transparent to the incident wavelength) allows the use of thicker films, since light can get all the way through the resist.<sup>[151]</sup> To complete the reactions started during the exposure, a postexposure bake is often required to optimally tune the following development step. In our process, the photoresist is exposed for 6s at a incident light intensity of  $10 \text{ W}/\text{cm}^2$ . No post-exposure bake is done.
- **Development (e):** Following exposure and postexposure bake, the photoresist undergoes a development step where certain areas are selectively removed. The wafer is immersed in the development solvent and the removal is possible by an introduced change in the molecular weight of the polymer (crosslinking or chain scission), reactivity or polarity change.<sup>[151]</sup> For positive photoresists aqueous alkaline developers can be used, whereas aqueous or organic developers are normally used for negative resists. Depending on the type of photoresist and film thickness used, the development time needs to be adjusted.<sup>[153]</sup> In our process, development is done for 2 minutes in diluted AZ351B (20% v/v in  $\text{H}_2\text{O}$ ), rinsed with  $\text{H}_2\text{O}$ , and dried.
- **Pattern deposition and photoresist removal (f):** The next step is then either the selective deposition of another material (additive patterning) or etching of the exposed areas (subtractive patterning). For the fabrication of the 3D CNT structure step is a lift-off patterning process is used, In our process, e-beam PVD is used to evaporate solid  $\text{Al}_2\text{O}_3$  (10 nm) and Fe (1 nm) onto the substrate, creating thin films of controlled thicknesses. The e-beam locally melts the

## 1 Carbon Nanotubes (CNT) Overview

---

material which then leads to a thermal evaporation. Due to the low pressure, the material encounters few intermolecular collisions on the way to the substrate. The advantage of this methods is the high quality of the films, the low source contamination and the possibility for high deposition rates (50 - 500 nm/min). In our process, the photoresist is then lifted off by sonicating the patterned wafer for 8 min in acetone and twice for 3 min in isopropanol. This protocol dissolves the photoresist, leaving a patterned Si-wafer with catalyst ready for CNT growth.<sup>[151]</sup>

The entire process can be iterated to pattern layer after layer. When multiple layers are created, the first one must be aligned with the following layers before their exposure, thus a mask needs alignment marks and an alignment step will be added before exposure.<sup>[153]</sup>

**Photoresist chemistry**<sup>[151]</sup> Typically a photoresist consists of a polymer (base resin), a sensitizer and a casting solvent. The casting solvent supports the formulation of the other two components. It supports the thin layer formation and the spin application of the layers. The polymer undergoes a structural change when exposed to light with the sensitizer controlling this photochemical reaction. Photoresist without a sensitizer are one-component systems, with sensitizer they form two-component systems. Photoresists are defined by their way of reacting to the radiation. *Positive* photoresists show a decrease in the molecular weight of the polymer after the exposure; this can be caused by chain rupture or scission. Thus, it becomes soluble in the developer. Positive photoresists keep the areas that are not exposed. *Negative* photoresists show an increase in molecular weight after exposure based on free-radical-initiator crosslinking or photopolymerization, or photochemical transformation where hydrophobic groups are converted into hydrophilic groups. Those reactions change the solubility of the photoresist, making it insoluble in the developer. Negative photoresists, respectively, keep the areas that are exposed. This can schematically be seen in figure 1.16. A detailed comparison of positive and negative photoresist characteristics can be found in table B1 in appendix B. The photoresist has to be carefully selected based on the desired pattern, resolution and exposure type.

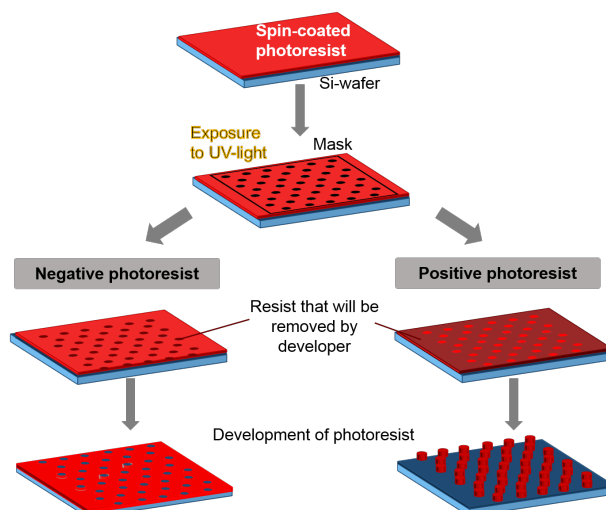


**Fig. 1.16** The difference between a negative and a positive photoresist is shown here with the same mask used. For the negative photoresist, the areas exposed to UV-light are crosslinked and thus will not be removed by the developer, whereas for the positive photoresist the polymer chains in the exposed areas are cut and those affected polymers are removed afterwards. The choice of photoresist can invert the pattern on the mask.

The photoresist that was used in this thesis is AZ5214E. It is comprised of a novolak resin and naphthoquinone diazide as photoactive compound. The solvent is propylene-glycol-mono-methyl-ether-acetate. The novolak resin is prepared by acid copolymerization of cresol and formaldehyde.

**Masks and exposure to UV-light**<sup>[151]</sup> The masks used for the photolithography are on nearly transparent glass with an absorber pattern metal, such as Chromium. It can be a bright field or a dark field mask, depending on which areas are patterned. This mask is then used to create a pattern on the photoresist coated Si-wafer. Contact printing with a hard contact step is used for the fabrication of the features in this thesis.

#### 1.4.2 CNT forest patterning by colloidal lithography

Colloidal lithography, also called natural<sup>[154]</sup> or nanosphere lithography,<sup>[155]</sup> was pioneered by Deckman et al.<sup>[154]</sup> It is defined as the use of self-assembled colloidal particle arrays as a large area lithographic mask.<sup>[154]</sup> It provides an inexpensive, high through-put, flexible way to pattern 2D arrays of various nanostructures.<sup>[156,157]</sup> Recently, it has been shown<sup>[158]</sup> that hexagonally arranged colloidal crystals can be fabricated on a large scale with a throughput of 3000 wafer/h using a technique called micro-propulsive injection and tuning the parameters. This makes it industrially feasible to use colloidal lithography for scalable applications.<sup>[158]</sup> However, it is limited to repetitive patterns and suffers from dislocations.

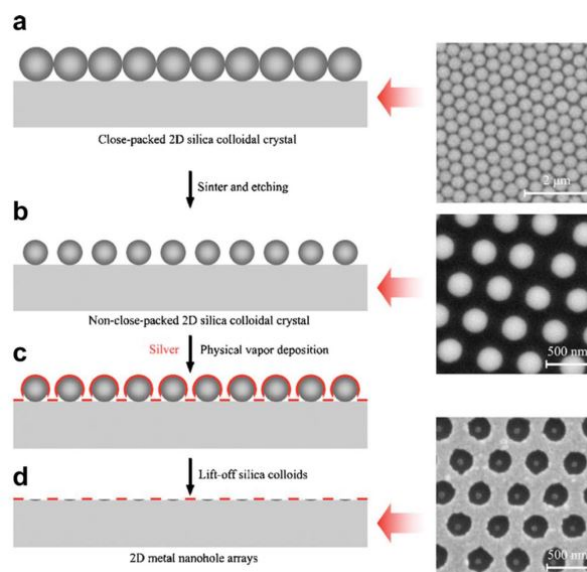


**Fig. 1.17** The hexagonally packed colloidal monolayer (a) is etched (b). The shrunk spheres are then used as a mask for Ag deposition (c). After the removal of the spheres, hexagonally ordered spherical holes are created (d).<sup>[159]</sup>

Self-assembled particles act as templates or masks for further molecule deposition, thus creating a high versatility for structures.<sup>[160]</sup> One important class of those self-assembling nanoparticles are polystyrene (PS) spheres<sup>[161]</sup> which Fischer et al.<sup>[162]</sup> used as a mask for platinum and Deckam et al.<sup>[154,156]</sup> for silver (Ag). An example for a typical colloidal lithography process with silica spheres as a template is shown in figure 1.17.<sup>[159]</sup> After forming a monolayer of silica spheres (figure 1.17a), the hexagonally packed spheres are etched to increase the spacing between them (figure 1.17b). Then these particles are used as a mask to deposit Ag (figure 1.17c) leading to spherical patterns after removal of the spheres (figure 1.17d).

The formation of colloidal monolayers is a prerequisite of most colloidal lithography structures and thus will be discussed more detailed in the following paragraph.

### 1.4.2.1 Fabrication methods for colloidal monolayers

Colloidal crystals are periodically ordered arrays of colloidal particles and have applications in many fields, such as photonic crystals, catalysis, sensing, and wetting.<sup>[163]</sup> Consequently, many groups have reported strategies to self-assemble monodisperse spherical particles into different types of periodic structures, e.g. hexagonally-close packed (hcp) or non-close packed crystals.<sup>[157]</sup>

Monolayer colloidal crystals are of high interest for many applications, in our case for colloidal lithography. Hence, it is important to identify easy and scalable fabrication methods to create those crystals, preferably with a highly ordered packing. Hexagonally-close packed crystals can be prepared in various ways which are shown in figure 1.18.<sup>[163]</sup> Those methods include drop-coating (1.18a) requiring great control over the evaporation rate and dip-coating (1.18b) where the rate of water evaporation and substrate withdrawal is crucial for the crystal packing. Spin-coating (1.18c) is reliant on the spin-speed as well as the colloidal suspension parameters. Charged nanospheres can also be packed using electrophoretic deposition (1.18d), where direct or alternating current fields are applied to achieve rapid self-assembly. Another facile and efficient route is self-assembly at interfaces, e.g. gas/liquid interface (1.18e) as there is only a monolayer formed at this interface, so there will be no variation in the layer thickness when this method is applied.

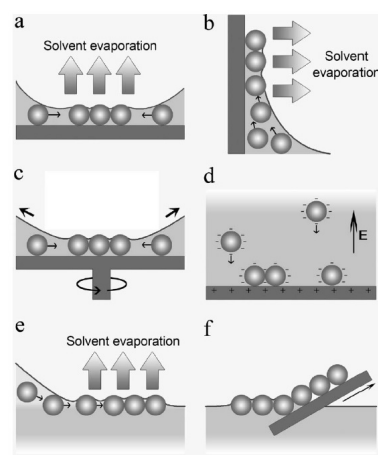


**Fig. 1.18** Methods for the creation of hexagonal-close packed colloidal crystals are (a) drop-coating; (b) dip-coating; (c) spin-coating; (d) electrophoretic deposition; (e) self-assembly at the gas/liquid interface; (f) transfer from the gas/liquid to the gas/solid interface.<sup>[163]</sup>

The following paragraphs describe the basics of colloidal stability as well as direct and interface assembly more in detail.

**Colloidal stability and crystallization** When discussing the formation of colloidal crystals, it is important to understand the underlying principles, such as colloidal stability. The particles in colloidal dispersions are below 1  $\mu\text{m}$ , so there is a high surface to volume ratio. Attractive van der Waals forces and steric or electrostatic repulsive forces influence the stability of a colloidal dispersion.<sup>[164]</sup>

## 1 Carbon Nanotubes (CNT) Overview

The DLVO-theory by Derjaguin and Landau, and Verwey and Overbeek describes the interaction potential for two spherical particles which is created by the sum of these forces, as seen in figure 1.19.<sup>[164]</sup> Initially at a very small distance the Born repulsion prevents the particles from overlapping. In regime (I) a potential minimum is reached where the particles are irreversibly agglomerated. This is induced by the strong van der Waals interaction at very close distances and can be prevented by the energy barrier from the strong electrostatic repulsion. In regime (II) a potential maximum can be seen which is introduced by electrostatic repulsion of the spheres. The height of this energy barrier determines the stability of the colloids. Regime (III) shows a second minimum that is called flocculation and represents the reversible agglomeration of the spheres.<sup>[164]</sup>

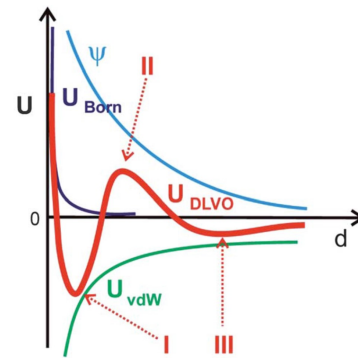


**Fig. 1.19** DLVO interaction potential in dependence on the distance between two particles as a sum of the attractive and repulsive forces.<sup>[164]</sup>

Two ways colloids can be stabilized are sterically or electrostatically. For colloids at interfaces, in addition to the already mentioned forces, capillary and dipole interaction change the interaction potential.

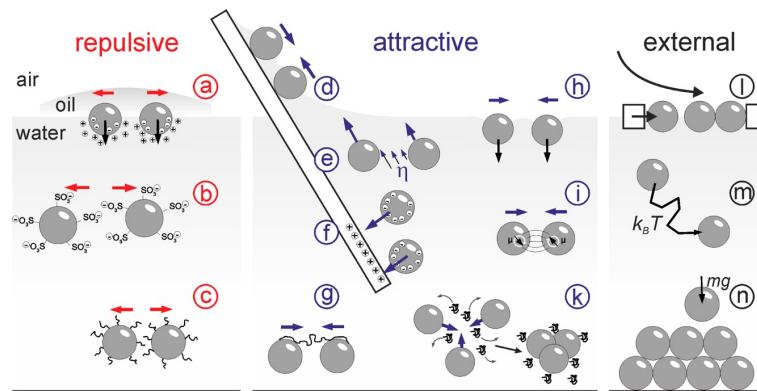


**Fig. 1.20** The forces and interaction that occur on interfaces and in solutions shown schematically. The repulsive forces are (a) dipolar repulsion by partial ionic dissociation, (b) Coulomb repulsion and (c) steric repulsion. For the attractive interactions there are (d) immersion capillary forces, (e) hydrodynamic coupling/ drag forces, (f) Coulomb attraction to oppositely charged surfaces, (g) bridging attraction/flocculation, (h) flotation capillary forces, (i) van der Waals attraction, and (k) depletion attraction. External forces that occur during the monolayer formation are (l) barrier compression or forced convection (effectively resulting in particle aggregation), (m) Brownian motion, and (n) gravitational sedimentation.<sup>[165]</sup>

Dipole interactions result from the different dielectric constants of the media, leading to an asymmetric counter-ion cloud. Colloidal particles induce the formation of an energy well that traps them in a fixed position between the two media, since both media try to minimize their interfacial energy. Removing a colloid from the minimum energy position can require an energy of about one million  $k_B T$  and thus the particle is efficiently trapped.<sup>[164]</sup> When two or more particles are deposited at an interface, capillary forces, which are long-range and attractive, dominate. In figure 1.20 an overview of all the occurring forces at interfaces and in solutions is shown.<sup>[165]</sup>

**Direct assembly** Direct assembly includes evaporation induced methods, convective assembly and external force induced methods. Drop-coating,<sup>[163,166]</sup> sedimentation<sup>[156,167]</sup> and convective assembly<sup>[157,163,168]</sup> can lead to monolayers but these are often not uniform across a large scale substrate. Spin-coating and electrophoretic deposition create more uniform monolayers, and thus are more favorable.

**Interfacial assembly** Interfacial assembly is often used to create monolayers. First the particles are assembled at an interface and subsequently the assembled monolayer is transferred to the target substrate to create 2D crystals. This leads to high quality monolayers since the interface allows good particle ordering.

The standard technique involves pipetting a colloidal dispersion in a solvent onto a water/ air-interface. After the evaporation of the solvent, the particles form a highly ordered floating film which then can be transferred onto the substrate. The ordering of the colloids can be assisted by surfactants like sodium dodecyl sulfate (SDS) to lower the surface tension. A variety of factors, such as the particle concentration, zeta potential of the particles in the suspension, surface tension of the water phase, and addition of a salt in the suspension, influence this process.<sup>[157]</sup> To support the monolayer formation, the Langmuir-Blodgett technique can be used to compress the floating particles into a monolayer which is then deposited onto the substrate.

Retsch et al.<sup>[168]</sup> added an additional step of distributing particles onto a silanized substrate (parent substrate) which is then slowly immersed into water. This helps form a highly ordered colloidal monolayer that can then be transferred onto the target substrate. Those particles on the parent substrate were either spin-coated onto the substrate or drop-coated and dried inclined. It was found that the parameters that influence the monolayer formation in this process are the electrostatic interaction between the oppositely charged colloidal particles and the parent substrate surface, long range capillary attraction and short range electrostatic repulsion forces during particle assembly, the pH of the solution medium and the addition of surfactants like SDS. Vogel et al.<sup>[169]</sup> used a glass slide to slowly spread an alcoholic PS colloid dispersion onto a water surface. A schematic overview can be seen in figure 1.21.

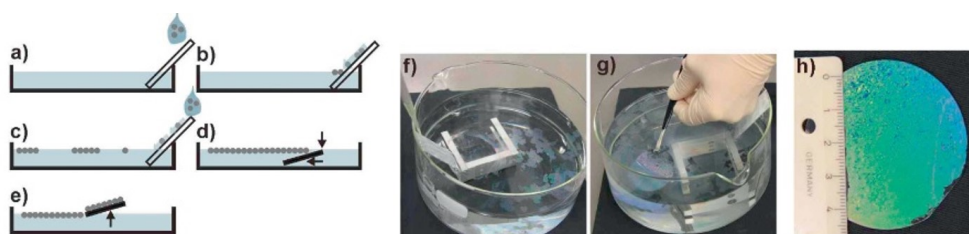


**Fig. 1.21** A schematic overview of the process used by Vogel et al.<sup>[169]</sup> to create a highly ordered monolayer. A drop of the colloidal dispersion is put onto a glass substrate (a) and is slowly spread onto the water surface (b). Repeating this process leads to individually highly ordered monolayer patches (c) that will assembly into one big batch (d) that can then be transferred onto a substrate (e). Photos are taken of the individual patches (f), the transfer onto a 2" wafer (g) and the dried wafer (h).

## 1 Carbon Nanotubes (CNT) Overview

---

The patches on the surface assemble into one highly ordered monolayer upon addition of more colloidal dispersion. Thus, no additional compression is necessary and large area monolayers can be produced as it can be seen in figure 1.21h. Assembly of colloidal monolayers onto a water-oil interface has also been reported.<sup>[157]</sup> Here the surface pressure of the interfacial tension is used to compress the colloidal spheres together.

In this thesis, the water subphase composition is taken from Vogel et al.<sup>[169]</sup> (0.1 mM SDS, pH  $\sim 10$ ), whereas the deposition method for the spheres on the interface is adapted slightly, as a lot of the PS sphere solution got stuck on the glass slide and thus was lost for the monolayer formation. The PS sphere solution is deposited using an Eppendorf pipette, immobilized by a micromanipulator with the tip in direct contact with the surface. This is similar to the report from Zhang et al.<sup>[170]</sup> where a needle tip flow method directly in contact with the interface and the monolayer arrays are created by slowly and smoothly spreading the solution. It was also found that larger monolayer areas can be produced by not only relying on the self-assembly of the PS spheres on the interface but also by applying a small external force to push the assembled patches together. This is done using the barriers in the Langmuir-Blodgett-trough. An image of the set-up can be found in the experimental section.

The self-assembly at the gas/liquid interface, in general, is efficient, facile and scalable route to produce colloidal crystal without any variation in layer thickness, as it can be the case when using convective assembly on solid substrates.<sup>[163]</sup>

### 1.4.2.2 Etching of colloidal monolayers

The previously described colloidal crystals can be used for the creation of many different structures. This needs further processing of the monolayer e.g. by etching to create a lithography mask of the right size. Etching or deformation of colloidal crystals, such as annealing slightly over glass transition temperature of polymer spheres, causing deformation of spherical beads, are commonly used techniques to add structural complexity.<sup>[156]</sup> It also introduces another tunable parameter to the lithography process. Thus, understanding the etching parameters is crucial. There are several reports for different etching systems.

Plettl et al.<sup>[160]</sup> used a reactive ion beam inductively coupled plasma (RIE-ICP) system to achieve good control over the etching process for PS particles smaller than 300 nm, while conserving their spherical shape (figure B3 in appendix B). Hanarp et al.<sup>[171]</sup> and Vogel et al.<sup>[169]</sup> investigated the influence of plasma etching (oxygen and argon) on PS particles. Vogel et al.<sup>[169]</sup> reported etching rates for different parameters, such as substrate temperature and particle size (as seen in figure B4 in appendix B). In this thesis, O<sub>2</sub> plasma is used for the etching of the PS spheres.

### 1.4.3 CNT forest shaping by elastocapillary self-aggregation of CNTs

From the lithographically patterned catalyst layers, CNT forests can be grown, which then can be further processed into novel structures by 'densification'. 'Densification' of the CNT forests refers to a process whereby CNTs are brought in closer packing using capillary forces (figure 1.22).<sup>[172]</sup>

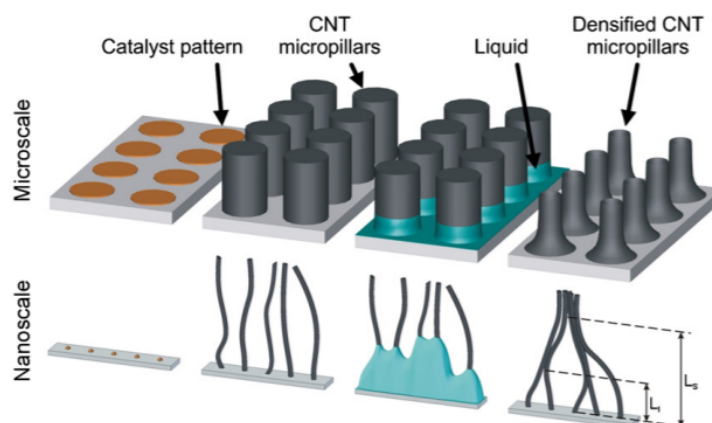


**Fig. 1.22** Schematic overview showing the CNT growth into micropillars and their subsequent densification by solvent evaporation on microscale and on nanoscale. The solvent treatment causes the CNTs to aggregate on nanoscale and thus introduces the structure change on microscale.<sup>[172]</sup>

It adds advantages like stability (100-fold enhancement of Young's modulus for densified CNT-pillars over an as-grown CNT forest<sup>[173]</sup>), electrical properties (e.g. decrease in resistance<sup>[172]</sup>) or structural changes in the forest. This process is driven by elastocapillary self-aggregation.

**Elastocapillary self-aggregation methods** The influence of capillary forces during wetting or drying of a liquid that cause mechanical deformation and change the arrangement of filaments is called elastocapillary self-aggregation.<sup>[94]</sup> This self-aggregation is influenced by the way a substrate is exposed to the liquid. Various methods are briefly described in the following paragraph and can be seen in figure 1.23.<sup>[53]</sup>

- **Immersion:** The substrate is immersed into a solvent (typically organic) without a specified direction. The orientation of the substrate should be parallel to the liquid surface before the solvent is evaporated under ambient conditions.
- **Directed immersion:** The substrate is immersed into the solvent at a specific direction which e.g. can change the orientation of the nanofilaments when removing the substrate from the liquid due to direction of the capillary forces.
- **Dipping:** For dipping, only the tips of the structures on the substrate are wetted by bringing them in contact with the surface of the solvent. The liquid is drawn in between the filament by capillary forces.

## 1 Carbon Nanotubes (CNT) Overview

- **Condensation:** The liquid is boiled until a uniform vapor front is formed. This vapor then condenses onto the inverted substrate. It presents a gentle method for fragile structures and densification of individual groups on a substrate.

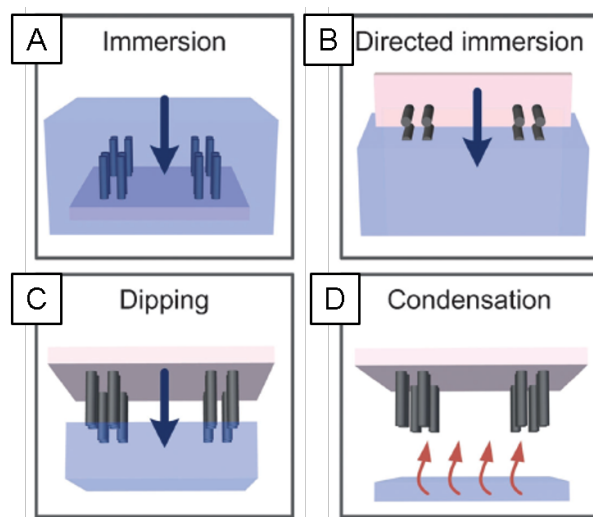


**Fig. 1.23** Schematic images showing densification techniques, such as (A) immersion (substrate parallel to liquid interface, liquid is evaporated), (B) direct immersion (substrate is kept at an angle during immersion and removal), (C) dipping (only the tips of the structure touch the liquid interface) and (D) condensation (vapor front condenses on the inverted substrate).<sup>[53]</sup>

Direct immersion as well as condensation are the methods used in this thesis.

**Driving forces in the densification process** Chakrapani et al.<sup>[174]</sup> showed a cellular foam formation by immersion of a CNT structure into solvent. The strong capillary forces during solvent evaporation cause shrinkage and crack formation in the CNT structures. Strong van der Waals forces hold the densified nanotubes together causing stable cellular structures. It was found that the micro-crack formation is induced by the drying of the structure and followed by further in-plane shrinkage and bending of the CNTs, which results then in the open cellular foam formation. A schematic illustration of the cell formation can be seen in figure 1.24 where the cracks start to form (b), the CNTs bend (c) until the final open cellular structure is reached (d).

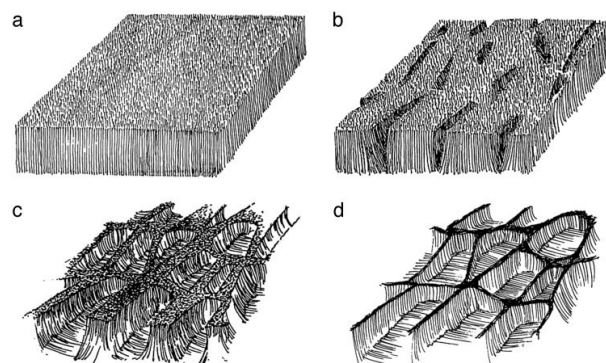


**Fig. 1.24** The process of CNT foam formation is shown here schematically. First, cracks start to form (b) in the initial CNT forest (a). Those cracks propagate and the CNTs start bending (c) until the final structure is formed (d).<sup>[174]</sup>

During drying, the CNTs bend, caused by the pressure difference between the air and the solvent in the narrow spacing between the CNTs. The bending is dependent on the CNT length and the force is supplied by the capillary forces. Futaba et al.<sup>[54]</sup> have shown a 20-fold increase in mass density for packed SWNT forests and a reduction in the empty space in forests from 97 % to ~50 %. Further research on CNT foam formation was done by Kaur et al.,<sup>[175]</sup> evaporating water and acetone on as grown and "inverted" (transferred onto Si-wafer) CNT forests. They found that the "inverted" arrays result in a translation of the CNTs rather than bending due to the lower interaction with the substrate as well as four-fold increase in current density through CNT arrays for the densified structures.

De Volder et al.<sup>[94]</sup> reported an overview of methods and mechanisms of elastocapillary self-aggregation of CNT forest structures. Aggregation of the filaments occurs if the lateral forces induced by the receding meniscus are stronger than the elastic restoring force. When the elastic restoring force is smaller than the pillar interaction forces, an irreversible deformation even after the evaporation of the liquid can be observed. This means that the maximum size of aggregated filaments is determined by the balance of the capillary forces and the elastic restoration force, whereas the adhesion and elasticity determine how many stay aggregated after drying. When pillars bend towards each other, the decrease in the spacing in-between causes the capillary energy to decrease and the elastic bending energy to increase. If the cluster size is higher, the outer pillars bend more than the inner ones and thus increase the bending energy. A theoretical model used for 4 pillars in the corners of a square can predict the minimum elastic modulus  $E_{crit}$  that is necessary to resist the elastocapillary aggregation:<sup>[176]</sup>

$$E_{crit} = \frac{32\sqrt{2}\gamma\cos^2\theta h^3}{3d^4} f(r) \quad (1.3)$$

Here  $\gamma$  is the surface tension,  $\theta$  the contact angle,  $h$  the height and  $d$  the diameter of the pillar and  $f(r)$  is a function of the diameter and the spacing of the pillars ( $r$ =spacing/ $d$ ). It decreases with increasing  $r$ . This correlation can also be used to understand the behavior of clusters with larger filaments. This model shows that elastocapillary self-aggregation is dependent on the liquid used for densification (surface tension, contact angle), the pillar material (Young's modulus, surface chemistry) and geometry ( $h$ ,  $d$ ). When considering the aggregation behavior of CNTs, it is important to note that the models apply to isolated and parallel pillars whereas CNTs can be wavy and entangled. Thus the aggregation also depends on the organization and overall shape of the population of filaments.<sup>[53]</sup>

**CNT structure designs** By elastocapillary self-aggregation (=densification) various geometries can be achieved by lithographic patterning of the catalyst. An overview of a range of possible surface designs is shown in figure 1.25 including the densification methods that can be used to create it and the amount of pillars used in it.<sup>[94]</sup>

- **Top gathering:** This process describes pillars aggregating at their tips and is significantly influenced by spacing and aspect ratio of nanofilaments.
- **Winding:** Winding is the aggregation of pillars into chiral structures which can happen when a balance between adhesion, elasticity and capillarity is reached.

# 1 Carbon Nanotubes (CNT) Overview

- **Folding:** Folding is introduced by capillary forces between the substrate and the filament and is discussed more in detail by Tawfick et al. [177]
- **Foaming:** Foaming of CNT forests has been researched by several groups. [172-174,178] Randomly distributed voids are created by an interplay of capillary forces, stiffness and adhesion to the substrate. By patterning the CNT forests, void formation can be directed into specific patterns, e.g. honeycombs. [173,179]
- **Forming:** By forming a variety of intricate 3D patterns can be engineered where the final geometry is defined by the density and alignment of CNTs in the forest.

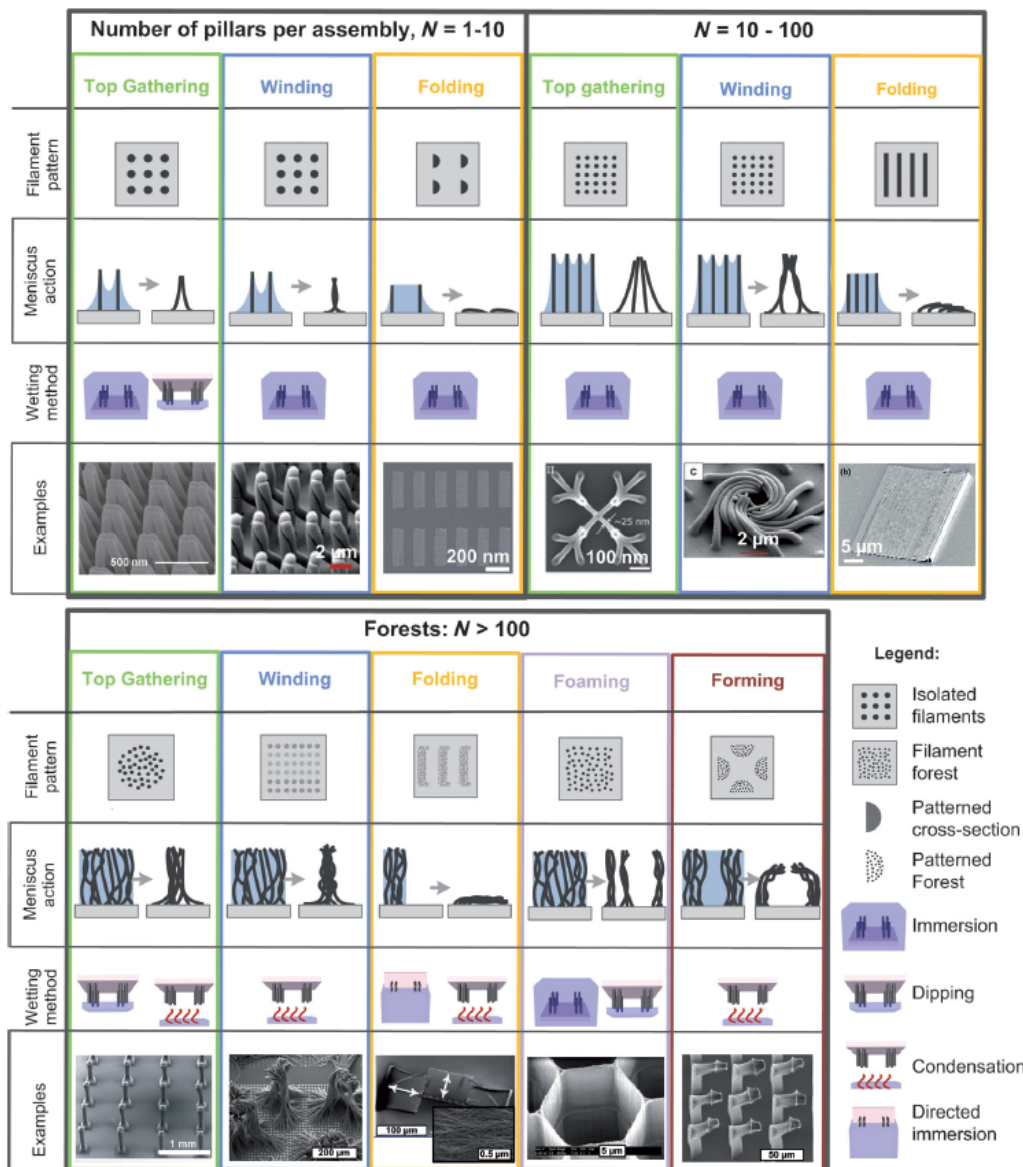
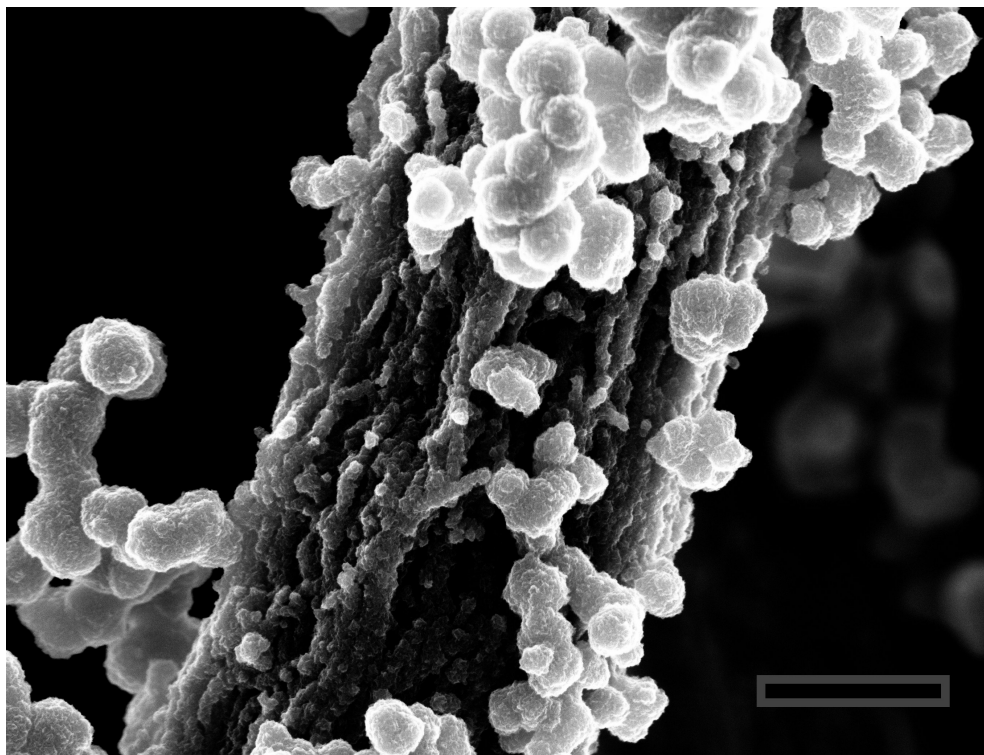


**Fig. 1.25** Overview of the different surface designs that can be created, depending on the number of pillars and specifying the densification method used. [53]

## Chapter 2

# Chemical Modification of Carbon Nanotubes



CNT strand coated with TiO<sub>2</sub>, scale bar 2  $\mu$ m.

## 2 Chemical Modification of Carbon Nanotubes

---

While CNTs possess impressive properties, for many applications they only go half way. They can, for example, provide high surface area which is great for sensors but are too unselective and unsensitive without further modification. For their application in batteries, they provide great electron conductivity, surface area and electrochemical stability, but have very low intrinsic capacity.<sup>[180,181]</sup> Thus, this chapter is discussing the surface modifications of CNTs to add the additional desired properties. A lot of research is being done on coupling organic moieties onto CNT surfaces<sup>[182–187]</sup> or modifying them with polymers,<sup>[188–193]</sup> however, the focus here will be on inorganic functionalization of CNT powders and forests, as this is the needed surface chemistry modification for the application in energy storage. Dai's group has shown that direct growth of inorganic nanomaterials occurs on oxygen-containing or defect sites and allows for a strong covalent coupling in inorganic-nanocarbon hybrids, supporting a rapid electron transfer from the active materials which is highly desirable for electrodes.<sup>[68–71]</sup> Thus, in addition to inorganic CNT modification using gas and liquid phase techniques, methods to introduce oxygen groups as reactive sites will be discussed.

### 2.1 Nucleation theory

The goal in this thesis is the decoration of CNTs with inorganic nanoparticles, thus it is key to understand what drives the nucleation of the components on the surface of the CNTs. This chapter discusses the basics of homo- and heterogeneous nucleation.

Classic nucleation theory presents the most common theoretical model used to understand the timescales involved in nucleation. Nucleation describes the rearrangement of atoms or molecules of a reactant phase into clusters that are large enough to grow irreversibly to a macroscopically larger size. There are two types of nucleation: (1) *homogeneous nucleation* where nucleation happens in bulk solution when the supersaturation exceeds a critical value, and (2) *heterogeneous nucleation* where the nucleus forms in the presence of a solid phase. Homogeneous nucleation is less common than heterogeneous, as it is often less energetically favorable.<sup>[194]</sup>

Prior to nucleation, clusters form as a result of molecule collisions in the bulk solution. They continuously break apart and reform until they are stable enough to grow. This stability depends on the balance between the free energy necessary for the formation of a new interface and the energy released by the formation of bonds in the bulk structure. Thus, the Gibbs free energy is a critical factor.<sup>[194]</sup> It is defined as

$$G = H - TS, \quad (2.1)$$

where  $H$  is the enthalpy,  $T$  is the temperature and  $S$  is the entropy. The most thermodynamically stable state of an arrangement of atoms is the one with a minimum Gibbs free energy and  $dG=0$ . During cluster formation, the Gibbs free energy of the system changes as shown in equation 2.2, where  $\Delta G$  is the free energy of nucleation,  $r$  is the radius of the formed particle,  $\gamma_{SL}$  the surface tension on the solid/ liquid interface and  $\Delta G_V$  is the difference in free energy per unit volume between the phase that nucleation is occurring in, and the phase that is nucleating.<sup>[195]</sup>

$$\Delta G = -4/3 \pi r^3 \Delta G_v + 4\pi r^2 \gamma_{SL} \quad (2.2)$$

The creation of a small volume of solid thus has a negative contribution due to the lower free energy of the bulk solid (left term of the equation- volume term), whereas the creation of a new interface has a positive contribution (right term - surface contribution). The relationship between the particle radius  $r$  and  $\Delta G$  is schematically shown in figure 2.2A. If the radius  $r$  is below the critical radius  $r^*$ , the system can lower its free energy by dissolution of the solid, whereas when  $r > r^*$ , the free energy of the system decreases when the solid grows. Hence a particle radius below the critical radius leads to unstable solid particles that dissolve again, whereas once the radius is above the critical radius, those particles (now called nuclei) are stable and grow into larger particles.  $\Delta G^*$  shows the energy barrier needed to be overcome for the formation of a stable nucleus.<sup>[195]</sup> The critical radius  $r^*$  for the formation of a stable particle can then be defined as:

$$r^* = -2\gamma_{SL}/\Delta G_v \quad (2.3)$$

In heterogeneous nucleation, the solid phase introducing nucleation can be particles of a different phase or crystals of the phase that is crystallizing. It can be considered a surface catalyzed nucleation process. The activation energy needed is significantly lower than for homogeneous nucleation, as seen in figure 2.2B, thus it is kinetically more favorable. It is important to note here that the critical radius of the nucleus is independent of the type of nucleation.<sup>[195]</sup> As the nucleation barrier arises from the surface term in equation 2.2, the contribution changes with the shift from a spherical nucleus, where the energy is related to the surface area times surface tension of the sphere, to nucleation on the surface, introducing a range of other factors like the contact angle. Thus the Gibbs free energy for heterogeneous nucleation can be written as:<sup>[196]</sup>

$$\Delta G_{heterogeneous} = \Delta G_{homogeneous} \cdot f(\theta) \quad (2.4)$$

where  $f(\theta)$  is a function of the contact angle

$$f(\theta) = \frac{2 - 3\cos\theta + \cos^3\theta}{4} \quad (2.5)$$

where  $\theta$  is the contact angle between the heterogenous surface and the nucleating particle. If  $\theta$  is  $0^\circ$ , complete wetting of the surface takes place and thus the reaction is fully catalyzed without a barrier to nucleation at the surface. If  $\theta$  is  $180^\circ$ , there will be no wetting of the surface and thus no catalysis of the reaction by the surface, making this case similar to homogeneous nucleation.

## 2 Chemical Modification of Carbon Nanotubes

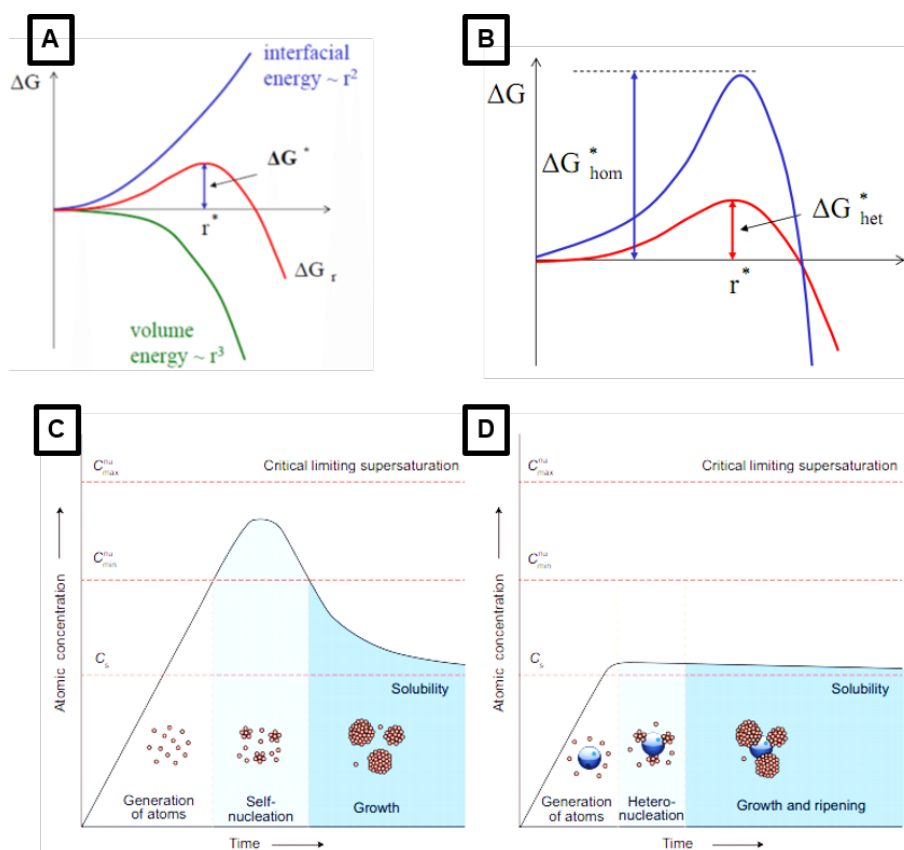


**Fig. 2.2** The graph shows (A) the free energy change associated with homogeneous nucleation of a sphere of radius  $r$  and (B) the free energy change as a comparison of homogeneous and heterogeneous nucleation.<sup>[195]</sup> It can be seen that the activation barrier for heterogeneous nucleation is lower, but the critical radius remains the same. The bottom graph shows the reaction time vs. concentration diagrams, explained by the LaMer theory for the formation of nanoparticles by (C) homogeneous and (D) heterogeneous nucleation.  $C_s$  is the saturation concentration of the precursor in the reaction solution.<sup>[197]</sup>

LaMer's nucleation theory links the concentration change occurring by nucleation to the involved timescales. A driving force in nucleation and crystal growth is supersaturation. Supersaturation occurs once the solubility limit  $S$  or the saturated vapor pressure  $P_{\text{sat}}$  of a substance have been exceeded. A solute-rich phase separates out from the solvent. Small particles nucleate then and grow by two mechanisms: (1) coalescence and/ or (2) *Ostwald ripening*, depending on whether the forces between the particles are attractive or repulsive. During *Ostwald ripening* individual molecules move by diffusion through the solvent from the smaller to the larger particles.<sup>[194]</sup> This change causes the concentration in solution to decrease to a metastable regime below the critical saturation concentration, stopping nucleation but favoring growth. This process is shown in figure 2.2C for homogeneous nucleation and figure 2.2D for heterogeneous nucleation. This suggests that the synthesis of monodisperse colloids needs to be designed in a way that the concentration increases rapidly above the saturation concentration, causing nucleation with the formation of a large number of nuclei in a short space of time which then start growing.<sup>[198,199]</sup>

In this thesis, heterogeneous nucleation on CNTs is crucial to the inorganic modification. While there are many reports for the modification of graphitic surfaces,<sup>[71,200]</sup> the influence factors, mechanisms

and models to further understand heterogeneous nucleation are rarely discussed in detail which makes the selection and adjustment of the syntheses challenging.

## 2.2 CNT functionalization

The modification techniques used for CNT powders and CNT forests can be split into gaseous and liquid phase synthesis methods. As both techniques are used in this thesis, short overviews of relevant types of both techniques are given here with focus on their use for CNT modification. In general, CNT powder modification is usually done in the liquid phase whereas gaseous phase methods are more commonly used for CNT forest modification. Much work has been done on modifying CNT powders, whereas the functionalization of CNT forests is still facing a range of challenges due to detachment from the substrate and unwanted changes in the aligned structures, such as foaming,<sup>[183]</sup> limiting the amount of reports available, even though aligned CNT structures are highly desirable for a range of applications. This clearly shows the gap in literature that is addressed in this thesis where aligned CNT structures are modified with inorganic nanoparticles.

### 2.2.1 Gaseous phase modification

Gaseous phase modification can be defined as methods where a gaseous precursor interacts with the surface to be modified. Ozonolysis and plasma treatments, as well as chemical (CVD) and physical vapor deposition (PVD) are important methods in this category.

#### 2.2.1.1 Ozonolysis and plasma treatment for CNT oxidation

Defects sites are necessary not only as nucleation points for a range of reactions,<sup>[68-71]</sup> but also for an improved dispersibility in water-based solutions for further modification. The process of generating defect sites for further reactions on CNTs is called "activation" and is mostly referring to the oxidation of the carbon bonds in the side wall to introduce carboxylic, hydroxyl or carbonyl groups. This activation can be achieved in several ways, such as liquid oxidation with acids or oxidation with ozone or plasma.

Plasma functionalization, in general, is a versatile technique, as a range of chemical groups can be introduced on the CNT surface, depending on the feed gas (e.g. Ar, O<sub>2</sub>, CHF<sub>3</sub>, and SF<sub>6</sub>).<sup>[201-203]</sup> Activation of MWNTs was shown using a variety of plasma technologies, such as oxygen and air dielectric barrier discharge plasma<sup>[204,205]</sup> or an atmospheric pressure plasma jet.<sup>[206]</sup> MWNTs were treated using a microwave excited Ar/H<sub>2</sub>O surface-wave plasma to improve their dispersion capability in water.<sup>[207]</sup> A comparison of heating in air flow, oxygen-plasma and acid-oxidation on MWNTs was reported by Ago et al.<sup>[208]</sup> They found that heating MWNTs in air flow introduces mainly hydroxyl and carbonyl groups, plasma treatment destroyed the  $\pi$ -conjugation and forms an amorphous carbon phase, acid-oxidation preferentially introduces carboxylic acid groups on the surfaces of MWNTs. Another

## 2 Chemical Modification of Carbon Nanotubes

---

comparison between plasma functionalization and acid treatment<sup>[186]</sup> in regard to the structure and electrical properties of MWNTs found plasma treatment to have a lower damaging effect and to not change the electrical surface resistivity.

Ozone oxidation presents another way to activate CNTs. Ozonolysis is a common way to oxidatively break carbon-carbon double bonds at low temperatures<sup>[209,210]</sup> Ozone can easily be generated by ultraviolet excitation of molecular oxygen.<sup>[211]</sup> It has been found that room temperature UV-generated ozone leads to an irreversible increase in the electrical resistance of SWNTs<sup>[212]</sup> and MWNTs,<sup>[211]</sup> due to the oxidation on the sidewalls. Dissociation of ozone by 254 nm UV light can generate highly reactive singlet oxygen atoms and molecules, which could either oxidize defects or create new defects. Ramos et al.<sup>[213]</sup> reported that the wettability of CNT forests can be changed by oxygen pulsed direct-current (DC) plasma, as this creates oxygen containing groups on the CNTs, similar to the plasma treatment of powders. The wettability change by oxygen DC plasma for CNT forests was shown to also have a very brief treatment time.<sup>[214,215]</sup> Kim et al. found that the structural defect density linearly scales with the oxygen plasma treatment time.<sup>[216]</sup>

### 2.2.1.2 Physical vapor deposition (PVD) for inorganic modification

PVD was used for all early semiconductor technologies to deposit metal layers. It is a technique that can use solid, liquid or vapor as a raw material to deposit thin films on substrates. PVD can be categorized by the way the deposition is achieved.<sup>[151]</sup> A comparison between sputtering and evaporation as techniques can be found in appendix A table A1.<sup>[151]</sup> Thermal evaporation is often used to deposit the catalyst layers for the vertically aligned CNT growth.<sup>[139,173]</sup> Further, metal coating on CNTs can be achieved using PVD methods like sputtering or e-beam evaporation. An example was published by Tawfick et al.<sup>[217]</sup> where gold layer was deposited onto CNT pillars at a specified angle and the pillars were densified afterwards inducing bending. This presents a different approach to create slanted nanopillars for anisotropic wetting compared to the formation of polymer nanohairs.<sup>[218]</sup>

### 2.2.1.3 Chemical vapor deposition (CVD) for inorganic modification

CVD presents another way for thin film creation. A vaporized precursor (often diluted with an inert gas) chemically reacts with a surface, depositing a solid film. CVD is a very versatile method which operates at low or atmospheric pressure and at low temperatures. It is scalable and enables the depositions of a variety highly defined films (metals, semiconductors, organic compounds) with a high degree of purity, control and economy.<sup>[151]</sup> Sample surface chemistry, its temperature and thermodynamics influence which compounds are deposited. Reactions are promoted by heat (thermal CVD), higher frequency radiation such as UV (photo-assisted CVD) or a plasma (plasma-enhanced CVD).<sup>[219]</sup> Important phenomena influencing the film formation at the surface are surface adsorption, surface diffusion, surface reaction, desorption and film and crystal growth.<sup>[151]</sup> A more detailed overview of the reaction mechanism is described in figure 2.3.

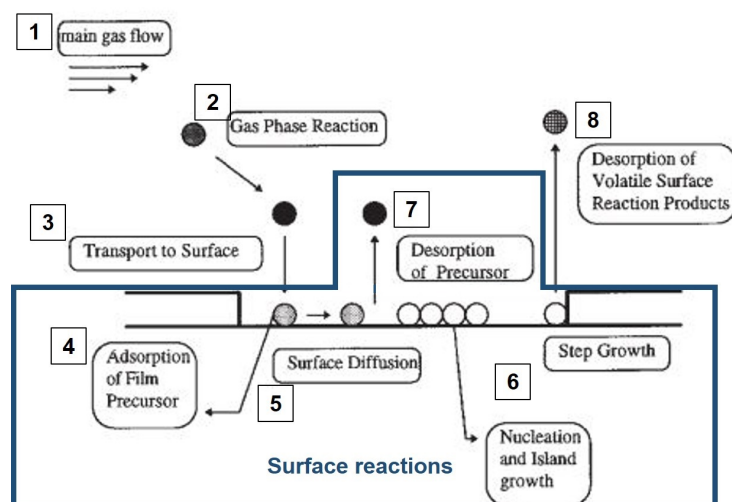


**Fig. 2.3** This schematic shows the reaction mechanisms and stages involved in a CVD process.<sup>[219]</sup>

The evaporation and transport of the precursors in the bulk gas to the adsorption site are shown as the first step (1). Then the precursors react in the gas phase to form intermediates (homogeneous reaction) and by-products (2). Those intermediates are then transported onto the surface (3) and adsorb there (4). Surface reactions (heterogeneous) occur selectively at the heated surface and surface diffusion to the growth sites can be observed (5). At the growth sites, those reactants are incorporated into the film (nucleation), leading to island and film formation (6). By-products and precursors desorb from the surface and are transported away from the deposition zone (7,8). The film growth rate in this process is influenced by the temperature of the substrate, the operating pressure of the reactor and the composition and chemistry of the gas phase. For example, in the low-pressure CVD, the surface reaction is the rate limiting step, whereas in the atmospheric pressure CVD the mass-transport is the rate limiting step.<sup>[151,219]</sup>

A special type of CVD is atomic layer deposition (ALD).<sup>[219]</sup> It is used to e.g. deposit layers of  $\text{Al}_2\text{O}_3$  or  $\text{TiO}_2$  as it allows to grow high-quality, conformal thin films through alternate self-limiting surface reactions. In ALD gaseous precursors are introduced sequentially to the substrate surface and the reactor is purged with an inert gas, or evacuated, between the precursor pulses. It is important that surface reactions dominate and that thermal decomposition of the precursor is minimized or avoided altogether. Thus, ALD processes are done at substrate temperatures between 200–350 °C, which is below the thermal decomposition temperature of most precursors. The advantage of ALD is that it can produce high quality, dense and pin-hole free films over large areas which show very good uniformity. Also their thickness and composition can be controlled at an atomic level. However, it suffers from a low effective deposition rate, impurity incorporation and limited material selection.<sup>[219]</sup> ALD produces a smooth conformal coating on CNTs. It is used to coat CNTs with a range of materials, such as platinum,<sup>[220]</sup> ruthenium,<sup>[221]</sup> and metal oxides (e.g. titania,<sup>[222]</sup> vanadium oxide<sup>[223]</sup> or alumina<sup>[224,225]</sup>), as it leads to uniform coatings with a controllable thickness. Stano et al.<sup>[226]</sup> reported the conformal coating of a CNT forest by ALD with  $\text{Al}_2\text{O}_3$  which lead to an 100-fold increase in mechanical stiffness, improved thermal stability towards oxidation and a change in wetting

## 2 Chemical Modification of Carbon Nanotubes

properties from hydrophobic to hydrophilic. [139,226] Coating of CNT forests via ALD has also been shown for other materials, such as zinc oxide, [227] Pt [228] and TiO<sub>2</sub> [229]

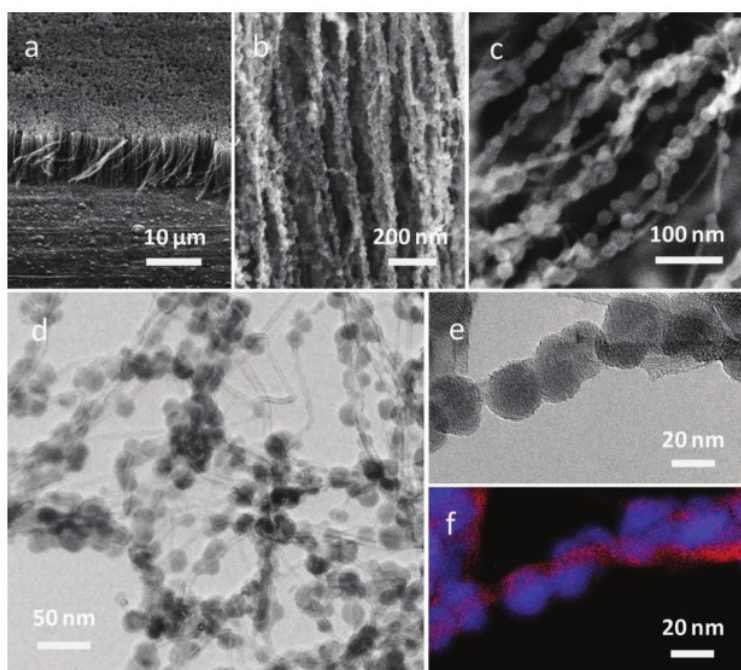


**Fig. 2.4** SEM images of the vertically aligned CNTs (VACNTs) coated with CVD silicon can be seen in (a-c), a TEM image with low magnification in (d) and high magnification in (e), clearly showing the silicon particles. (f) shows a coated CNT strand (carbon-red) with silicon (blue) using energy spatially resolved energy-filtered TEM. [64]

A coating with uniformly dispersed silicon or silicon nitride can be achieved by CVD. [64,230] The modification of a CNT-forest with silicon can be seen in the image in figure 2.4. A CVD process for the formation of silicon nanowires [231,232] is used in this thesis for the coating of 3D CNT structures.

### 2.2.2 Liquid phase modification

While the gaseous phase synthesis is often less destructive, liquid synthesis offers access to a large range of chemical reactions that can easily be scaled up in volume. A wet chemical route enables access to all parts of the structure and hence a more uniform coating, e.g. compared to PVD which often fails to coat the inside of the structure. Commonly used liquid phase techniques for the decoration of CNTs with inorganic nanoparticles include the following methods:

- **Thermal solution chemistry:** A standard flask process with stirring for a certain amount of time at a set temperature to react the precursors is used, often followed by an annealing step. The synthesis of Au, Pd, Ag and Pt nanoparticles on CNT using a thermal reduction method and annealing was reported by Xue et al. [233] For high Pt loading, sodium dodecyl sulfate (SDS) can be used as a surfactant and reacted with urea and ethylene glycol (EG) on the surface of CNTs, as shown by Fang et al. [234] Another way is to adsorb poly(allylamine hydrochloride) via

electrostatic self assembly onto the CNTs and then use EG to reduce the Pt-precursors. [235] Those Pt-particles can be used as catalysts for further reactions, as shown by Cui et al. [236] who reported the growth of Ag-nanowires on CNTs by using Pt catalysts for antimicrobial properties. An aqueous chemical synthesis resulting in fcc crystals of Cu and Ag on the surface of CNTs was described by Mohan et al. [237]

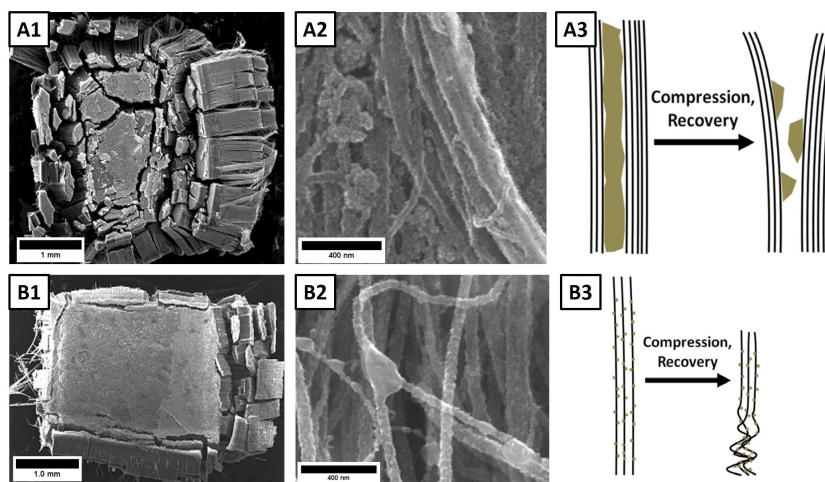


**Fig. 2.5** The modification of forests with  $\text{SnO}_2$  can be seen in the SEM images A1 and A2. The modification with  $\text{MnO}_2$  is shown in B1 and B2. It can be observed that the forest with  $\text{MnO}_2$  is less damaged and the coating is rather on the single CNTs or bundles. This behaviour causes better recovery after compression (A3 and B3). [238]

Raney et al. [238] showed an in-situ synthesis of  $\text{SnO}_2$  and aqueous synthesis of  $\text{MnO}_2$  with subsequent annealing and investigated the differences in the mechanical properties between those two materials. A comparison between the two metal oxides can be seen in figure 2.5.  $\text{SnO}_2$  mostly coats bundles whereas  $\text{MnO}_2$  actually coats single CNT strands, thus causing a better recovery after compression, rather than breaking.

Cu particles were deposited on CNT forests by Stano et al. [239] by impregnation with a copper salt solution and subsequent calcination and  $\text{H}_2$  reduction, which presents a method that is possible to adapt to other metal nanoparticles. In 2003, Lee et al. [240] demonstrated the formation of anatase  $\text{TiO}_2$  particles by hydrolysis and condensation of a precursor. The functionalization of CNTs with  $\text{MnO}_2$  by a dipping method was reported by Lee et al. [34] in 2010. CNT forests were decorated with Pt nanoparticles for underwater vehicle propulsion, reported by Marr et al., [241] using a one-step deposition process by reduction of chloroplatinic acid. Iron oxide modification was reported using an aqueous synthesis by Gupta et al. [13] leading to a mixture of iron oxides phases on the CNTs.

- **Electroplating:** The deposition of metal oxides on CNT forests add versatility to the CNT forests for many applications, such as an active material for batteries or supercapacitors. Electrodeposition of  $\text{V}_2\text{O}_5$  onto CNT forests as an anode and cathode material for Lithium-ion batteries was reported by Lu et al. [242] This method can also be used for a  $\text{TiO}_2$  coating on

## 2 Chemical Modification of Carbon Nanotubes

VACNTs.<sup>[243]</sup> The electrodeposition of manganese oxide nanoflowers was shown by Zhang et al.<sup>[62]</sup> also for capacitive storage. Jiang et al.<sup>[32]</sup> added oxidized Ni-particles for pseudo-capacitor electrodes (figure 2.6).

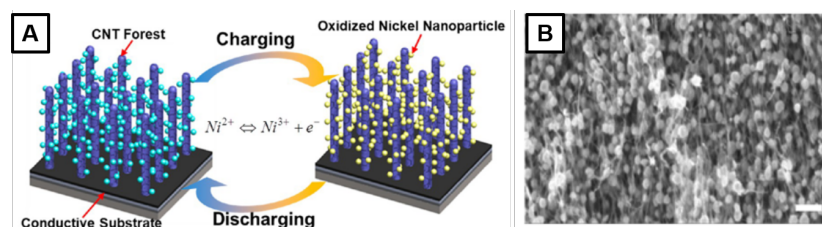


**Fig. 2.6** The modification of a CNT forest with Ni particles using electroplating is shown schematically in (A). The SEM (B) shows the particles on the aligned CNTs.<sup>[32]</sup>

- **Particle deposition from solution:** Dropcasting of quantum dots to densify the CNT structure and to incorporate CdSe@ZnS core-shell particles was reported by Lim et al.<sup>[244]</sup> for field emission measurements using a suspension of the quantum dots in toluene. Yang et al.<sup>[245]</sup> reported a method with nebulized ethanol assisted infiltration for metal oxide modification of CNT forests to ensure a uniform infiltration of the forests, combined with a subsequent annealing step. Metal-oxide formation on CNTs was also reported by Ajayan et al.,<sup>[246]</sup> creating a  $V_2O_5$  coating by mixing with the nanoparticle powder and subsequent heating. Ahmad et al.<sup>[65]</sup> reported the formation of flexible batteries with vertically aligned CNT structures and  $Fe_2O_3$ -particles dropcasted onto them.

Dai's group has shown that a strong coupling between the nanoparticle and the carbon substrate leads to a significant improvement of the electrochemical performance of the material<sup>[68–71]</sup> which makes syntheses resulting in covalent bonds beneficial over other methods, such as dropcasting. They also showed that for the nucleation of nanoparticles on graphitic materials O-containing groups or defects are needed.<sup>[71,247]</sup> Thus, for this thesis the vertically aligned CNT structures are first activated (=oxidation of CNTs) to create multiple nucleation sites for the nanoparticle formation and subsequently modified with nanoparticles by a liquid phase modification method called hydrothermal synthesis, as well as a modified dropcasting protocol and gas phase methods. This type of synthesis has attracted a huge amount interest due to its potential for environmentally friendly and versatile synthesis with good energy utilization through short reaction times, non-toxic solvents and a large range of possible precursors.<sup>[248]</sup>

### 2.2.2.1 Liquid phase CNT oxidation

For the creation of defect sites,  $O_2$ -plasma or UV-ozone can be used. However, liquid oxidation is considered the most efficient method. Oxidants such as  $HNO_3$  or  $H_2SO_4$ -  $HNO_3$  mixtures are used to purify CNTs as they dissolve the residue metal catalyst particles and introduce defects.<sup>[249]</sup> However, they can cause significant destruction to the CNTs which is especially an issue for SWNTs that can

loose crucial properties, such as electrical conductivity.<sup>[201]</sup> When combined with another strong oxidant, such as sulfuric acid, SWNTs can even be cut into very short pieces by this treatment.<sup>[250]</sup>

Applied to CNT forests this harsh treatment can lead to the detachment of the CNTs from the substrate and thus the destruction of the structure. Hence, a HNO<sub>3</sub>-based wet treatment for oxidation of the tubes cannot be used. However, Shulga et al.<sup>[251]</sup> have reported HNO<sub>3</sub> vapor oxidation to introduce carbonyl and carboxyl groups, while avoiding condensation of the vapor onto the substrate by a high substrate temperature.

Due to the detachment of the CNT forest, dry modification, mostly by plasma treatment, is preferred for the activation of forests in this thesis.

### 2.2.2.2 Hydrothermal nanoparticle synthesis

Hydrothermal synthesis refers to any heterogeneous reaction in the presence of aqueous solvents or mineralizers under high pressure, high temperature conditions. A broader definition that includes many of the recent papers on “mild hydrothermal conditions” as well as the application of hydrothermal synthesis to nanomaterials is “any heterogeneous or homogeneous chemical reaction in the presence of a solvent, aqueous or non-aqueous, above room temperature and at pressure greater than 1 atm in a closed system.”<sup>[248]</sup> This is the definition that will be used here. Other commonly used terminologies are “conventional hydrothermal” for aqueous solvent based reactions and “solvothermal” for non-aqueous solvents with low to high temperatures, as well as further differentiation by the solvent used, such as “glycothermal” or “alcothermal.”<sup>[248]</sup>

Compared to conventional techniques, hydrothermal synthesis offers several advantages. Compounds with elements in oxidation states otherwise difficult to obtain can be synthesized (e.g. ferromagnetic chromium (IV) oxide).<sup>[248]</sup> Additionally it can be used for homogeneous precipitation using metal chelates, decomposition of hazardous chemical substances, monomerization of high molecular weight polymers like polyethylene terephthalate and often manages to avoid the calcination step in chemical synthesis. A variation of hydrothermal synthesis is supercritical hydrothermal synthesis, which uses temperatures and pressures above the critical point of water. Thus, it utilizes the abnormal behaviour of water in this region, such as the fact that water also becomes a good solvent for nonpolar components, is fully miscible with many organic and inorganic compounds or can act as an acid, a base or an acid-base catalyst at near-critical or supercritical conditions. This enables a wider range of reactions conditions as well as product recovery by a change in conditions, such as adjusting the temperature and pressure.<sup>[252]</sup> In hydrothermal processing the solvent plays multiple roles. It acts as an absorbent, solvent, and reactant in addition to being the transfer medium. Surfactants are often necessary to control the nucleation of a desired phase and ensure the right size, shape and homogeneity of the synthesized particles.<sup>[248]</sup>

A detailed comparison of hydrothermal synthesis with other powder synthesis methods can be found in table A2 in appendix A.<sup>[253]</sup> With water being the environmentally most friendly and cheapest solvent as well as the processing conditions requiring low energy consumption, hydrothermal synthesis

## 2 Chemical Modification of Carbon Nanotubes

is a highly favorable way of chemical synthesis and holds a lot of promise for the future for bio-, nano-, and geotechnology.

Hydrothermal synthesis is not only used for a range of nanoparticle synthesis,<sup>[254–256]</sup> but also for graphene/ nanoparticle and CNT/ nanoparticle hybrids.<sup>[71,257,258]</sup> Wu et al.<sup>[185]</sup> reported a hydrothermal method followed by calcination to create TiO<sub>2</sub>-nanosheets. Hollow  $\alpha$ -Fe<sub>2</sub>O<sub>3</sub> nanohorns can be grown on CNTs as shown in figure 2.7.<sup>[259]</sup>

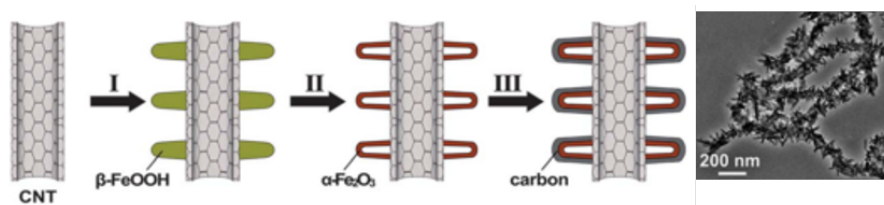


**Fig. 2.7** The process for the growth of hollow  $\alpha$ -Fe<sub>2</sub>O<sub>3</sub> nanohorns onto CNTs is shown here. After the multiple step synthesis, a uniform coating on the individual CNTs can be achieved (TEM image on the right).<sup>[259]</sup>

Due to their conductivity, CNT metal-oxide composites are very promising for Lithium-ion batteries and thus, several reports give an overview of the performance of those hydrothermally synthesized hybrid structures, e.g. Wu et al.<sup>[260,261]</sup> for the synthesis of SnO<sub>2</sub>, TiO<sub>2</sub> and Fe<sub>2</sub>O<sub>3</sub> on CNTs. The functionalization of CNTs with MnO<sub>2</sub> was reported by Xia et al.<sup>[262]</sup>

**Microwave-assisted, hydrothermal nanoparticle synthesis** Hydrothermal reaction kinetics can be enhanced by activation processes using microwaves, ultrasound, mechanical mixing and electrochemical reactions. This is called multi-energy processing of materials and enables the reduction of the duration of the reactions. Microwave and sonar possibilities have been explored by the Materials Research Lab at Penn State in the 1990s and then became very popular for a wide range of reactions.<sup>[248]</sup>

Microwave radiation ranges from 30 GHz to 300 MHz, a wavelength of 1 m to 1 cm and its applications are within communication and heating. Microwave chemistry is of high interest, as high-quality syntheses are possible using microwaves. Thus, it has spread into most chemistry fields, especially inorganic chemistry. A detailed overview of all the different fields for microwave radiation and microwave chemistry can be found in figure A1 in appendix A.<sup>[263]</sup>

Microwaves heat the sample directly by interaction of the electromagnetic radiation with the molecules, thus decreasing the time of heat conduction significantly compared to conventional heating and advancing the reaction rates. It affects the rotation of dipoles and induces translational motion in the reaction media. As microwave radiation produces an oscillating field, these dipoles constantly realign in the electric field, producing kinetic energy that gets converted into heat due to molecular friction and collisions.<sup>[264]</sup>

A comparison between the temperature profiles of water after 60s of microwave irradiation and heating in an oil bath can be seen in figure 2.8. Microwave radiation heats the reaction volume simultaneously,

whereas an oil-bath clearly shows a temperature gradient from the walls to the inside. The difference in the temperature profile can cause non-uniform nucleation and a change in the reaction kinetics. The advanced reactions rates make it a very attractive method for polymer, organic and inorganic syntheses. For inorganic synthesis, calcination and sintering of ceramics was reported in 1972 and many fundamental studies followed around 1980.<sup>[263]</sup>

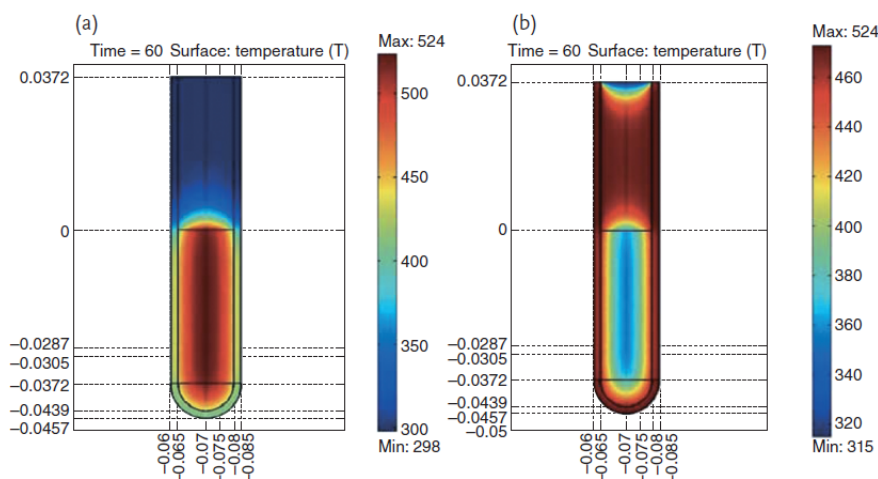


**Fig. 2.8** This schematic shows the temperature profile after 60s for water heated by microwave irradiation (a) and in an oil-bath (b). The microwave heating raises the temperature of the whole solution simultaneously whereas for the oil bath the walls are heated first. The temperature scale is in Kelvin and '0' on the vertical scale indicates the position of the meniscus.<sup>[263]</sup>

This microwave technique can be combined with hydrothermal processing, leading to even more advantages in nanoparticle synthesis, such as no need for a reducing agent and a very reduced reaction time when performing, e.g. a silver nanoparticle synthesis.<sup>[264]</sup> Those two techniques combine rapid uniform heating, a short reaction time, increased reaction rates and fast kinetics of crystallization, and a high uniformity of particles. The microwave and hydrothermal effects contribute significantly towards a green chemistry route, being able to save energy and time for nanomaterial preparation. Additionally, microwave radiation is very promising for carbon nanotube oxidation, purification, and modification. In the presence of electrical conductors, microwaves can be absorbed very effectively due to the strong interaction of the electric field of the waves with the nearly free moving electrons.<sup>[264]</sup> When heating CNTs with microwave irradiation, the presence of ions and metal catalyst impurities is the main cause of localized hot spots, leading to increased temperatures in the proximity of the CNTs. This makes microwave irradiation a powerful tool for CNT functionalization.<sup>[263]</sup>

Microwave-assisted, hydrothermal synthesis has been applied to a range of nanomaterials, such as ZnO, Ag, and Fe<sub>2</sub>O<sub>3</sub>.<sup>[263]</sup> A study for the tuning of aspect-ratio, size and shape of Fe<sub>2</sub>O<sub>3</sub> nanoparticles has been reported by Hu et al.<sup>[265]</sup> They found that the amount of iron precursor plays an important role in the morphology of  $\alpha$ -Fe<sub>2</sub>O<sub>3</sub> nanoparticles.<sup>[263]</sup>

Mazloumi et al.<sup>[266]</sup> reported metal oxide and vertically aligned CNT hybrid structures with a high diversity in shape and composition using microwave synthesis and a subsequent annealing step. These hybrid structures of Co<sub>3</sub>O<sub>4</sub>/CNT, ZnO/CNT and MnO<sub>2</sub>/CNT were then tested as electrode materials

## **2 Chemical Modification of Carbon Nanotubes**

---

for supercapacitive storage. Very few reports on microwave-assisted, hydrothermal synthesis used for patterned, vertically aligned CNT structures were found which clearly shows the gap in literature that this thesis is addressing.

This part gave an overview on how CNTs are made, structured and modified. The next part will discuss the results of the PhD project, starting with the fabrication of vertically aligned 3D CNT structures with (I) nanoscale patterns and (II) microscale honeycomb shaped patterns. Following the fabrication, the modification of those structures with selected active materials is discussed, before testing them for Lithium-ion battery and solar watersplitting electrodes.

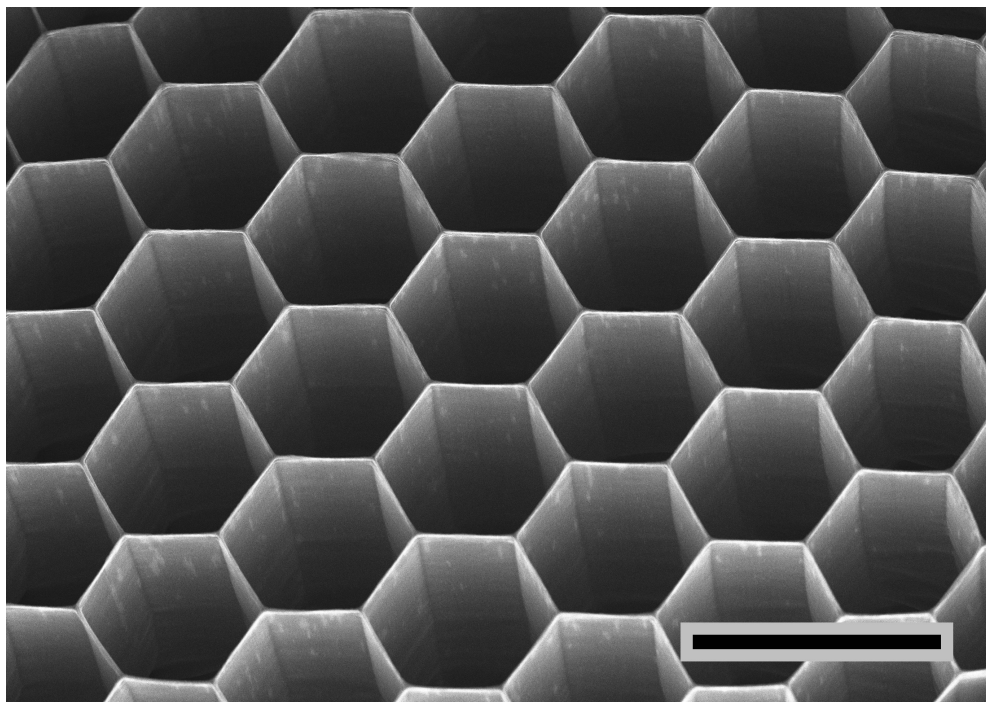
## **Part III**

# **Results**



## Chapter 3

# Fabrication of 3D CNT Structures with pores



Vertically aligned CNTs shaped into honeycombs, scale bar 100  $\mu\text{m}$ .

Results in this chapter were achieved in collaboration with Dr. D. Copic and Dr. S. Ahmad.

### 3.1 Introduction

For energy storage applications, controlling the material porosity and tortuosity is key. As mentioned before, this thesis focusses vertically aligned CNT structures that will be used as advanced electrode structures in Lithium-ion batteries (LIBs) and solar watersplitting.

A limitation in increasing the electrode thickness in LIBs is the need to sustain good Li-ion diffusion and electron conductivity throughout the thickness. Anisotropy can be used to enhance the transport through the thickness of the film. Thus, vertically aligned CNT structures (3D CNT structures) with hexagonally ordered pores are created to provide Li-ion pathways into the structure through the holes and a conductive pathways throughout the thickness by the aligned CNTs.

For solar watersplitting, the photoelectrodes require a high surface area to absorb as many photons as possible, as well as a good charge carrier separation, thus good conductivity. To address these requirements a honeycomb-shaped 3D CNT structure is fabricated that supplies good electron conductivity, good mechanical stability and a high surface area.

Additionally, CNTs offer a platform that can easily be modified with a range of materials, as discussed in chapter 2. This makes not only the structure itself, but also the material very suitable, as a wide variety of active materials can be synthesized onto the CNTs themselves, as discussed further in chapter 4. Depending on the application, pore sizes in the micrometer or nanometer range are needed. Hence, this chapter discusses the fabrication of these 3D CNT structures with pores on micro- and nanoscale.

### 3.2 CNT honeycomb fabrication

The previously introduced CNT forests can be shaped into complex CNT structures using capillary aggregation (i.e. densification).<sup>[94]</sup> Very promising structures due to their mechanical stability and pores are honeycombs. Honeycombs made from vertically aligned CNTs have been reported before, e.g. by laser etching after CNT growth<sup>[179,267]</sup> or foaming of a CNT forest.<sup>[174]</sup> However, the control of structure parameters, such as honeycomb cell size, can be very low especially during foaming. A prepatterned substrate allows for a more targeted fabrication. UV-lithography is a scalable and straightforward way to achieve the necessary hexagonally ordered, circular pattern to create honeycomb shaped structures on microscale. This section focusses on the fabrication of these CNT honeycomb structures and provides a more detailed study of the parameters that influence to fabrication of defect free CNT honeycombs.

#### 3.2.1 CNT honeycomb fabrication process

The fabrication of CNT honeycomb structures can be split into two main steps: (1) CNT forest growth and (2) CNT structure densification, as seen in figure 3.2. During the first step, the catalyst template created by UV-lithography, as shown in figure 1.15, is used to grow vertically aligned CNTs in an ambient pressure chemical vapor deposition (CVD) furnace (see experimental section for details).

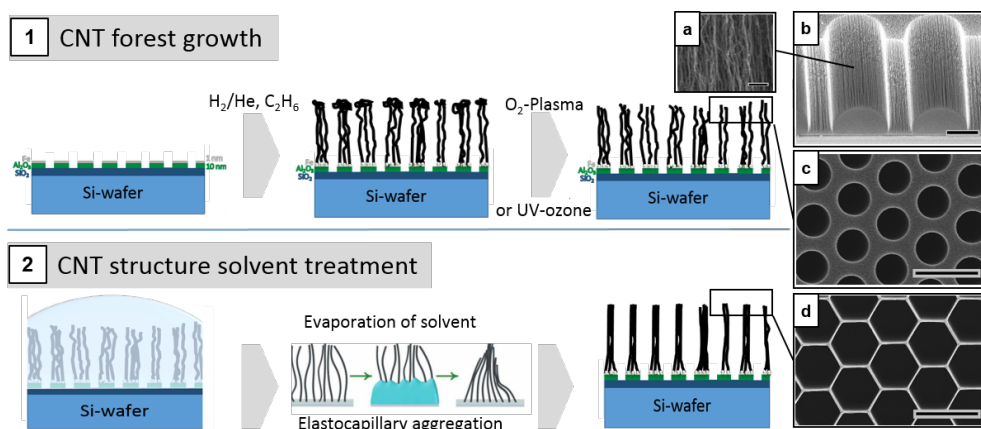


**Fig. 3.2** The first step is the CNT forest growth from the catalyst template and etching of the crust on top of the structure. The second step is the solvent treatment of the CNT structure which leads to elastocapillary aggregation; thus forming CNT honeycombs. The SEMs on the right show the aligned CNTs (a) after growth, the side view of the initial structure (b), a top view of the initial structure (c) and a top view of the densified honeycomb structure (d). Scale bars are 300 nm in (a) and 20  $\mu\text{m}$  in (b-d).

During the initial self-organization phase of the CNT growth, a tangled CNT mesh is formed which ends up being the “crust” on top of the CNT structure after growth,<sup>[109]</sup> as explained in section 1.3.2. It can impede the capillary aggregation in the solvent treatment process (= densification) due to its increased stiffness and thus it is important to remove it (see figure B1 in Appendix B). This can be done by  $\text{O}_2$ -plasma oxidation or UV-ozone treatment. Most of the initial experiments are done by  $\text{O}_2$ -plasma, later the process is switched to a UV-ozone system due to better availability.

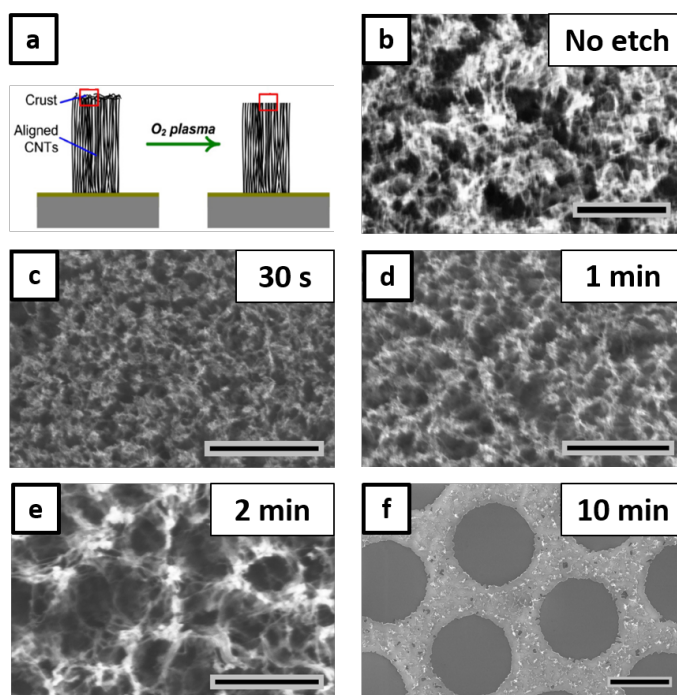


**Fig. 3.3** Different etching times of the CNT crust in  $\text{O}_2$  plasma. Scale bars are 800 nm in (b-e) and 20  $\mu\text{m}$  in (f).

### 3 Fabrication of 3D CNT Structures with pores

The etching time needs to be kept as short as possible to not damage CNTs, but must be long enough to remove the crust (figure 3.3a). For this reason increasing etching times in O<sub>2</sub>-plasma (Diener plasma system, 0.8 mbar O<sub>2</sub>) are studied for a honeycomb structure grown at 700 °C for 2 minutes (figure 3.3b). An etching time of 30 s (figure 3.3c) does not remove the small horizontal CNTs that indicate the crust. After ten minutes (figure 3.3f) the complete CNT structure is entirely etched away. No real difference can be seen in the SEM images in figure 3.3 d and e, both of them showing no more horizontal CNTs. Thus an etching time of 1 minute for the given conditions is chosen as sufficient for crust removal.

After the crust is removed, a drop of acetone is put onto the honeycomb structure and then evaporated (see figure 3.2, step 2, immersion densification). During the evaporation, densification of the hexagonally ordered holes into honeycomb structures takes place.

The phases in this densification process can be seen in figure 3.4, where the undensified hole structure is visible on the left and is getting gradually more densified towards the right of the structure with a complete densification at the very edge. It shows that, when the densification process is not completed yet, there are triangular holes at the connections of the three walls which later on close up and form the sharp corners of the hexagons. The influence of growth and patterning parameters on the honeycomb formation process is discussed in the next sections.

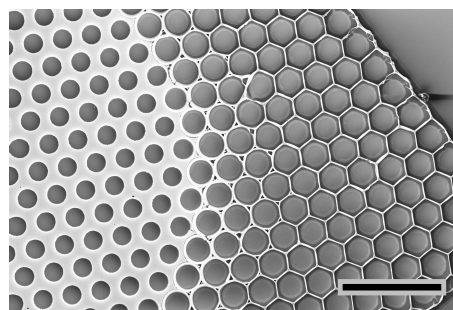


**Fig. 3.4** This SEM shows a stepwise densification leading to a CNT honeycomb structure from the left to the right. Scale bar is 200  $\mu\text{m}$ .

Additionally, modelling of this process is done in a collaboration with Prof. David Seveno (KU Leuven) to further the understanding of parameters involved in this process. Initial results indicate that the tortuosity of the vertically aligned CNTs is a crucial parameter for the overall densification into honeycombs rather than the formation of individual pillars. They might be critical for the balance between the CNTs.

Several parameters influence the CNT honeycomb formation process. Those parameters can be CNT growth parameters (such as growth time) or pattern design parameters (such as diameter of the circles). The following sections discuss the influence of some of those parameters.

#### 3.2.2 Influence of temperature on CNT honeycomb formation and the underlayer on growth height

**Growth temperature** The formation of a defect-free honeycomb structure is only observed to be possible for certain parameter ranges. It was found to work best for a pattern diameter of 30  $\mu\text{m}$  and a spacing between the holes of 10  $\mu\text{m}$  (CNT wall thickness) with a growth time of 5 minutes at 720 °C. The significant influence of a change in growth temperature on the resulting honeycomb structure can

be seen in figure 3.5. A higher growth temperature leads to more cracking in the structures (780 °C, figure 3.5a) or incomplete densification (740 and 760 °C, figure 3.5b and 3.5c). The structure grown at 700 °C shows a undamaged honeycomb pattern (figure 3.5d). All structures were grown for 2 minutes at the temperatures indicated in figure 3.5.

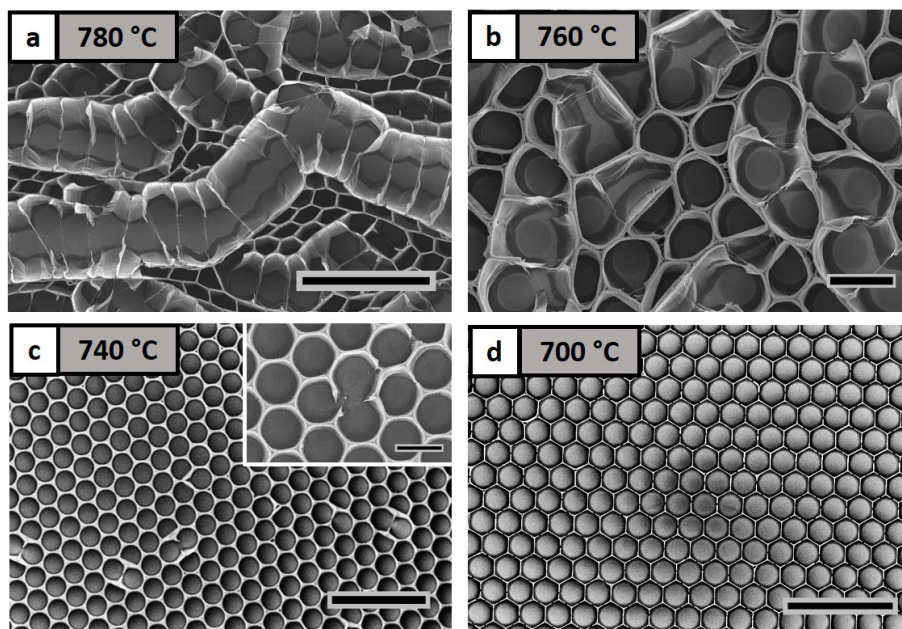


**Fig. 3.5** The influence of the growth temperature on the CNT honeycomb structure can be seen in the SEM images where the ones grown at 780 °C (a) show significant cracks and detachment from the substrate, the ones grown at 760 and 740 °C (b,c) show an incomplete densification with triangular holes where the three walls meet and the ones grown at 700 °C (d) have a perfect honeycomb shape. All samples were grown for 2 minutes under exactly the same conditions. Scale bars are 200  $\mu\text{m}$  in (a), (c), (d) and 50  $\mu\text{m}$  in (b) and inset (c).

This change in patterns is not surprising, as it has been found that the growth rate (as well as other parameters like diameter, density, and crystallinity of CNTs) is influenced by the temperature used in the growth process.<sup>[268,269]</sup> An increased temperature leads to faster growth and thus higher forests/ longer CNTs, as shown also in figure 3.6. Looking at equation 1.3 describing the critical elastic modulus that is needed to resist elastocapillary aggregation, height is a very relevant parameter. With an increased height more energy is required to resist the capillary aggregation. What can be observed here is that the capillary forces in a higher forest seem to be significantly higher than the ones holding the CNT honeycomb walls together. This leads to ripping of the walls and crack formation rather than a balanced interaction between the forces holding the walls together and densifying the structure. Investigating the influence of the temperature further is complicated, as the tortuosity and other CNT properties might change with a change in temperature. Thus, there is not only one influence parameter but a range to consider.

**Underlayer type** The standard underlayer used in this thesis is the native  $\text{SiO}_2$  on an Si-wafer with  $\text{Al}_2\text{O}_3$  and Fe as catalyst layers on top. However, for several applications such as watersplitting or batteries a conductive substrate is required. This can be achieved in two ways: by transferring

### 3 Fabrication of 3D CNT Structures with pores

the CNT structures afterwards onto conductive films (see chapter 4.3.3) or by using a conductive underlayer for the catalyst. Molybdenum was reported as a conductive substrate with the lowest contact resistance for an electrode with a CNT forest grown on it by Jiang et al.<sup>[32]</sup> which is why molybdenum (Mo) is deposited as a layer between SiO<sub>2</sub> and Al<sub>2</sub>O<sub>3</sub> for the conductive substrates in this work. They also reported that such a catalyst system shows dense forest growth which is desirable for the applications pursued in this thesis. Additionally the successful use of molybdenum as a conductive underlayer for the growth of CNT forests was reported by J. Cools et al.<sup>[270]</sup> for microelectrode arrays.

Pint et al.<sup>[271]</sup> showed that the use of Molybdenum as an additional catalyst with Fe introduced a decrease in the optimal growth temperature of the single-walled CNT. For the honeycomb formation it is thus important to understand relevant changes caused by the addition of Mo compared to the standard Al<sub>2</sub>O<sub>3</sub>-Fe catalyst system. The growth height has a significant influence on the honeycomb formation, hence making this a crucial parameter to be investigated. As shown in figure 3.6, two catalyst systems (molybdenum-aluminium-iron and molybdenum-alumina-iron) and our standard Fe-Al<sub>2</sub>O<sub>3</sub> system are examined for their influence on the growth rate. All samples have been grown at 740 °C and 750 °C for 30 minutes with all other conditions constant.

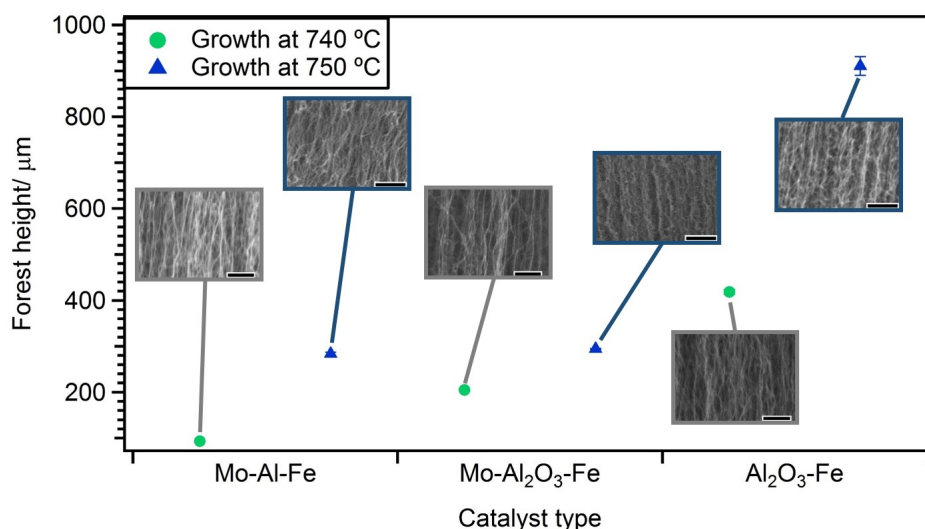


**Fig. 3.6** CNT forest height (grown at 740 °C and 750 °C for 30 minutes) is measured from SEM images for three different catalyst systems (alumina-iron (standard catalyst, 10 nm-1 nm), molybdenum-alumina-iron (40 nm-10 nm-1 nm) and molybdenum-aluminium-iron (40 nm-10 nm-1 nm)). There is an approx. 350 % increase in forest height for the standard catalyst at 740 °C and approx. 220 % at 750 °C. The SEM images for each growth condition show no significant change in the tortuosity or density of the CNT forest. Scale bars are 400 nm.

There is an approx. 350% increase in forest height for the standard catalyst at 740 °C compared to the growth with the Mo-Al-Fe catalyst and approx. 220 % at 750 °C can be measured. When an aluminium layer instead of an alumina layer is used, the forest height seems to be lower for a growth temperature of 740 °C. This might be due to different activation energies needed for the growth with different catalyst systems. SEM images taken of the middle part of the forest for each of the growth conditions show that there is no significant visible change in the CNT density or tortuosity, as far

as it can be told from the SEM images. Raman spectroscopy could be used to further analyze the influence of the change in underlayer on the quality of the tubes.

These data show that the use of molybdenum as an underlayer slows down the growth rate, thus leading to decreased forest heights. This suggests a changed interaction of the catalyst layers with the molybdenum, leading to a variation in particle size or maybe particle crystallinity during the growth process, similar to the changes reported by De Volder et al.<sup>[139]</sup> for a TiN underlayer that decreases the CNT growth rate due to the formation of larger catalyst particles compared to the catalyst on SiO<sub>2</sub>.

Overall, growth height, whether influenced by the type of underlayer or the growth temperature, has been found to be crucial for the 3D honeycomb formation process.

### 3.2.3 Influence of mask design parameters and growth time on CNT honeycomb formation

The main failure mode of honeycombs is by forming *cracks*. These start by the splitting of one wall of the CNT honeycomb structure. This first crack then can propagate through the whole structure. Eventually, if there are too many cracks, too much variability is introduced in the structure, making it unsuitable for certain applications. Thus, this section focusses on determining the factors which influence the crack formation.

The monitored parameters are hole diameters on the mask pattern of 5, 10, 15, 20  $\mu\text{m}$  with spacings of 5 and 10  $\mu\text{m}$ , as well as three growth times (2, 4, 6 minutes). The analyzed output parameters are growth height of the initial structure and the percentage of the cracked area. In total, 54 experiments were run with 2 repetitions for each condition. An overview of those experiments is shown in the table B2 in appendix B. For all those experiments the standard underlayer-system is used and the growth temperature is fixed to 720 °C.

It is well known that the growth height depends on the growth time, thus the height is calculated as an average of all the samples (18 samples) grown for the same time. After densification, the percentage of the cracked area on a sample is determined by analyzing representative SEM images for each sample using ImageJ. The area without honeycombs (cracked area) is calculated as a percentage of the overall area, giving a value for the crack percentage. This is done for a range of diameter and spacing combinations. The results can be seen in figure 3.7 as a color map with some example SEM images. The color shows the percentage of cracks in the structure: green means there are less than 10% cracks, whereas red means the crack percentage is higher than 50%.

### 3 Fabrication of 3D CNT Structures with pores

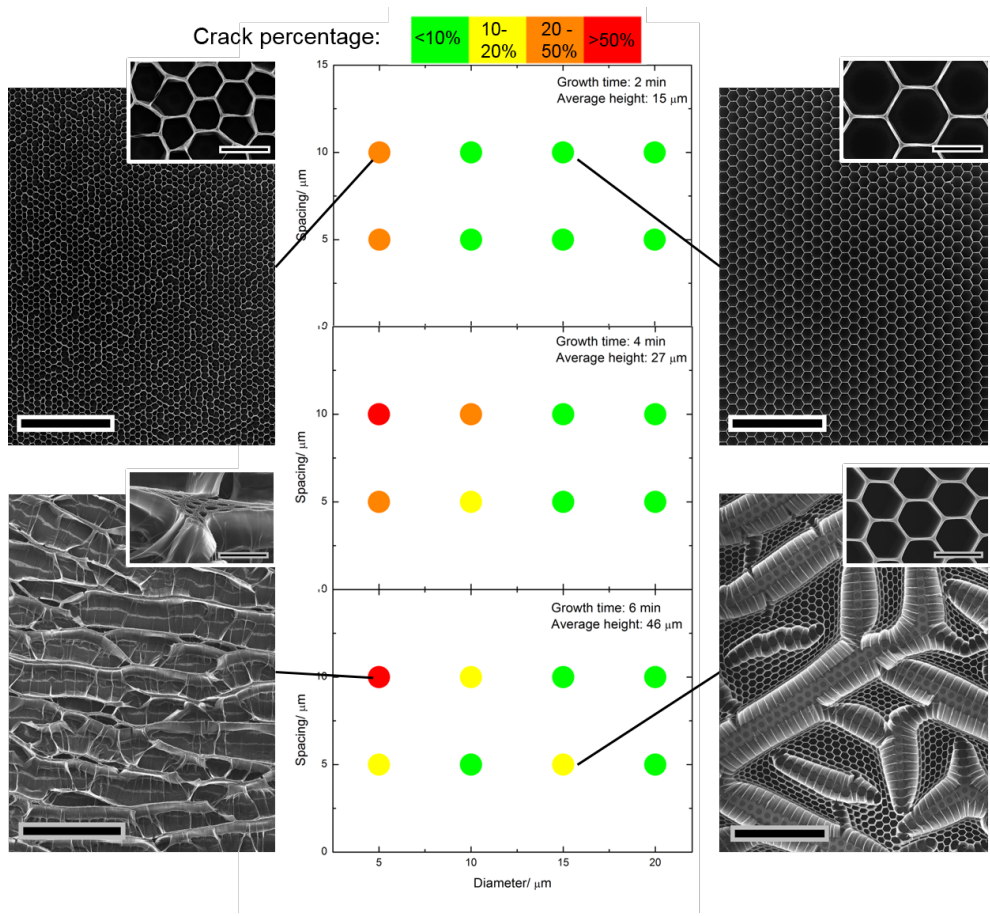


**Fig. 3.7** The graphs show a color map of the percentages of the cracked areas as a function of the diameter and spacing of the circular hole pattern used to form the honeycomb structures and with an increasing growth height from the top graph to the bottom one. Additionally, SEM images as examples for each of the crack percentage ranges are provided. Scale bars are 200 μm and 20 μm in the insets.

The SEM images illustrate as an example how the crack percentages influence the formed structure for each of the four area. A crack percentage below 10% (upper right) hardly shows any visible cracks, whereas there is no substantial amount of CNT honeycombs left for a crack percentage of over 50% (lower left). However, these images also show the difficulty in the analysis. The SEM on the top left with more than 20% cracks looks better than the one on the bottom right, with less than 20% cracks. The top left image thus shows more broken CNT walls which in the analysis lead to a higher percentage of damaged area. However, the length of the cracks might also matter for their further use. Single cracked walls might be less problematic than cracks propagating through the whole structure (as seen in the lower right SEM), even though the crack percentage in the analysis done here is lower.

Overall, the percentage of the cracked area tends to be lower for larger diameters and larger spacings (green points in the graphs, less than 10% cracks) for all three growth times. Furthermore, there are fewer cracks for lower growth times which supports the finding in the previous chapter that the growth height is relevant for the formation of honeycombs.

This graph gives a first indication of factors influencing the fabrication of high quality honeycomb structures, but it also shows that there might be interdependencies among the individual factors, meaning growth time and diameter and spacing are linked. Some processes profit from ultra-small pores that are very high, however, this study showed that these might not necessarily be achievable with this process. Understanding the limitations requires a more detailed analysis of the experimental data and possibly more experiments. *Design of experiments* (DOE) is a methodology to systematically apply statistics to experimentation. It can be used in research to comprise experiments and understand how changes in input or control variables interact to produce changes in output variables. Multifactor design is used instead of one-factor-at-a-time analysis. DOE presents a promising way to further analyze the data and gain a deeper understanding of the 3D honeycomb formation. Those considerations of the amount of cracking become especially relevant when applications for the CNT honeycomb structures are considered. Depending on the choice of application, there might be very little tolerance for cracks e.g. in filters. Thus, future work will be to further evaluate the available data from already run experiments, using *design of experiments* as a method.

### 3.2.4 Introduction of stress relief features to avoid cracking

As shown in figure 3.5, higher structures often tend to form a large number of cracks. However, for some applications tall CNT honeycombs are required. The process might be inherently limited to a defined parameter space (to be determined by DOE). However, one way around the formation of unpredictable cracking is to introduce lines to relieve stress. Thus a pattern is designed on the UV-lithography mask that is supposed to introduce cracks in certain areas to release the stresses formed during densification in a controlled way and hence avoid random cracks. This enables the expansion of the parameter space in which higher CNT honeycomb structures can be formed.

Figure 3.8a shows a design of hexagons with empty trenches between them to reduce stress. The hexagon structure ensures the most efficient use of the available space on the substrate, while the trenches act as stress relief features where cracks can form. The hexagons have a diameter of 450  $\mu\text{m}$  and pattern dimensions inside the hexagons are [30,10]. These pattern dimensions are chosen because they have been shown to reliably densify into defect-free honeycombs at short heights. Those structures are grown to three different heights (15  $\mu\text{m}$  in 3.8b, 30  $\mu\text{m}$  in 3.8c, and 85  $\mu\text{m}$  in 3.8d) and subsequently densified by a drop of acetone. Even the highest of those structures shows no crack formation, which proves that stress relief features can be used to avoid cracking in higher CNT honeycomb structures. For comparison, an SEM of a structure grown and densified with a height of 90  $\mu\text{m}$  can be seen in figure B2 in appendix B, showing that stress relief features at this height are necessary to form undamaged honeycombs.

### 3 Fabrication of 3D CNT Structures with pores

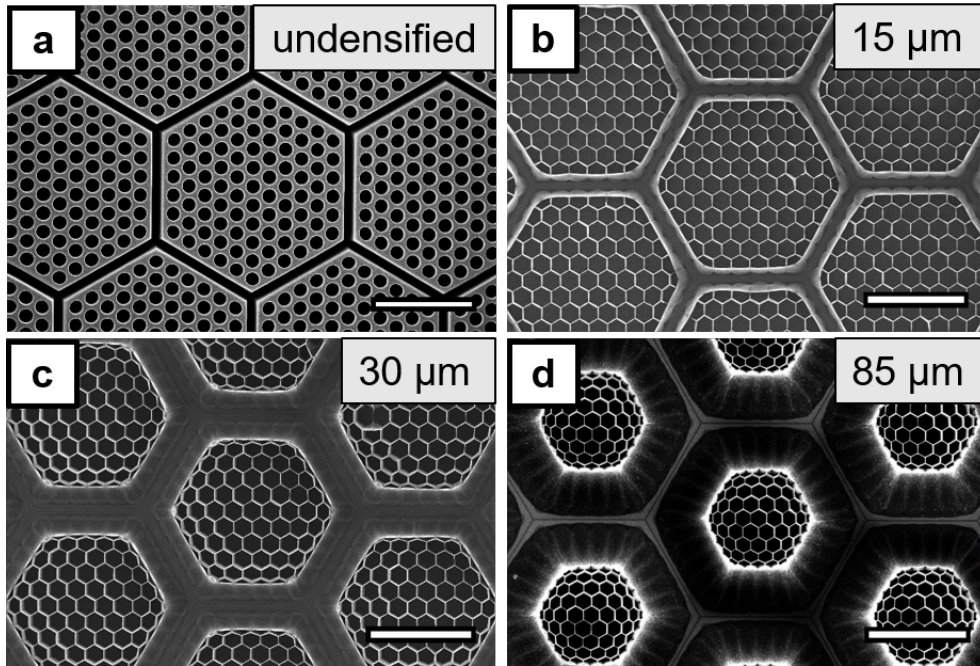


**Fig. 3.8** The influence of the stress relief feature pattern on the honeycomb formation is shown for three growth heights in the SEM images: 15  $\mu\text{m}$  in (a), 30  $\mu\text{m}$  in (b) and 85  $\mu\text{m}$  in (c). Even for a height of 85  $\mu\text{m}$  CNT honeycomb structures can still be formed without cracks forming and the walls breaking. Scale bars are 200  $\mu\text{m}$ .

When those stress relief features are introduced, optimal substrate coverage is no longer guaranteed - the more of the empty trenches are needed, the less CNT structures can be fitted onto a certain area. Thus, another parameter to investigate is how large the CNT honeycomb hexagons can be made before cracking occurs inside them.

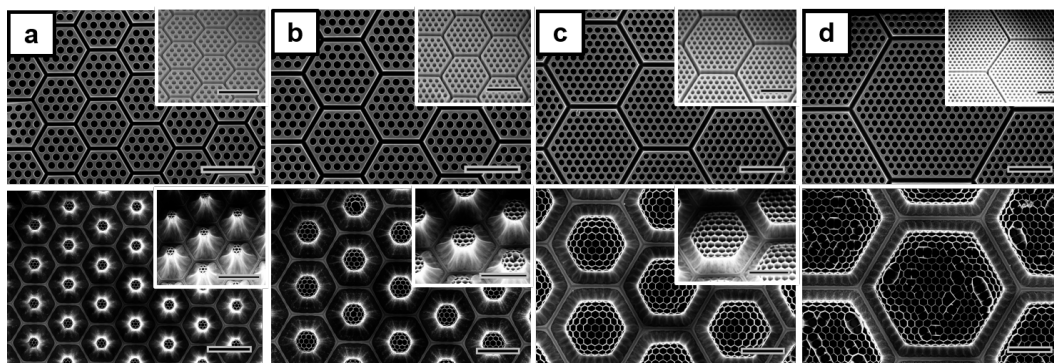


**Fig. 3.9** The diameters of the hexagons used as stress relief features are 200  $\mu\text{m}$  (a), 300  $\mu\text{m}$  (b), 450  $\mu\text{m}$  (c) and 750  $\mu\text{m}$  (d). Only the largest size shows cracks in the formed honeycombs after the densification. The insets are tilted images at 35° to show the height of the structures. Scale bars are 200  $\mu\text{m}$ .

The influence of the size of the hexagons on the honeycomb formation is shown in figure 3.9. While the spacing of the hexagons (10  $\mu\text{m}$ ) and the growth time (8 minutes) and thus height ( $\sim 85 \mu\text{m}$ ) remains the same, their diameter is changed from 200  $\mu\text{m}$  (figure 3.9a), to 300  $\mu\text{m}$  (figure 3.9b), to 450  $\mu\text{m}$  (figure 3.9c) and the largest one is 750  $\mu\text{m}$  (figure 3.9d). It can be seen that diameters of up

### 3.3 Fabrication of 3D CNT structures using colloidal lithography

to 450  $\mu\text{m}$  (figure 3.9a,b,c) lead to undamaged honeycombs after densification, whereas increasing the size to 750  $\mu\text{m}$  (figure 3.9d) leads to crack formation inside the honeycombs and thus is too large for stress relief features.

Additionally, it can be seen that the smaller hexagons show a very large bending of the outer CNTs. The area of the top of the structure decreases to 31 % of the initial area for the smallest feature, but only to 73 % of it for the largest feature (measurements in table B3 in appendix B). This might be due to the fact that only a certain amount of honeycomb cells on the outside always collapses whereas the inside of the areas forms the CNT honeycomb structure.

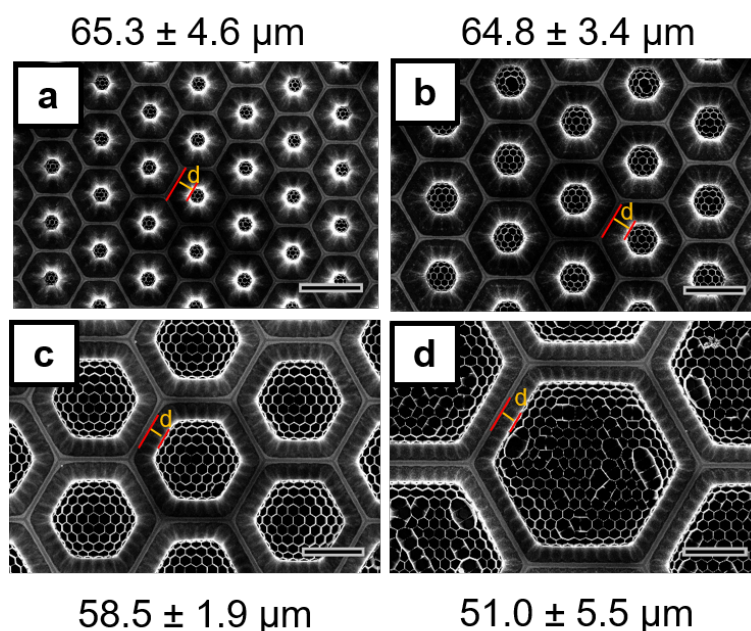


**Fig. 3.10** The collapsed outside honeycomb dimensions are measured for the different sizes of hexagons of 200  $\mu\text{m}$  (a), 300  $\mu\text{m}$  (b), 450  $\mu\text{m}$  (c) and 750  $\mu\text{m}$  (d). The average of 10 measurements is taken. This collapsed area slightly decreases with increasing hexagon size. However, the difference is only  $\sim 10$   $\mu\text{m}$ . Scale bars are 200  $\mu\text{m}$ .

When the length  $d$  of this collapsed part is measured in the SEM images (figure 3.10) for the different structure sizes, it is found to slightly increase from the smallest pattern to the largest. However, this increase is within  $\sim 10$   $\mu\text{m}$ , while the area of the hexagons increases by more than an order of magnitude. This indicates that in all the cases the about same amount of bending is introduced in the outside areas of the hexagons.

Overall, stress relief features present a promising way to be able to fabricate honeycomb structures with an increased height while avoiding cracks and can overcome the limitations in the CNT honeycomb formation.

### 3.3 Fabrication of 3D CNT structures using colloidal lithography

For the creation of smaller pores in CNT forests, the lithographic patterning method needs to be changed. UV-lithography cannot easily be used on submicron scale. An overview of a range of

### 3 Fabrication of 3D CNT Structures with pores

nanopatterning techniques was given by Tawfick et al.,<sup>[159]</sup> including nano-imprint and colloidal lithography. As the 3D CNT structures require a hexagonal pattern, colloidal lithography provides an inexpensive, flexible way of creating the desired hole arrays.

#### 3.3.1 Fabrication of 3D CNT structures from colloidal templates

In the first step of the colloidal patterning process, a monolayer of polystyrene (PS) spheres is packed on a liquid-air interface using a modified version of a protocol described by Vogel et al.<sup>[169]</sup> Instead of sliding the PS-particle solution onto the liquid-air interface using a glass slide, the particles are deposited using an immobilized Eppendorf pipette where the tip is positioned directly at the interface (an image of the setup can be found in the experimental section). This helps avoid disturbance of the interface.

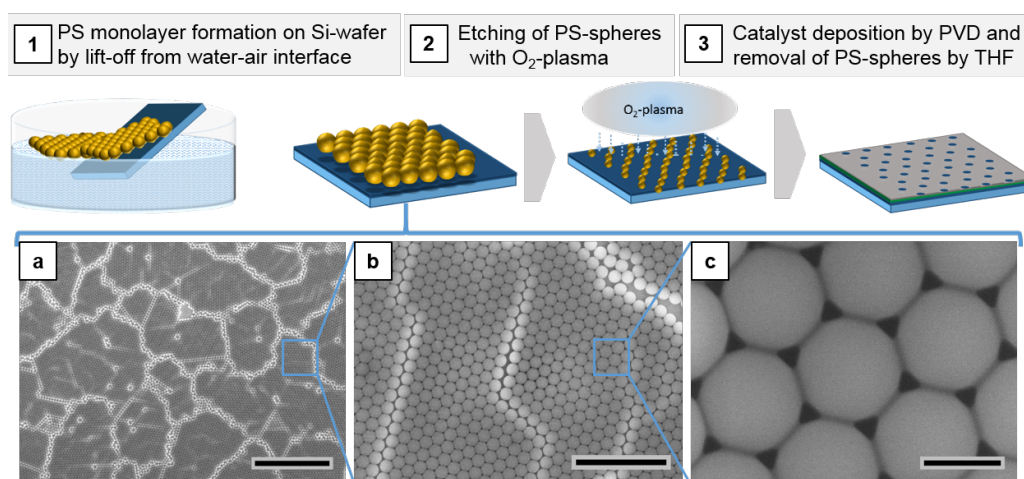


**Fig. 3.11** This process shows the steps to create a template for CNT growth using colloidal lithography. In step (1) a monolayer of PS spheres is formed on the water-air interface and is then transferred onto a silicon wafer. The spheres are etched with O<sub>2</sub>-plasma in step (2). Subsequently they are used as a template for catalyst deposition and are afterwards removed using THF in step (3). The SEM images below show an overview of the ordered PS-sphere layer (a), the size of one domain (b) and a high magnification image of the 800 nm spheres with their hexagonal packing (c). Scale bars are 20 μm in (a), 5 μm in (b) and 500 nm in (c).

The barriers in the Langmuir-Blodgett trough are then slowly closed until a densely packed monolayer is created (visible by the iridescent color). In this case, the surface tension was not measured. This layer of hexagonally packed PS spheres is then transferred to a Si-wafer, which is manually, slowly pulled through the surface from below at an angle of 45° and then dried at a 45° angle (1). The dried spheres are then etched with O<sub>2</sub>-plasma (2) and used as a template for catalyst deposition. Subsequently, the PS spheres are removed by tetrahydrofuran (THF) (3). An overview of these process steps can be seen in figure 3.11. The SEMs in the bottom row show the resulting PS sphere monolayer with a domain size of ~20 μm over large areas (a and b) and a perfectly hexagonal order of the 800 nm spheres within those domains (c).

### 3.3 Fabrication of 3D CNT structures using colloidal lithography

**Tuning the hole size by etching time** The etching time is a critical parameter in this process, as it determines the size of the resulting spheres and the gap between them. Various pore sizes and consequently different wall thicknesses in the 3D CNT structure can be achieved when the etched PS-particles are used as a template. The graph in figure 3.12 shows change of the particle diameter for 800 nm diameter PS spheres with an etching time of 1,2,5,10 and 20 minutes using O<sub>2</sub>-plasma (with a Diener plasma etcher at 0.8 mbar), the corresponding SEM images can be found in figure 3.13.

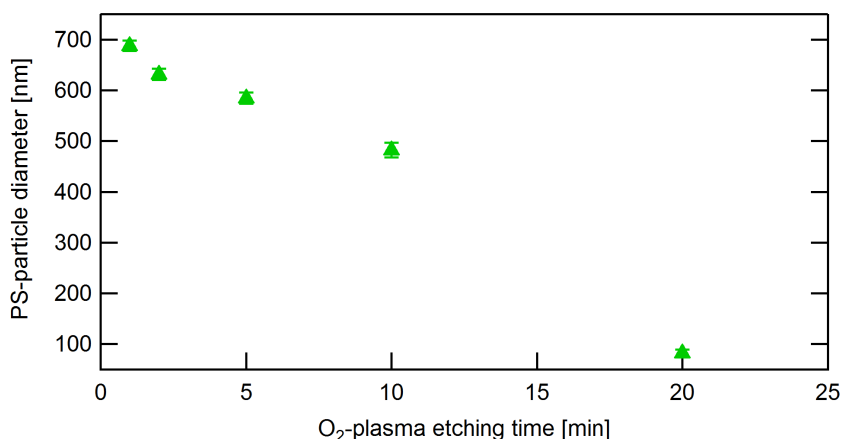


**Fig. 3.12** This graph shows the change in PS-particle diameter with an increasing O<sub>2</sub>-plasma etching time for 800 nm particles. The points show the average of 10 measurements with the standard deviation.

The first minute leads to a decrease in particle size of ~100 nm but bridges between the spheres are still connecting them. These are probably PS that wasn't fully etched away. After another minute, the spheres shrink slightly more and the bridges decrease. These bridges were expected since they have previously been reported by Plettl et al.<sup>[160]</sup> However, a more linear etch rate was reported. This might be due to slightly different characteristics of the plasma used, e.g. less pumping time and thus more N<sub>2</sub> present in the beginning of the etching, changing the etching rates. For etching times of 5 and 10 minutes there is a significant decrease in size (from 800 to 580 nm for 5 min and to 480 nm for 10 minutes). After 20 minutes etching, the PS-particles have reached a diameter of ~80 nm and are barely visible in the SEM images. Tilted SEM images of those PS spheres after 2 minutes and 10 minutes etching are shown in figure B4 in appendix B.

### 3 Fabrication of 3D CNT Structures with pores

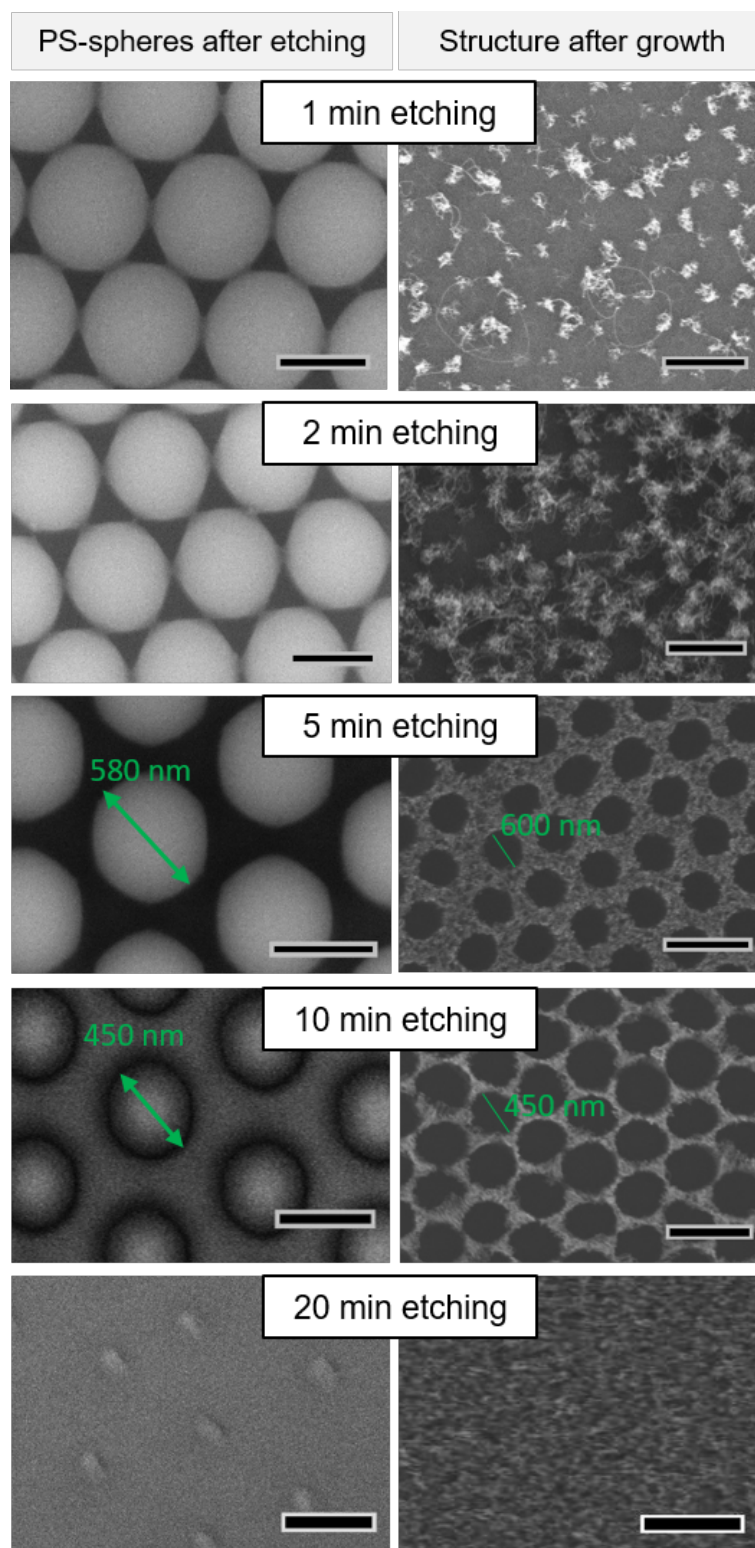


**Fig. 3.13** The left row shows a decrease in size of the PS spheres with increasing  $O_2$ -plasma time. The spheres with an etching time of 1 minutes have not changed much yet and are still connected by bridges, whereas the spheres after 20 minutes etching are barely visible anymore and have significantly shrunken in size. The right row shows the CNT forest structure. After one minute there is barely any CNT growth visible as the template did not have much space for catalyst deposition, whereas after 20 minutes the holes by the spheres are so small that they are not visible in the forest anymore. Scale bars in left column 500 nm, in right column 1  $\mu\text{m}$ .

### 3.3 Fabrication of 3D CNT structures using colloidal lithography

CNTs are then grown on the patterned substrates from a Fe-Al<sub>2</sub>O<sub>3</sub> catalyst in an ambient pressure CVD furnace at 750 °C for 1 minute. Experimental specifics can be found in the methods section 7.1.2. The growth on substrates prepared by colloids with different etching times are shown in the SEM images in right column of figure 3.13. Only the colloids etched for 5 and 10 minutes show uniformly patterned forests. Triangular shapes are grown on substrates with etching for only 1 or 2 minutes. This is due to the fact that the bridges prevented catalyst deposition anywhere else than the triangles. The amount of neighboring CNTs in those triangles might not be enough to form a self-supporting structure that enables the CNTs to lift off the substrate and grow vertically, or the catalyst might not be uniform enough. After 20 minutes etching time, the walls are thick and the templated holes cannot be seen in the SEM images. They might also be closed due to the tortuosity of the grown CNTs and the small diameter of the holes.

**Tuning the aspect ratio by growth height** By adjusting the growth time and temperature, the height of the structure and, thus, the aspect ratio of the pores can be tuned. Figure 3.14a illustrates that a large area patterning is possible using this method with vertically aligned pores of a diameter  $\sim 450$  nm. Figure 3.14b shows that with a growth height of around 330  $\mu\text{m}$  pores with an aspect ratio of more than 700 (450 nm pores for a height around 330  $\mu\text{m}$ ) can be created. Such a high aspect ratio is usually hard to achieve and is shown for the first time using colloidal lithography for vertically aligned CNT with such pores. Park et al.<sup>[272]</sup> recently achieved very high aspect ratio CNT structures using nanoimprint lithography as a method. These structures are very interesting for diffusion limited processes, such as electrodes in Lithium-ion batteries which will be discussed later in chapter 4.4.

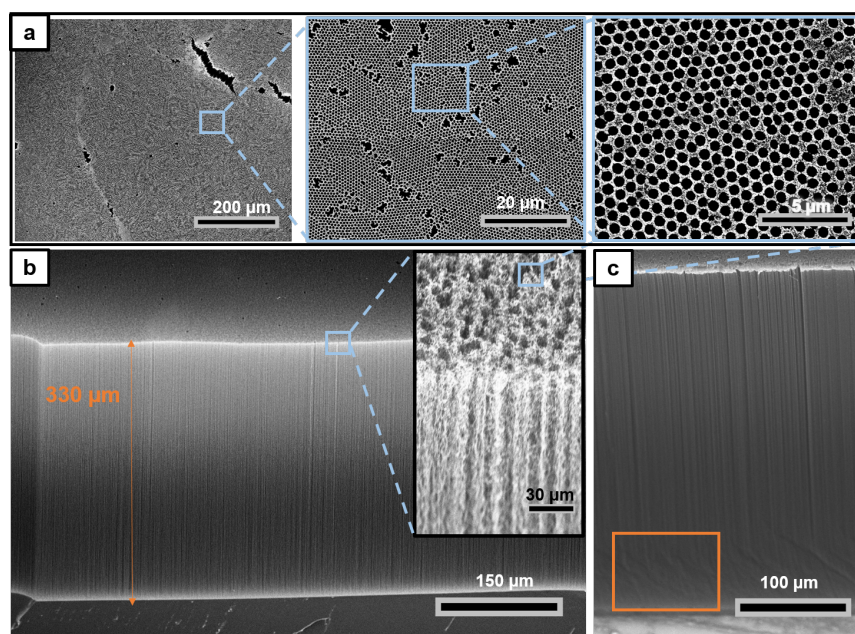


**Fig. 3.14** The SEM images in (a) show the large area that can be covered by the structure with 450 nm holes on several levels of magnification, in (b) the height of the forest from the colloidal structures is shown. The forest in (c) shows a possible failure mode in this growth where the structure slightly collapses with increasing height (see orange square).

### 3 Fabrication of 3D CNT Structures with pores

---

A possible failure mode that terminates the height of the structure is classical forest termination, as seen in figure 3.14c. Some samples show a collapse of the CNT forest structure with increasing heights, indicated by the orange square. Here the self assembled structure is not able to support itself anymore. This is due to the catalyst poisoning in the termination stage, as explained by Bedewy et al.<sup>[109]</sup> and discussed in section 1.3.2. It can be observed at a lower forest height in the colloidal structure than in patterned 3D structures with larger hole dimensions. This might be due to the difference in the amount of neighboring CNTs in the CNT network. The walls in the colloidal structure are between 120 - 200 nm thick, having a very low amount of neighboring CNTs, whereas the wall thickness in the microscale structures is around 10  $\mu\text{m}$ , showing a two orders of magnitude increase in distance and thus more neighboring CNTs. These CNTs are the ones forming the self-supporting structure. Whereas it is common during CNT growth that some CNTs terminate, the neighboring CNTs are usually still able to support the overall structure. If there aren't enough CNTs to keep up the structure, the forest collapses as seen in figure 3.14c. Thus a decrease in amount of neighboring CNTs can lead to a forest that collapses at an earlier point in the growth process and thus a lower height.

The growth height needs to be carefully adjusted for those structures to make sure the fabricated structures are not collapsed at the bottom, as this might close off the small holes.

#### 3.3.2 Influence of change in initial particle size

The hole size can not only be adjusted by the plasma etching time, as mentioned in the previous section. Using PS spheres of a different size not only changes the hole size, but also the lattice spacing. If the structures can be etched to holes sizes of 100 nm and grown to the previously shown 330  $\mu\text{m}$ , the aspect ratio of the porous CNT structure can be increased to over 3000, making this a very promising method for fabricating high aspect ratio structures.

As an example, PS particles with a diameter of 300 nm have been used for the monolayer formation. The domain size in figure 3.15a is  $\sim 10 \mu\text{m}$  with a nice hexagonally ordered packing inside those domains. The domains are about half the size compared to 800 nm particles. This is not surprising as it has been reported before that the size of PS-particles has an influence on the monolayer formation on a liquid-air interface. Zhang et al.<sup>[170]</sup> found that the degree of order in the monolayer decreases with decreasing particle size (particles of 2  $\mu\text{m}$  worked best whereas 235 nm particles showed the least order) and attributed it to a decreased stability of the thinner particle arrays. Nevertheless, the degree of order in the 300 nm spheres monolayer is satisfactory for a growth template, as grain sizes are no significant problem for CNT growth.

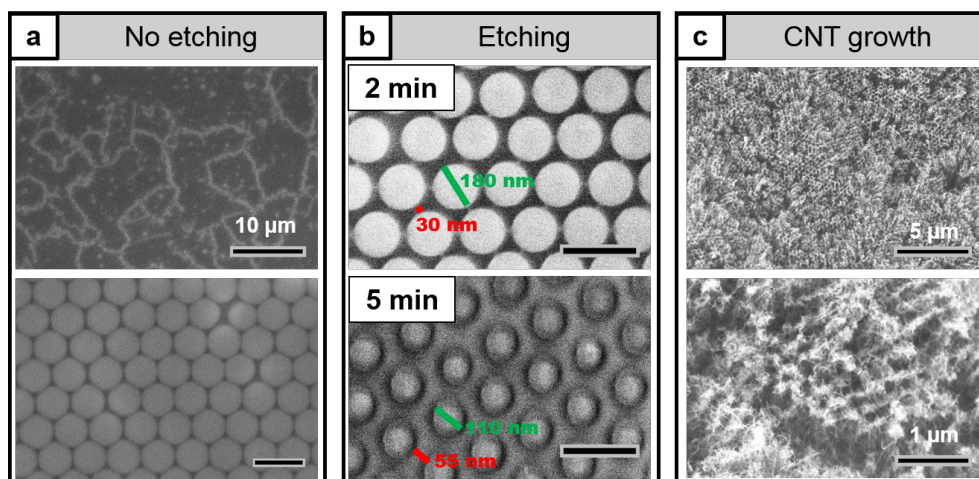


**Fig. 3.15** The monolayer formation with a clear hexagonal packing of the 300 nm spheres within the  $\sim 10 \mu\text{m}$  domains is shown in (a), the influence of an etching time of 2 and 5 minutes is shown in (b) and the subsequent growth from the template etched for 5 minutes can be seen in (c). Scale bar 400 nm if not otherwise indicated.

Those PS spheres are etched in  $\text{O}_2$ -plasma for 2 minutes and 5 minutes (figure 3.15b). After 2 minutes etching, the particles size can be decreased to  $\sim 180 \text{ nm}$  with spacings of  $\sim 30 \text{ nm}$ . However, there are still bridges between the particles visible. Thus, a 5 minute etching time is preferred which decreases the particle size to  $\sim 110 \text{ nm}$  with spacings of  $\sim 55 \text{ nm}$ . This template is then used to grow CNTs. As it can be seen in figure 3.15c, a high degree of tortuosity of the CNTs is visible and the hole pattern can clearly be seen. However, the growth is not uniform and the CNTs seem to not easily grow vertically. The even smaller wall thickness in those structures ( $\sim 55 \text{ nm}$ ) and the very low amount of neighboring CNTs that can form the self-supporting structure, which is necessary for vertically aligned growth, might be a possible reason to observe this type of CNT growth. Again, non-uniform catalyst deposition might also be a reason. For future experiments it might be better to use slightly larger PS spheres which are then etched to the 100 nm size, leaving larger distances between them (around 200 nm should work as shown for the 800 nm PS particles) or shorter etching times for increased wall thicknesses and thus potentially more neighboring CNTs that can form a self-supporting structure.

These trials with 300 nm spheres show that it is possible to achieve smaller hole sizes using smaller PS particles but that the wall thickness/ distance between the spheres after etching needs to be carefully adjusted to still enable self-supporting CNT forest growth.

For further experiments in this thesis, the structures with 800 nm PS particles, etched for 5 and 10 minutes are used, keeping the aspect ratio a bit lower but serving as a well working model system for nanoscale patterned CNT forests.

### 3.3.3 Densification of nanoscale 3D CNT structures

As mentioned before, the next step to achieve a robust honeycomb structure is densification, which is done by depositing a drop of acetone on the substrate and letting it evaporate for the CNT

### 3 Fabrication of 3D CNT Structures with pores

honeycomb structures. This process is applied to the sample of 800 nm particles that was etched for 5 minutes and grown for 5 minutes at 720 °C. Figure 3.16a shows a random agglomeration of the CNTs rather than a defined densification. As it might be a too vigorous densification method for such nanoscale structures, the more gentle method of vapor deposition reported by De Volder et al.<sup>[172]</sup> for elastocapillary densification is then used, as explained in section 1.4.3. Another sample was put into acetone vapor for about 1 second (figure 3.16b). The CNT structure seems slightly densified. It is not fully densified into honeycombs yet, which indicates that the time in the acetone vapor was too short. However, it can already be seen that the walls start cracking, making it very likely that these cracks propagate with increasing densification. Thus, it will be hard to achieve a nice densification of those nanoscale structures. This is why the colloidal structured were used without densification in their application for Lithium-ion batteries, as discussed later in chapter 4.4.

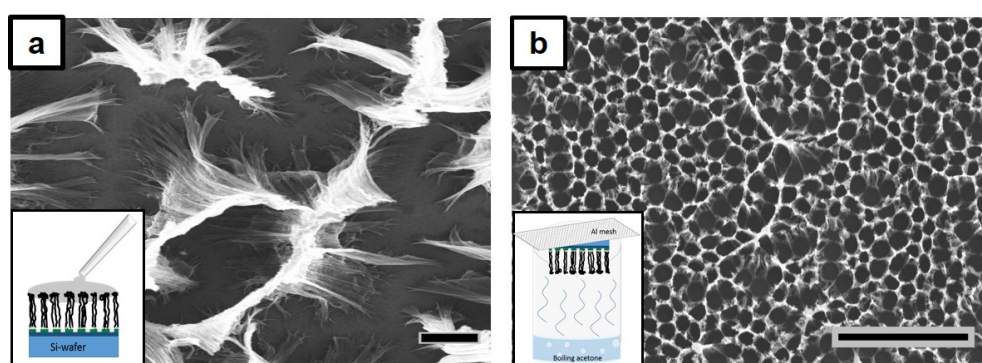


**Fig. 3.16** Putting a drop of acetone onto the 450 nm diameter structures leads to a random agglomeration of the CNTs rather than a defined densification into honeycombs (a). When densified by acetone vapor<sup>[172]</sup> for 1 second (b), a slight densification of the structures occurs. However, the structures did not completely convert into honeycombs and crack formation can already be observed. Scale bars 5  $\mu\text{m}$ .

### 3.4 Conclusion

This chapter showed the fabrication of 3D CNT structures with different pore sizes. For the microscale pore sizes, CNT honeycomb structures were formed using elastocapillary self-aggregation. The temperature and underlayer system were shown to influence the growth height and thus the honeycomb formation. The use of Mo as a conductive underlayer reduces the growth rate and an increase in temperature from 700 °C to 780 °C increases the height of the CNT structure, leading to more cracking in the CNT honeycombs. Studying the influence of different growth times, diameters and spacing on the crack percentage in the resulting honeycombs showed a strong interaction between these three parameters that needs to be investigated further, e.g. using DOE. The concept of stress relief features was introduced to enable the fabrication of CNT honeycomb structures with increased height while avoiding crack formation.

As many applications require smaller pore sizes, the lithographic patterning method was changed to colloidal lithography. This enables the inexpensive fabrication of nanoscale pores. CNT forests were grown from those templated layers after different etching times, showing that 5 and 10 minutes

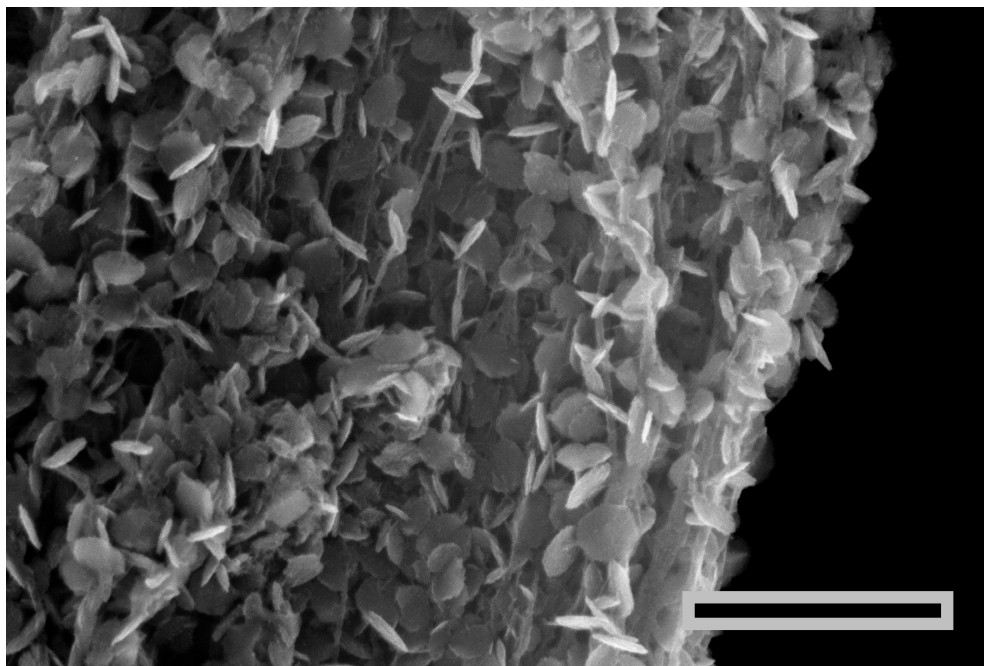
O<sub>2</sub>-plasma etching time worked best for reliable growth of vertically aligned CNTs from 800 nm spheres. When the sphere size was decreased to 300 nm, ordered monolayers could be formed but the etching time still needs to be adjusted further to promote vertically aligned CNT growth. It was shown that by varying the initial particle parameter and tuning the etching time, a range of hole sizes and lattice parameters can be achieved. These open pathways for the fabrication of tunable structures with very high aspect ratios that are promising for applications with diffusion limited processes.

The fabricated 3D CNT structures are modified for their desired applications in the following chapters. The CNT structures with nano- and microscale pores are used as electrodes for Li-ion batteries, and the CNT honeycomb structures are modified for their use as photoelectrodes in solar watersplitting.



## Chapter 4

# Inorganic Modification of 3D CNT Structures for Lithium-Ion Batteries



Vertically aligned CNTs coated with Fe<sub>2</sub>O<sub>3</sub>, scale bar 1  $\mu$ m.

Results in this chapter were achieved in collaboration with Dr. D. Copic, S. Engelke and Dr. S. Ahmad.

## 4 Inorganic Modification of 3D CNT Structures for Lithium-Ion Batteries

---

This chapter focusses on the modification of the created 3D CNT structures with inorganic materials. This hybrid material is promising for advanced electrodes for lithium-ion batteries to overcome the diffusion-limitation during the creation of thicker electrode films. This vision guides the material selection and initial electrochemical characterization is provided at the end of the chapter. The chapter first gives an overview over lithium-ion batteries and the challenges faced, and then focusses on the modification of the 3D CNT structures with two active materials,  $\text{Fe}_2\text{O}_3$  as a conversion battery material and Si as an alloy material, for the fabrication of the porous electrode structure. It also contains the first report to our knowledge of a microwave-assisted hydrothermal coating method for 3D CNT structures.

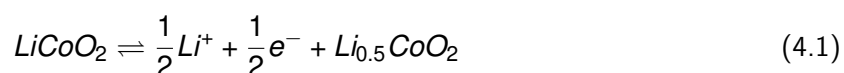
### 4.1 Introduction to lithium-ion batteries

Rechargeable solid-state batteries are interesting as a power source for a wide variety of applications. A battery is defined as an electrochemical device which stores electrical energy as chemical energy in its anode and cathode during charging and then releases it as an electrical output during discharge.<sup>[273]</sup>

Lithium-ion batteries (LIB) have become more and more important in portable electronics due to the fact that they have a higher energy density capability than conventional nickel-cadmium, nickel-metal hydride and lead acid battery systems.<sup>[274]</sup> They also exhibit a long cycle life and no memory effect, and thus were commercially introduced in 1991 by Sony Inc.<sup>[273,275]</sup> LIB cells with a voltage around 3.7 V have energy densities ranging from 200-225  $\text{Whkg}^{-1}$  and power densities from 500 - 2000  $\text{Wkg}^{-1}$ , with a very low self-discharge at a maximum of 5% a month.<sup>[58,276]</sup>

A battery consists of multiple components: the anode (defined as the part that stores Li-ions upon charge), the cathode, a separator in between the two electrodes to avoid short-circuiting and an electrolyte. The reactions governing a LIB cell are reversible Li-ion intercalation-de-intercalation cycles between the two layered compounds, as seen in figure 4.2.

The original Sony Li-ion battery system is graphite- lithium cobalt oxide ( $\text{LiCoO}_2$ ). The cathode reaction and delithiation can be described by the following equation:<sup>[277]</sup>



The Li-ions can intercalate into the graphite anode reversibly following this reaction:<sup>[277]</sup>



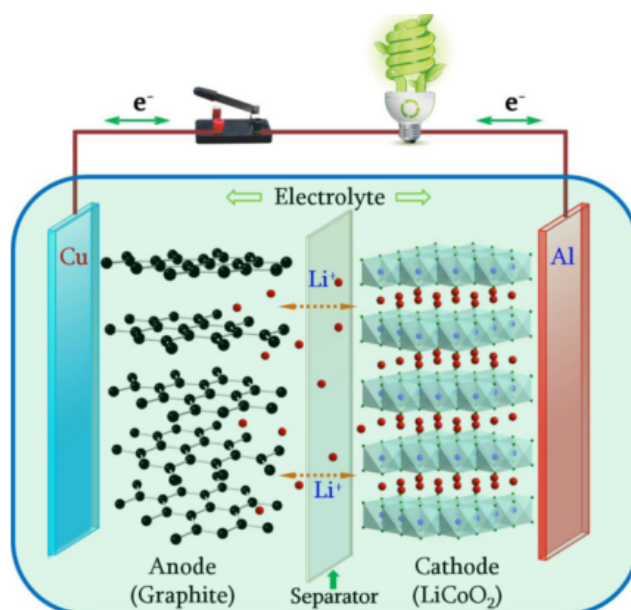


**Fig. 4.2** Schematic overview of the original Li-ion battery. The cathode material is lithium cobalt oxide ( $\text{LiCoO}_2$ , (right)) with an aluminium current collector and the anode material is graphite (left) with a copper current collector. During charging and discharging Li-ions move from the one electrode to the other through the separator.<sup>[278]</sup>

A way to evaluate batteries is by their energy and power density. Energy density is the amount of energy stored in a given system per unit volume. Here it describes the amount of Li-ions that can be stored and is given by the specific capacity of the used materials. Power density describes the power that can be stored in a material by unit volume. It is closely linked to the charging rates that can be applied in the battery. The higher the power density, the faster the Li-ions can be moved into the active material. The ideal battery has a high energy density (=high specific capacity), high power density, low cost and long cycle lifetime. The right materials have to be found for this.

Much research has been put into anode and cathode materials using nanocomposites, as this helps to optimize ionic and electronic conduction pathways. The formation of a good solid-electrolyte interface (SEI) presents another important parameter during electrode design. This layer acts as a protection of the electrode to prevent side reactions and avoid electrolyte decomposition. An ideal SEI layer should be thin, minimally porous, electrochemically inert, electronically resistive, and ionically conductive.<sup>[58,273]</sup>

For cathode materials, due to the high cost of  $\text{LiCoO}_2$ , especially for electric vehicles, nanostructured  $\text{LiFePO}_4$  for higher power density, longer lifetime and improved safety,  $\text{LiMn}_2\text{O}_4$  for an efficient Li-ion removal and insertion mechanism and  $\text{LiNi}_{1-x-y}\text{Mn}_x\text{Co}_y\text{O}_2$  for a high reversible capacity with excellent capacity retention have been widely researched and partly employed already.<sup>[273]</sup> As a choice of the electrolyte solution, alkyl carbonates, binary solvent mixtures, e.g. ethylene carbonate and dimethyl carbonate (EC-DMC) and lithium hexafluorophosphate ( $\text{LiPF}_6$ ), are commonly used. EC-DMC and  $\text{LiPF}_6$  is the preferred standard solution for Li-ion battery systems. This is due to the melting point of both solvents and their stability. Furthermore,  $\text{LiPF}_6$  is soluble in all alkyl carbonate solvents, making this a highly conducting solution. It forms stable, highly passivating surface films

## 4 Inorganic Modification of 3D CNT Structures for Lithium-Ion Batteries

with graphite, that create a good SEI for Li-ions due to the carbonate and alkoxy moieties that are bridges and linked together by Li-ions.<sup>[277]</sup>

The range of anode materials can be categorized in three groups, depending on the interaction mechanism with the Li-ions: (1) intercalation and insertion materials, such as graphite and titania, (2) conversion materials, such as metal oxides, metal sulfides, metal fluorides and metal phosphides, and (3) alloy and de-alloy materials, such as tin and silicon alloys.<sup>[242,274,277]</sup> The interaction with the Li-ions in these three mechanism can schematically be seen in figure 4.3. During intercalation, Li-ions are stored between layers intrinsic to the material, during the conversion mechanism, they react with the material, forming  $\text{Li}_2\text{O}$ , whereas during the alloying mechanism, they form an alloy with the corresponding metal during lithiation (=reduction reaction). De-lithiation (=oxidation reaction) can lead to a breaking of the structure into smaller parts, as seen for the conversion and alloying mechanism.

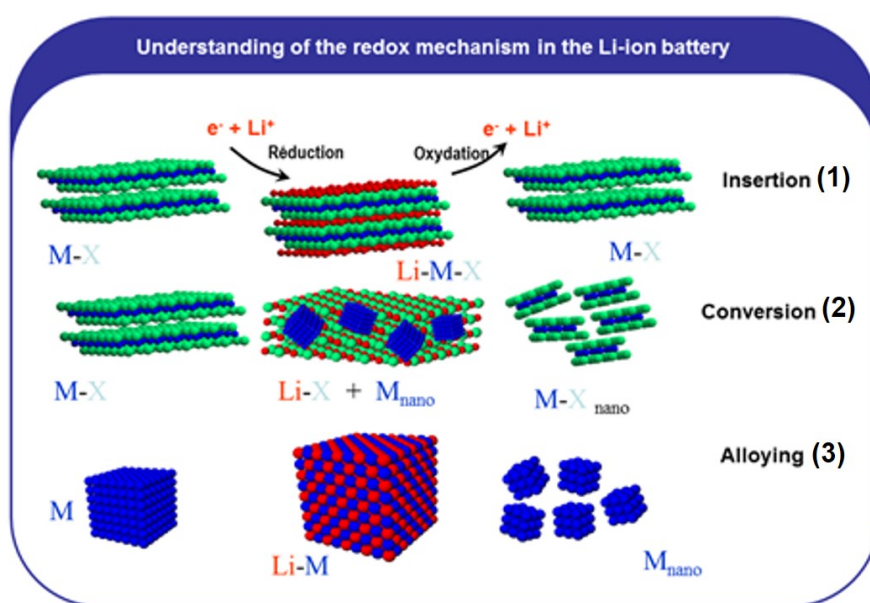


**Fig. 4.3** Schematic overview of the three different mechanism in which Li-ions can react with anode materials: (1) insertion reaction where Li-ions are inserted into the layers in the material (e.g. graphite), (2) conversion reaction where the Li-ions react with the material to form  $\text{Li}_2\text{O}$  (e.g.  $\text{Fe}_2\text{O}_3$ ), and (3) alloying where the Li-ions form alloys with the anode material (e.g. Si).<sup>[279]</sup>

A comparison of anode materials based on their theoretical capacity can be seen in figure 4.4. The current standard graphite shows a capacity of  $372 \text{ mAhg}^{-1}$ . However, there is a range of materials with a higher theoretical capacity, such as metal oxides. These are the most diverse and very promising anode type materials and thus have been researched widely.<sup>[275]</sup>

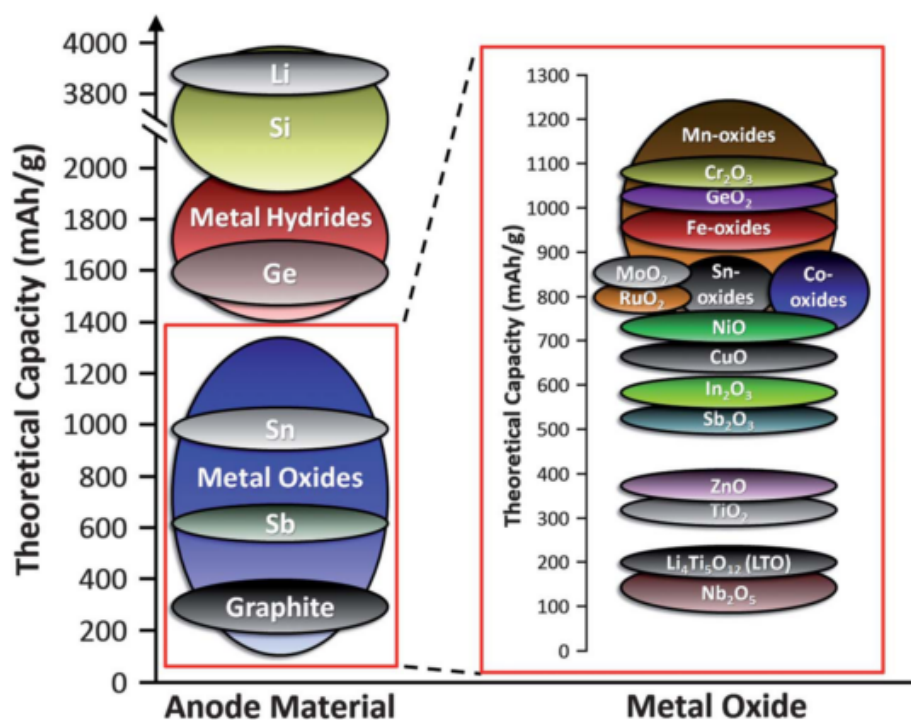
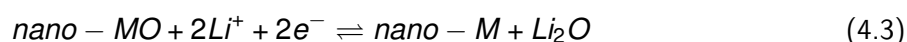


**Fig. 4.4** This graph shows an overview of the theoretical capacities for anode materials. Metal oxides are the most diverse and widely researched ones of these, which is why the right shows a magnified version of this specific class of materials. [275]

Due to their potentially better chemical stability and higher effective surface area, some nanostructured metal oxides have attracted a lot of attention in recent years as anode materials for LIBs. [280] Transition metal oxides, like CuO, Fe<sub>2</sub>O<sub>3</sub> and CoO, are conversion materials, where the structural integrity and chemical identity of the reactants changes completely. [277] Li<sub>2</sub>O is formed while the metal nanoparticles are reduced respectively, [281] as it can be seen in equation 4.3. [277]



Even though some metal oxides show a higher capacity than the graphite electrodes, their reversibility is rather poor due to the loss of electrical contact between the active material and the current collector or the kinetics of the conversion reaction. [190] In addition to metal oxides, silicon as a material with a high theoretical capacity, around 4200 mAhg<sup>-1</sup>, is highly promising. [71] However, Si shows a volume expansion of up to 400 % during lithiation which requires specific designs of the electrode to accommodate for it, e.g. nanostructuring. [273,275]

**Current challenges of LIBs** Current LIBs face a range of challenges which already have been partly addressed in the previous introduction. The two key performance metrics that need improvement are the volumetric and gravimetric energy and power density. Given that the dimensions of several battery components are set (collector electrodes and separator are ~10 μm thick and the battery housing has set dimensions) and that the active material coated on the electrode is typically only

## 4 Inorganic Modification of 3D CNT Structures for Lithium-Ion Batteries

---

50  $\mu\text{m}$  thick, the active material is not the majority component in current systems. Hence, the most logical approach to improve battery metrics is to increase the electrode thickness to achieve high areal loading. Thick electrodes, however, hold challenges of their own: (i) high electric resistance through the electrode which results in high ohmic losses; (ii) Slow ion diffusion, which results in slow charging and discharging and thus low power density; (iii) Poor dissipation of the internally generated heat, which causes safety concerns, and (iv) increasing the electrode thickness has major implications on the manufacturing process including slower drying of the electrodes, segregation of components and cracking or flaking of the electrode.<sup>[58,282]</sup>

Additional challenges during the fabrication of LIBs include the formation of a passivation layer, which can prevent the reversible insertion of Li-ions into the electrode, and thus limit the lifetime of the electrode,<sup>[277,281]</sup> and the disintegration of electrodes due to stresses caused by the severe volume expansion during lithiation over many charge-discharge cycles. This expansion depends on the material that is used<sup>[255]</sup> and on its lithiation mechanism. It is largest for Si, as mentioned before. Nanostructuring of Si and the creation of core-shell structures, e.g. with carbon additives, has been reported to allow for better accommodation of the volume expansion.<sup>[275]</sup>

Graphite is itself very conductive, but when materials with higher Li-ion storage capabilities are used, such as  $\text{Fe}_2\text{O}_3$  or Si, a design is needed that electrically connects all the battery components. Composite materials with conductive additives, such as CNTs and graphene, have been reported to overcome these electrical conductivity problems. The deposition of active materials onto highly conductive nanomaterials to create composite electrode materials presents a promising strategy to gain high power, energy and good cycle performance. The added carbon in the form of CNTs improves the electron-transport to and within the nanoparticles, is electrochemically stable and has a good thermal conductivity.<sup>[190,283]</sup>

**CNTs as electrode material and conductive additive** CNTs are of high interest for energy storage materials due nanometer size and electrical properties.<sup>[71,190]</sup> CNTs in batteries can be used as conductive additives (e.g. in flexible batteries<sup>[146,259,284–286]</sup> or commercially<sup>[53]</sup>) but they also have a Li-ion storage capacity of their own.

Che et al.<sup>[287]</sup> showed for the first time that CNTs can intercalate Li-ions and show a capacity of  $490 \text{ mAhg}^{-1}$  for template synthesized CNTs as an anode. Further investigations found that this reversible capacity varies with the CNT specifics. Ganau et al.<sup>[288]</sup> have shown that there is an optimum diameter of SWNTs for the Lithium-ion interaction (4.68 Å). Zhang et al.<sup>[181]</sup> investigated MWNTs with different diameters for LIB anodes and found the highest specific capacity ( $187.4 \text{ mAhg}^{-1}$  for a charge/discharge rate of  $50 \text{ mA} \text{ g}^{-1}$ ) for MWNTs with a diameter of 40–60 nm. Short CNTs ( $\sim 200 \text{ nm}$ ) have been shown<sup>[180]</sup> to have a higher specific capacity (up to  $266 \text{ mAhg}^{-1}$ ) than longer CNTs (5  $\mu\text{m}$ ) due to the easier insertion/extraction of Li ions and lower electrical resistance. There is a range of studies supporting the finding that the electrochemical performance of CNTs is dependent on the synthesis conditions, treatments and their specific measurements.<sup>[190,289–294]</sup> Nevertheless, the specific capacity of pure CNTs as anode materials is too low to be interesting on their own, thus CNTs are often used in hybrid materials.

## 4.2 Coated 3D CNT structures as advanced electrode architectures

**Diffusion pathways in LIBs** One of the mentioned challenges is the ion transport in thick batteries. Danner et al.<sup>[295]</sup> reported that while higher energy densities in their thicker cathode could be reached, there were significant limitations due to electron and mass transport, leading to a short cycle life. In their theoretical studies focussing on the transport in the thick Li-ion batteries, they showed that at high rates there is a strong limitation of the Li-ion transport in the electrolyte leading to a capacity loss, while small inhomogeneities in the carbon black distribution did not have a significant influence. They pointed out the need for an advanced electrode structure to improve the Li-ion transport and the lifetime and capacity of thick batteries.

Looking at diffusion properties in CNTs, Izadi-Najafabadi et al.<sup>[296]</sup> used aligned CNT films as membranes in their set-up and then monitored the ion conductivity in the solvent compartment over time to determine the concentration profile. They have shown that for SWNTs the ion diffusion along a vertical aligned array of those tubes (parallel to the tubes) is 12x faster than the diffusion perpendicular to the tubes, hence demonstrating the desirability of vertically aligned CNT structures for diffusion-limited applications. They also showed that the ion diffusion in activated carbon is significantly lower than in CNTs. Figure 4.5 shows an overview of the ion diffusion coefficients.

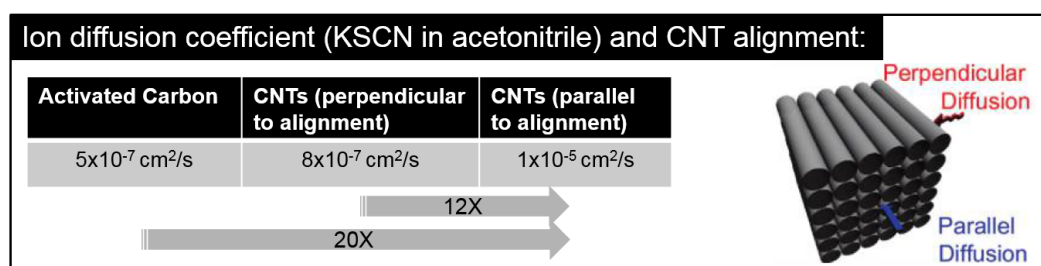


**Fig. 4.5** The changes in ion diffusion coefficients are shown for a diffusion with activated carbon, and parallel and perpendicular diffusion in aligned CNTs. The diffusion coefficient increases 20x in a comparison between activated carbon and parallel to the CNT alignment.<sup>[296]</sup>

## 4.2 Coated 3D CNT structures as advanced electrode architectures

In order to address some of the challenges in LIBs, the electrode architecture for thick batteries needs to be revisited. A promising route is to create hierarchical composite structures.<sup>[12,67,258,297–300]</sup>

Hierarchical anode structures relying on AAO templates<sup>[297]</sup> and inverse opals<sup>[301]</sup> have shown promise to improve diffusion through thick electrodes. CNTs are interesting for creating hierarchical backbone structures due to their high electrical conductivity, light weight, mechanical strength, and electrochemical stability,<sup>[53,190]</sup> in conjunction with the range of techniques to structure CNTs. It has been shown that vertical CNT alignment exhibits better ion diffusivity and electron conduction.<sup>[190]</sup> Creating hybrid nanostructures of high capacity anode materials with carbon materials increases their electrochemical performance.<sup>[302–305]</sup> So far, hierarchical CNT-active material composites have been reported using ice-templating<sup>[306]</sup> or CVD synthesis of vertically aligned CNTs, either plain forests<sup>[32,238,239,296]</sup> or pre-structured into cones<sup>[65]</sup> and pillars.<sup>[242,307]</sup> However, to our knowledge, no attempts have been made to optimize the pore structures of these materials for fabricating thick electrodes.

## 4 Inorganic Modification of 3D CNT Structures for Lithium-Ion Batteries

In our approach for the fabrication of thick electrodes, we first aim to increase the areal loading using the conductive micro-structured CNT backbone coated with the active material. This backbone consists of vertically aligned CNTs (figure 4.6) and is structured using UV-lithography. Then we advance this structure further by creating nanopores instead of micropores using colloidal lithography. Contrary to a dense film made from a slurry, the nanopores in the new structure support Li-ion diffusion and the backbone enhances the electron transport.

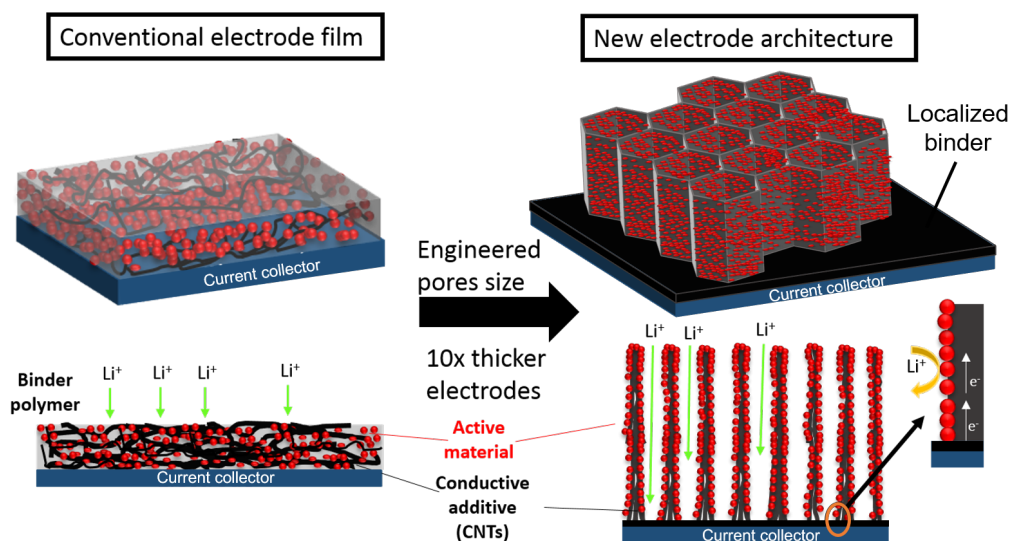


**Fig. 4.6** Schematic overview of the suggested advanced electrode structure. Instead of a film cast from a slurry of the components, the new electrode architecture is a porous 3D microstructure made of vertically aligned CNTs with the active material grown on top of the structure. The holes enable fast ion diffusion and thus an increase in electrode thickness and rate performance. The conductive backbone ensures the electrical transport.

These advanced architectures allow to address the issues flagged above for thick battery electrodes. (i) The electrical transport issues are addressed by the CNT backbone running through the thickness of the electrodes and connecting the active material directly to the current collector. (ii) The holes at the center of the 3D CNT structure provide a fast ion diffusion path and thus enable higher rates and an increased thickness of up to 10x. (iii) The excellent thermal conductivity of the CNTs may help addressing thermal issues (though not tested here) and (iv) because of their radically new morphology, these electrodes do not suffer from flaking or phase segregation issues during manufacturing. The binder in our thick electrode structure is only applied locally at the interface of the CNTs with the current collector, thus making it unnecessary to have binder throughout the thick electrode structure and minimizing the binder effects. Further, the 3D CNT structure provides a good mechanical stability and can act as a buffer for volume change and aggregation, as shown before;<sup>[308]</sup> the cell size and the height of this CNT structure are tunable and CNTs can be combined with a range of modifications, creating very promising templates for the reduction of losses and high rates in batteries.

The microscale 3D structure for advanced areal loading is then coated with the conversion material iron oxide, whereas the alloying material silicon is used as the active material for the nanopore structures. Both are abundant, their synthesis is well known and they show a significantly higher theoretical capacity than the current standard graphite.

### 4.2.1 Iron oxide as an anode material

Iron oxides present an interesting material for LIB anodes due to the fact that they are cost effective, abundant, environmentally compatible and have a high specific capacity.<sup>[309]</sup> They can occur in various phases, the most common ones being hematite, maghemite and magnetite,<sup>[310]</sup> and have been synthesized in many morphologies utilizing sol-gel, hydrothermal and thermal growth methods. Microwave-assisted synthesis has been shown for nanoparticles with controllable size and shape. It requires lower temperatures and shorter reaction times to form particles comparable to standard synthesis.<sup>[311–313]</sup>

Hematite has the highest theoretical capacity of the iron oxides,  $1007 \text{ mAhg}^{-1}$ ,<sup>[314]</sup> but also magnetite shows a high theoretical capacity of  $926 \text{ mAhg}^{-1}$ .<sup>[255]</sup> Hematite ( $\alpha\text{-Fe}_2\text{O}_3$ ) nanoparticles were reported in the shape of nanorods,<sup>[315,316]</sup> nanotubes,<sup>[317,318]</sup> hollow nanoparticles,<sup>[170,319–321]</sup> nanoflowers<sup>[322]</sup> and nanoflakes.<sup>[280,323]</sup> Reddy et al.<sup>[280]</sup> showed an increase in capacity stability for  $\alpha\text{-Fe}_2\text{O}_3$  nanoflakes compared to  $\alpha\text{-Fe}_2\text{O}_3$  nanoparticles or nanotubes, making this an interesting morphology to investigate.

**Challenges for Iron Oxides in LIBs** Transition metal oxides can show three main drawbacks: (1) low electron conductivity; (2) large volume changes during lithiation/ de-lithiation, leading to pulverization and failure of the electrical contact; and (3) aggregation of metal/ metal oxide nanoparticles during the cycling process due to their high surface area and activity.<sup>[324]</sup> Thus, iron oxides suffer from limited lithium diffusion kinetics during the intercalation/de-intercalation process. Carbon-based materials are often added to improve the electrochemical performance of these electrodes.<sup>[325,326]</sup>

These hybrid structures for improved battery performance<sup>[260,302–305]</sup> can be created in two ways: (1) Iron oxide particles are coated with carbon nanomaterials<sup>[31,158,327–330]</sup> or (2) carbon nanomaterials are coated with iron oxide, e.g. CNT powders,<sup>[259,308,331–334]</sup> or graphene.<sup>[324,335]</sup> A combination of both ways was reported by Wang et al.<sup>[336]</sup> as carbon-coated  $\alpha\text{-Fe}_2\text{O}_3$  hollow nanohorns on the CNT backbone that exhibited a very stable capacity retention of  $800 \text{ mAhg}^{-1}$  over 100 cycles at a current density of  $500 \text{ mA g}^{-1}$ .

A very recent report on a hybrid CNT/  $\text{Fe}_2\text{O}_3$  structure is shown in figure 4.7. CNTs are coated with  $\gamma\text{-Fe}_2\text{O}_3$  using ALD for 100 (ALD-100), 300 (ALD-300) and 500 (ALD-500) cycles. The coating thickness increases with increasing cycle number (figure 4.7a-c, materials). Additionally, the specific capacity increases with increasing ALD cycles due to the increased content of  $\gamma\text{-Fe}_2\text{O}_3$  in the particles. Overall, they demonstrate good high rate capability, long lifetime and high specific capacity ( $\sim 900 \text{ mAhg}^{-1}$ ). The CNTs here form a conductive network, and thus allow for those improved parameters.<sup>[308]</sup>

## 4 Inorganic Modification of 3D CNT Structures for Lithium-Ion Batteries

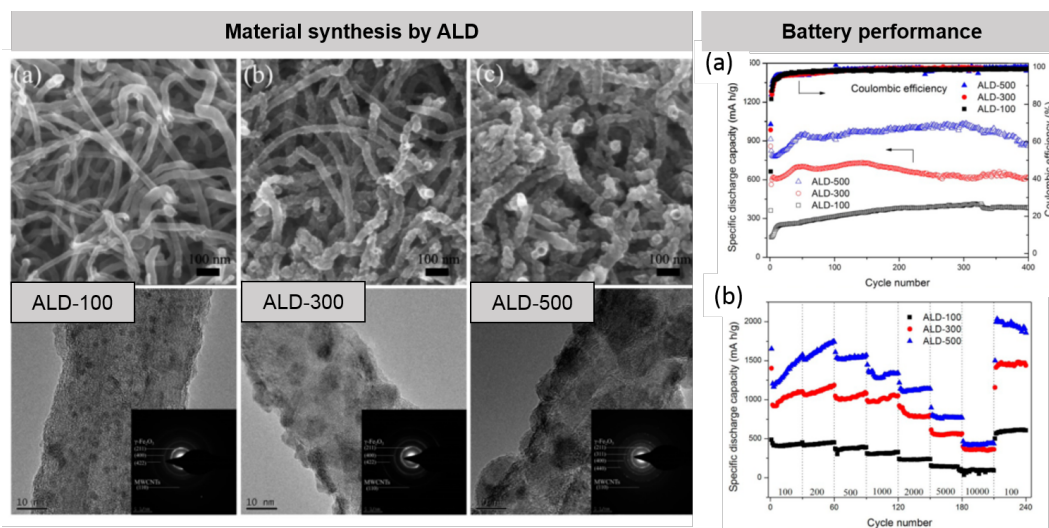


**Fig. 4.7** CNTs are coated with  $\gamma$ -Fe<sub>2</sub>O<sub>3</sub> using multiple ALD cycles (100, 300 and 500 cycles). The battery performance is shown on the right. More coating cycles lead to an increase in capacity due to an increased  $\gamma$ -Fe<sub>2</sub>O<sub>3</sub> content. Overall, the CNT/ Fe<sub>2</sub>O<sub>3</sub> composite exhibits a high capacity, long lifetime and good high rate performance.<sup>[308]</sup>

### 4.2.2 Silicon as an anode material

As silicon can alloy with up to 4.4 times Li-ion to form Li<sub>4.4</sub>Si, it has a very high specific capacity of around 4200 mA h g<sup>-1</sup>, more than 10 times that of graphite.<sup>[71]</sup> It is a naturally abundant material and can be produced at a large scale at a low cost. Hence, it has stirred much interest over the past decade as a promising high energy density anode.<sup>[337]</sup>

**Challenges of Si-anodes** Nevertheless, the Si electrodes face several challenges due to its intrinsic volume expansion during lithiation of up to 400%.<sup>[338,339]</sup> This leads to pulverization and a loss of electrical contact to the electrode, thus fast capacity fading,<sup>[340]</sup> which significantly limits large-scale applications and prevents the fabrication of thick films.

**Solution strategies** Many studies are looking into further development of Si-electrodes. An improved performance has been reported for nanostructured silicon,<sup>[341–343]</sup> such as silicon nanowires<sup>[344,345]</sup> or nanotubes.<sup>[346]</sup> Another area of research is the development of C-Si composites to provide three dimensional conductive networks and/or a layer to accommodate the volume expansion. Those hybrid materials combine Si with amorphous carbon,<sup>[347–352]</sup> graphene/ graphene-oxide<sup>[353,354]</sup> or CNTs.<sup>[355–358]</sup> Cui et al.<sup>[359,360]</sup> found that a direct growth of Si onto the current collector helps to significantly improve the performance, due to the improved kinetics of the Li-ion transport and facile strain relaxation.

Various methods for the electrode formation have been studied such as electrospinning<sup>[361,362]</sup> and spraydrying.<sup>[363]</sup> Also CVD is used as a process to deposit silicon.<sup>[231]</sup> Silicon deposition by hydrogen reduction of SiCl<sub>4</sub> using CVD as a method was reported the first time very early by Pring et al.<sup>[364]</sup> in 1909 and by Hoelbling et al.<sup>[365]</sup> in 1927 when the use of thin film silicon in electronics became

## 4.2 Coated 3D CNT structures as advanced electrode architectures

more widespread and promising.<sup>[219]</sup> More detailed recent reviews of silicon as anode materials, the progress and challenges, are given by Zuo et al.<sup>[366]</sup> and Jin et al.<sup>[367]</sup>

Coating our conductive, hierarchical CNT structure with silicon particles helps not only address the general issues of thicker batteries but also might help tackle the issue of volume expansion and loss of electrical contact, known for silicon. This structure provides a good contact between current collector and active material, a high surface area of active material and diffusion pathways for Li-ions as well as room for Si expansion through the pores in the structure.

A combination of hierarchical vertically aligned CNTs with Si as an active material has been reported before for pillars<sup>[307]</sup> and unpatterned forests,<sup>[368]</sup> as shown in figure 4.8. Both parts (A) and (B) show a schematic of the material preparation process, SEM images of the resulting composite material and then battery measurements to the right of the material preparation. The upper part of the figure (A) shows the coating of CNT forests ( $\sim 20\mu\text{m}$ ), reported by Wang et al.,<sup>[368]</sup> and the lower part (B) shows the coating of CNT pillars ( $\sim 2\mu\text{m}$ ) reported by Fan et al.<sup>[307]</sup>

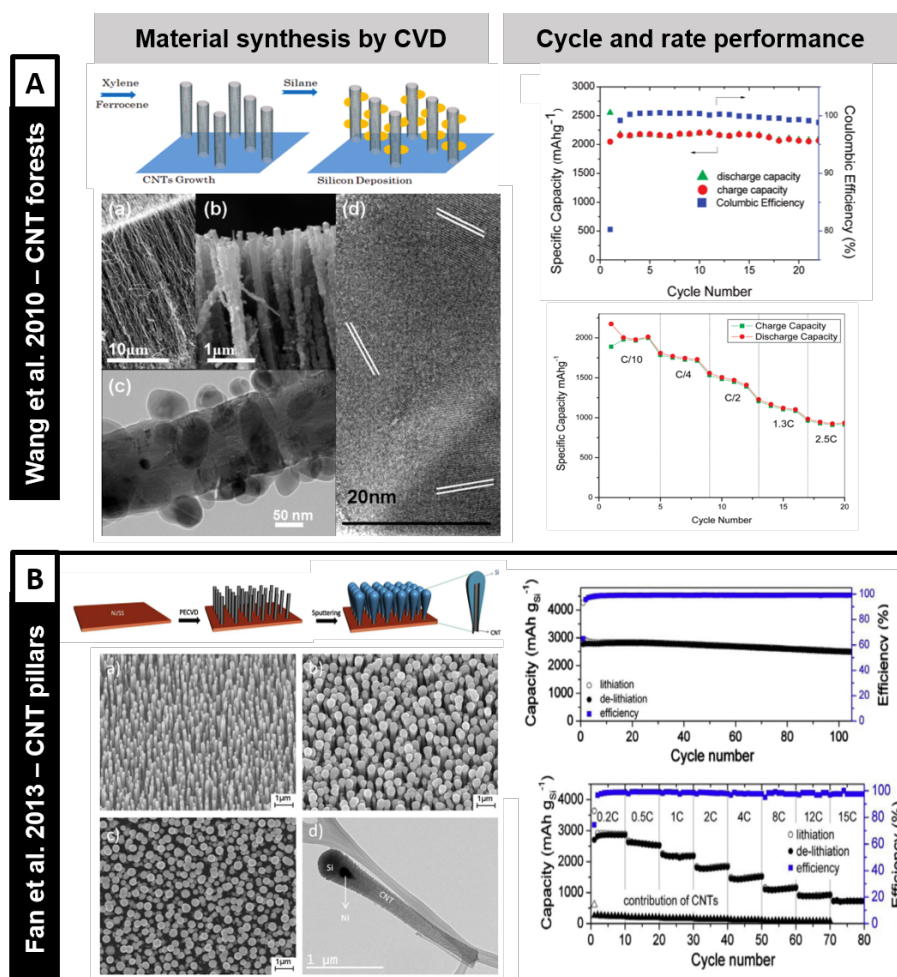


**Fig. 4.8** The figure shows the material preparation of the Si-CNT anode composites and their electrochemical performance. In the upper part (A) this is shown for the coating of a CNT forest with Si-CVD<sup>[368]</sup> and in the lower part (B) for the coating of CNT-pillars with Si-CVD.<sup>[307]</sup>

#### **4 Inorganic Modification of 3D CNT Structures for Lithium-Ion Batteries**

---

For the CNT forests a high charge storage capacity ( $\sim 2000 \text{ mAhg}^{-1}$ ) with a  $\sim 90\%$  capacity retention over 100 cycles can be seen in addition to a good high rate performance ( $\sim 750 \text{ mAhg}^{-1}$  at 2.5 C). For the CNT pillar structure, an even higher charge storage capacity ( $\sim 2750 \text{ mAhg}^{-1}$ ) with a capacity retention of more than 90% over 100 cycles is shown. At higher charge/discharge rates of 0.5, 1, 2, 4, 8, 12 and 15 C, the composite still retains a high de-lithiation capacity. Those structures are very promising but still lack height ( e.g. the height in 4.8B is 2  $\mu\text{m}$ ) and thus have a poor volumetric capacity and areal loading.

## 4.3 Modification of 3D CNT structure with iron oxides ( $\alpha\text{-Fe}_2\text{O}_3$ )

### 4.3.1 Fabrication process of the 3D CNT structure with iron oxides

This section provides a short overview of the process for the fabrication of the advanced electrode architecture with iron oxides. It can be split into four subsequent steps (figure 4.9). Step C and D have been used interchangeable depending on the specific synthesis pathway. Initially the transfer was done after the modification, later on the transfer was done before the synthesis.

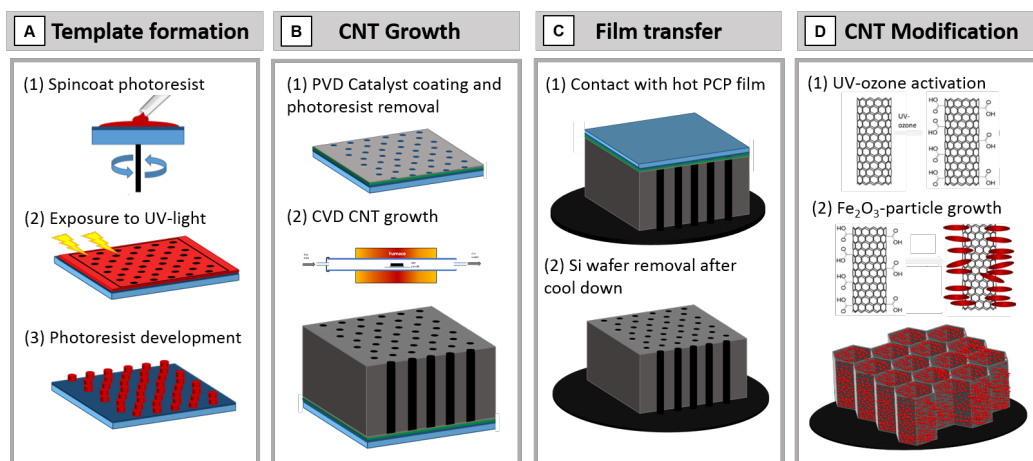


**Fig. 4.9** The fabrication process for iron oxide coated 3D CNT structures can be divided into four steps: (A) Template formation by UV-lithography, (B) CNT growth using an ambient pressure CVD furnace, (c) film transfer from the Si-wafer onto a conductive polymer film to provide a good contact with the current collector and (D) CNT modification with iron oxides using two different approaches: microwave-assisted, hydrothermal synthesis and e-beam PVD.

- (A) **Template formation:** The silicon wafer is patterned by UV-lithography to create hexagonally packed holes after the catalyst deposition. The pattern has a hole diameter of 20-30  $\mu\text{m}$  and a spacing of 10  $\mu\text{m}$ . First the photoresist is spincoated onto the substrate (1), then it is exposed to UV-light with the mask creating the pattern on the photoresist (2) and finally the photoresist is developed, leaving the desired pattern on the Si-wafer (3).
- (B) **CNT growth:** After the catalyst deposition and photoresist lift-off (1), vertically aligned CNTs are grown using a ambient pressure CVD furnace (2). The growth height of the structure is 520  $\mu\text{m}$  before the transfer onto the conductive film.
- (C) **Film transfer onto conductive substrate:** The grown 3D CNT structure is transferred onto a heated conductive film (PCP film) made from poly(vinylidene fluoride) (PVDF) with CNTs and methanofullerene phenyl C61 butyric acid methyl ester (PCBM) using microcontact printing, as reported by Ahmad et al.<sup>[65]</sup> This ensures a conductive substrate and helps anchoring the CNTs into the film which then is placed onto a copper current collector.
- (D) **Modification with iron oxides:** After transfer the PCP film with the 3D CNT structure is exposed to UV-ozone to create carboxylic and hydroxyl groups on the surface that can act as

## 4 Inorganic Modification of 3D CNT Structures for Lithium-Ion Batteries

---

nucleation points for the subsequent synthesis.<sup>[214]</sup> The structure is then coated with iron oxide nanoparticles using two different methods, a PVD process and a microwave-assisted hydrothermal reaction, with a range of protocols.

### 4.3.2 Modification on Si-wafer before transfer onto polymer film

The initial modifications of the 3D CNT structures are made on the Si-wafers. Thus, it is important that the adhesion of the CNTs to the wafer is strong enough to survive the subsequent chemical synthesis. Initial experiments failed due to the delamination of the CNT structure from the wafer. One of the postdocs in the group introduced a 'fast cooling process' for CVD grown CNTs to increase the adhesion. In this process, the cooling step in the CNT growth is done while the C<sub>2</sub>H<sub>2</sub>/H<sub>2</sub> gas mixture is still flowing. This change in the growth conditions was found to significantly enhance the adhesion and was thus added to all further experiments where good adhesion was required.

#### 4.3.2.1 Microwave-assisted, hydrothermal synthesis

Most coating methods mentioned for plain forests<sup>[32,238,239]</sup> or specific structures like cones<sup>[65]</sup> and pillars<sup>[242,307]</sup> use either dry gas phase deposition, electrodeposition or drop-casting of pre-synthesized particles to not destroy the delicate hierarchical structure. This significantly limits the range of materials that can be used and in the case of dropcasting relies on physical adsorption of the active material onto the backbone, generating composites (physical interaction) rather than hybrid structures (chemical interaction).

In this section, the in-situ coating of a 3D CNT structure with Fe<sub>2</sub>O<sub>3</sub> is shown without losing the CNT alignment or microstructure. A microwave-assisted, hydrothermal synthesis is used to uniformly coat the CNTs. This type of synthesis is particularly suited to decorate CNTs, as they absorb microwave radiation very efficiently creating hotspots that can help introduce nucleation.<sup>[263]</sup> We are able to reduce the synthesis time by 75% compared to standard hydrothermal protocols by introducing the microwave heating and ensure more uniform heating in the reactant solution.<sup>[263]</sup> Additionally, growing the active material directly onto the conductive material has been shown to improve the interface between both material systems and to enhance electrical transport between them.<sup>[369]</sup>

**Fe<sub>2</sub>O<sub>3</sub> synthesis on CNT honeycomb structures** Li et al.<sup>[370]</sup> reported the synthesis of highly porous, thin  $\alpha$ -Fe<sub>2</sub>O<sub>3</sub> nanosheets on metallic substrates which showed a high reversible capacity, enhanced cycling stability and rate capability. Due to its high surface area and promise for LIBs, this solvothermal synthesis is initially adapted for the coating of the 3D CNT structures, using the microwave-assisted method.

O<sub>2</sub>-plasma and UV-generated ozone can be used to create reactive sites on CNTs.<sup>[211,213,216]</sup> This provides nucleation points for subsequent synthesis<sup>[68-71]</sup> and changes the contact angle to higher hydrophilicity, decreasing the activation energy for the heterogeneous nucleation. Every sample is treated with O<sub>2</sub>-plasma for 10 minutes or UV-ozone for 60 minutes before the wet syntheses. CNT

### 4.3 Modification of 3D CNT structure with iron oxides ( $\alpha\text{-Fe}_2\text{O}_3$ )

honeycomb structures ( $\sim 30\ \mu\text{m}$  height) are used for the first experiments, as they have an increased mechanical stability after the densification.  $\text{Fe}_2(\text{SO}_4)_3$  is used as a precursor and ethylene glycol as a solvent. In the 2-step process, first porous precursor nanosheets are formed which then are converted to crystalline  $\alpha\text{-Fe}_2\text{O}_3$  by a thermal treatment in nitrogen atmosphere.

The most critical step here is the first synthesis step, as the adhesion to the substrate as well as the nucleation on the CNT structure needs to be evaluated. Thus, the samples are imaged right after this step (figure 4.10). The CNT honeycomb structure is undamaged and did not flake off during the microwave-assisted synthesis (figure 4.10A). The nanoflake coating can clearly be seen on the side walls (figure 4.10B). This proves that the heterogeneous nucleation is favored here over the homogeneous nucleation. Those flakes create up to a  $2\ \mu\text{m}$  thick coating on either side of the CNT wall (figure 4.10C). The EDX measurements in figure 4.10D prove that the CNT honeycomb structure is indeed coated with some iron oxide or iron hydroxide without any residue precursor visible (no sulfur signal shown in EDX).

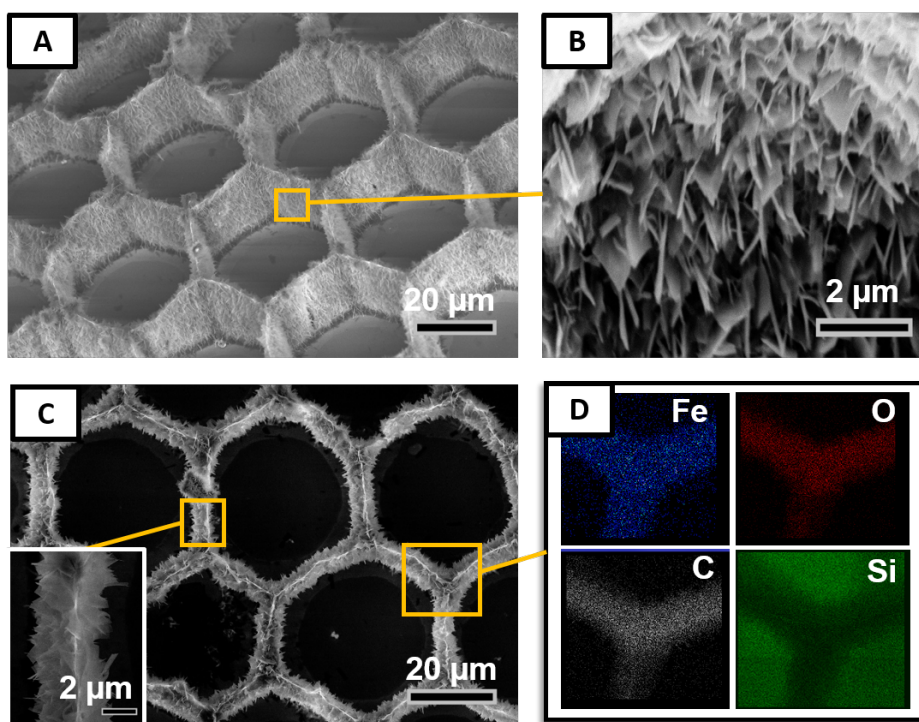


**Fig. 4.10** The CNT honeycomb structure with a height of  $\sim 30\ \mu\text{m}$  is undamaged (A) after the microwave-assisted, solvothermal synthesis, where the walls are coated with dense nanoflakes (B). Those nanoflakes show a length of up to  $2\ \mu\text{m}$  on each side of the CNT backbone (C) and no more precursor can be found on the prepared samples, as verified by EDX (D).

**Change to nanoscale dimensions** Volumetric performance is a very important for batteries. Microscale honeycombs, however, have a lot of dead volume in the pores. Thus, the synthesis is next used on the 3D CNT structures with nanoscale pores fabricated by colloidal lithography. The initial structure has a low height of  $2\ \mu\text{m}$  to see if any coating is possible without detachment of the forest, especially because no densification is done, or if coating problems occur due the smaller pores. After

#### 4 Inorganic Modification of 3D CNT Structures for Lithium-Ion Batteries

the synthesis, the coated structure remains undamaged (figure 4.11A). However, in addition to the nucleation on the structure, it is covered with small spherical particles, as seen in figure 4.11B.

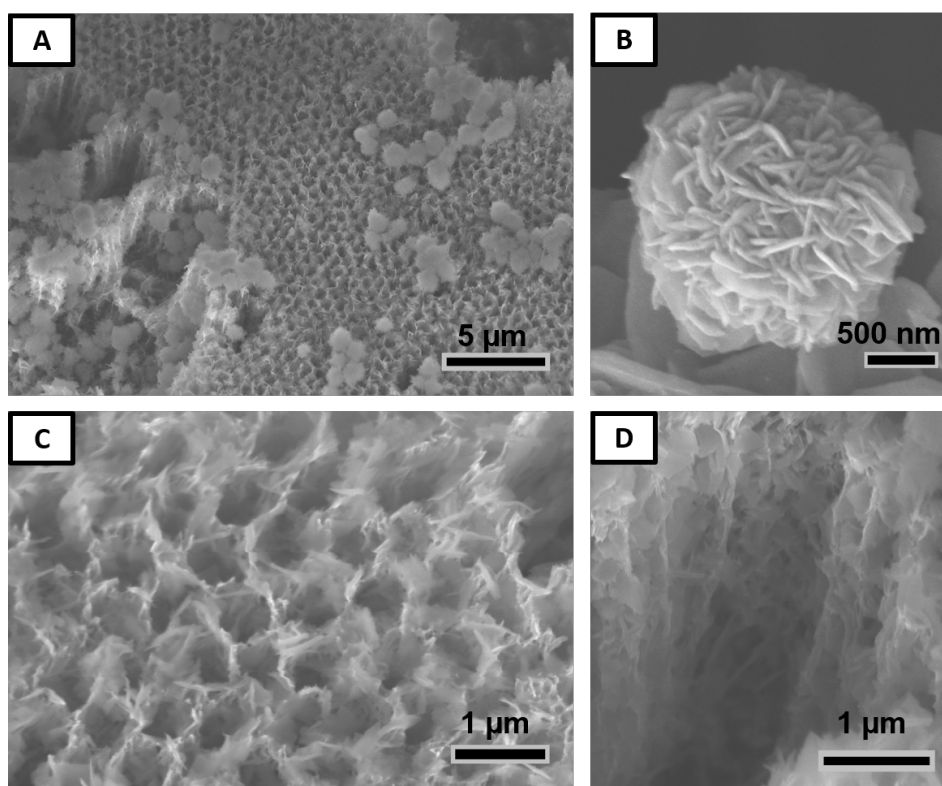


**Fig. 4.11** The overall coated structure (A), has spherical particles (close-up in (B)) on top of it, indicating that the nucleation of the iron oxide particles not only occurs on the CNT structure but also in solution. The coating on the colloidal structure is not thick enough to close the 450 nm holes, as seen in (C). It clearly covers the side walls of the CNT structure (D).

This means that in addition to the nucleation on the CNT structure, there is also nucleation in the solution itself. While heterogeneous nucleation on the hotspots might be favored, after coating the structure homogeneous nucleation happens in solution over growth. It was reported that using mixture solvents such as DMF–water and ethanol–water could suppress the hydrolysis reaction rate in free solution,<sup>[71]</sup> which should be kept in mind, in case the synthesis needs to be optimized later. The additional particles are not an issue in this synthesis, as they can be rinsed off and don't negatively affect the uniform coating on the CNT structure. The coating is thin enough to not close the 450 nm sized holes (figure 4.11C), suggesting that the nanoflakes in this synthesis are slightly smaller than in the first one, supporting the previous theory about homogeneous nucleation over growth. The uniform coating on the walls with dense nanosheets is shown in figure 4.11D, however, it is not clear how well the inside of the small pores is coated and how large the flakes there are.

It is very promising to see that the coating works on both type of initial structures. For the evaluation of its electrochemical performance as an electrode, it is crucial that the coated structure is transferred onto the conductive PCP film, as a conductive collector electrode is needed, as the silicon wafer would start alloying and decomposing during battery cycling.

### 4.3 Modification of 3D CNT structure with iron oxides ( $\alpha$ -Fe<sub>2</sub>O<sub>3</sub>)

---

**Transfer of the structure onto a conductive film** The PCP film is casted following the instructions in the publication.<sup>[65]</sup> When the transfer of the coated 3D CNT structures is attempted by microcontact printing, it is found that they have a strong adhesion to the Si-wafer. It is not possible, even by applying pressure by weight addition on top of the Si-wafer during transfer, to increase the overall adhesion to the film enough for the structure to delaminate from the Si-substrate.

As one of the most critical steps for the application is not possible with this synthesis, it is not further characterized and optimized.

#### 4.3.2.2 E-beam PVD coating with Fe

A good adhesion of the CNTs to the substrate is required for a wet chemical synthesis route. As shown before, this adhesion is too strong to transfer the structure onto the conductive film afterwards.

A simple and straightforward method for Fe<sub>2</sub>O<sub>3</sub> flake formation, reported by Reddy et al.,<sup>[280,371]</sup> is the coating of a substrate with a Fe film of about 700 nm, followed by a temperature treatment step of 5h at 300°C in air. They used a Cu-substrate that could then immediately act as a current collector in the electrochemical measurements.

**Nanoflakes on ~100  $\mu$ m 3D CNT structures** This method is applied to coat a ~100  $\mu$ m 3D CNT structure. The e-beam evaporation of Fe does not significantly affect the overall 3D CNT structure (figure 4.12A). Before the temperature treatment no flakes are visible yet (figure 4.12B) which is in agreement with Reddy's published results. The structure is coated uniformly on top of the honeycomb. The coating on the side walls is not as uniform as on the top. Fe-islands have formed which are spread all over the side walls. This is a typical feature during e-beam evaporation. After the temperature treatment, nanoflakes form on top of the CNT structure, but not on the side walls of the structure (figure 4.12C). Additionally the coating starts to delaminate from the CNT structure. This delamination might be due to poor adhesion of the Fe onto the CNTs, as well as Ostwald ripening occurring at the higher temperature. Due to the delamination and flake formation only on parts of the structure, those samples were not characterized further.

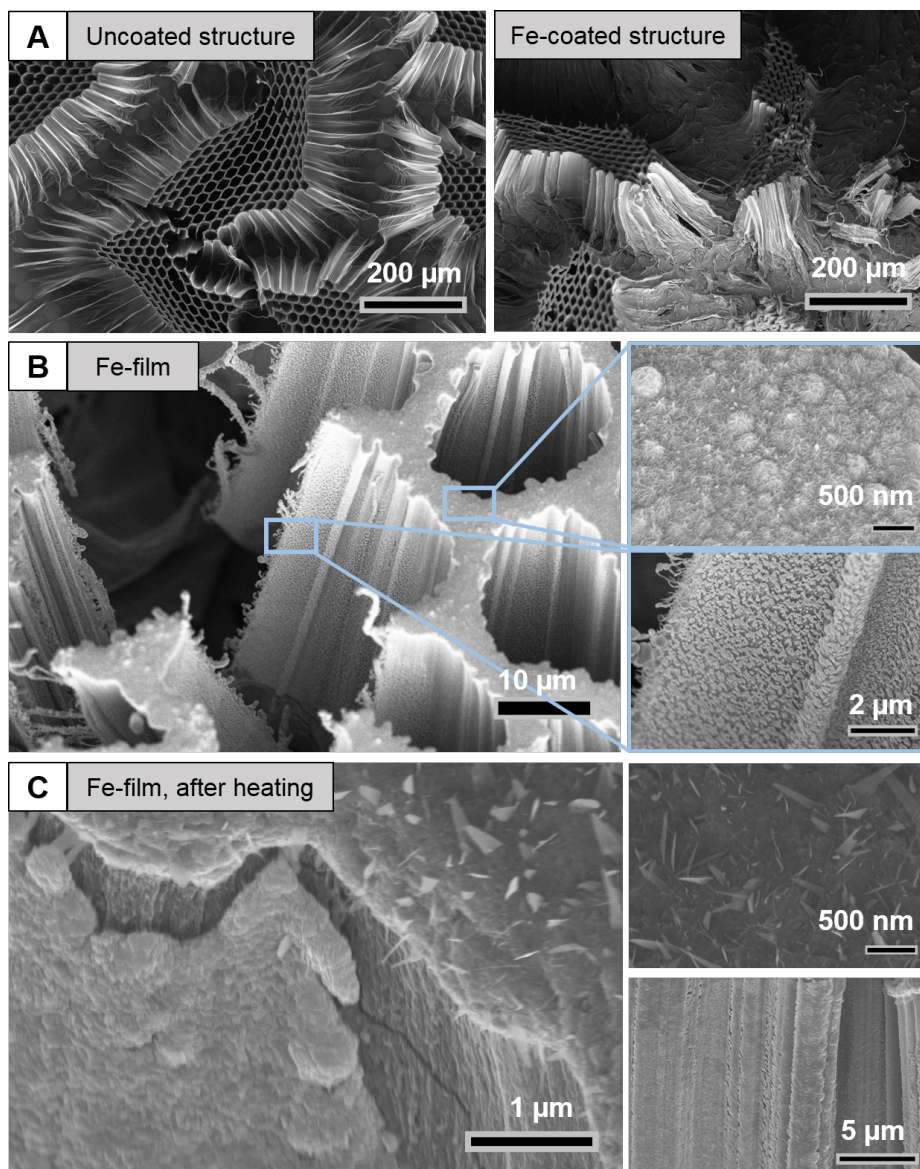


**Fig. 4.12** Following a protocol by Reddy et al.,<sup>[280]</sup> a high 3D CNT structure ( $\sim 100 \mu\text{m}$ ) is coated with Fe by e-beam PVD. The gas-phase Fe-deposition does not significantly change the initial structure (A). The Fe-film is uniformly coating the top of the structure and forms small islands on the side walls, covering most of the area on the walls (B). After the temperature treatment, nanoflakes form on top of the 3D CNT structure, but not on the side walls and the Fe-film delaminates from the side walls (C).

**Nanoflakes on  $\sim 30 \mu\text{m}$  3D CNT structures** As the high structure shows cracking already before the coating, as well as delamination after the temperature treatment, a lower CNT structure ( $\sim 30 \mu\text{m}$ ) is densified into CNT honeycombs for additional mechanical stability and then coated. The coating of the Fe-film does not change the CNT honeycomb structure (figure 4.13A). The holes are filled with a thicker Fe film which seems to delaminate from the side walls of the honeycomb structure. However, looking closer at that interface, the side walls are still coated, only with a thinner layer. After the temperature treatment, thin nanoflakes can be seen on the top of the structure (figure 4.13B) while a delamination of the film can be observed on the side walls.

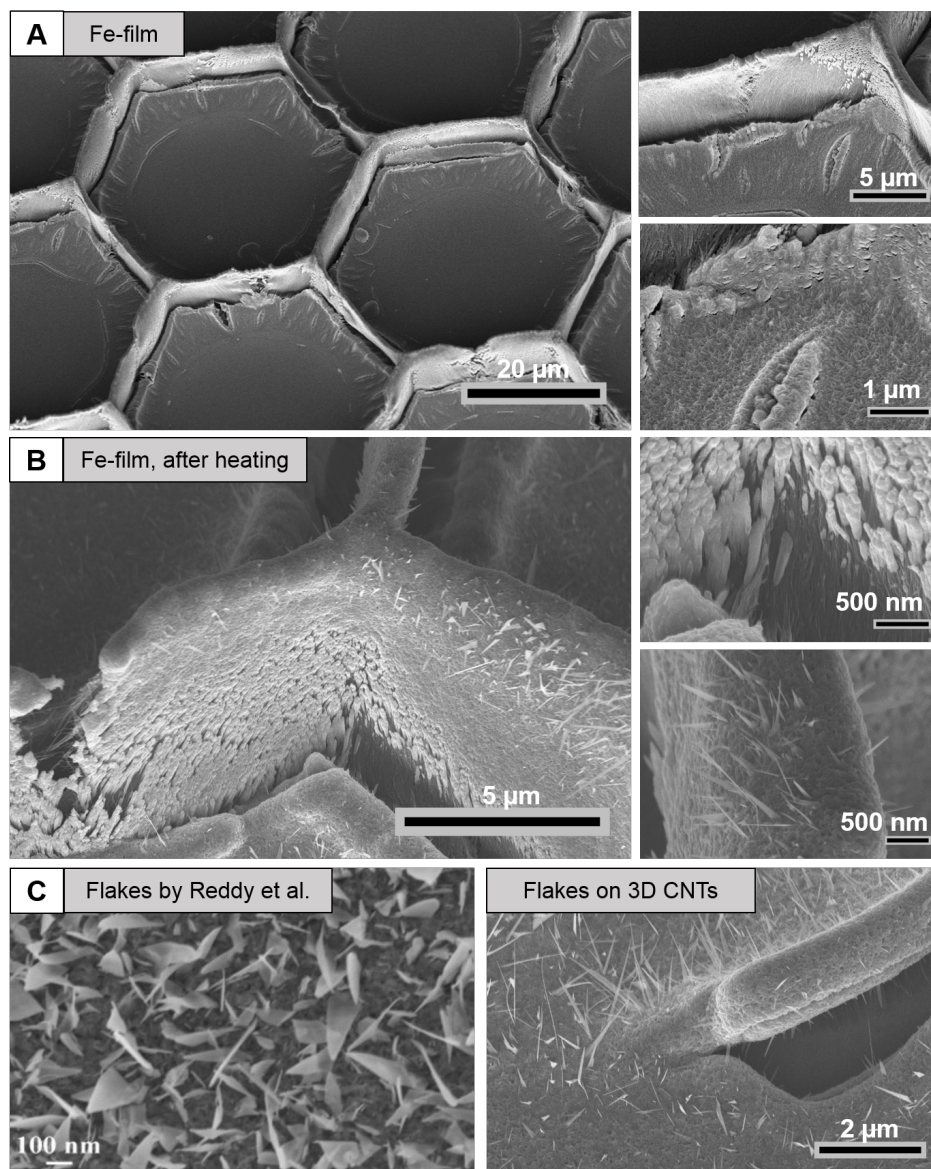


**Fig. 4.13** The CNT honeycombs structure is coated with an Fe-film using e-beam evaporation. This fills up some of the pores slightly and also coats the walls uniformly (A). After the temperature treatment step, nanoflakes appear on top of the structure, but delamination can be seen on the side walls (B). Comparing the flakes reported in the paper by Reddy et al.<sup>[280]</sup> to the ones in our process, it can be seen that the density on the surface is significantly lower and the coating is not as uniform (C).

Comparing the achieved flakes of our process with the ones reported by Reddy et al.<sup>[280]</sup> (figure 4.13C), the density of our nanoflakes is significantly lower. Also the coverage of the structure with the flakes is very poor. This might be due to the different deposition method for the film. In the paper, they used radio frequency magnetron sputtering whereas here we used e-beam evaporation, which might have an influence on impurities. It definitely influences the step coverages, as e-beam evaporation is not the most suited PVD method for good step coverage. Also a variation in the temperature treatment process might be the cause of the deviating results. Similar to the report, a hot-plate was used for the heating step. However, this process can then be affected by the surrounding temperature, humidity etc. which might have prevented some of the nanoflake growth. We have also

## 4 Inorganic Modification of 3D CNT Structures for Lithium-Ion Batteries

---

changed the substrate here and as Yu et al.<sup>[371]</sup> reported before this process significantly depends on the substrate used. It might not be possible to use exactly the same conditions for the CNT structure as for the Cu-foil, as the nucleation characteristics might be different.

**Transfer of the coated structures onto a conductive film** The coated 3D CNT structure has to be transferred onto a conductive film for the electrochemical measurements. This transfer onto the PCP film is tried multiple times using microcontact printing with weights of 10 g and 25 g on top of it. However, the structure is too well adhered to the Si-wafer. This might be due to the fact that the Fe-film provides further adhesion to the substrate.

Overall, this protocol does not lead to the desired outcome as the material delaminates from the structure after the heat treatment and the coated structure can not be transferred onto the conductive film which is a prerequisite for any electrochemical characterization.

### 4.3.2.3 Challenges

The transfer of the coated 3D CNT structures onto a conductive polymer film is not possible for both synthesis routes, even with long transfer times or an additional weight on the sample. In addition, the longer the PCP film is on a hotplate over 180 °C, the more it seems to degrade. This can be seen by the fact that the film starts curling up when removed from the glass substrate after more than 5 minutes transfer time. The PVDF starts softening when heated which is beneficial for the transfer. However, if the temperatures are above 180 °C, it starts to degrade, causing the film to curl up and to lose its smooth, flat structure. It can then no longer be used for the electrochemical measurements.

If the transfer onto a conductive substrate, especially a polymer film, is not possible after the reaction, the other approach is a transfer after CNT growth and subsequent chemical modification on the conductive film. This means that those two methods reported before are not feasible anymore due to the high temperatures that will affect the polymer film. A method that does not require a heating step over ~ 200 °C (melting point of the PVDF in the polymer films is 177 °C) is needed to avoid a change in the film and a potential loss of the polymer.

### 4.3.3 Transfer of honeycomb structures onto polymeric films

#### 4.3.3.1 Transfer of CNT honeycombs onto PVA film

A paper that describes the formation of fibrillar adhesives, such as gecko-toe-pad structures,<sup>[372]</sup> is adapted to transfer a 3D honeycomb structure with a height  $\sim 30\mu\text{m}$  onto a flexible polymer film (polyvinyl alcohol (PVA)). PVA is used as it provides a smooth surface for the transfer that is easy to fabricate.

A schematic of the transfer process and top-down SEM images of the initial and resulting structures are shown in figure 4.14. After the 3D honeycomb structure (figure 4.14A) is transferred onto the PVA film, the base of the initial structure can now be seen (4.14B). The pattern is circular rather than hexagonal due to the slanted base of the initial honeycomb structures. The inset shows a higher resolution image of the CNTs on the base where small bundles of CNTs can be seen. However, it is not possible to see whether the catalyst particles stay on the Si-wafer or are attached to the ends of the CNTs in the CNT honeycomb structure. The formation of the initial honeycomb structure is observed when the circular pattern is re-densified (4.14C). This shows that it is possible to densify the slanted base even after the initial densification and to form a honeycomb structure that does not have circular patterns on one side anymore.

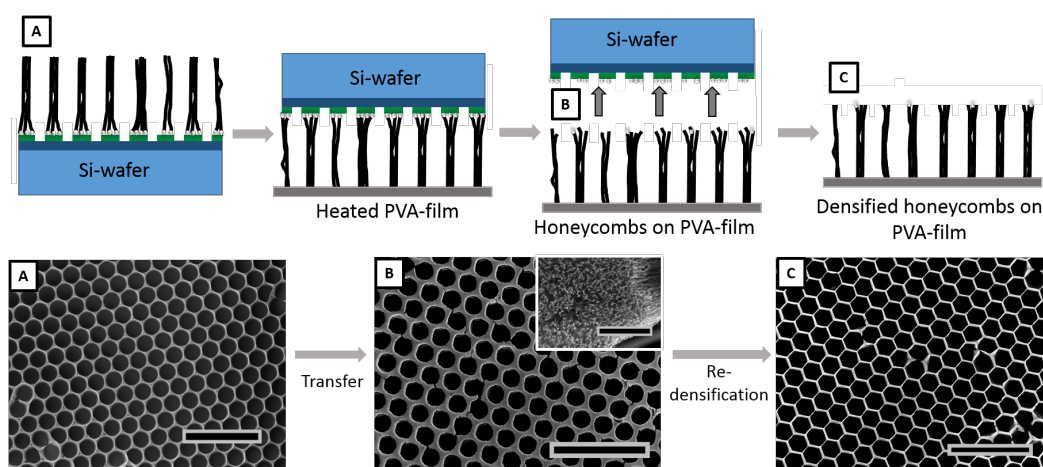


**Fig. 4.14** The upper part of the figure shows the process of the densification schematically, supported by the SEM images in the lower part of the figure. First, the honeycomb structure (A) is put onto a heated, soft PVA film. After cooling, the silicon wafer is removed and the structure is securely implanted in the PVA-film. The top-down SEM image (B) shows circular holes rather than hexagonal honeycombs due to the slanted base of the honeycombs. These can be turned into the honeycomb structure again by re-densification (C). Scale bars are  $200\ \mu\text{m}$ , and  $2\ \mu\text{m}$  in the inset in (B).

## 4 Inorganic Modification of 3D CNT Structures for Lithium-Ion Batteries

In order to understand better where the catalyst particles are located, the Si-wafer after the transfer is used again for CNT growth. The CNTs can be regrown on the substrate in a second growth and turned into honeycomb structures after etching and densification (figure 4.15). This finding proves that the adhesion between the substrate and the catalyst particles is stronger in most cases than the adhesion of the catalyst particles to the grown CNTs. Thus, most of the catalyst particles stay on the Si-wafer when the 3D CNT structure is transferred. This has also been reported by Ahmad et al.<sup>[65]</sup> where they found that the substrate can be regrown up to four times after the transfer.

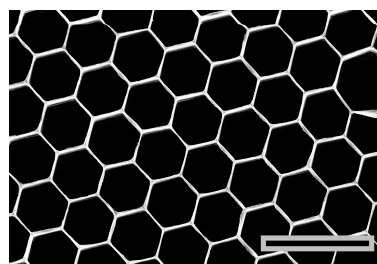


**Fig. 4.15** Due to enough catalyst particles, a honeycomb structure similar to the initial one can be regrown on an Si-wafer and formed again. Scale bar is 100  $\mu\text{m}$ .

For applications such as batteries, however, not only a flexible polymer, but a conductive film is needed. PVA is also water-soluble which additionally limits the range of applications.

### 4.3.3.2 Transfer onto conductive PCP film

As previously mentioned, a PCP film is used, which was created by a postdoc in our group and then first reported by him<sup>[65]</sup> as a substrate for CNT cone structures for flexible batteries. The PCP film and transfer are optimized for the structures in collaboration with Dr. S. Ahmad who first made that type of film.

Figure 4.16A shows the grown 3D CNT structure on the Si wafer. After the transfer, the structure looks the same from the top and a sharp edge at the rim of the structure is visible (figure 4.16B). This proves a complete and uniform transfer from the Si-wafer with the optimized process. As higher 3D CNT structures are used for their subsequent use as thick electrodes in batteries, no densification is done before the transfer. This would introduce cracks into the structure due to the height of the 3D CNT structure, as described in the previous chapter.

As expected, some buckling occurs during the transfer when a small force is applied, decreasing the height of the initial structure (520  $\mu\text{m}$ , figure 4.16C) to about 470  $\mu\text{m}$  (figure 4.16D).

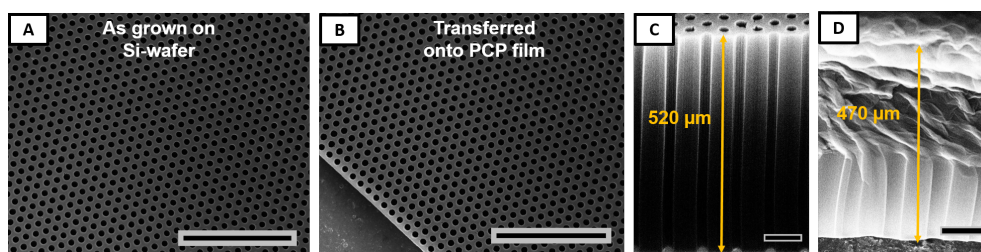


**Fig. 4.16** The 3D CNT structure before (A) and after the transfer (B) shows no difference in the structure itself and a sharp edge where the structure finishes, indicating a complete transfer. A decrease in height can be seen in a comparison before (C) and after the transfer (D) due to the influence of external stress that can cause local deformations and buckling in the CNTs. Scale bars are 300  $\mu\text{m}$  in (A) and (B), 100  $\mu\text{m}$  in (C) and (D).

### 4.3 Modification of 3D CNT structure with iron oxides ( $\alpha$ -Fe<sub>2</sub>O<sub>3</sub>)

This deformation mode of CNTs due to external stress or changed catalyst properties has been reported before. Cao et al.<sup>[373]</sup> have reported buckling of CNTs in vertically aligned structures, making them foam-like and super compressible. They also showed a recovery of up to 30% of the height after 1000 compression cycles, making this a very interesting material to handle external stresses. De Volder et al.<sup>[139]</sup> reported this kind of local wrinkling and buckling when different growth speeds during strain engineering are involved. Maschmann et al.<sup>[374,375]</sup> have also pointed out the cooperative nature of the CNT network when considering axial compression and buckling stresses. Thus the deformation mode here during the transfer process is expected.

However, for nanometer sized holes the transfer needs to be more carefully executed, as a slight shear can lead to closure of the small holes and limitations in the modification of those structures after transfer, as can be seen in the SEM image in figure B5A and B in appendix B. If this deformation of the forest happens, etching the CNT structure for 2 min with O<sub>2</sub>-plasma (figure B5C) or 30 min with UV-ozone (figure B5D) does not help regain the initial porous structure.

#### 4.3.4 Low temperature modification on conductive polymer film

Modification of the 3D CNT structure on a conductive polymer film leads to certain limitations when selecting the synthesis method. The PCP-film dissolves in dimethyl formamide (DMF) and N-Methyl-2-pyrrolidone (NMP) and CNTs are etched by HNO<sub>3</sub>, thus not allowing these reagents as solvents. Additionally, temperatures above 200 °C will melt the PVDF in the PCP-film. This means that every metal oxide reaction that requires an annealing step cannot be used for this system. Those limitations complicate the selection of a suitable synthesis significantly.

The following section shows the results for a coating on the 3D honeycomb structure, adapting a hydrothermal synthesis method reported by Wang et al.<sup>[320]</sup> In this method, they formed hollow  $\alpha$ -Fe<sub>2</sub>O<sub>3</sub> spheres with enhanced Li-ion storage properties from an iron-sulfate precursor in a glycerol-water mixture as the solvent. A schematic of the synthesis, TEM and SEM images and a XRD measurement as characterization (as reported by Wang et al.<sup>[320]</sup>) can be found in figure B6 in appendix B. The produced iron oxide is hematite,  $\alpha$ -Fe<sub>2</sub>O<sub>3</sub>. Other Fe<sub>2</sub>O<sub>3</sub> synthesis have been attempted, too, but did not lead to the desired coating on the CNT structure. An example is shown in figure B7 in appendix B where a synthesis by Zhu et al.<sup>[328]</sup> was adapted.

Again the hydrothermal method reported is combined with microwave radiation to reduce the reaction time. Additionally, no annealing step is needed, thus enhancing the range of substrates that can be used significantly due to the low temperatures of  $\sim$  160 °C and one-step synthesis process, which makes this approach very promising for scale-up and cost-effective synthesis.

##### 4.3.4.1 Comparison of two oxidation states in the iron-precursor

Initially the influence of two different oxidation state of the iron source is investigated on a synthesis adapted from Wang et al.<sup>[320]</sup> The two different precursors supply different oxidation states of the iron-source. The oxidation state of materials can matter significantly during chemical reactions. A

#### 4 Inorganic Modification of 3D CNT Structures for Lithium-Ion Batteries

---

change from  $\text{Fe}^{3+}$  to  $\text{Fe}^{2+}$  for example will introduce the necessity of an oxidation step to form  $\text{Fe}_2\text{O}_3$  and thus might introduce a change in reaction kinetics. This is why a temperature screen for the 6 hour reaction (reduced from 24 hours due to microwave irradiation) with the two different precursors (120 mg precursor in 1:7 glycerol to DI water mixture) on 3D CNT structures on Si wafers with a 60 min UV-ozone activation time is run to see which temperature achieves the most crystalline result and which particle sizes or morphologies are obtained.

This overview of the SEM images is shown in table 4.1. In general, all temperatures led to a nucleation of the  $\text{Fe}_2\text{O}_3$  particles on the CNT structure. At lower temperatures, the coating for both iron sulfate salts seems to be less defined and more of an amorphous film. More facets/ spikes seem to be appearing in the coating for the  $\text{Fe}^{2+}$  salt around 160 °C and for the  $\text{Fe}^{3+}$  salt the platelet formation becomes more obvious starting from 175 °C. A dense coating with small nanoflakes can in both cases be seen at temperatures above 175 °C, indicating that above this temperature the reaction is complete after 6 hours and the crystallinity is potentially higher than in the initially formed particles.

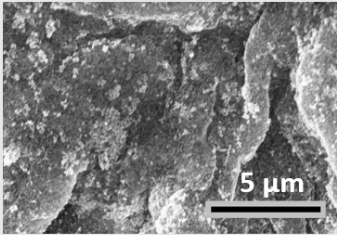
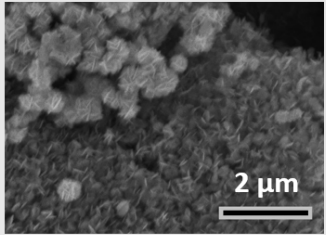
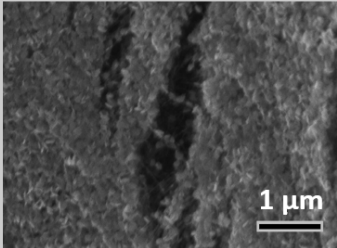
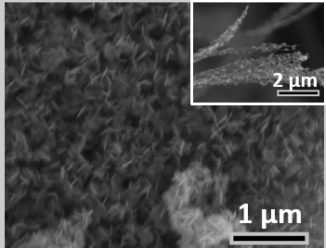
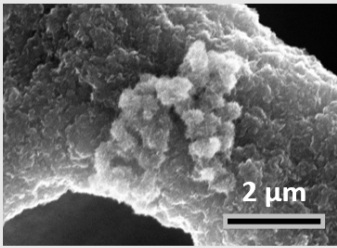
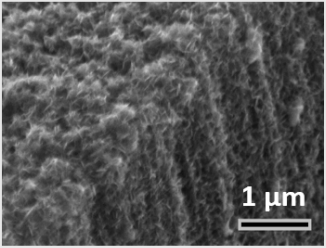
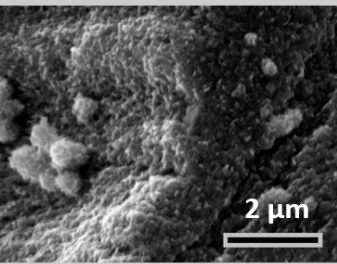
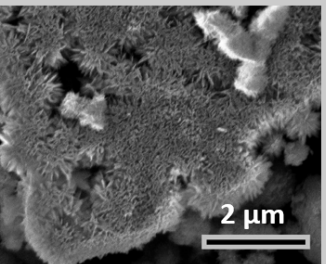
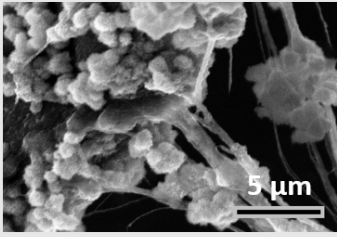
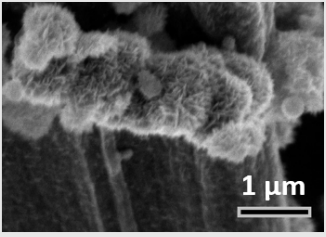
To verify the assumptions about crystallinity, XRD of the synthesized powders is measured (figure 4.17). At lower temperatures, the diffraction patterns show small crystalline peaks and an amorphous part. The diamond shaped labels indicate the position of the final peaks during the lower temperature synthesis, when they start to develop. The crystallinity of the iron oxide increases with increasing temperature for both precursors. Both precursors lead to the same material at a temperature 190 °C, showing that with the right temperature and reaction time, the same result can be achieved. Nevertheless, hematite can already be achieved at a temperature of 175 °C for both precursors.

The final particle shapes still look slightly different which indicates the crystal growth might be happening on different facets. Different from the assumption in the SEM, the material synthesized at 160 °C with the  $\text{Fe}^{3+}$  salt as a precursor already shows a higher degree of crystallinity than the material synthesized by the  $\text{Fe}^{2+}$  where hardly any clear peaks can be seen in the XRD measurement (reference patterns of hematite for the individual matched ICSD cards are provided in figure B8 in appendix B).

The fact that the  $\text{Fe}^{3+}$  precursor leads to a better crystallinity at a lower temperature might be because the additional oxidation step is not necessary here. This shows that the type of precursor matters when adjusting the parameters like temperature and reaction time and needs to be kept in mind in subsequent syntheses.

### 4.3 Modification of 3D CNT structure with iron oxides ( $\alpha$ - $\text{Fe}_2\text{O}_3$ )

**Table 4.1** The table shows SEM images with two types of precursors, one supplying  $\text{Fe}^{3+}$ -ions (left), the other one supplying  $\text{Fe}^{2+}$  (right) for temperatures ranging from 130 °C to 190 °C. It can be seen that the flake-like nature increases with increasing temperature, indicating that a higher crystallinity and more complete synthesis can be reached at those higher temperatures.

Reaction temperature	Precursor salt	
	$\text{Fe}_2(\text{SO}_4)_3 \cdot 5 \text{H}_2\text{O}$	$\text{FeSO}_4 \cdot 7 \text{H}_2\text{O}$
190		
175		
160		
145		
130		

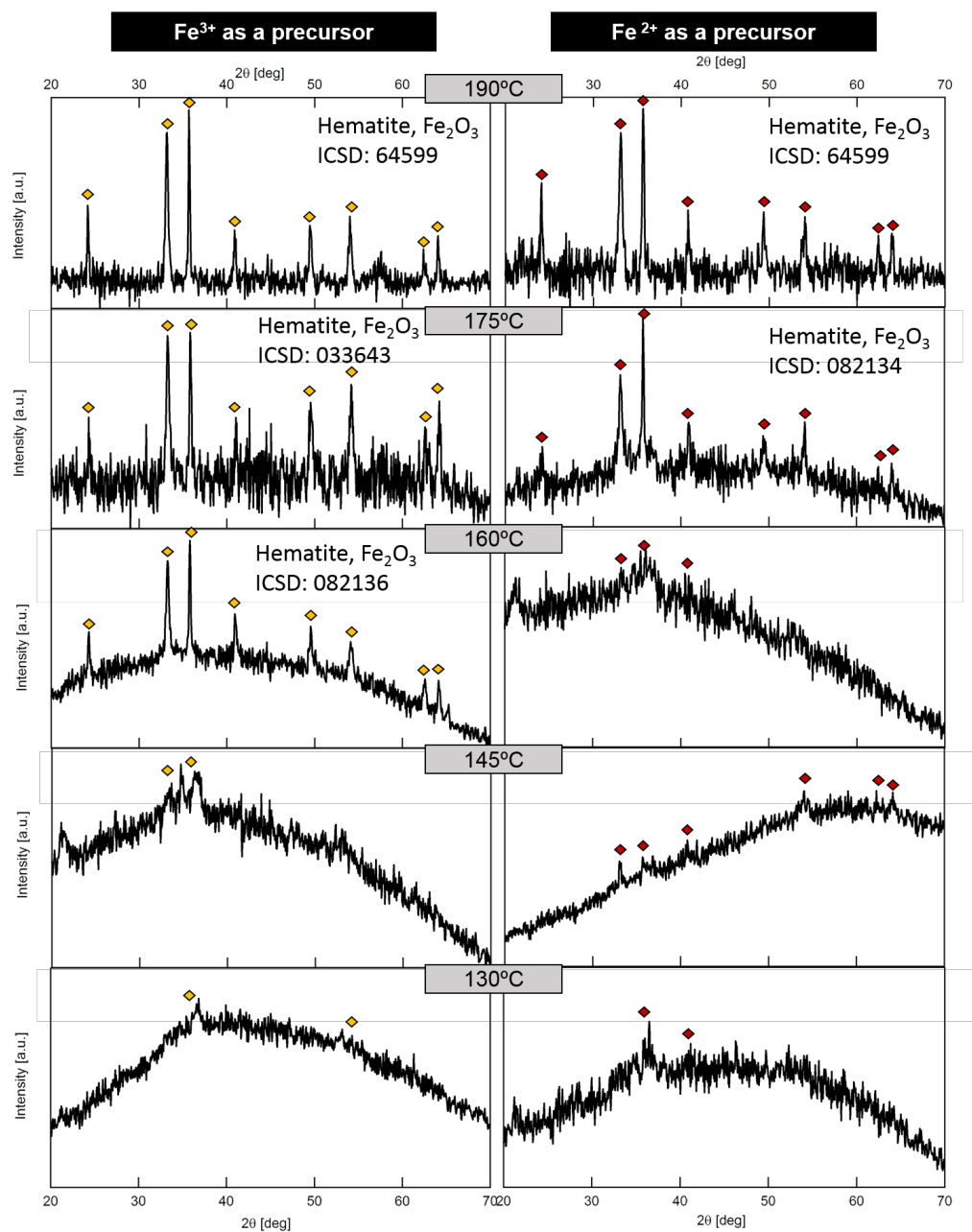


**Fig. 4.17** This figure shows an overview of the XRD patterns measured of the iron oxide particles synthesized at temperatures ranging from 130 to 190 °C with two precursor salts with different oxidation states of the Fe-source. The crystallinity after the 6 hour synthesis increases with increasing temperature. With the  $\text{Fe}^{3+}$  precursor hematite can be achieved at a lower temperature than for the  $\text{Fe}^{2+}$  precursor. The reference patterns for the matched hematite patterns are provided in figure B8 in appendix B.

It is also important to note that different precursors could lead to a change in the impurities. This has been reported by Ou et al.<sup>[376]</sup> for  $\text{Fe}^{3+}$  impurities in hydrothermally synthesized  $\text{LiFePO}_4$ . While no difference could be detected in the XRD, a change in the electrochemical properties could be measured.

Based on the results above, both precursors seem very promising to form crystalline hematite on the CNT structures and thus the modification of the 3D CNT structure with each of them will be

investigated further in the next sections, including electrochemical characterization in the end. The reaction will be done at 175 °C, as this is compatible with the PCP film and has been proven to lead to the desired  $\text{Fe}_2\text{O}_3$  phase.

#### 4.3.4.2 Synthesis with $\text{Fe}^{2+}$ as a precursor

For the following synthesis  $\text{FeSO}_4 \cdot 7\text{H}_2\text{O}$  containing  $\text{Fe}^{2+}$ -ions has been used as a precursor on high ( $\sim 500 \mu\text{m}$ ) 3D CNT structure and for lower nanoscale structures ( $\sim 100 \mu\text{m}$ ). The reaction time is 6 hours and the reaction is performed on structures transferred onto a PCP film.

**Time-dependence of the  $\text{Fe}_2\text{O}_3$  synthesis** To gain more insight into the performed reaction, the development of the particles at 175 °C at different time points is studied here. The XRD patterns in figure 4.18 are measured with another equipment and a lower step size than before. They show that already after 30 minutes, the nanoparticles show high crystallinity and can be identified as hematite ( $\alpha\text{-Fe}_2\text{O}_3$ ). A slight decrease in peak width is seen after 1 hour, suggesting a change in crystallite sizes. No significant changes are observed in the XRD measurements after this time.

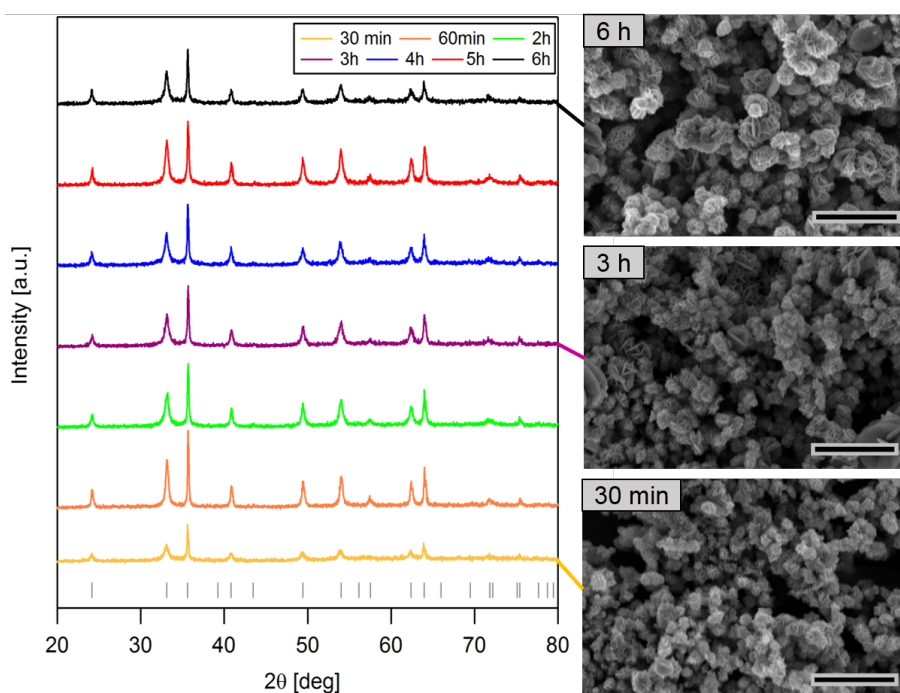


**Fig. 4.18** The development of the  $\text{Fe}_2\text{O}_3$  nanoparticles synthesized at 175 °C in the microwave-assisted hydrothermal process. The synthesis is stopped after certain times and XRD measurements are taken to see the change in crystallinity. Already after 30 minutes, the nanoparticles show good crystallinity and can be identified as hematite. There is no significant change after the first hour in the particle crystallinity. SEM images show an increase in the particle size, but also a high polydispersity of the synthesized particles. The XRD measurements here were done with a different equipment (D8-B3-Gen9 Bruker DAVINCI instead of D8-B1-Gen10 Bruker) and a smaller stepsize than before ( $0.025^\circ$  instead of  $0.05^\circ$ ).

For further insight into the particle sizes and morphology, SEM images are taken of the particles (selected ones shown in figure 4.18 for 30 min, 3h and 6h, complete set in figure B9 in appendix B).

#### 4 Inorganic Modification of 3D CNT Structures for Lithium-Ion Batteries

The particle size distribution is very polydisperse, suggesting that nucleation happens continuously in the solution, forming new particles all the time, while some of the particles grow larger. This means that a longer reaction time leads to more particles in the solution but also some larger ones. The yield after a short amount of time might be lower if the nucleation is not initiated uniformly, but happens throughout the whole reaction time. This would mean that a lot of precursor material is wasted if the reaction is stopped after the first hour instead of 6 hours. Thus, 6 hours are chosen as the reaction time for subsequent reactions.

It is important to keep in mind that these measured XRD patterns are only of the particles rather than the CNT-Fe<sub>2</sub>O<sub>3</sub> structure and their interaction with the CNTs might change for different reaction times. The optimal reaction time for a complete coating of the CNT structure can be determined in further experiments. Also TEM of the samples could be done to confirm their similarity or see any differences.

**Synthesis on high 3D CNT structures** A (~500 μm) 3D CNT structure is coated with Fe<sup>2+</sup> as a precursor at 175 °C for 6 hours.

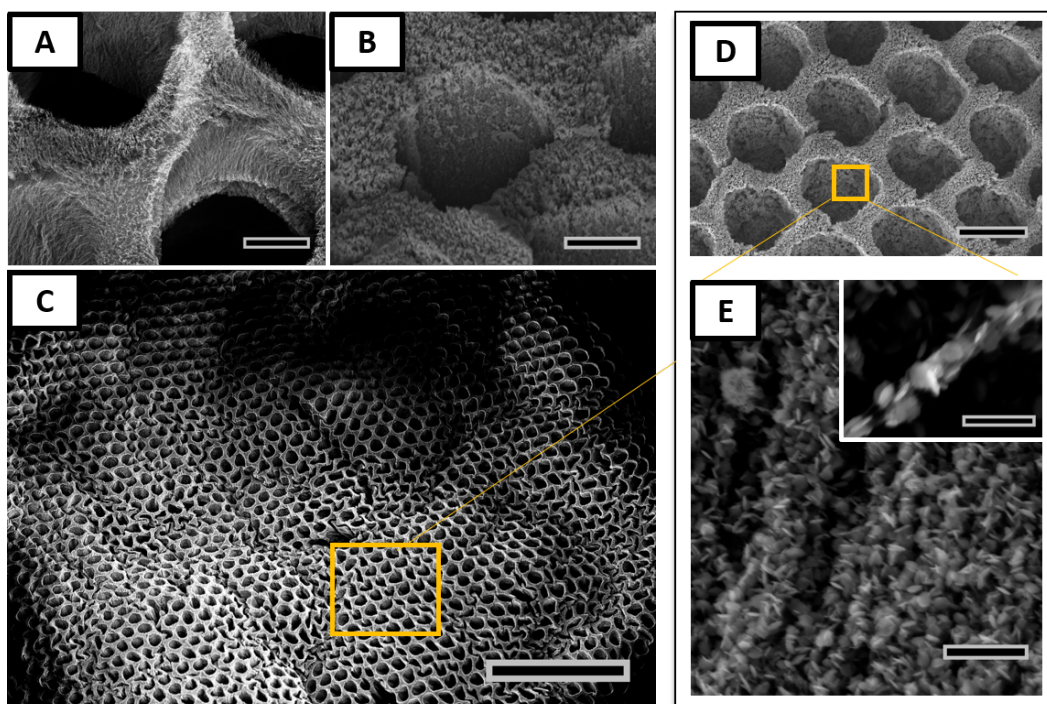


**Fig. 4.19** The image shows an uncoated structure (A) which is then coated with  $\alpha$ -Fe<sub>2</sub>O<sub>3</sub> (B). A large area view is seen in (C) where the synthesis introduces some wrinkling into the structure but no significant cracking. The structure is completely coated (D) with dense  $\alpha$ -Fe<sub>2</sub>O<sub>3</sub> nanoflakes (E) that emerge from the CNT strands. Scale bars are 10 μm in (A) and (B), 300 μm in (C), 30 μm in (D), and 1 μm in (E) with 500 nm in the inset.

First the uncoated top of the structure is shown in figure 4.19A where single CNT strands or small bundles in the structure are visible. After the modification those are coated with  $\alpha$ -Fe<sub>2</sub>O<sub>3</sub> (figure 4.19B). While the synthesis seems to introduce some wrinkles in the overall structure on the film

### 4.3 Modification of 3D CNT structure with iron oxides ( $\alpha\text{-Fe}_2\text{O}_3$ )

(figure 4.19C), it is undamaged and does not show any significant cracking. The coating is uniform (figure 4.19D) and is made from a dense array of  $\alpha\text{-Fe}_2\text{O}_3$  nanoplatelets covering the walls (figure 4.19E). These emerge from the CNT strands, ensuring a good contact between the CNTs and the nanoplatelets.

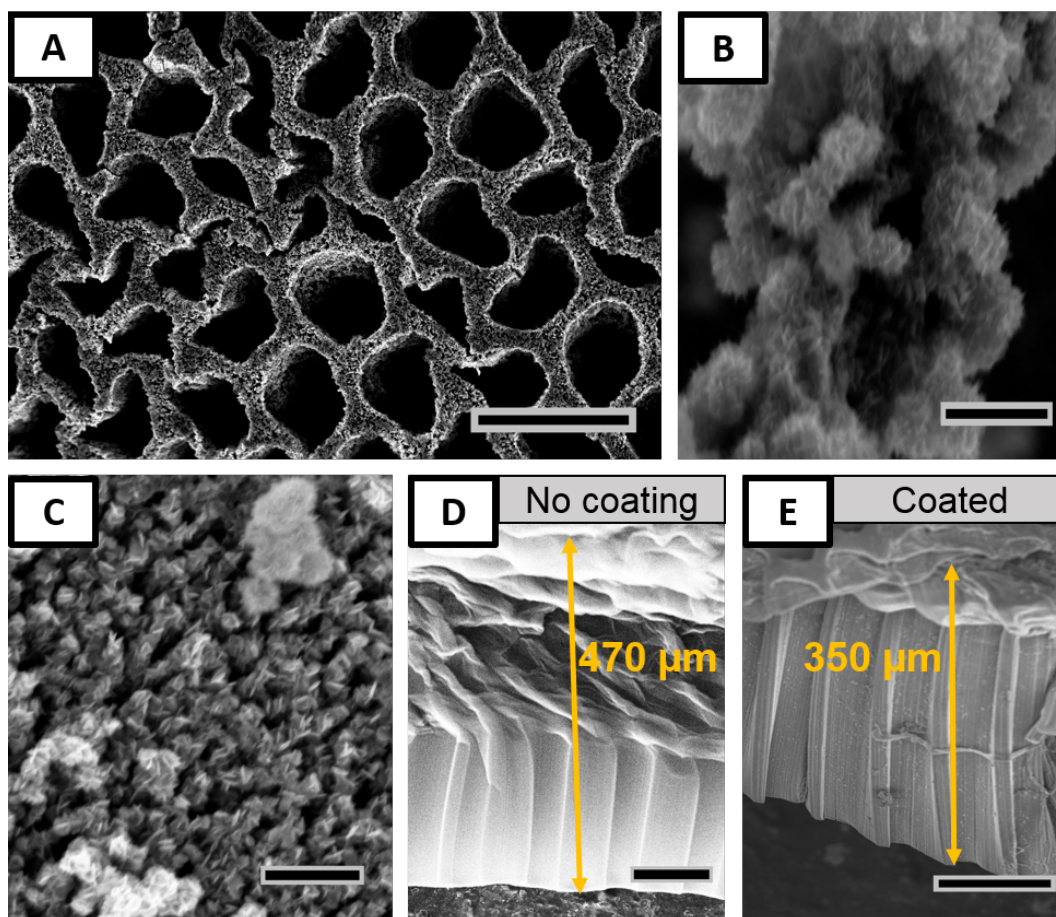


**Fig. 4.20** The densification of the initial structure into a honeycomb-like shape can be seen in (A). A CNT strand (B) and the top surface of the 3D CNT structure (C) show a complete coverage in the  $\alpha\text{-Fe}_2\text{O}_3$  nanoplatelets. The height changes from  $\sim 470\ \mu\text{m}$  before the coating and after the transfer (D) to  $\sim 350\ \mu\text{m}$  after the coating (E). Scale bars are  $50\ \mu\text{m}$  in (A),  $1\ \mu\text{m}$  in (B) and (C), and  $100\ \mu\text{m}$  in (D) and (E).

The initial structure densifies slightly into a more honeycomb-like shape (figure 4.20A). The evaporation of liquid can lead to a slight capillary aggregation, as observed here. The structures do not form very dense honeycombs as reported in the previous chapter, probably due to the fact that the particles nucleating on the CNTs prevent further densification. The dense coverage of a CNT strand in the structure (figure 4.20B), as well as on top of the structure with coated CNT bundles (figure 4.20C) indicates that the synthesis with the used conditions works very well for coating the overall 3D CNT structure with  $\alpha\text{-Fe}_2\text{O}_3$  nanoplatelets (phase determined by XRD in the previous section).

The loss in the overall structure height during the wet chemical synthesis changes from the initial height of  $\sim 470\ \mu\text{m}$  after the transfer onto the PCP film to  $370\ \mu\text{m}$  (figure 4.20). There is some bending on the edges of the structure (figure 4.20E) which makes it hard to determine the real height

## 4 Inorganic Modification of 3D CNT Structures for Lithium-Ion Batteries

in the center of the 3D CNT structure, but manages to give a rough estimation that the structure is at least  $\sim 370 \mu\text{m}$  high, if not higher in the central parts. This means those structures can provide ultra-thick (compared to the standard  $50 \mu\text{m}$ ) battery electrodes. Additionally as seen in 4.19C, it should be kept in mind that the overall area of the structure is not as bent as the edges, thus still showing long, open pores.

**Synthesis on nanoscale 3D CNT structures** When applying the same synthesis method to a  $\sim 100 \mu\text{m}$  high, nanoscale 3D CNT structure transferred onto a PCP film, the structure on the film gets damaged and capillary aggregation densifies the colloidal CNT structure into random pillars, as seen in figure 4.21A. The small pores ( $\sim 450 \text{ nm}$ ) are no longer visible on top of the densified pillars (figure 4.21B). They probably closed during the densification process. The dense nanoplatelet coating on top of those structures and the side walls (figure 4.21C), however, shows that it is not the reaction itself that has failed. Thus, the failure mechanism must be connected to the reaction not happening inside the pores or not stabilizing the structure enough with the coating to resist the complete densification and closing of the pores during drying after the synthesis.

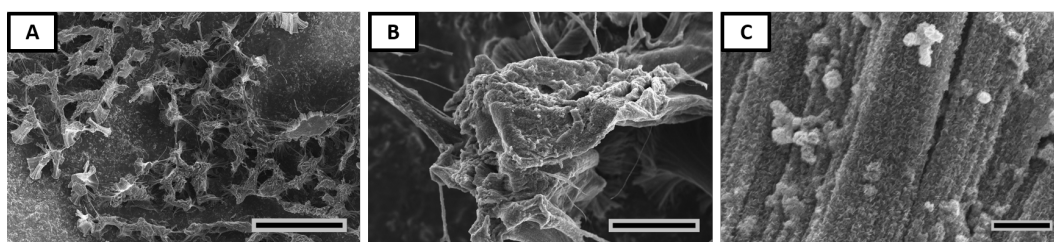


**Fig. 4.21** The densification into pillars after the microwave-assisted, hydrothermal coating of the colloidal structures with iron oxide from  $\text{Fe}^{2+}$  can be seen in (A). The pillars show no nanoscale holes on top of them anymore (B), indicating that these close during the densification process. However, the walls of those structures are fully coated with dense nanoflakes (C). Scale bar is  $200 \mu\text{m}$  in (A),  $20 \mu\text{m}$  in (B) and  $2 \mu\text{m}$  in (C).

The failed coating might be due to the high aspect ratio pores. It could be that the UV-ozone treatment for the activation of the CNTs to enhance the nucleation did not reach all the way into the pores, thus failing to create the right groups for the nucleation on the surface. Similarly, the capillaries might not be completely filled during the synthesis either due to wettability problems or air trapping. Another reason might be that the concentration of the precursor inside the pores is too low to enable a dense coating with the iron oxide nanoflakes. The microscale 3D CNT structures maybe allow for a better diffusion of precursor during the synthesis. For the nanoscale pores, it might be possible that, once the capillary is filled with precursor solution, this liquid stays trapped in there, and when the precursor is used up, no new precursor is supplied.

Overall, for the  $\text{Fe}^{2+}$  precursor, the wet chemical synthesis yields very promising results for the microscale 3D CNT structures, but there are several challenges to overcome if this method is applied to the nanoscale CNT structures.

### 4.3.4.3 Synthesis with $\text{Fe}^{3+}$ as a precursor

For the following synthesis  $\text{Fe}_2(\text{SO}_4)_3 \cdot 5\text{H}_2\text{O}$  containing  $\text{Fe}^{3+}$ -ions has been used as a precursor on high ( $\sim 300 \mu\text{m}$ ) 3D CNT structure and for lower nanoscale structures ( $\sim 100 \mu\text{m}$ ). Similar to the previous synthesis with the  $\text{Fe}^{2+}$  precursor, the reaction time is 6 hours with a UV-ozone activation time of 60 minutes (more details in experimental section) and the reaction is performed on structures transferred onto a PCP film. For a temperature of  $175 \text{ }^\circ\text{C}$ , the pressure is  $\sim 20\text{-}22 \text{ bar}$  (see figure 4.22).

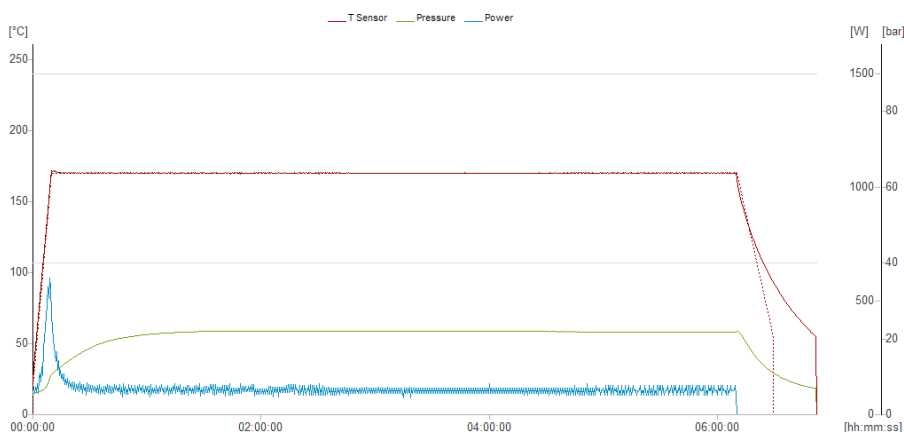


**Fig. 4.22** Monitored temperature, pressure and power graph during the synthesis of  $\text{Fe}_2\text{O}_3$  in the Anton Paar microwave reactor.

**Synthesis on high 3D CNT structures** First, high microscale 3D CNT structures are coated with the hydrothermal microwave-assisted method. The initial 3D CNT structure on the PCP film after the transfer (figure 4.23A) densifies slightly (figure 4.23B) but does not lift it off the film or suffer severe damages (figure 4.23C) during the modification. Thus, large areas can be coated using this method.

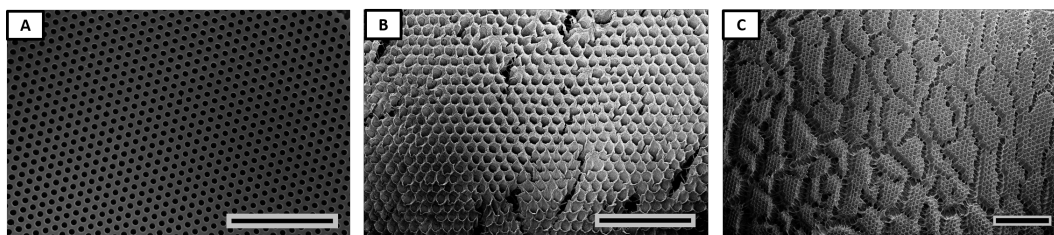


**Fig. 4.23** The microwave-assisted, hydrothermal synthesis is applied to the transferred 3D CNT structure on a PCP film (A). After the synthesis the structure shows some densification into a honeycomb-like structure (B) and a large area coating with a small amount of cracks (C). Scale bars are  $300 \mu\text{m}$ .

The higher magnification images in figure 4.24 show the initial structure with hexagonally ordered holes (A) coated and changed into a honeycomb-like shape (B), as already seen for the synthesis with the other iron-precursor. Dense nanosheets are coating the 3D CNT structure (figure 4.24C). These emerge from the CNT strands (figure 4.24D) and then grow further, surrounded by other

## 4 Inorganic Modification of 3D CNT Structures for Lithium-Ion Batteries

CNTs and thus might be very beneficial for their performance as battery electrodes. It guarantees the connection of the iron oxide with the conductive additive. Using XRD measurements on the collected particles, the iron oxide phase is determined to be hematite ( $\alpha$ -Fe<sub>2</sub>O<sub>3</sub>, ICSD-card 161293) without any other impurities or phases (figure 4.24E). Raman spectroscopy before and after coating (figure 4.24F) shows that the initial D/G ratio for the CNT structure decreases after coating. This can be explained by the fact that the  $\alpha$ -Fe<sub>2</sub>O<sub>3</sub> platelets react with the defect sites on the CNTs, thus decreasing the D/G peak ratio. As expected, the Raman signal after coating also shows several peaks associated to  $\alpha$ -Fe<sub>2</sub>O<sub>3</sub>.<sup>[377,378]</sup>

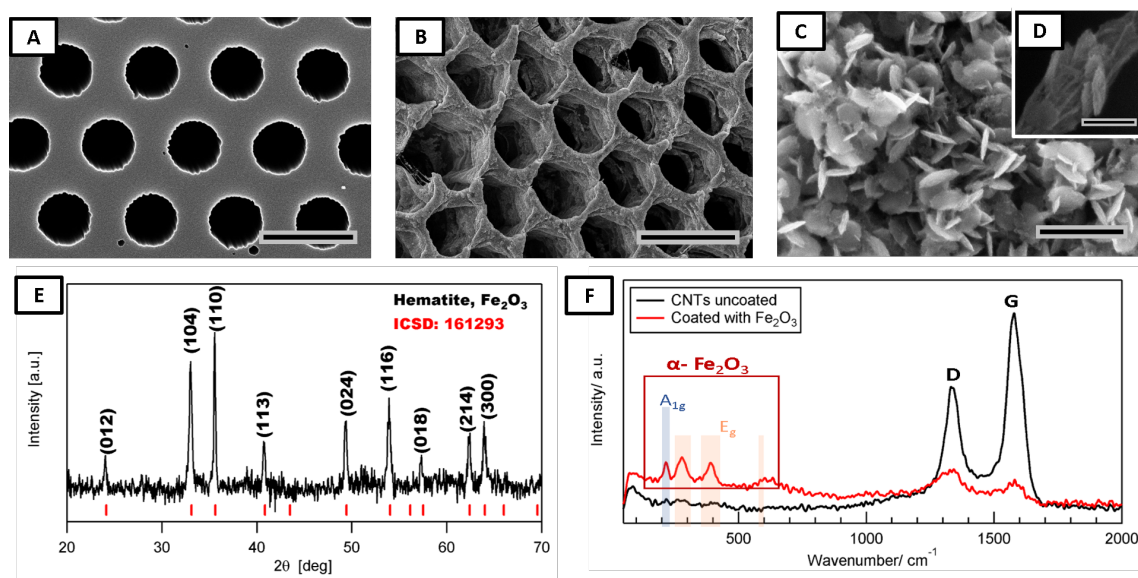


**Fig. 4.24** The initial structure (A) on a PCP film is coated with iron oxide using a microwave-assisted, hydrothermal method. The reaction densifies the circular structure into honeycomb-like pores due to the capillary aggregation (B). The structure is densely coated with iron oxide nanoflakes (C) which emerge from within the CNT strands (D) and are identified as hematite using XRD (E). The emerging hematite peaks can also be clearly seen in the Raman spectrum (F). Scale bars are 30  $\mu$ m in (A) and (B), 1  $\mu$ m in (C) and 200 nm in (D).

While there is some nucleation in solution, the heterogeneous nucleation is clearly favored in this synthesis, leading to a uniform coating on the CNT structure. Hence, this synthesis method works well on the high 3D CNT structures with microscale holes. Additional images of the coating can be seen in figure B10 in appendix B. The next step is coating of the colloidal structures.

**Synthesis on nanoscale 3D CNT structures** As the reaction works very well on the microscale structures, another attempt is made to modify the nanoscale 3D CNT structures of  $\sim$ 100  $\mu$ m height. The nanoscale structure on the film gets damaged, as seen in figure 4.25A and 4.25 B and the same densification into small random pillars (figure 4.25C) as in the synthesis with the other Fe-precursor can be observed. The small pores ( $\sim$  450 nm) are no longer visible on top of the densified pillars, having closed up during the densification process. Additionally, while to top of the structure is coated uniformly the side walls are also only partially coated (figure 4.25D).

### 4.3 Modification of 3D CNT structure with iron oxides ( $\alpha\text{-Fe}_2\text{O}_3$ )

Due to the fact that neither this reaction nor the previous one with another iron precursor have achieved the desired results on the nanoscale structures, a rough estimation is done to see whether the concentration of the Fe-precursor in the nanopores is enough to cover the inside of the pores in flakes. Those calculations assume that the whole pore is filled with precursor liquid and that there is no exchange of the liquid.

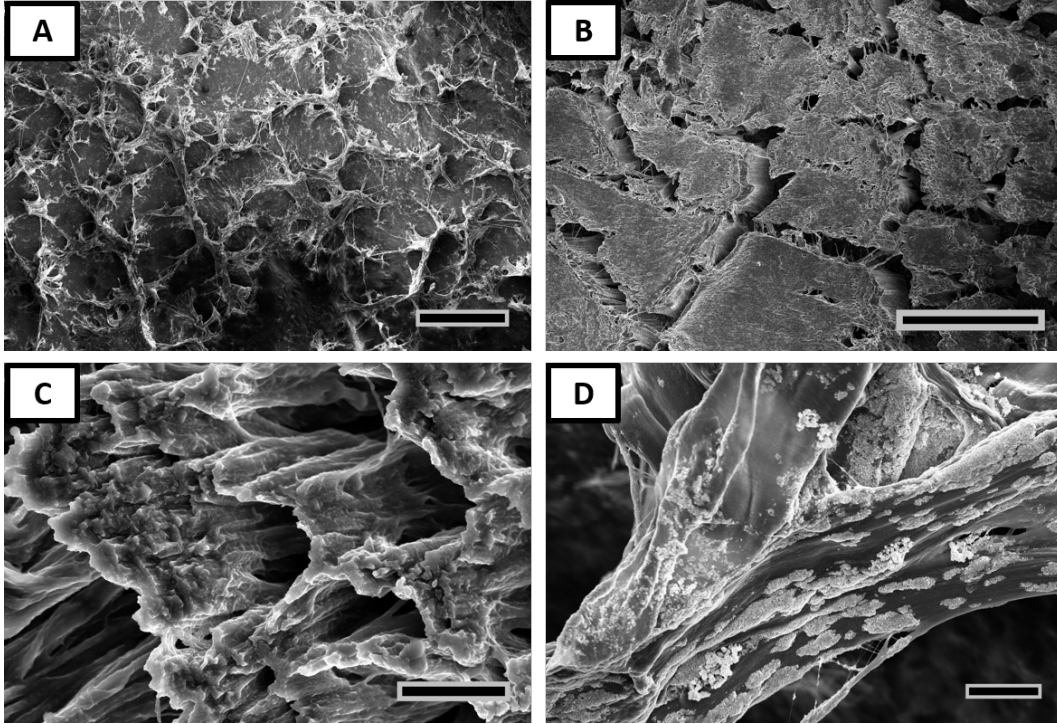


**Fig. 4.25** The initial colloidal structure is damaged during the coating with iron oxide using a microwave-assisted, hydrothermal method (A). The structure densifies into pillars and shows many cracks (B). On top of the pillars, no more nanoscale holes can be seen, indicating that these close during the densification process (C). The coating on the side walls is non-uniform and only in patches (D). Scale bars are 300  $\mu\text{m}$  in (A) and (B), 5  $\mu\text{m}$  in (C) and 10  $\mu\text{m}$  in (D).

The surface area of the inside of a pore is defined as  $A_{pore}$ :  $A_{pore}=2\pi r_{pore}h$ , with  $r$  as the radius of the pore and  $h$  the height of the pore.

The surface area of one of the  $\text{Fe}_2\text{O}_3$ -platelets is defined as  $A_{platelet}$ :  $A_{platelet}=\pi r_{platelet}^2$ , with  $r$  as the radius of the platelet.

The number of  $\text{Fe}_2\text{O}_3$ -platelets needed to cover the entire inside surface of the pores (if lying flat on the inside wall which assumes the minimum amount of platelets needed):

$$N_{platelets} = \frac{A_{pore}}{A_{platelet}} = \frac{2 \cdot r_{pore} \cdot h}{r_{platelet}^2} \quad (4.4)$$

Assuming a thickness of the platelets of  $\sim 20$  nm and a radius of the platelets of  $\sim 60$  nm (from SEM measurements), a pore radius of 225 nm and pore height of 100  $\mu\text{m}$ , the amount of platelets needed to coat the whole area of the pore is 12500.

#### 4 Inorganic Modification of 3D CNT Structures for Lithium-Ion Batteries

The next question is whether there is enough precursor to form this amount of platelets. This means the same mol-amount of  $\text{Fe}^{3+}$  needs to be available in the precursor as needed for the platelets.

The mol-amount of  $\text{Fe}^{3+}$  in one platelet can be calculated using equation 4.5, keeping in mind that the molar ratio of Fe to  $\text{Fe}_2\text{O}_3$  is 2:1 ( $2\text{Fe} + 3\text{O} \rightarrow \text{Fe}_2\text{O}_3$ )

$$n_{\text{Fe}^{3+}} = 2 \cdot \frac{m_{\text{Fe}_2\text{O}_3}}{M_{\text{Fe}_2\text{O}_3}} = 2 \cdot \frac{V_{\text{platelet}} \cdot \rho_{\text{Fe}_2\text{O}_3}}{M_{\text{Fe}_2\text{O}_3}} = 2 \cdot \frac{\pi r_{\text{platelet}}^2 \cdot t \cdot \rho_{\text{Fe}_2\text{O}_3}}{M_{\text{Fe}_2\text{O}_3}} \quad (4.5)$$

The density of  $\text{Fe}_2\text{O}_3$  ( $\rho_{\text{Fe}_2\text{O}_3}$ ) is  $5242 \text{ g l}^{-1}$  and the molecular weight ( $M_{\text{Fe}_2\text{O}_3}$ ) is  $159.69 \text{ g mol}^{-1}$ .

The mol-amount of  $\text{Fe}^{3+}$  in the precursor solution filling the volume of the pore is calculated in equation 4.6. The concentration of  $\text{Fe}^{3+}$  in the precursor solution is  $12.246 \text{ mmol/l}$ .

$$n_{\text{Fe}^{3+}} = c_{\text{Fe}^{3+}} \cdot V_{\text{pore}} = c_{\text{Fe}^{3+}} \cdot \pi r_{\text{pore}}^2 h \quad (4.6)$$

The amount of platelets N that can be produced with the precursor that is present in the nanopore is given by:

$$N_{\text{Fe}_2\text{O}_3\text{-platelets}} = \frac{n_{\text{Fe}^{3+}\text{precursor}}}{n_{\text{Fe}^{3+}\text{platelet}}} = 3.7 \cdot 10^{-5} \quad (4.7)$$

This shows that with the precursor concentration in the pore not even one platelet can be synthesized, thus a dense coating cannot be achieved with the currently used precursor concentration if no diffusion is assumed. The concentration has to be increased significantly, even if the platelets don't grow as large as in the micro-sized pores. This is also always assuming that a uniform coating inside the pore can be achieved and the whole volume is used. The amount of precursor in a microscale pore (following the same equations) would also not be enough to coat the complete pores ( $N=0.26$ ) if there is no diffusion. The fact that a uniform coating can be achieved in the microscale pores proves that this process is dependent on the precursor diffusion into the pores.

Those nanoscale coating issues are a major drawback for a wet chemical synthesis in small pores, which is why an alternative gas phase method is applied on the nanoscale 3D CNT structures for further coatings, as shown in the next section.

#### 4.3.5 Initial electrochemical characterization for $\text{Fe}_2\text{O}_3$

All electrochemical characterization is done by S. Engelke (PhD student in the same group). He operates the potentiostat and assembles the coin cells. The experiments are half-cell measurements with a copper current collector and Li metal as a counter electrode to test the anode performance of our electrodes.

**Electrochemical performance of  $\alpha\text{-Fe}_2\text{O}_3$  with  $\text{Fe}^{3+}$  as a precursor** The microwave-assisted, hydrothermal reaction leads to a uniform coating of dense nanoflakes on the 3D CNT structure.

### 4.3 Modification of 3D CNT structure with iron oxides ( $\alpha\text{-Fe}_2\text{O}_3$ )

Battery measurements of the material were performed on coated 350  $\mu\text{m}$  high structures. The charge-discharge curves at 0.05C (figure 4.26A) have a clear voltage plateau at 0.75 V which agrees with the CV measurements (figure 4.26B, 0.01 mV/s) where the reduction peak in the cathodic sweep can be found around this voltage. This peak corresponds to the conversion of  $\text{Fe}_2\text{O}_3$  into  $\text{Li}_2\text{O}$  in the presence of Li-ions. The other redox current peak in the CV is found at 1.75 V in the anodic sweep, corresponding to the oxidation reaction of Fe to  $\text{Fe}^{3+}$ . The first-cycle discharge capacity is high at  $\sim 1200 \text{ mAhg}^{-1}$  which then decreases to  $\sim 1000 \text{ mAhg}^{-1}$ . This decrease is probably due to the formation of the SEI with CNTs, which is typically high, and nanomaterials and leads to an irreversible capacity loss of about 17%.

Those findings are in agreement with the measurements shown in the published report the  $\alpha\text{-Fe}_2\text{O}_3$ -synthesis is adapted from.<sup>[320]</sup> This verifies that the microwave-assisted, hydrothermal method leads to similarly active material as the classic thermal one and is a promising active material.

For the capacity measurements over time another electrode is used which explains the slightly higher initial capacity due to sample to sample fluctuations. The capacity here remains stable over 50 cycles (figure 4.26C) at about  $900 \text{ mAhg}^{-1}$  (0.2C). Compared to a standard slurry made from the same active material ( $\alpha\text{-Fe}_2\text{O}_3$ ), PVDF as binder and CNTs as the conductive additive (80:10:10) in a standard film, cast at 100  $\mu\text{m}$  thickness, the coated 3D structure shows very little capacity fading, even though it is a  $\sim 5\times$  thicker electrode. Increasing the cycling rate leads to a decrease in capacity (figure 4.26D).

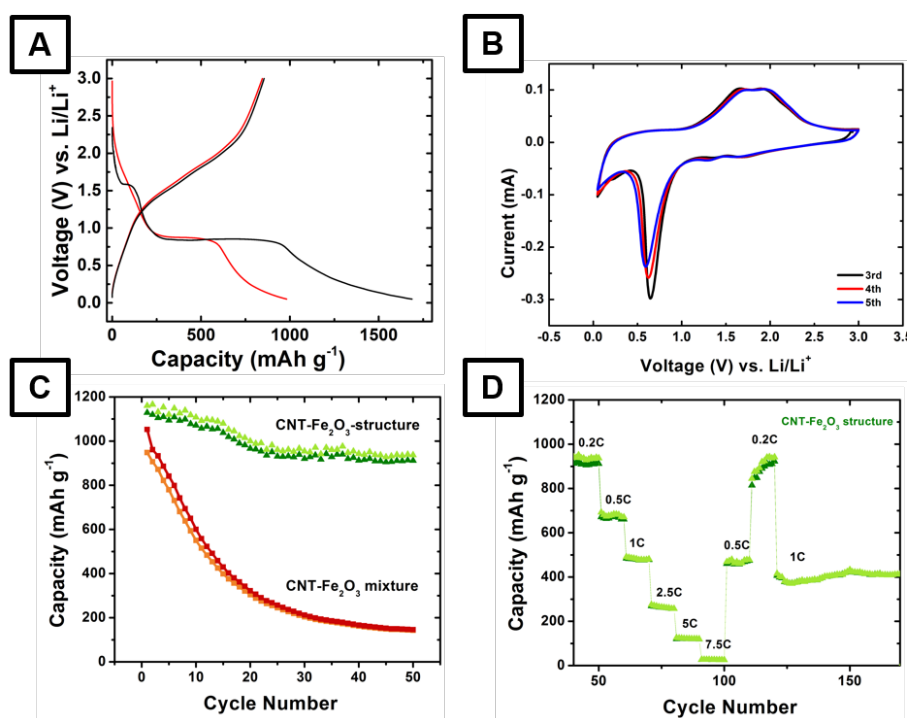


**Fig. 4.26** Electrochemical data of  $\text{Fe}_2\text{O}_3$ -CNT structure with  $\text{Fe}^{3+}$  as a precursor. (A) Charge-discharge curve of the first 2 cycles (0.05C), (B) CV (0.01 mV/s) for the coated 3D CNT-structure with a  $\text{Fe}^{3+}$  reduction peak at 0.75 V and the corresponding oxidation peak at 2.0 V for the 2nd, 3rd and 4th cycle, (C) capacities at 0.2 C over 50 cycles of the coated 3D CNT structure and a slurry made from the same active material and CNTs as conductive additive (cast to 100  $\mu\text{m}$  thickness), and (D) rate performance of the coated 3D CNT structure up to 7.5 C and recovery to 0.2 C.

## 4 Inorganic Modification of 3D CNT Structures for Lithium-Ion Batteries

The rate can be increased to 2.5 C and the capacity of the thick electrode is only slightly lower than the current standard, graphite. When using a 5 C rate, the capacity decreases to around  $110 \text{ mAhg}^{-1}$ . Even after going to 7.5 C, it is possible for the battery to recover to nearly the initial capacity and to keep cycling for over 50 cycles at a stable capacity  $\sim 400 \text{ mAhg}^{-1}$  at 1 C.

The areal loading of the 3D CNT structure is  $0.0100 \text{ mg/mm}^2$  (average of three samples), whereas the one for the standard battery film is  $0.0045 \text{ mg/mm}^2$ . Thus the areal loading was increased by 120% with the advanced electrode structure while keeping a good performance. An effort to create standard films as thick as the suggested electrode structure to increase the loading resulted in a large amount of cracking during drying ( $\sim 300 \text{ }\mu\text{m}$  film, as shown in figure B11 in appendix B) and thus does not provide a suitable route to increase the areal loading.

When the 3D CNT structure electrodes are opened after 40 cycles, the structure is still intact and no damage can be seen by the coin cell fabrication and subsequent cycling (figure 4.27A). Looking closer shows that no  $\text{Fe}_2\text{O}_3$  platelets can be seen anymore. This might be due to some leftover coating with the electrolyte or coverage by the SEI. Another reason could be that during the conversion reaction, the particles have been broken up into even smaller nanoparticles which makes them harder to see at this magnification. The fact that the 3D CNT structure is not affected by multiple cycles is very promising for further experiments with this advanced electrode.

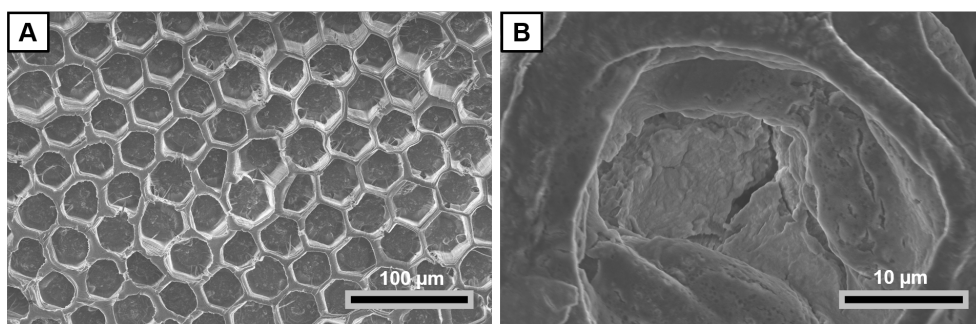


**Fig. 4.27** The coated 3D CNT structure electrode is opened after 40 cycles. The structure is still intact and no damage can be seen overall (A). It is hard to see the  $\text{Fe}_2\text{O}_3$  flakes in the magnified image (B). This might be due to still some coating with the electrolyte or because the particle have broken up into smaller nanoparticles due to the conversion reaction.

**Electrochemical performance of  $\alpha\text{-Fe}_2\text{O}_3$  with  $\text{Fe}^{2+}$  as a precursor** Initial measurements for the  $\alpha\text{-Fe}_2\text{O}_3$  with  $\text{Fe}^{2+}$  as a precursor are performed. There is a large loss in capacity between the first and second cycle (figure 4.28A) from  $\sim 1400 \text{ mAhg}^{-1}$  to  $\sim 800 \text{ mAhg}^{-1}$  in the charge-discharge measurement. The CV (figure 4.28B,  $0.01 \text{ mV/s}$ ) shows the expected  $\text{Fe}^{3+}$  reduction peak at  $0.75 \text{ V}$ , but the corresponding oxidation peak, expected in the anodic sweep just below  $2 \text{ V}$ , is missing. Thus, the formed Fe does not get oxidized again to  $\text{Fe}^{3+}$  and the Li-ions probably stay in the anode as  $\text{Li}_2\text{O}$ . This leads to a failure of the battery, making the capacity drop to below  $20 \text{ mAhg}^{-1}$  after the third cycle (figure 4.28C).

### 4.3 Modification of 3D CNT structure with iron oxides ( $\alpha\text{-Fe}_2\text{O}_3$ )

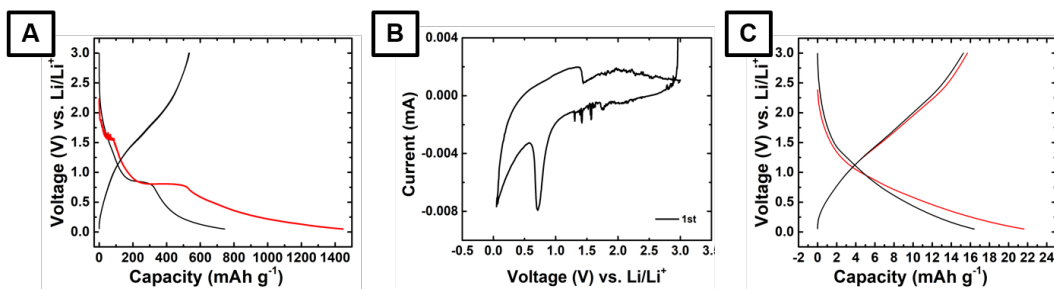


**Fig. 4.28** Electrochemical data of  $\text{Fe}_2\text{O}_3\text{-CNT}$  structure with  $\text{Fe}^{2+}$  as a precursor. (A) Charge-discharge curve of the first 2 cycles (0.05C), (B) CV (0.01 mV/s) for the coated 3D CNT-structure with a  $\text{Fe}^{3+}$  reduction peak at 0.75 V but unfortunately no clear oxidation peak around 2.0 V (as it would be expected), (C) charge-discharge curves for the third and fourth cycle, showing a capacity drop to below  $20 \text{ mAhg}^{-1}$ .

Even though the XRD characterization showed hematite for both precursors at  $175^\circ\text{C}$ , a close comparison of the spectra (figure 4.29) shows that the intensity of the peaks is not exactly the same, indicating that using  $\text{Fe}^{2+}$  as a precursor might require a higher temperature (spectra at  $190^\circ\text{C}$  are more similar). Less crystalline hematite might be the reason for the electrode failure. Another one could be a change in surface area due to the slightly different shape of the particles and thus an influence on the SEI formation. All the XRD patterns are measured on powders produced with the same reaction conditions, but not on the coated CNT structures themselves, as no signal could be measured from them due to the very thin coating. This means that there could be a change in phase/material on the CNT structure. Additionally, the particles might not be well enough adhered to the 3D CNT structure, thus detaching during cycling and losing their electrical conductivity which might influence the battery performance significantly.

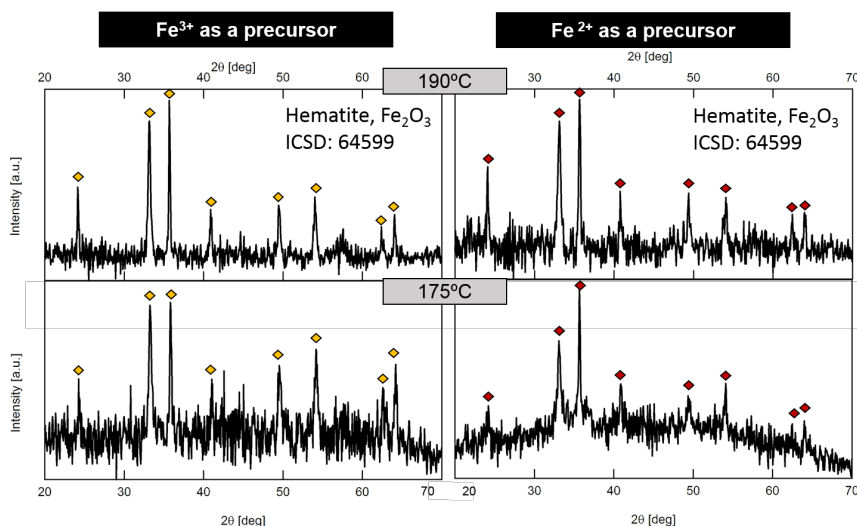


**Fig. 4.29** A comparison of the XRD patterns for reactions at  $175^\circ\text{C}$  and  $190^\circ\text{C}$  for both precursors is shown here. It can be seen that at  $190^\circ\text{C}$  the two materials are exactly the same whereas at  $175^\circ\text{C}$  the intensity of the peaks slightly varies. It seems that the  $\text{Fe}^{2+}$  precursor might need a slightly higher temperature to form more crystalline  $\text{Fe}_2\text{O}_3$ .

### 4.3.6 Conclusion

Overall, we used advanced 3D CNT collector electrodes here in combination with microcontact printing onto a thin conductive film as a binder for an increased areal loading. The 3D CNT structure is coated with  $\alpha\text{-Fe}_2\text{O}_3$  using microwave-assisted, hydrothermal synthesis for the first time successfully on patterned CNT forests to create carbon-metal oxide hybrids. This is a versatile method that opens up a new range of materials that can now be used to modify aligned CNT structures while decreasing the reaction time and potentially avoiding the high temperature annealing step. With this hybrid structure is possible to enhance the areal loading of the electrode by 120% while keeping a good long-term stability equal to standard electrode films and a higher rate capability compared to the standard films. It is also possible to retain the electrode structure, as shown in post mortem images of the battery, making this a promising electrode architecture.

## 4.4 Modification of the nanoscale 3D CNT structure with silicon

As the wet chemical synthesis route was unsuccessful for the coating of the nanoscale 3D CNT structures, another approach is chosen. Gas phase modification has been proven to work for CNT forests and other structures. Thus a gas phase modification is done with silicon as a very promising high capacity anode material for the colloidal structures.

### 4.4.1 Fabrication process of the nanoscale 3D CNT structure with silicon

Combining a gas-phase Si-coating process with the nanoscale 3D CNT structure, as discussed above, will lead to the possibility of thicker, high capacity LIB electrodes that are not limited by diffusion. The nanoscale pores not only support the Li-ion diffusion, but also enable a good coating throughout the thickness, as the coating of unpatterned forests has been proven hard throughout the whole thickness. A schematic overview of the preparation process can be seen in figure 4.30. For the Si-coated structures, colloidal templates with hole sizes of 450 nm are created (1), as explained earlier in section 1.4.2. Those are then grown using an atmospheric pressure CVD to a height of  $\sim 150 \mu\text{m}$  (2) to make sure that there is no collapse of the CNT forest structure close to the bottom as reported before in section 3.3 (figure 3.14c). The grown 3D CNT structure with nanoscale holes is then coated with silicon using either a CVD or a PVD method (see further). The SEM shows a coating using thermal CVD (3).

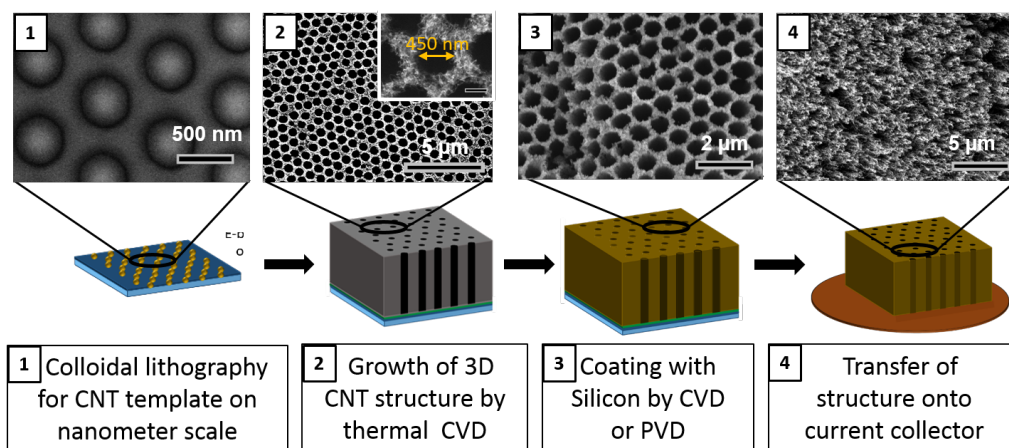


**Fig. 4.30** The figure shows the four steps for the fabrication of a Si-CNT electrode. First the template is created using colloidal lithography (1), which is then grown by thermal CVD into a 3D CNT structure with holes of about 450 nm (2). This structure is coated with silicon using a CVD or PVD process (3) and afterwards transferred onto a current collector which in this case is copper tape. The adhesive on the copper tape is carbonized after the transfer using a temperature treatment (4). The order of step 3 and 4 can be changed depending on the modification conditions. Scale bar in the inset in (2) is 300 nm.

The coated structure is then transferred onto a current collector (4). Instead of using the conductive polymer film (PCP) reported earlier, copper tape is used. While PCP is the better choice for the conductivity and binder function, Cu tape is used for its easier transfer due to the increased stickiness

## 4 Inorganic Modification of 3D CNT Structures for Lithium-Ion Batteries

of the adhesive on the tape. This, however, introduces a temperature treatment step after the transfer to carbonize the adhesive. The carbonized adhesive is possibly not giving as good of an electrical contact throughout. However, it was not possible to achieve the transfer onto a PCP film as the adhesion of the structure after the Si-coating is very high, thus the measurements are done with carbonized Cu tape as a current collector. The order of step 3 and 4 can be changed depending on the modification conditions and requirements.

For the coating of the colloidal CNT structure two gas phase methods are tried. The first one is coating by a thermal CVD method with two different coating times, the second one a coating by PVD. The crucial parameters for the evaluation of the coating afterwards in both cases are the transfer ability onto the Cu-tape and the amount of oxygen in the Si-coating to ensure there is not too much SiO<sub>2</sub> present rather than Si.

### 4.4.2 Thermal CVD-process for Si-deposition

A thermal CVD process using SiH<sub>4</sub> as a precursor in an argon atmosphere is used to coat the nanoscale 3D CNT structures.

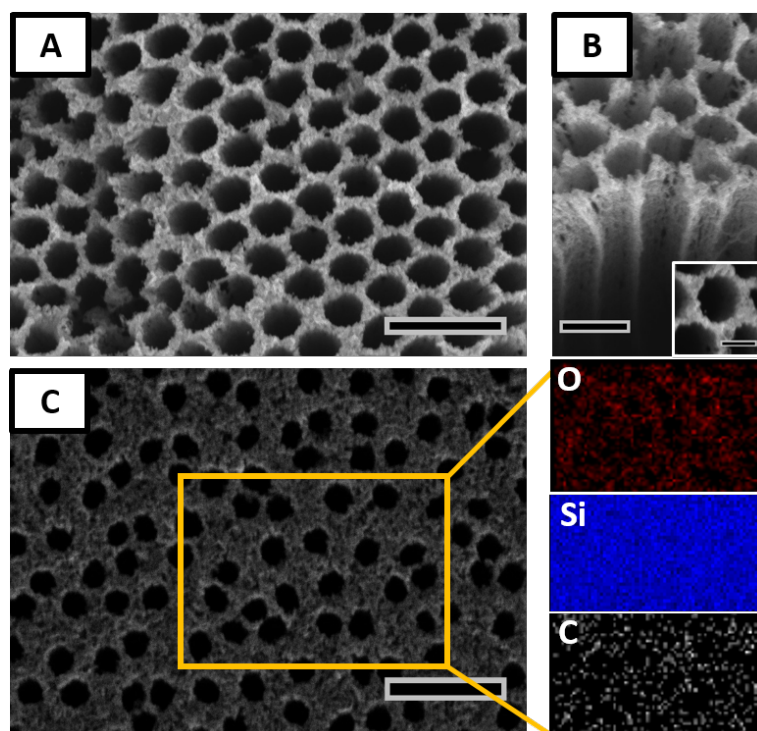


**Fig. 4.31** The coating of a nanoscale 3D CNT structure with Si from a thermal CVD process is shown in (A). A tilted image of the side walls can be seen in (B). The SEM image in (C) shows another sample (with less dense holes) where EDX mapping is done on top of the structure. The colloidal structure is covered in silicon, with carbon (CNTs) and oxygen (potentially a thin oxide layer) as the other two detected elements. Scale bars are 2  $\mu\text{m}$  in (A), 1  $\mu\text{m}$  in (B) and 500 nm in the inset, and 2  $\mu\text{m}$  in (C).

The coating of the samples is done with the help of Yanting Jin, a PhD student in the Department of Chemistry who used a process initially reported by Ogata et al.<sup>[231]</sup> from their group and then by Y.

#### 4.4 Modification of the nanoscale 3D CNT structure with silicon

Jin herself<sup>[232]</sup> for the formation of Si-nanowires. The deposition is run at 550 °C for 15 minutes with the colloidal structure on a Si-wafer (more details in experimental section).

This results in a uniform coating (figure 4.31A), also on the side walls (figure 4.31B). The holes are still visible in the inset in figure 4.31B. To prove that there is silicon on the structure, another sample (with a little less regular holes) is analyzed using EDX mapping (figure 4.31C). The whole top of the sample is coated with silicon, the other two detected elements being carbon (from the CNTs) and oxygen (there might be a small oxide layer on the Si).

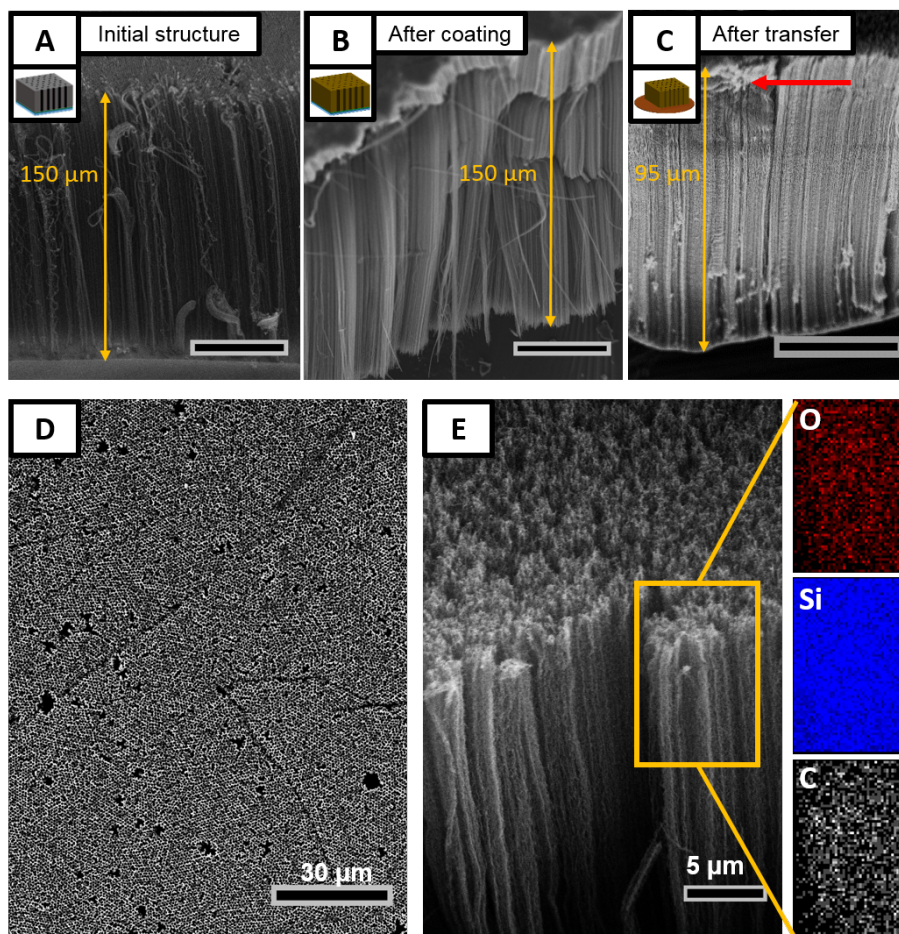


**Fig. 4.32** While only a small change in height from 150 μm (A) to 145 μm (B) is seen during the modification, the transfer decreases the height of the coated 3D CNT structure to about 2/3 (C). An overview of the coated area is shown in image (D) and the EDX mapping (E) for the initial bottom of the structure (after transfer now the top) shows oxygen, carbon and silicon, thus proving that there is a silicon coating all the way through the structure to the bottom during modification. Scale bars are 50 μm if not otherwise indicated.

The structure is then transferred onto a copper tape as the current collector for electrochemical characterization. The height change during the process is shown in figure 4.32 A-C and an overview image of the uniformly, nearly defect-free coated area before transfer is shown in figure 4.32D. Initially the nanoscale 3D CNT structure is 150 μm high (figure 4.32A). After the coating the height doesn't change (figure 4.32B). After the transfer onto the copper tape, the sample is about 2/3 of the initial height (figure 4.32C) which can be explained by the pressure applied during the transfer and

## 4 Inorganic Modification of 3D CNT Structures for Lithium-Ion Batteries

subsequent buckling of the CNT forest, as reported earlier. This buckling can be seen at the top left of the CNT forest (figure 4.32C, indicated by the red arrow).

This also indicated that the coating there might be thinner than on the initial top of the structure. A coating gradient on the Si-sample is not surprising given the small pores of the structure. To ensure the coating has reached through the pores all the way to the bottom of the structure, EDX mapping is done after the transfer at the top (which previously was the bottom), as seen in figure 4.32E. Oxygen, silicon and carbon are the detected elements, thus proving that there is still a silicon coating on the colloidal structure. This gives a first indication that the coating method is good enough to coat the structure all the way through the small pores.

To ensure that the carbonization step does not significantly change the composition of the active material, the percentage of the oxide compared to the silicon is evaluated before and after carbonization in inert atmosphere at 500 °C. EDX data as an average of three measurements is taken before the carbonization and after the carbonization on top of the sample. The results in table 4.2 show that the percentage of oxygen is relatively low, ensuring that the sample is coated mostly with silicon. After the carbonization step, the oxygen content increases slightly but not much.

**Table 4.2** The table shows the atomic percentages of oxygen and silicon on the sample before and after the carbonization step. A slight increase in the oxygen levels can be seen but it is still lower than 15% which indicated that there is mostly pure Si rather than SiO<sub>2</sub>

Atomic%	Before carbonization	After carbonization	
		Top	bottom
Si	94.88	88.31	85.56
O	5.12	11.69	14.45

An EDX mapping of the bottom after the transfer is shown in figure B12 in appendix B. The element maps clearly show the presence of copper in addition to Si, C and O after the transfer onto the Cu-tape.

**Increase in coating thickness** The coating on the colloidal CNT structure appears to be very thin, especially at the bottom of the structure on the Si-wafer. To achieve an increased mass loading on the same surface area, the coating time is doubled. Thus a thicker coating is achieved on the colloidal structure (figure 4.33A and 4.33B). The pores are still open which means there might be space for a further increase in thickness. The view of the side walls (figure 4.33C) shows a continuous thick coating. However, when the transfer is attempted, the structure is stuck on the wafer. The adhesion of the 3D CNT structure to the Si-wafer is significantly improved by the thicker coating, making it impossible to get the structure transferred onto the Cu-tape. Even larger weights of 50 g and higher temperatures (150 °C and 200 °C) during the transfer are not enough to change the adhesion. It was also tried to get the structure off the wafer by using a razorblade, but it didn't work.

Nevertheless, it was managed to isolate a strand of coated CNTs with a length of about 110 μm structure with the razor blade which made it possible to analyze the coating on both sides (figure

4.33D). It was not clear which part of this strand was on the top and bottom of the initial structure but both side show very good Si-coating (insets next to D), indicating that those conditions lead to a good coating through the pore structure, if the transfer could be done.

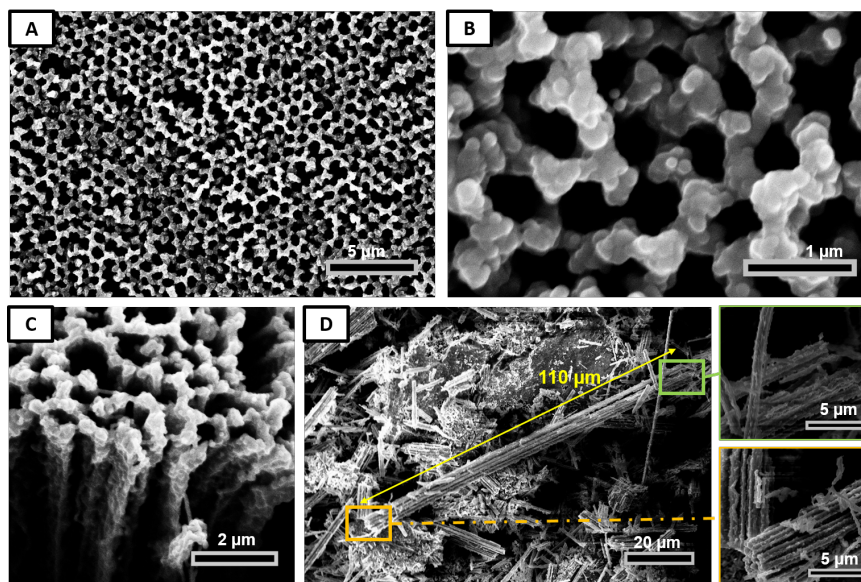


**Fig. 4.33** A thicker coating by an increase in coating time on the 3D CNT structure with nanoscale pores can be seen in (A)-(C). The transfer of this coated structure is attempted but it leads to breaking and incomplete transfer of it onto the Cu-tape (D). The adhesion to the substrate has significantly increased during the longer coating time. The long, coated CNT strand with the two higher magnification images at the top and bottom of the strand indicates that a good coating all the way through the pores could be achieved.

**Challenges** A very well coated sample cannot be transferred onto Cu-tape as a current collector. A transfer before the coating is also not possible with this thermal CVD system, as no copper tape is allowed in the coating operating system, as it is feared that impurities might be introduced. If a transfer before the coating cannot be done, the thicker Si-coating cannot be used for further characterization as electrodes, even though it would be of interest due to the higher active material loading.

### 4.4.3 PVD-process for Si-deposition

Thus, further samples are coated in a different system with the help of Jordi Cools at imec in Leuven. Our samples are coated using their PVD system and then sent back to us. The advantage of their coating system is that the 3D CNT structure can be transferred onto the Cu-tape before the modification. This makes it possible to get thicker coating onto the structure without having to balance it with the adhesion of the structure to the initial Si-substrate.

The first coatings are done on microscale 3D CNT structures, as they are easier to make than the nanoscale ones and work well for first tests. A coated 3D CNT structure is shown in figure 4.34A. Single CNT strands are still distinguishable, indicating that the coating might be very thin and could probably be increased in further runs (figure 4.34B).

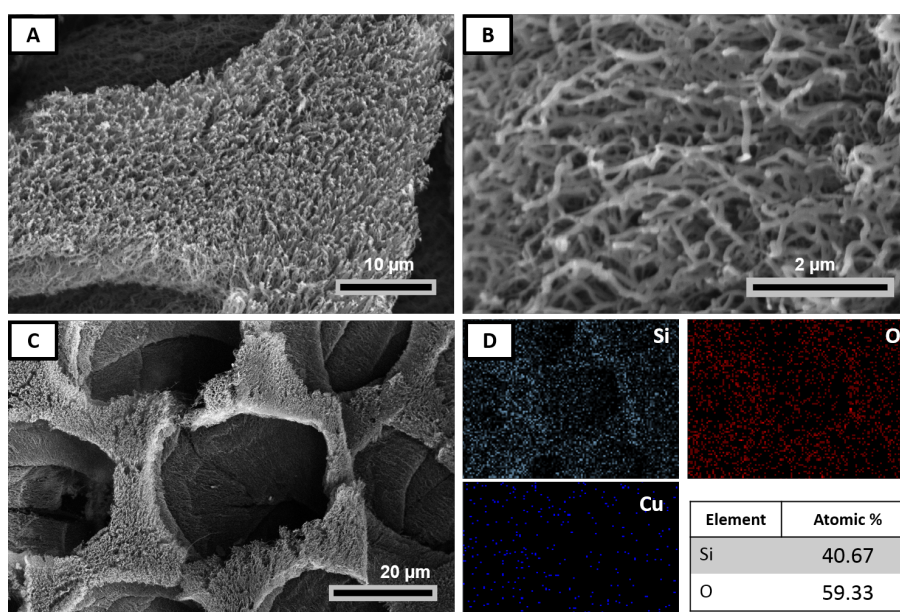


**Fig. 4.34** The SEM images show a coating on the 3D CNT structure with microscale holes in (A), (B) and (C). EDX mapping is shown in (D) with carbon, Si, O, and Cu from the copper tape as the detected elements. A quantitative EDX analysis of the atomic percentages shows that there is a higher amount of oxygen than silicon which could mean that it is mostly  $\text{SiO}_2$ .

The SEM of the coated structure with EDX mapping is shown in figure 4.34C and D. The elements seen in the mapping in addition to carbon are Si, O and Cu (from the tape). A quantitative analysis of the Si and O percentages using EDX shows that the O-content with this method is significantly higher than in the previously reported one (the measurements are averages of three spots on three different samples). This means that either most of the silicon is actually  $\text{SiO}_2$  or some of the copper foil has oxidized and the signal of that is adding to the sample. It might also be a combination of both.

Further investigation of the exact composition of the coating needs to be done to determine where the large atomic percentage of oxygen comes from. As the electrochemical performance is the critical parameter for the evaluation of the whole fabrication process, the fabricated samples are made into half-cells for further electrochemical characterization, before any further analysis is done.

## 4.4.4 Initial electrochemical characterization for silicon

Also on this project, the electrochemical characterization is done by S. Engelke. The anode materials are measured in half-cell configuration with Li-metal as counter electrodes with  $\text{LiPF}_6$  in EMC and DEC as electrolyte and a glass fibre disc as separator.

## 4.4.4.1 CVD-Si coating for nanoscale 3D CNT structures

The nanoscale 3D CNT structure coated with thermal CVD (as reported before) and transferred onto copper tape as a current collector shows a  $\sim 33\%$  decrease in capacity during the initial charge/discharge cycles. This probably corresponds to the SEI formation of the sample.

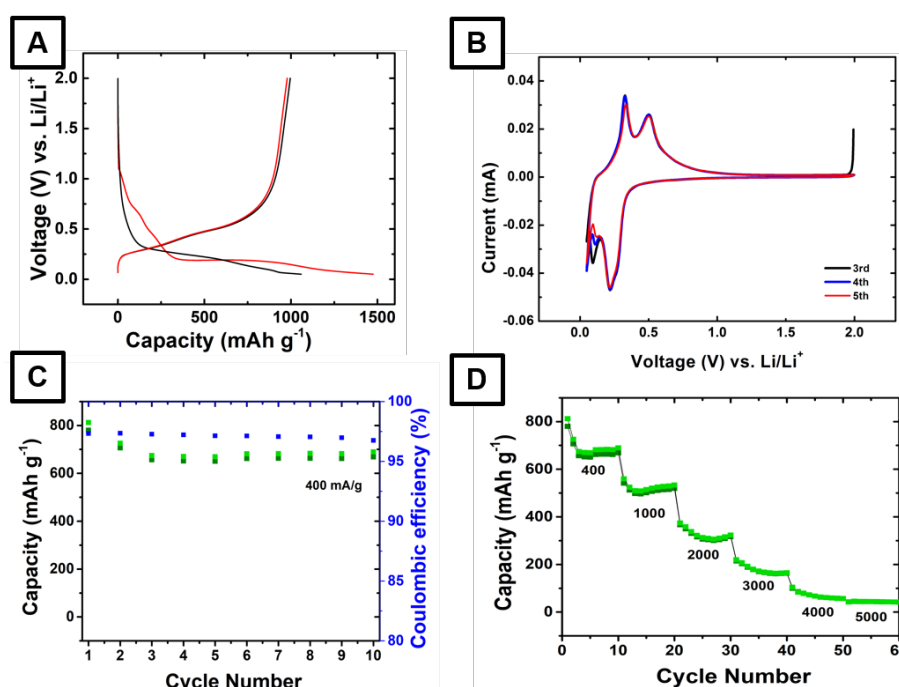


**Fig. 4.35** Electrochemical characterization of a nanoscale 3D CNT structure with CVD-grown Si: (A) Charge/ discharge curve of the first two cycles, (B) CV (0.01 mV/s) with peaks corresponding to the (de)lithiation of amorphous silicon, (C) Capacity and coulombic efficiency over 10 cycles at 400  $\text{mA g}^{-1}$  and (D) Rate performance of nanoscale 3D CNT structure with Si with 100  $\text{mA g}^{-1}$ , 400  $\text{mA g}^{-1}$ , 1000  $\text{mA g}^{-1}$ , 2000  $\text{mA g}^{-1}$ , 3000  $\text{mA g}^{-1}$ , 4000  $\text{mA g}^{-1}$  and 5000  $\text{mA g}^{-1}$ .

All the data presented here is from one cycled electrode. The weight of the electrode could not be determined as exact as necessary, as balanced was used that wasn't precise enough. The weight is between 0.2 mg and 0.3 mg. The higher loading is assumed here to account find the minimum achieved rate. The maximum specific capacity values (with the lower loading) would be around 2200  $\text{mAh g}^{-1}$  for the first cycle and 1500  $\text{mAh g}^{-1}$  for the second cycle if 0.2 mg was assumed. This experiment will be repeated as soon as the CVD-coating system is fixed to gain more insight into the definite value of the specific capacity. Nevertheless, conclusions about the stability, crystallinity and rate of the material can already be made.

## 4 Inorganic Modification of 3D CNT Structures for Lithium-Ion Batteries

---

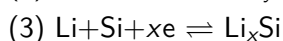
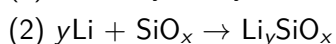
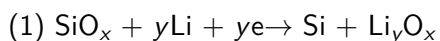
The CV curve for the coated 3D-CNT structure with silicon as an anode material shows two sharp peaks during lithiation (figure 4.35B, 0.01 mV/s). The first can be assigned to the high voltage lithiation of amorphous silicon at  $\sim 0.25$  V and the second peak to the low-voltage lithiation of amorphous silicon near 0 V. During the delithiation process, two peaks corresponding to the sequential extraction of the Li-ions ( $a\text{-Li}_{x'+x''}\text{Si} \rightarrow a\text{-Li}_{x'}\text{Si} + x''\text{Li} \rightarrow a\text{-Si}+x'\text{Li}$ ) are found at 0.3 V and 0.5 V. The shape of this curve is consistent with previous reports of amorphous silicon.<sup>[307,358,379]</sup> This is slightly different from the data reported by Jin et al.<sup>[232]</sup> They used the same process, however, on a Au-substrate which led to crystalline silicon, whereas the Si on the 3D CNT structure seems to be amorphous, as reported for Si coatings on CNTs before.<sup>[307,358]</sup>

The capacity over 10 cycles remains stable at  $\sim 650$  mAhg<sup>-1</sup> with a coulombic efficiency about 97% (figure 4.35C). Cycling at higher rates slowly decreases the capacity; at a rate of 5000 mA g<sup>-1</sup> nearly all capacity is gone (figure 4.35D). However, it remains to be seen whether it is completely reversible when decreasing the rate again, thus not damaging the structure.

### 4.4.4.2 PVD-Si coating for microscale 3D CNT structures

The electrochemical performance of microscale 3D CNT structures coated with PVD-Si is evaluated here. The CV looks significantly different from the previously shown one for amorphous Si. This supports the assumption from the EDX-measurements that the coating is mostly SiO<sub>2</sub>.

The charge/ discharge curve (figure 4.36A) shows a significant decrease in capacity on the first cycle discharge ( $\sim 4400$  mAhg<sup>-1</sup>) to the second discharge ( $\sim 1000$  mAhg<sup>-1</sup>) due to a large SEI formation and the formation of electrochemically inactive and thermodynamically stable lithiumsulfate in the SiO<sub>2</sub>. The reactions during the lithiation of SiO<sub>2</sub> are the following:<sup>[380]</sup>



As the Si-phase sometimes increases with time in this material, an increase in capacity can often be seen.<sup>[380]</sup> Another reason for the observed decrease in capacity could be due to delamination of the structure from the Cu film.

In the CV (figure 4.36B, 0.01 mV/s), the cathodic sweep shows multiple peaks in the first cycle, one at 1.4 V which is attributed to the beginning of the SEI formation due to reactions between the electrode and electrolyte, and one broader peak at  $\sim 0.40$  V where further SEI formation and decomposition of the electrolyte occurs.<sup>[380]</sup>

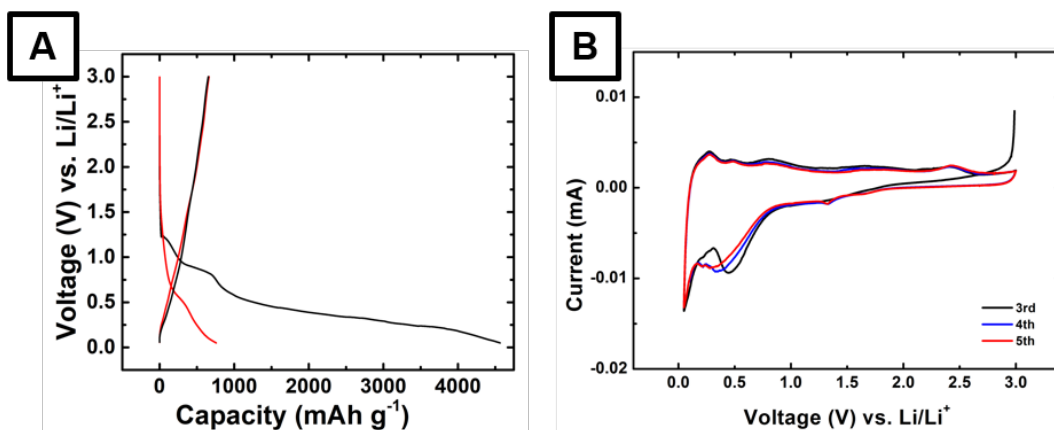


**Fig. 4.36** Electrochemical characterization of a microscale 3D CNT structure with PVD-grown Si: (A) Charge/ discharge curve of the first two cycles and (B) CV (0.01 mV/s) with peaks corresponding to the (de)lithiation of  $\text{SiO}_2$ .

The small peak at 0.25 V corresponds to the formation of lithiumsilitates and Si from the  $\text{SiO}_2$ , whereas the one at around 0 V is the alloying reaction of Si. In the anodic sweep, the reactions at about 0.34 V and 0.4 V can be attributed to the de-alloying of Si from two different reversible lithiumsilitates formed.<sup>[381]</sup> Those findings are in agreement with other reports published on  $\text{SiO}_2$  as a battery material.<sup>[380–382]</sup>

The electrochemical characterization shows that the material is not Si but rather  $\text{SiO}_2$  which was already suspected with the large measured oxygen content in the EDX spectra. Thus it exhibits a lower capacity than expected. Nevertheless, it might be a promising alternative for thick batteries as this capacity can be nearly three times as high as graphite.

#### 4.4.5 Conclusion

The 3D CNT structure with nanoscale holes was fabricated in a novel way using colloidal lithography and then coated with the high specific capacity anode material silicon by CVD and with  $\text{SiO}_2$  by a PVD process. Those gas phase processes enable a coating without destruction of the aligned structure and potentially uniformly throughout the pores.

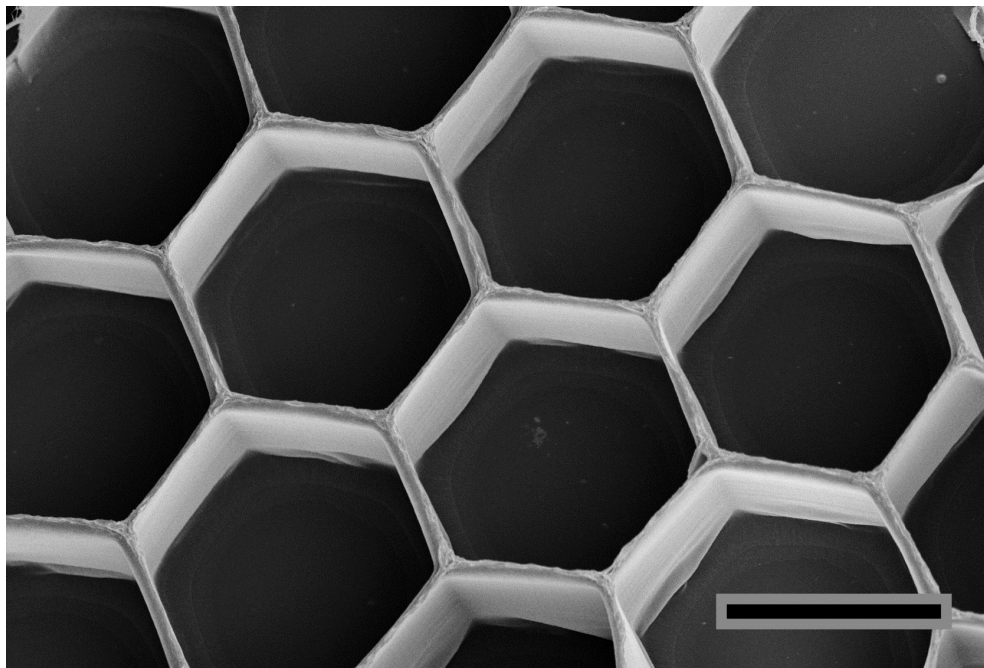
The thickness of the overall electrode structure is significantly higher than previously reported hybrid structures. It is 5x higher than the reported Si-hybrid structures by Wang et al.<sup>[368]</sup> (20  $\mu\text{m}$ ) and 50 times higher than the one reported by Fan et al.<sup>[383]</sup> (2  $\mu\text{m}$ ). Despite the increased thickness it is possible to achieve a stable capacity and a good high rate performance for the Si-hybrid structure. Our capacity is lower than the reported ones; however, as mentioned earlier, this might be due to weighing errors.

For the  $\text{SiO}_2$  coating the capacity is around  $900 \text{ mAhg}^{-1}$  after the initial SEI formation which is promising for the material and compares well to the capacity found for hollow  $\text{SiO}_2$  nanocubes<sup>[382]</sup> and nanotubes.<sup>[380]</sup> The stability of the capacity is currently investigated to gain further insight into the promise of this electrode composition.



## Chapter 5

# Inorganic Modification of CNT Honeycomb Structures for Watersplitting



CNT honeycombs coated with BiVO<sub>4</sub>, scale bar 30  $\mu\text{m}$ .

Results in this chapter were achieved in collaboration with Dr. J. Rongé (KU Leuven).

## 5.1 Introduction to solar watersplitting

With the current drive for more sustainable energy sources and reduction in CO<sub>2</sub> emissions, a suitable feedstock for synthetic renewable fuels needs to be found. As water is cheap, abundant and non-toxic, it is very promising for gaining clean energy from its hydrolysis, generating H<sub>2</sub> as a fuel.<sup>[384]</sup> The generation of hydrogen can be split into two steps: (i) the oxidation of two water molecules to form O<sub>2</sub> and protons, and (ii) the subsequent reduction of protons to molecular H<sub>2</sub>. While photovoltaics (PV) present a way of converting solar energy into electricity, when thinking about efficient storage, electricity is not the most efficient and convenient way to do so. Storing energy in the chemical bonds of fuel molecules, such as hydrogen, is more efficient. A Ragone plot in figure 5.2 compares fuel cells to batteries and supercapacitors, clearly showing the high-energy capability of fuel cells.<sup>[385]</sup>

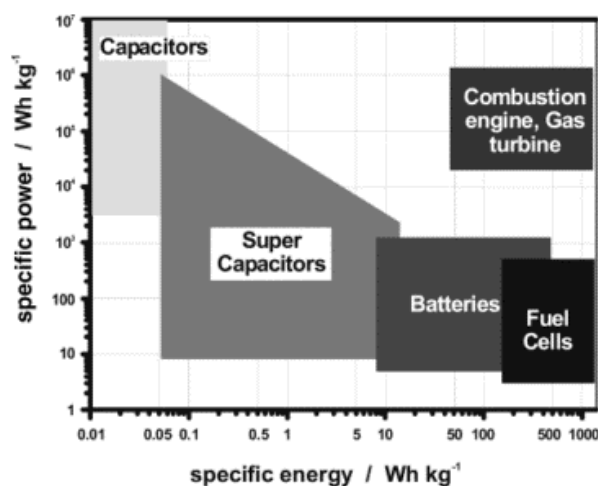


**Fig. 5.2** A comparison of the energy and power densities of batteries, supercapacitors and fuel cells.<sup>[385]</sup>

Currently produced hydrogen, however, is expensive due to material costs in the process, such as expensive electrolysers i.e. noble metals.<sup>[386]</sup> Thus, the production of solar hydrogen by means of the photo electrochemical (PEC) splitting of water has gained much scientific attention, trying to enhance efficiency and reduce costs. Water oxidation is the hardest step for watersplitting. This step is needed to produce the protons that then can be used for the CO<sub>2</sub> reduction and for providing the electrons in the proton reduction half reactions.<sup>[66,67]</sup> This makes water oxidation a crucial step on the way to use CO<sub>2</sub> as a feedstock for renewable fuels.

To achieve an improved water oxidation, PV systems have been successfully coupled to water electrolysis to achieve hydrogen production of up to around 18% efficiency.<sup>[387]</sup> One step further towards higher efficiency and lower costs is by creating one single system that combines light harvesting and water splitting components. This system is called a photo electrochemical (PEC) cell. A schematic of a full PEC cell in figure 5.3 with the photoanode, photocathode and the reactions on each of them indicated, shows how the reactions are linked and fuel can be gained from watersplitting and CO<sub>2</sub> reduction.<sup>[384]</sup>

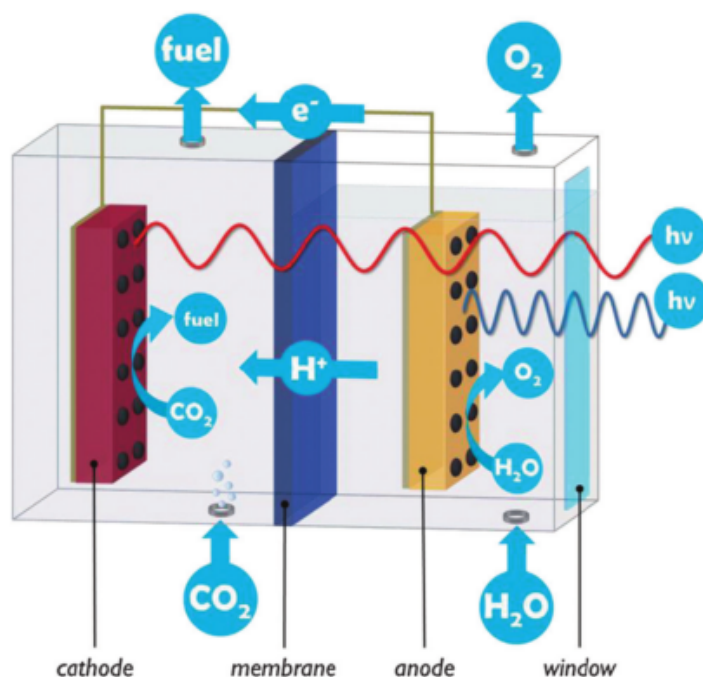


**Fig. 5.3** Schematic of a liquid-phase, two-compartment PEC cell with photoanode, photocathode and proton exchange membrane. Incident light pathways, reactive species and reagents are also shown. <sup>[384]</sup>

The photoelectrode often consists of a semiconductor. This semiconductor needs to absorb efficiently in the visible region and have a good conductivity to transport the resulting charges. <sup>[384]</sup> Such a system was first proposed by Fujishima and Honda in 1972 <sup>[388]</sup> when they reported the watersplitting properties of a  $\text{TiO}_2$  photoelectrode. The process for photo electrochemical watersplitting begins with the absorption of incident photon which creates electron-hole pairs in the absorbing material, e.g. the mentioned semiconductor material, such as  $\text{TiO}_2$ . The holes drive the oxygen evolution reaction on the one side while the electrons are consumed by the hydrogen evolution reaction at a separate electrode or surface. <sup>[384,387]</sup> A lot of effort was put into the investigation of semiconductors for solar hydrogen formation and the development of the a fitting photocatalyst with high efficiency and low-cost. Especially in the last decade, the focus shifted to earth-abundant materials with higher efficiency and better cost-effectiveness. <sup>[384]</sup> Those materials have a range of requirements that need to be kept in mind during the selection. They must have a suitable band gap for light absorption, long term stability in an aqueous environment, as well as low cost and material availability. <sup>[387]</sup>

Many inorganic semiconductors show high stability and acceptable efficiency and thus are promising light harvesting materials. As mentioned, the band gap must be suitable for light absorption. A band gap specifies the energy difference between the valence band and the conduction band. When a photon is absorbed, an electron is excited from the valence band to the conduction band. This can only happen if the energy of the incident photon is high enough. An overview of the bandgap positions of a range of semiconductors can be seen in figure 5.4.

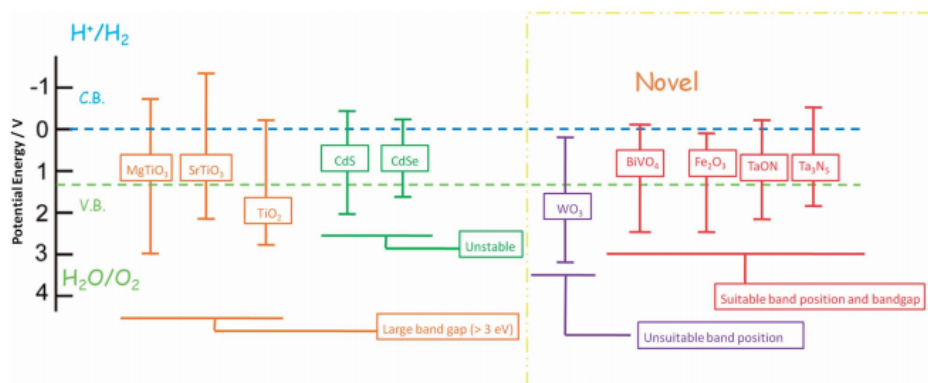


**Fig. 5.4** Schematic illustration of bandgap positions of several semiconductor photocatalysts. [389]

Additionally, the minimum voltage requirement to split water at standard temperature and pressure is of 1.23 V, thus necessitating at least a 1.23 eV band gap semiconductor. In practice, however, entropic losses, reaction overpotentials, and other losses can increase the overall band gap requirement. [387] Simply put, the band gap must be large enough to provide the necessary photovoltage to split water but as small as possible to absorb the greatest portion of the solar spectrum. [387] The band-gap of  $\text{TiO}_2$  for example is  $\sim 3.0$  eV [390] and thus it needs higher energy light (UV-light) to get excited. Other materials like the bimetallic ternary oxide bismuth vanadate have a smaller bandgap (2.4 eV) and thus can be used with visible light. [390] This makes  $\text{BiVO}_4$  a very promising material for light harvesting, as UV-light is only occupying 4% of the whole solar energy, while visible light is accounting for 45%. [391]

In addition to the band gap of the light-harvesting material, the charge carrier separation and transport is an important aspect to think about. Recombination timescales can be faster than the interfacial reaction and thus need to be enhanced to ensure efficient charge separation. Crucial for this is also good electron transport, underlining the need for good conductivity in the material. Co-catalysts can be added to accelerate and selectivate the half-reactions. They are usually electrocatalysts, but can be photoactive as well. A co-catalyst might be necessary if the single material doesn't fulfill all of the following functions: (i) light absorption, (ii) charge separation and charge carrier transport, and (iii) electrocatalysis. [384]

### **$\text{BiVO}_4$ as a photoelectrode**

A range of photocatalysts has been reported, including binary metal oxides. However, they are not providing the right band gap for visible light absorption (e.g.  $\text{TiO}_2$  or  $\text{WO}_3$ ) or have extremely poor charge transport properties (e.g.  $\text{Fe}_2\text{O}_3$ ). [390] The bimetallic ternary oxide bismuth vanadate ( $\text{BiVO}_4$ ) has attracted much attention as the most promising photocatalyst for PEC watersplitting, since it has both a narrow band gap of  $\sim 2.4$  eV [392–394] compared to  $\text{TiO}_2$  and a suitable valence band edge ( $\sim 2.4$  V vs. RHE) which provides a strong driving force for water oxidation by photogenerated holes. [395,396] The low band gap means it absorbs in the visible region, while semiconductors with larger band gaps such as  $\text{TiO}_2$  ( $\sim 3.0$  eV) [390] absorb in the UV region.  $\text{BiVO}_4$  also is cost effective, abundant and has a good stability. [67,396,397]

Theoretically  $\text{BiVO}_4$  should be able to achieve a solar-to-hydrogen conversion efficiency of about 9.2%. However, due to low photo-induced electron transportation, slow kinetic for oxygen evolution and low conduction band level, the actual conversion efficiency is below the expected one. Especially the slow charge transportation leads to a recombination of 60 - 80% of the electron-hole pairs.<sup>[67]</sup> A study by Kweon et al.<sup>[398]</sup> showed that the charge transportation is electron limited.

$\text{BiVO}_4$  exists in three different polymorphs: monoclinic sheelite, tetragonal zircon and tetragonal sheelite<sup>[393]</sup> with band gaps of 2.40, 2.34 and 2.90 eV, respectively.<sup>[389]</sup> Photocatalytic properties of  $\text{BiVO}_4$  are strongly related to their crystal phase. The monoclinic phase showed much higher photocatalytic activity than the others,<sup>[399]</sup> making it a highly desirable one. Since  $\text{BiVO}_4$  was first reported as a photocatalyst in 1999,<sup>[393]</sup> many reports have emerged on its synthesis by a range of methods, such as using chemical synthesis and subsequent annealing,<sup>[394,395]</sup> precipitation from aqueous, acidic media<sup>[396]</sup> with subsequent calcination,<sup>[400]</sup> solid state synthesis,<sup>[401]</sup> hydrothermal<sup>[402,403]</sup> or solvothermal,<sup>[404]</sup> and sonochemical.<sup>[391]</sup>

There are several ways of enhancing the properties of  $\text{BiVO}_4$  as a photocatalyst:<sup>[67]</sup> (i) Metal and non-metal doping, e.g. tungsten or molybdenum,<sup>[405]</sup> can improve the charge separation in the case of  $\text{BiVO}_4$ . (ii) Facet engineering is used to create more surface active sites.<sup>[402,406]</sup> (iii) Morphology control presents another way of influencing the photocatalytical performance, as such a control can assist in collection and separation of electron-hole pairs, e.g. nanorods.<sup>[404]</sup> (iv) The creation of heterostructures, e.g. by co-grafting of co-catalysts, such as  $\text{Fe}^{3+}$  or  $\text{Cu}^{2+}$ , has also been reported to enhance the photocatalytic activity.<sup>[67,407]</sup>

Recently, there have been reports that try to address the drawbacks of  $\text{BiVO}_4$  as a photoelectrode by carefully engineering the electrode structure on a nanoscale.<sup>[389]</sup> To avoid the charge recombination due to the long diffusion length of the photo-induced electrons, porous  $\text{BiVO}_4$  structures have been suggested.<sup>[327,408]</sup> Core-shell technologies with a conductive backbone are of interest, such as using  $\text{WO}_3$  nanowires as electron conductors with a  $\text{BiVO}_4$  shell, reaching an incident photon-to-current conversion efficiency of  $\sim 60\%$  at 300 - 450 nm, as reported by Rao et al.<sup>[390]</sup> (figure 5.5A) and Su et al.<sup>[409]</sup> Porous structures with high electrical conductivity materials, such as carbon, metal or metal oxides, are highly promising to improve the photo-induced electron transportation. Recently, there have been a range of reports of  $\text{BiVO}_4/\text{MWNT}$  composites. Sun et al.<sup>[410]</sup> reported a hydrothermal synthesis of a  $\text{BiVO}_4/\text{MWNT}/\text{Ag}@\text{AgCl}$  compound with improved catalytic performance. Zhao et al.<sup>[411]</sup> reported the formation of hierarchical structures of carbon-doped  $\text{BiVO}_4$  with MWNTs by hydrothermal synthesis and subsequent ultrasonication with a MWNT-solution, showing that the transient photocurrent densities of the C- $\text{BiVO}_4$  and C- $\text{BiVO}_4@\text{MWNT}$  are much higher than that of  $\text{BiVO}_4$  (figure 5.5B). They attributed this to the scattering effect of C- $\text{BiVO}_4$  and the excellent electrical conductivity of MWCNT. They also reported a one-step hydrothermal synthesis for a  $\text{BiVO}_4/\text{MWNT}$ -composite with uniformly embedded MWNTs in monoclinic  $\text{BiVO}_4$ .<sup>[412]</sup>

## 5 Inorganic Modification of CNT Honeycomb Structures for Watersplitting

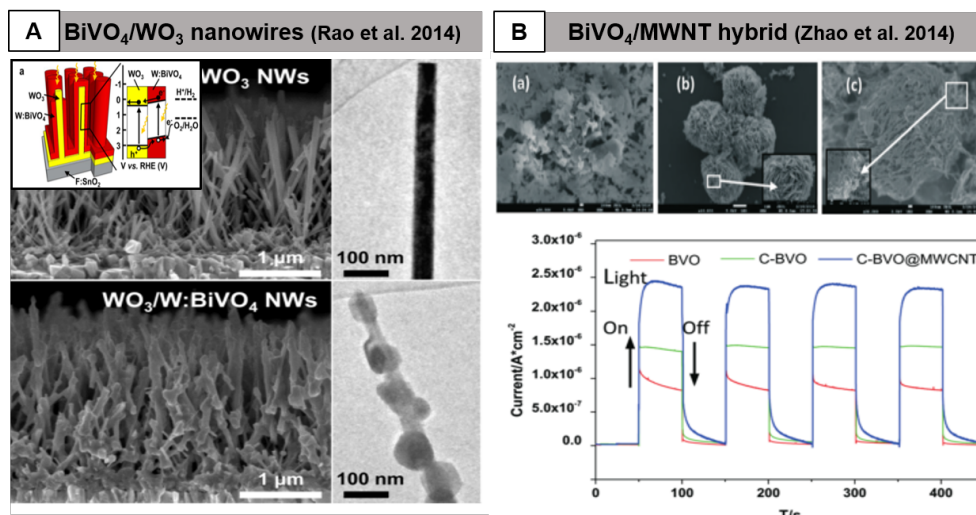


**Fig. 5.5** This figure shows two examples for BiVO<sub>4</sub> combined with conductive materials: (A) an advanced electrode structure made from WO<sub>3</sub> nanowires coated with BiVO<sub>4</sub><sup>[390]</sup> and (B) carbon-doped BiVO<sub>4</sub> particles with MWNTs as a conductive material, showing a significant increase in the photocurrent compared to unmodified BiVO<sub>4</sub>.<sup>[411]</sup>

BiVO<sub>4</sub> can not only be used as a photocatalyst under visible light, but also for paints due to its distinct yellow color.<sup>[413]</sup> It presents an attractive and nontoxic substitute for lead- and cadmium-based yellow pigments.<sup>[389]</sup> This adds an optical control during the characterization to immediately determine whether the reaction was successful.

Overall, not only the materials are important, also electrode design needs careful thought. Monolithic cells can be created that operate similar to artificial leaf reported by Reece et al.<sup>[414]</sup> where a wireless design for a PEC cell was proposed. Due to the range of processes to be kept in mind, such as illumination, charge separation, electrical conduction, and molecular transport, this is a very challenging task<sup>[384]</sup> which is addressed in this chapter by the fabrication and testing of an advanced photoelectrode made from a 3D-CNT structure coated with BiVO<sub>4</sub>.

### 5.2 BiVO<sub>4</sub>-coated CNT honeycombs as photoelectrodes

The hybrid structure concept is similar to the architecture proposed by Rongé et al.,<sup>[384]</sup> as shown in figure 5.6A for a 3D structure with core-shell nanotubes. This one-dimensional structure shows a large penetration depth to maximize the absorption of the incident light, in addition to the absorption depth of materials (~250 nm for BiVO<sub>4</sub>).<sup>[384]</sup> When thinking about the thickness of the coating, it is important to keep the hole diffusion length (~150 nm for BiVO<sub>4</sub>) and the electron diffusion length in mind (~10 nm). The nanostructure helps to shorten the necessary diffusion pathways for charge separation, thus avoiding charge recombination.<sup>[384]</sup>

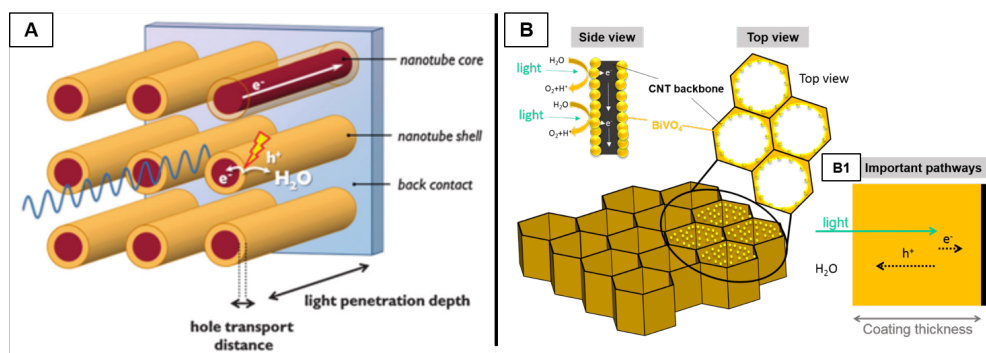


**Fig. 5.6** Schematic illustration of a suggested photoelectrode structure by J. Rongé<sup>[384]</sup>(A) and the adapted concept for a BiVO<sub>4</sub> coated CNT honeycomb structure (B). Here the side view shows the reactions taking place on the photoelectrode surface and the diffusion direction of the electrodes. The

The proposed photoelectrode is a similar hybrid structure made from a conductive CNT honeycomb network coated with the photocatalyst BiVO<sub>4</sub> (figure 5.6B). With this approach, we hope to be able to address some of the drawbacks of BiVO<sub>4</sub> as a promising photocatalyst: (i) With a conductive CNT backbone in the structure, electron transport should no longer be an issue in the material and thus make it possible to avoid high recombination rates (shown in the side view and important pathways). (ii) In addition to enhancing the electron transport, the CNT honeycomb structure provides a high surface area, which is beneficial for the generation of many active species and thus can improve the efficiency of the electrode.<sup>[67]</sup> This concept is suggested by J. Rongé (KU Leuven) who also does all the electrochemical characterization.

The CNT honeycomb synthesis and coating with BiVO<sub>4</sub> is done in Cambridge and thus is the main focus of this thesis chapter. The CNT honeycombs are formed by densification as described in chapter 3.2.1 and a range of coating methods and recipes for BiVO<sub>4</sub> modification is examined, as shown in the following sections. The optimal coating thickness for the BiVO<sub>4</sub> still needs to be experimentally determined.

## 5.3 Modification with bismuth vanadate - BiVO<sub>4</sub>

### 5.3.1 Microwave-assisted, hydrothermal growth of BiVO<sub>4</sub> on CNT structures

The first coating attempts with BiVO<sub>4</sub> on the CNT honeycomb structure are made using microwave-assisted, hydrothermal synthesis due to the advantages described in the previous chapters. A uniform film of about 100 nm is targeted to get most of the absorption depth but to stay below the hole diffusion length to avoid recombination.

As the application requires a conductive substrate, the honeycomb structure is transferred onto the conductive PCP film before the modification. The transfer of the 3D CNT structure onto the film is done right after growth. Then the structure is densified into honeycombs (figure 5.7A and 5.7A1) and subsequently coated with the chosen protocol, here with olive-like BiVO<sub>4</sub> particles<sup>[415]</sup> (figure 5.7B and 5.7B1, more details on the synthesis itself will be discussed in the next sections). The transfer

## 5 Inorganic Modification of CNT Honeycomb Structures for Watersplitting

and honeycomb formation of the  $\sim 30\mu\text{m}$  structures works very well over large areas (see chapter 3.2.1) and does not get damaged by the modification.

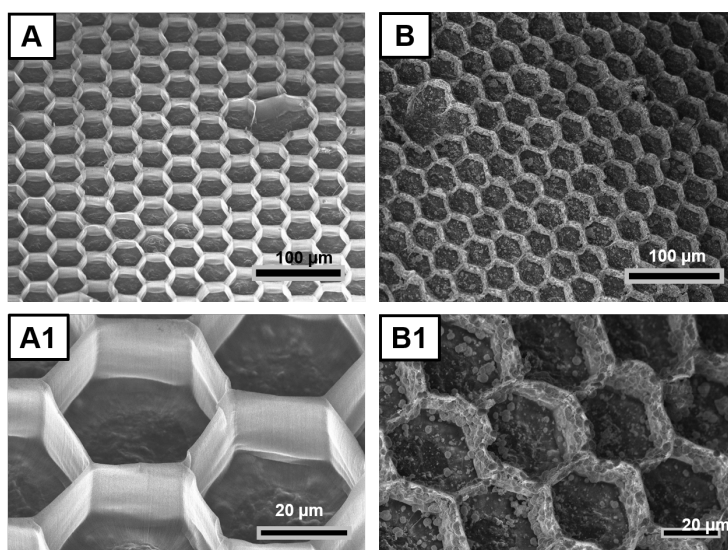


**Fig. 5.7** The 3D CNT structure is transferred onto the conductive PCP film and densified into honeycombs (A, A1). Then it is coated with the desired protocol (B, B1) - here it is coated with olive-like  $\text{BiVO}_4$  as an example.<sup>[415]</sup>

The use of the PCP film limits the reaction temperature to below  $200\text{ }^\circ\text{C}$  due to melting of the PVDF in the film. In an initial experiment, a hydrothermal reaction by Zhang et al.<sup>[416]</sup> is reproduced with a reaction time of 6 h ( $\frac{1}{4}$  of initially reported time) at a temperature of  $180\text{ }^\circ\text{C}$  (more details in experimental section). This causes the CNT structure to completely delaminate from the film. SEM images of the particles and an XRD measurement can be seen in figure B13 in appendix B, proving that the reaction itself worked and produced  $\text{BiVO}_4$  particles. However, for these reaction conditions the adhesion to the film is too low - a method with shorter reaction times and/or a lower temperature is needed. In addition to those restrictions, the use of concentrated  $\text{HNO}_3$  at high temperatures needs to be monitored carefully, as it might damage the CNT structure. Hence, many protocols for the formation of  $\text{BiVO}_4$ , using  $\text{HNO}_3$  as a solvent for the metal salts, were avoided for the microwave-assisted, hydrothermal synthesis.

The  $\text{BiVO}_4$  coating attempts are done, adapting three different hydrothermal protocols in the microwave reactor with the transferred CNT honeycomb structures of a range of heights. All of the protocols do not use  $\text{HNO}_3$  and have reaction times in the microwave reactor ( $\frac{1}{4}$  of initial reaction time) below 6 h with a maximum temperature of  $160\text{ }^\circ\text{C}$ . The standard activation method is a 30 minute UV-ozone treatment.

### 5.3.1.1 Coating with a dumbbell shaped $\text{BiVO}_4$ structure (Shang et al.<sup>[256]</sup>)

A hydrothermal protocol for the formation of dumbbell shaped  $\text{BiVO}_4$  on  $\text{TiO}_2$  nanofibres<sup>[256]</sup> is adapted for the synthesis on the CNT structure instead of the  $\text{TiO}_2$  nanofibres. The reaction time

is shortened to 1 h at 140 °C with bismuth nitrate pentahydrate and ammonium metavanadate as precursors in ethylene glycol.

Some growth of nanoparticles can be seen on the sidewalls of the 3D CNT structure (figure 5.8A). The growth, however, is not uniform but in small patches (figure 5.8B) with particles clearly emerging from the CNTs (inset figure 5.8B). The color of the product is light yellow and not the expected deep yellow that is typical for BiVO<sub>4</sub>, indicating that the nanoparticles have not formed the desired composition. This is confirmed by XRD that shows other bismuth vanadium oxides (Bi<sub>8</sub>O<sub>17</sub>V<sub>2</sub> and Bi<sub>4</sub>O<sub>11</sub>V<sub>2</sub>); a larger image can be found in figure B14 in appendix B.

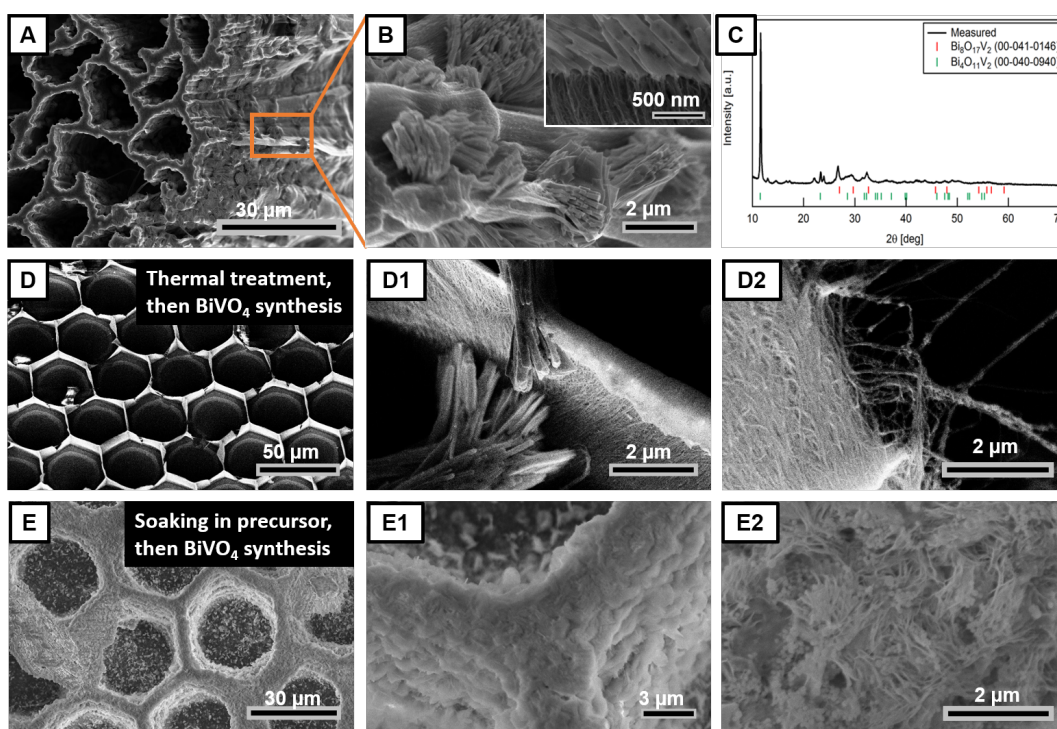


**Fig. 5.8** The microwave-assisted synthesis did not change the overall structure (A). However, it only led to nucleation in some parts of the CNT structure (B), where nanoparticles can be seen emerging from the CNTs. Those particles show a different composition of bismuth vanadium oxide (C), not the desired BiVO<sub>4</sub>. Changing the activation method for more nucleation sites on the CNT structure (D) does not lead to a better coverage of the side walls with nanoparticles (D1), leaving many areas uncoated (D2). Soaking in the vanadium precursor leads to more coverage of the CNT honeycombs with nanoparticles (E, E1), but there is a range of particle shapes present (E2). Additionally the powder is white, indication that the right composition could not be formed.

The low nucleation of the particles on the CNT backbone (figure 5.8A and 5.8B) might be due to the fact that there are not enough reactive groups for this synthesis on the surface of the 3D CNT structures, thus the activation method is changed. Menzel et al.<sup>[417]</sup> reported a thermal treatment for their CNT powders before they start polymerizations on them. They first pre-oxidized the CNT powders by heating them in air at 670 °C and then did the activation step in inert atmosphere at 1000 °C for 2 hours. This method is adapted to the 3D CNT structures. The activation temperature is lowered to 500 °C as the CNTs burn off at the reported temperature of 1000 °C. This might be to a higher defect density and lower quality of the substrate grown CVD CNTs compared to the

## 5 Inorganic Modification of CNT Honeycomb Structures for Watersplitting

---

ones used for the experiments in the paper. After the thermal treatment the nanoparticle synthesis is started immediately to avoid any change in the generated active groups. The overall structure remains undamaged (figure 5.8D). Nanoparticles nucleate in some areas on the side walls (figure 5.8D1) but many areas remain uncoated (figure 5.8D2). Thus this method does not significantly increase the nucleation on the CNTs.

Another approach to achieve a more uniform coating is to soak the structure overnight in the vanadium precursor. It is then taken out and put into the bismuth precursor for the reaction. This also leaves the CNT honeycomb structure undamaged (figure 5.8E) and leads to an increased amount of particles covering the CNTs, not leaving any CNTs bare (figure 5.8E1). The size of those particles, however, is very polydisperse and shapes show a mixture of elongated rod shaped ones and small spherical ones (figure 5.8E2). They are white, rather than yellow, indicating the wrong composition.

As mentioned by the authors, the synthesis conditions are crucial and increasing the precursor concentrations slightly, changes the overall morphology. This might be why the soaking in the vanadium-based precursor did not work to form the right type of particles. Another reason could be that the 1:1 stoichiometry of Bi:V is no longer guaranteed in the soaking process, leading to a change in precursor ratio and thus a change in the reaction pathways.

Lower concentrations or longer reaction times as well as a change in reaction temperature could be other ways to achieve a more uniform coating and the right particle composition. The reaction conditions probably have to be changed due to the fact that we used CNTs as substrates for the nucleation instead of their reported TiO<sub>2</sub> fibres. In order to use this protocol, those influence factor have to be investigated further.

### 5.3.1.2 Coating with an olive-like BiVO<sub>4</sub> (Ma et al.<sup>[415]</sup>)

Ma et al.<sup>[415]</sup> reported a hydrothermal method with water and ethylene glycol as solvents to create olive-like, monoclinic BiVO<sub>4</sub> (figure 5.7B1). The reaction time is shortened to 1/4 of the initial one due to the microwave reactor used, making it 4 h at 160 °C with bismuth nitrate pentahydrate in EG and ammonium metavanadate in DI-water as precursors.

The initial reaction showed a thick coating on parts of the structure, whereas other parts showed no coating at all (figure 5.9A) The nanoparticles are monoclinic BiVO<sub>4</sub>, as verified by XRD (figure 5.9B).

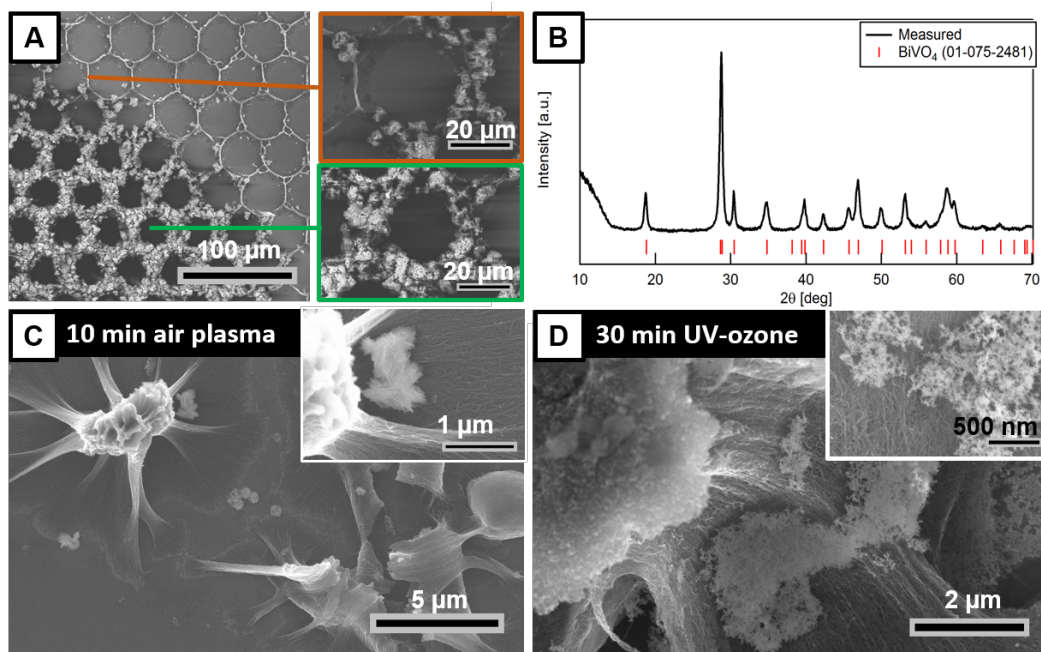


**Fig. 5.9** After the microwave-assisted hydrothermal synthesis, half of the structure is nicely coated, whereas other parts are not coated at all (A). The composition of the particles from this reaction is monoclinic BiVO<sub>4</sub> (B). A comparison between 10 minutes air plasma (C) and the standard 30 minute UV-ozone treatment (D) shows no difference for the nucleation on the CNTs. Both activation strategies only lead to patches of nanoparticles on the side walls, leaving most CNTs uncoated.

To gain further insight on the nucleation on the CNTs with this protocol, two different activation methods are thus tried in the same run to see if there is a change in nucleation on the CNT surface over the initial sample. Non-perfect honeycomb structures were used for those trials, thus some look like pillars and broken. A 10 minute treatment in air plasma (figure 5.9C) is compared to the standard method of 30 UV-ozone treatment time (figure 5.9D). It can be seen that in both cases the nucleation only happens in small patches on the CNT side walls rather than covering the whole structure as partly seen in the initial sample, leaving many CNTs uncoated. This might be due to wetting imbalances of the water and ethylene glycol on the CNTs. While the mixture of both solvents works perfectly for the formation of BiVO<sub>4</sub> nanoparticles in solution, there might not be the case on the CNT surface. Balamurugan et al.<sup>[418]</sup> published a study with molecular dynamics simulations, showing that ethylene glycol molecules aggregate around CNTs expelling water molecules due to hydrophilic- hydrophobic interaction. This might mean that the vanadium precursor (in water) cannot get to the CNT surface as efficiently as the bismuth precursor (in ethylene glycol) and thus preventing the reaction that relies on stoichiometric balance.

To avoid the wettability problem, the structure is soaked in the vanadium precursor (ammonium metavanadate in DI water) overnight, dried and then put into the bismuth precursor for subsequent reaction. This way the vanadium precursor might be already in the structure and thus might help avoid the competing reaction between the precursor solution in ethylene glycol and the one in water for the wetting of the CNTs. The overall structure is coated in nanoparticles (figure 5.10A).

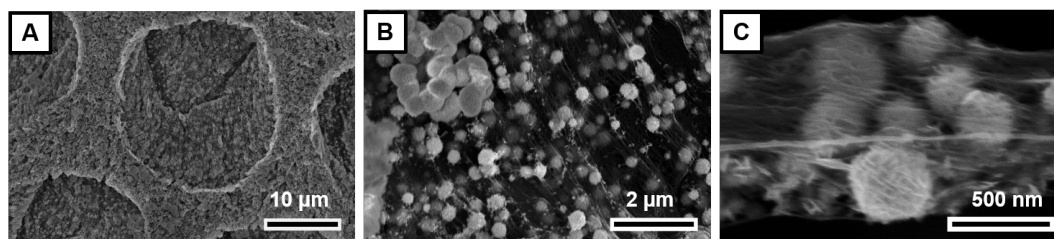


**Fig. 5.10** Soaking the 3D CNT structure in the vanadium precursor and drying it before the reaction with the bismuth precursor leads to a coverage of the overall structure with nanoparticles (A). Those spherical particles are spread all over the CNT side walls (B) and are emerging from the CNT strands (C). However, they don't show the right color and thus not the right composition.

Spherical particles can be seen on the CNT walls (figure 5.10B). Their density is too low to provide a uniform coating but they are nicely interlinked with the CNTs, emerging from the individual strands (figure 5.10C). More images of this coating can be found in figure B15 in appendix B. Thus the soaking in the precursor definitely leads to an improvement for the coverage of the CNTs with nanoparticles. However, the achieved bismuth vanadium oxide powder shows a white color rather than yellow, indicating an undesirable composition. A reason for this might be the stoichiometric imbalance between the bismuth and vanadium which cannot be addressed with the current method easily.

### 5.3.1.3 Coating with $\text{BiVO}_4$ by first reported hydrothermal method (Liu et al.<sup>[413]</sup>)

Liu et al.<sup>[413]</sup> reported the hydrothermal method for  $\text{BiVO}_4$  initially. In this one-step synthesis, water is used as the solvent for both precursors, eliminating the wetting imbalance between two solvents and CNTs as reported before. The precursors are bismuth nitrate pentahydrate and sodium vanadium oxide, the reaction temperature is 140 °C for 3 hours.

After the synthesis the CNT honeycomb structure is coated in nanoparticles, the CNT sidewalls barely visible within the particles (figure 5.11A). The side walls are also coated and show no visible bare CNT patches (figure 5.11B). The XRD indicated that the particles have the right composition (figure 5.11C), thus making this a very promising first result.

There clearly is an excess of particles which results from homogenous nucleation either after there are no more nucleation sites for the heterogeneous nucleation or as a competing mechanism. Thus, the precursor concentration is reduced to  $1/10$  to prepare less particles to reduce homogeneous nucleation. Looking at sample 1, two different areas are found (figure 5.11D): one where there are coated CNT honeycomb structures (figure 5.11D1) and another where most of the CNT honeycomb structures disappeared. Instead a regular structure of large and small particles can be found (figure 5.11D2). However, this phenomenon could not be seen on any other further samples and could not reproduced.

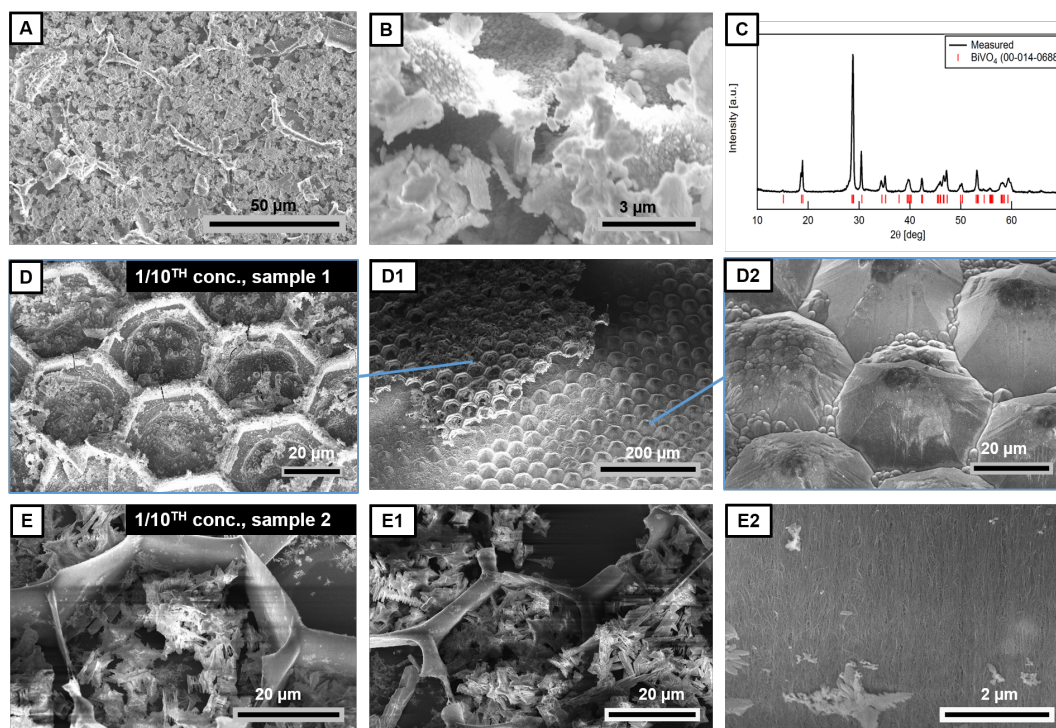


**Fig. 5.11** The hydrothermal, microwave-assisted protocol<sup>[413]</sup> shows a large amount of nanoparticles that cover the CNT honeycomb structure (A), coat the sidewalls (B) and are of the desired composition, monoclinic BiVO<sub>4</sub>(C). A decrease in concentration leads to one sample that is split in two different areas (D1), one with nicely coated honeycombs (D) and the other one where the honeycombs are no longer visible or on the substrate but many large and small ordered particles are covering the substrate instead (D2). A more representative sample of the reaction with a lower concentration is shown in (E). While the honeycombs remain intact (E1), no uniform coating can be seen on the sidewalls (E2).

Sample 2 shows a more representative overview of the samples coated with  $1/10$  of the concentration (figure 5.11E). Particles aggregate in the pores of the CNT honeycomb structure (figure 5.11E1). Most CNTs are uncoated with small particle patches nucleating on the side walls (figure 5.11E2). This indicates that in this reaction homogeneous nucleation is favored over heterogeneous nucleation on the CNTs. Particles are formed in the solution and then seem to sediment onto the sample.

The reaction is then done in a stirred reactor without microwave radiation with the originally reported reaction time to see whether avoiding microwave heating might lead to a better nucleation on the CNTs (figure 5.12A). The particle shapes change completely after the reaction to a more fern-like structure, emerging from some parts of the CNT side walls as well as being deposited from solution (figure 5.12A1). However, no uniform coverage of the CNTs can be seen here either (figure 5.12A2). A change in the activation protocol to the thermal method, reported by Menzel et al.,<sup>[417]</sup> shows no change in the structure itself (figure 5.12B) and results in a coating with small particles on it (figure 5.12B1). A closer look, however, still shows a large amount of uncoated CNTs (figure 5.12B2).

## 5 Inorganic Modification of CNT Honeycomb Structures for Watersplitting

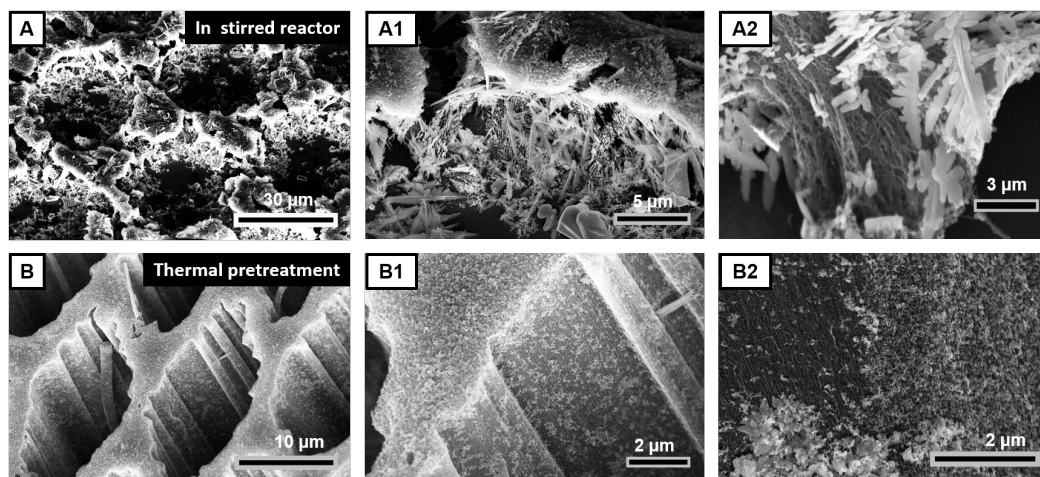


**Fig. 5.12** The reaction is attempted in a stirred reactor (A), leading to a fern-like structure all over the honeycombs (A1) but no uniform coating on the CNT side walls (A2). A thermal activation method does not change the overall 3D CNT structure (B) and only leads to a partial coverage of the CNT side walls (B1) with very small particles (B2).

None of the attempted hydrothermal, microwave-assisted  $\text{BiVO}_4$  syntheses lead to a continuous nucleation of monoclinic  $\text{BiVO}_4$  on the 3D CNT structure. Thus, this approach did not look promising and was abandoned.

### 5.3.2 Hotcasting of $\text{BiVO}_4$ on CNT structures

As the microwave-assisted hydrothermal synthesis does not lead to the desired results and it is hard to get the right crystalline phase as well as nucleation on the CNTs, another synthesis method is attempted to coat the CNT honeycomb structures.

For the new coatings, the CNT honeycomb structure is grown onto a Si-wafer, densified and then coated with a range of precursor solutions on a hotplate. This approach on the wafer allows for higher temperatures during the reaction. After precursor deposition, the substrate is heated up to  $\sim 300$  °C to evaporate the solvent and start the  $\text{BiVO}_4$  formation. The last step is an annealing step to finish the  $\text{BiVO}_4$  crystallization. The coating thickness can be varied by the coating cycles done. We call this method **hotcasting** and it was adapted by J. Rongé from reports by Sayama et al.<sup>[392]</sup> and Ma et al.<sup>[419]</sup> It was further improved during a 2-months project by M. A. Jones. Very initial results with different methods and solvents by J. Rongé are shown in figure B16 in appendix B. All of them showed a good coating on the 3D CNT structure. However, the composition of this coating was not evaluated. Building on those results, together with M. A. Jones, a range of protocols with various precursors, solvents and concentrations is examined (overview in table 7.2 in the experimental section). Additionally, the temperature for the hotcasting is changed to 25, 100 and 200 °C.

The synthesis with acetic acid (for the bismuth nitrate pentahydrate) and acetylacetonate (for the vanadyl acetylacetonate) as solvents shows no damage to the overall honeycomb structure (figure 5.13A) and results in a uniform coating on the top of the structure (figure 5.13B) and the side walls (figure 5.13C) with some excess particles spread over the substrate. XRD analysis shows,

however, that the composition of the sample is a bismuth oxide (Bi<sub>2</sub>O<sub>2.5</sub>) and a different bismuth vanadium oxide phase (Bi<sub>2</sub>VO<sub>5</sub>). This change in phase might be due to the fact that the VO(acac)<sub>2</sub> precursor did not dissolve very well in acetylacetone (despite the fact that it was repeatedly reported as a solvent<sup>[420,421]</sup>) and thus the desired 1:1 molar ratio of Bi:V cannot be guaranteed. The XRD measurements also show peaks of SiO<sub>2</sub> or Si. This is due to the fact that the structures are on Si-wafers, and thus those peaks are expected and not considered impurities.

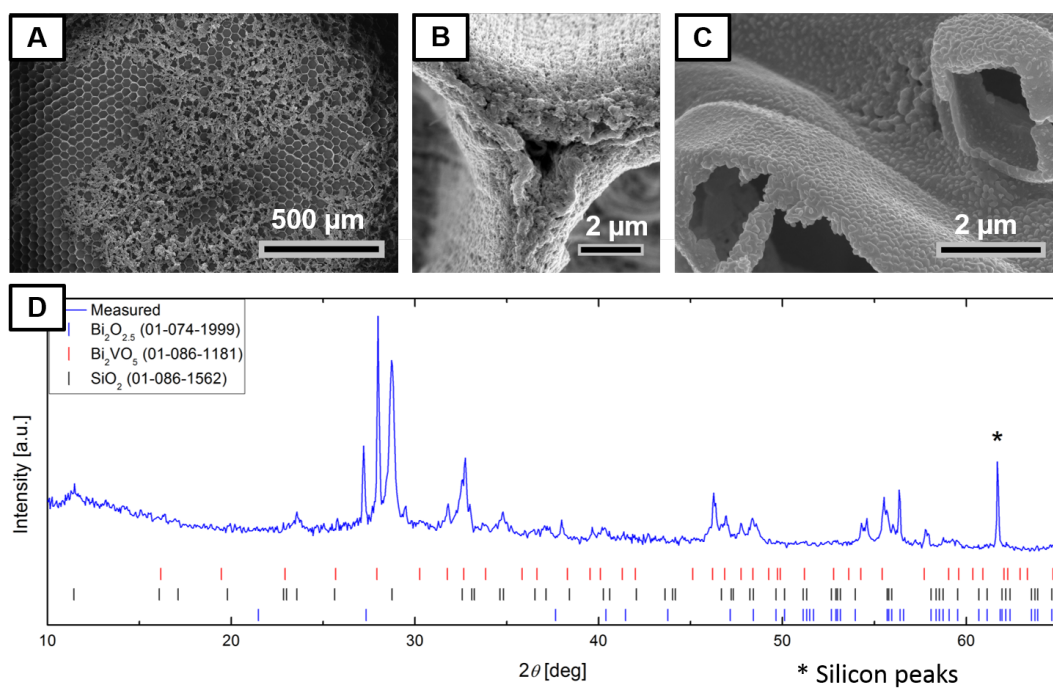


**Fig. 5.13** The undamaged CNT honeycomb structure (A) is coated uniformly on the top (B) and the side walls (C). The XRD shows SiO<sub>2</sub> peaks from the substrate and two bismuth vanadium oxide phases, but none of them is the desired monoclinic BiVO<sub>4</sub>.

After trying variations of the protocol reported by Shang et al.<sup>[256]</sup> (bismuth nitrate pentahydrate and ammonium metavanadate in ethylene glycol) without any improvement in the phase, the hotcasting procedure is changed to the protocol as reported by Ma et al.,<sup>[415]</sup> which also was already tried for the microwave-assisted, hydrothermal synthesis. The vanadium source (ammonium metavanadate) is dissolved in water, the bismuth precursor (bismuth nitrate pentahydrate) in ethylene glycol. A uniform coating with no damage to the structure over large areas can be seen in figure 5.14A-C. The XRD shows some monoclinic BiVO<sub>4</sub>, as well as unfortunately another bismuth vanadium oxide (Bi<sub>17</sub>V<sub>3</sub>O<sub>33</sub>) as an impurity. Changing the temperature in the hotcasting procedure for this protocol did not lead to any improvement of the composition. This might be due to the previously discussed interaction of ethylene glycol and CNTs, dispelling the water phase, and thus leading to an imbalance in the molar ratios needed for the formation of the desired BiVO<sub>4</sub> composition.

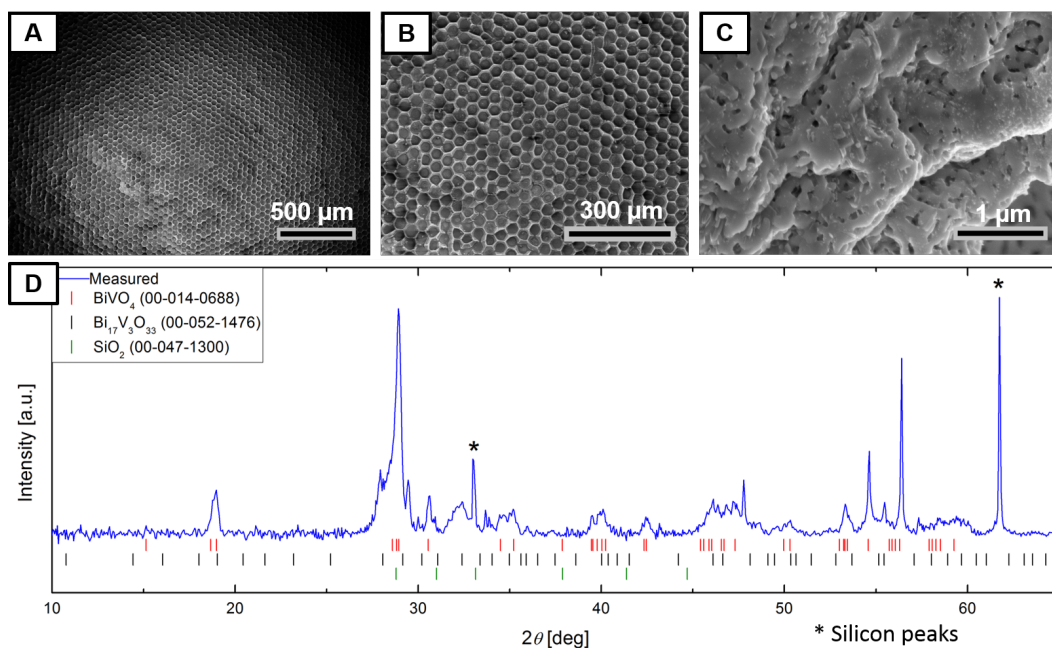


**Fig. 5.14** The CNT honeycomb structure does not show any defects over large areas (A) using a precursor composition reported by Ma et al.<sup>[415]</sup> A uniform coating can be found on the structure (B,C). The XRD shows, in addition to the substrate signal, monoclinic  $\text{BiVO}_4$  and another bismuth vanadium oxide as an impurity.

Many  $\text{BiVO}_4$  synthesis rely on  $\text{HNO}_3$  as a solvent for the precursors. While it was avoided during the microwave-assisted synthesis due to the long reaction times with high temperatures and its damaging effect to the CNTs, it is considered here as a possibility and thus bismuth nitrate pentahydrate and vanadium oxide are dissolved in 2M  $\text{HNO}_3$  as precursors for the hotcasting. The time at a high temperature is very short ( $\sim 2$  minutes) and hence the oxidation effect of the  $\text{HNO}_3$  on the CNTs should be minimal. After the hotcasting with the precursors in  $\text{HNO}_3$  the structure remains undamaged (figure 5.15A) with a uniform coverage on top of the structure (figure 5.15B) and on the side walls (figure 5.15C). Except for the peaks from the substrate, no other phase than monoclinic  $\text{BiVO}_4$  can be found in the XRD measurements, making this a successful protocol to use. The presence of  $\text{HNO}_3$  may help facilitate the process by partially oxidizing the CNTs and aiding the surface-wetting ability of the aqueous solutions, thus enabling the formation of the right phase.

All of the reported syntheses appeared to give a uniform coating of nanoparticles on the CNT surface when analysed by SEM, however, only the ones with nitric acid as a solvent lead to the right composition (monoclinic  $\text{BiVO}_4$ ).

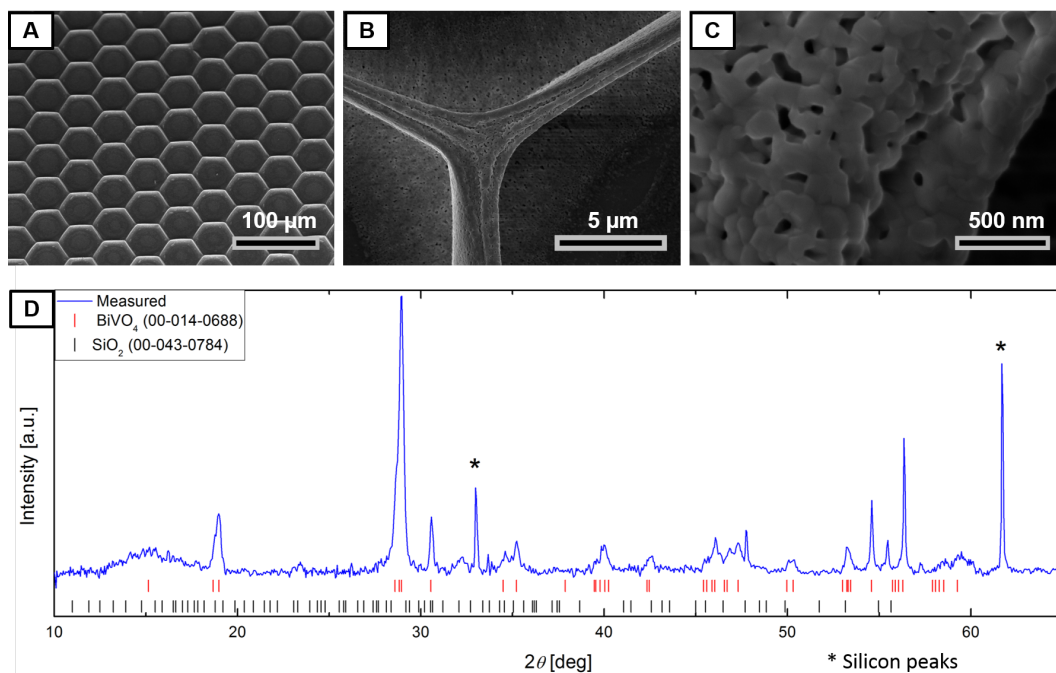


**Fig. 5.15** A coating with precursors in nitric acid leads to no damage of the overall CNT honeycomb structure (A) and a uniform coating on top (B) and on the side walls (C). The XRD shows substrate peaks ( $\text{SiO}_2$ ) but otherwise no other phase than monoclinic  $\text{BiVO}_4$ , making this a successful protocol for the formation of  $\text{BiVO}_4$  particles on CNTs.

Hence, this preparation procedure is repeated on Si wafers with a Mo-underlayer for conductivity (figure 5.16 left) and then these samples are sent to J. Rongé at KU Leuven for the photoelectrode characterization.

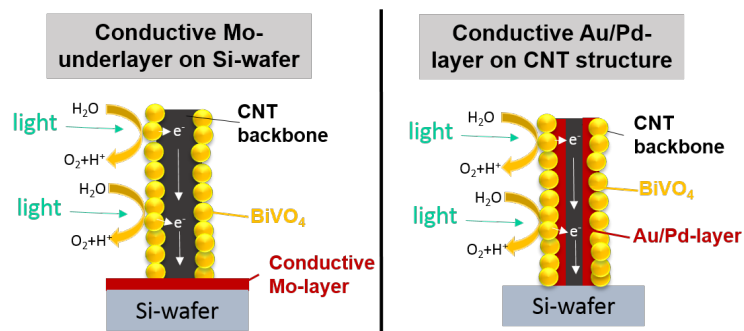


**Fig. 5.16** The two different configurations of the tested photoelectrode are shown here. On the left the conductive layer is a Mo-underlayer on the Si-wafer. On the right the conductive layer is a Au/Pd coating on the CNT backbone before the  $\text{BiVO}_4$  coating.

However, as seen in figure 5.17 in the next chapter, the photocurrent was very low and there is no effect of light visible. Thus a better conductive coating is needed. This is done by adding a thin layer of gold/palladium between the CNT structure and the bismuth vanadate coating (figure 5.16 right). This makes the CNTs no longer the conductive backbone but a scaffold structure. Nevertheless, it is still a promising advanced electrode design. The electrochemical characterization of all those samples is shown in the next chapter.

### 5.4 BiVO<sub>4</sub> photoelectrode characterization

As mentioned previously, the electrochemical characterization of the produced samples is done by J. Rongé at KU Leuven. A three-electrode configuration with graphite as a counter electrode and Ag/AgCl as a reference electrode is used with sodium sulfite (Na<sub>2</sub>SO<sub>3</sub>) as a hole scavenger to determine the efficiency of the BiVO<sub>4</sub> photoelectrode for converting light into charges. BiVO<sub>4</sub> is oxidizing the sodium sulfite and the ionic transport in our system is through the liquid electrolyte without a membrane.

Cyclic voltammetry (CV) and chronoamperometry (CA) measurements are performed for the characterization. The potential range is scanned while measuring the current (under illumination and in the dark) to determine the performance of the material. The set-up used is shown in the experimental section.

Initial experiments on the samples with the Mo-underlayer show a low current density and no difference with or without light, as seen in the graph in figure 5.17 with the change in current density depending on the potential vs. RHE (reversible hydrogen electrode, reference electrode). The low current density indicates a high resistance and a low active surface area. The fact that there is no significant effect of light suggests a high resistance between the BiVO<sub>4</sub> and the contact point, maybe even higher than the one between the bare surface and the contact point. The high dark current also indicates that probably bare CNTs are exposed to the solution. Since sulfite is easily oxidized, this results in currents, even without illumination.

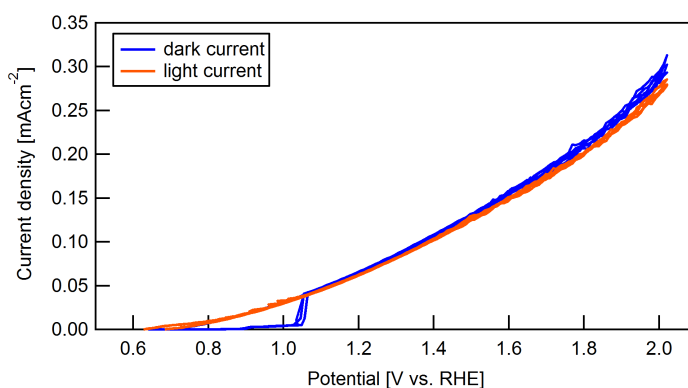


**Fig. 5.17** This graphs shows the change in the current depending on the potential applied. The current here is very low and there is no significant effect of light. This might be due to a large resistance in the sample.

Seeing those results it is clear that the sample modification needs to be changed. A wafer with low resistance or a Mo-underlayer does not show good enough conductivity for the photoelectrodes.

In the next experiments gold/palladium as a conductive layer between the CNT honeycomb structure and the BiVO<sub>4</sub> coating is introduced, making the CNT structure more of a scaffold for high surface area rather than a conductive backbone.

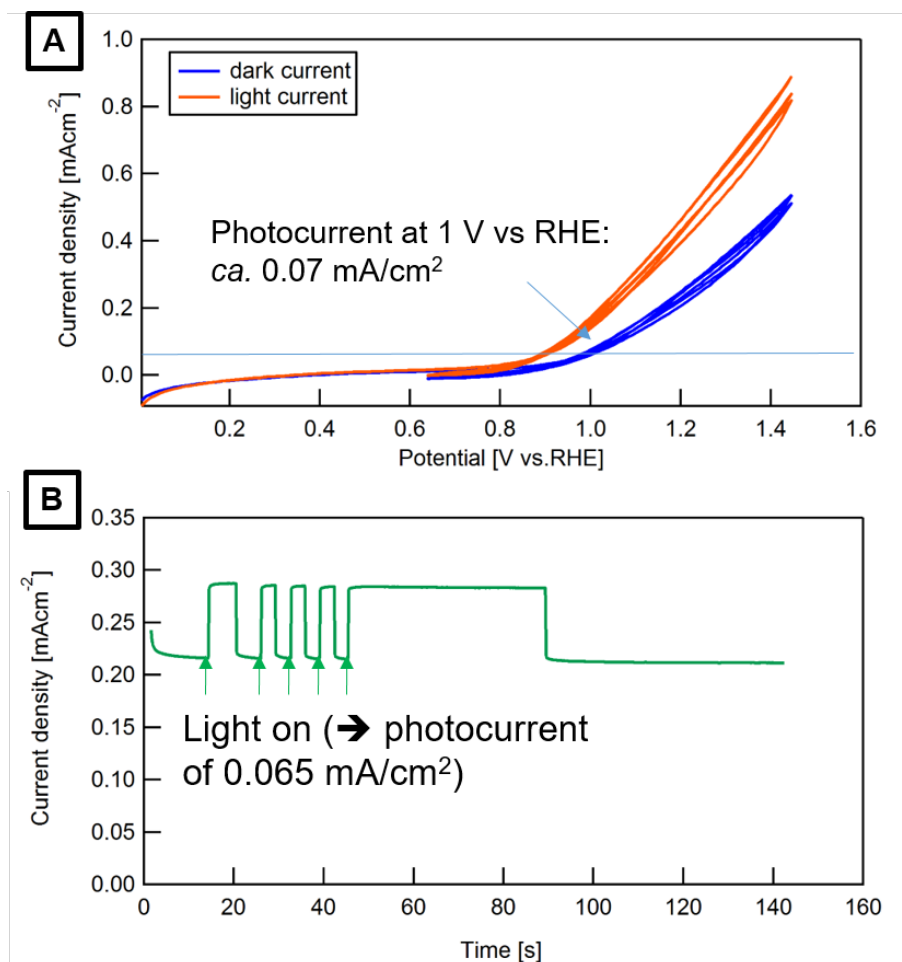


**Fig. 5.18** These graphs show (A) the change in the current depending on the potential applied. An improvement of the current can be seen when light is added (orange line). The photocurrent at 1 V vs. RHE is  $0.07 \text{ mAcm}^{-2}$ . (B) shows the chronoamperometry measurements at 1 V vs. RHE for the response of the current density to light exposure where a photocurrent of  $0.065 \text{ mAcm}^{-2}$  can be detected.

The CV measurement (figure 5.18A) shows a current density that responds to light (orange line). The photocurrent at 1 V vs. RHE is  $\sim 0.07 \text{ mAcm}^{-2}$ . When CA measurements are done at 1 V vs. RHE (figure 5.18B), a clear change with light can be detected in the current. The measured photocurrent is slightly lower at  $0.065 \text{ mAcm}^{-2}$ , which is expected due to time effects. The quick CV scan usually leads to higher currents than a prolonged CA scan. Thus with the new coating system an improvement could be achieved that holds promise for further experiments. As those samples are also active without light and the light effect is fairly small, optimization steps for those electrodes are necessary. The thickness of the Au coating can be increased to have better conductivity, and/ or a thicker BiVO<sub>4</sub> coating to have more active material, and a high uniformity of the coating. However, the optimal thickness still needs to be determined, as charge recombination becomes a problem in too thick BiVO<sub>4</sub> films.

For further characterization of the watersplitting potential of our photoelectrode the characterization set-up needs to be adapted. A co-catalyst, suitable counter electrode with good hydrogen evolution

## 5 Inorganic Modification of CNT Honeycomb Structures for Watersplitting

---

kinetics, membrane to split the gases and a second semiconductor have to be carefully selected. Those measurements have not been started yet.

### 5.5 Conclusion

The fabrication of a high surface area photoelectrode has been demonstrated here. After failure of a range of microwave-assisted, hydrothermal protocols a uniform coating of monoclinic  $\text{BiVO}_4$  on the CNT honeycomb structure was achieved using hotcasting as a method. Here bismuth nitrate and vanadium oxide were used as precursors in the two step synthesis.

The initial photoelectrode characterization with an Mo-underlayer as a conductive layer showed no change with the incident light, suggesting too low conductivity. Thus, the electrode architecture was redesigned and a Au/Pd layer was added onto the structure. This new electrode design showed a change in the current with incident light. With those promising initial results, this structure will be further optimized.

## **Chapter 6**

### **Summary**

### Fabrication of 3D CNT Structures

The fabrication of the patterned vertically aligned CNT structures (3D CNT structures) is discussed in detail in chapter 3 (first results chapter). Two different approaches for catalyst patterning were used, UV lithography for microscale patterning and colloidal lithography for nanoscale patterning. A particularly interesting 3D CNT structure are CNT honeycombs which can be formed by elastocapillary aggregation of the microscale CNT structures patterned with hexagonally ordered holes, as reported before.<sup>[53,172,173]</sup> Vertically aligned CNTs were grown in an atmospheric pressure CVD furnace.

Densification was used on the microscale 3D CNT structures of different dimensions and growth times to gain more understanding about the formation of defects and the parameters that influence the CNT honeycomb formation. For lower heights, smaller spacings and diameters of the patterned structure formed less cracked honeycombs, while for increased heights small diameters and spacings led to an increased percentage of cracks in the CNT honeycomb structure. Hence there is a strong correlation between mask pattern dimensions, such as diameter and spacing, and the CNT structure height.

To reduce the cracking in the overall structure, stress relief features were introduced as a concept. The idea here is by artificially providing points for crack formation in the structure, cracking within the honeycombs patches is avoided, thus introducing larger undamaged areas. Those patches were hexagonally shaped areas that have a 5 or 10  $\mu\text{m}$  spacing between them. It was possible to achieve at least a feature height of 85  $\mu\text{m}$  without a significant amount of cracks compared to  $\sim 30$   $\mu\text{m}$  in the standard structures. The maximum size of the hexagonal areas was between 300- 700  $\mu\text{m}$  diameter for a forest height of  $\sim 85$   $\mu\text{m}$  and a feature size of 30  $\mu\text{m}$  diameter and 10  $\mu\text{m}$  spacing. At 300  $\mu\text{m}$  honeycombs without defects were formed within the honeycomb patches, with 700  $\mu\text{m}$  diameter, however, cracks could be seen in the honeycomb patches. Thus the ideal size of the honeycomb patches for the given parameters was found to be between these measurements. These were first useful insights when designing a CNT honeycomb structure for a specific application with certain dimensions and height.

For nanoscale dimensions, colloidal lithography was used for the first time to pattern a catalyst layer for structured CNT forest growth. A hexagonally ordered polystyrene sphere monolayer was created and then used as a mask for catalyst deposition after etching the spheres. By tuning the etching time as well as the size of the polystyrene spheres, hole sizes down to 180 nm could be introduced in the CNT forests. This enabled the fabrication of CNT structures with an aspect ratio of up to 3000 which is very promising for diffusion-limited applications where long narrow pores in a backbone structure are needed.

Overall in this chapter, first insights were gained into the interlinking parameters during CNT honeycomb formation and a way to increase the height of those structures for specific applications was found by adding stress relief features to the design. Colloidal lithography was demonstrated as a way for inexpensive, large area substrate patterning on nanoscale for CNT growth for the first time.

---

## Modification with Inorganic Materials for Li-ion Batteries

Structured electrodes are needed for many energy storage applications to further improve their gravimetric and volumetric capacity. This chapter focussed on the fabrication of CNT-inorganic hybrid architectures to be used as thick electrodes for Lithium-ion batteries.

The above mentioned 3D CNT structures were coated with active materials for thick Lithium-ion battery electrodes. Due to their hierarchical structure, conductivity and high surface area they are promising backbone structures to modify with the chosen active material. The active materials discussed in chapter 4 are iron oxide and silicon. Both are anode materials with a high specific capacity (three times higher than the current standard graphite for iron oxide and 100 times higher for silicon). Iron oxide as a conversion material suffers from fast capacity fading due to the reaction with Li-ion and a very low electron conductivity. Silicon also shows a low conductivity in addition to a large volume expansion during lithiation which usually leads to a loss of contact with the current collector. These issues can be addressed with the 3D CNT structure coated with the active material, as it ensures electron pathways through the conductive backbone to the active material and space for the volume expansion of silicon. In addition, it enables the creation of thick electrodes by introducing Li-ion diffusion pathways and a higher areal loading due to the high structures with an increased surface area.

For the fabrication of the hybrid CNT-iron oxide structures with microscale pores, many different protocols were tried<sup>[280,370]</sup> with a range of techniques for the CNT modification. For the successful electrode fabrication, the CNT structure was transferred onto a conductive polymer film by a microcontact printing after growth. This film acts as a localized binder between the electrode structure and the current collector in the battery cell, as a good contact between the electrode structure and the current collector is crucial. This structure was then successfully coated adapting a protocol by Wang et al.<sup>[320]</sup> for a microwave-assisted, hydrothermal synthesis which presents a fast and versatile way of synthesizing nanoparticles. This type of synthesis was reported for the first time for coating of patterned CNT structures. It is a one-step synthesis with low temperatures, non-toxic reagents and no annealing step. The CNT structure was uniformly coated with hematite ( $\alpha$ -Fe<sub>2</sub>O<sub>3</sub>, XRD) nanoflakes. The microscale hybrid structures with Fe<sub>2</sub>O<sub>3</sub> were used as thick Li-ion battery anodes with an increased areal loading (twice as high compared to the standard film). The battery half-cell measurements showed a stable capacity over 50 cycles ( $\sim 900 \text{ mAgh}^{-1}$ ) and a good high rate performance without damage to the overall electrode structure.

For the coating of 3D-CNT structures with nanoscale pores with silicon a gas-phase CVD method<sup>[231]</sup> was used. The coating thickness can be adjusted by the reaction time in the CVD furnace. Here the structure was coated on the initial Si-wafer and then transferred onto Cu-tape as a current collector. The nanoscale hybrid structure enables more advanced electrodes with a higher specific capacity material, better areal coverage and Li-ion diffusion pathways to ensure the thick batteries will not be diffusion limited. The thickness of the Si-CNT hybrid electrode was up to 50 times higher than the previously reported ones<sup>[368,383]</sup> and the battery half-cell characterization showed a stable capacity over the first 10 cycles and a promising high rate performance.

## 6 Summary

---

Overall, coating of high 3D CNT structures with nano- and microscale pores was achieved using different techniques and problems with the adhesion of the structure to the substrate during coating were overcome by changing the step order as required for each synthesis. Electrochemical characterization showed the promise of those structures as thick electrodes.

### Modification with $\text{BiVO}_4$ for Watersplitting

Photoelectrodes for solar watersplitting require a high surface area to increase the area of photocatalyst that interacts with the incoming light. The 3D CNT structures were shaped into honeycombs by densification, as explained above, for the application as a conductive backbone for those photoelectrodes. The CNT honeycombs were coated with bismuth vanadate, a promising photocatalyst with absorption in the visible region, to achieve a high surface area electrode that enhances the light absorption area as well as provides a conductive backbone for enhanced charge separation. A range of protocols and methods was tried<sup>[256,413,415,416]</sup> to achieve a uniform coating with monoclinic  $\text{BiVO}_4$ . Hotcasting with  $\text{HNO}_3$  as a solvent was found to work best. Here the CNT structures were on the Si-wafer and the reaction precursors were dropcasted onto the structure. Then the sample was heated up to 300 °C for the evaporation of the solvent with subsequent annealing step. The optimized solvent-precursor system (2M  $\text{HNO}_3$  and bismuth nitrate/ vanadium oxide) yielded the desired bismuth vanadate phase (monoclinic  $\text{BiVO}_4$ ) on a Si-wafer with a Mo-underlayer. This underlayer was used to provide the necessary conductivity for the photoelectrode. The electrochemical performance, however, was decreased by a high resistance in the fabricated device. Thus, the electrode architecture was adapted slightly and Au/Pd was introduced as a conductive layer between the CNT honeycomb structure and the  $\text{BiVO}_4$  coating. The photoelectrode performance was measured and showed a clear increase in current density when exposed to light. Hence, coating of the 3D CNT honeycomb structures with monoclinic  $\text{BiVO}_4$  by hotcasting has proven promising as a photoelectrode.

### Future work

This thesis reported the use of 3D CNT structures for Li-ion battery anodes and as a photoelectrode with  $\text{BiVO}_4$  for watersplitting. The same concept and reasoning for the use of the hybrid structure with diffusion pathways can be applied to electrode fabrication with other active materials, such as  $\text{LiFePO}_4$  for cathodes.<sup>[273]</sup>

The 3D CNT structures with different heights and pore sizes also show much promise for a range of other applications. Some examples of projects using these structures in other areas are shown in the following sections.

### Stress relief features with connections

Using the honeycomb structure for sensors or batteries often relies on a continuous conductive network as well as a high surface area. Thus, stress relief features can be used to increase the height but the

hexagons also need to be connected to keep the conductivity of the whole backbone. This can be done by allowing for catalyst deposition between the hexagons and subsequent CNT growth. During densification this leads to foaming in those areas, as seen in figure 6.1 and thus connections between the hexagons and a continuous CNT structure.

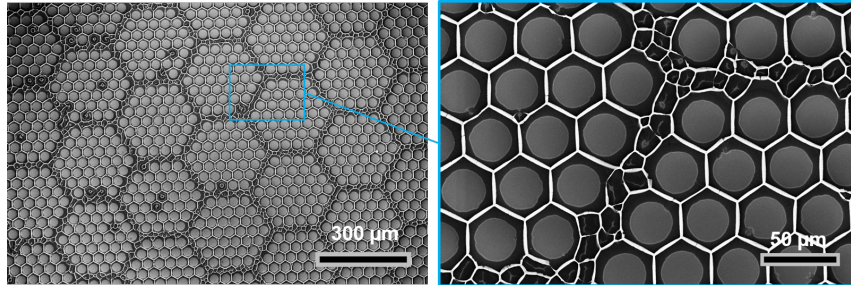


**Fig. 6.1** Catalyst deposition between the hexagon structures in stress relief features allows for the growth of CNT forests. These show foaming during the densification and thus introduce connections between the honeycomb patches.

Alternatively a more controlled way to introduce those connections is by adding serpentine shaped links to the structure design, as shown in figure 6.2. Those serpentine structures were originally reported by J.A. Rogers' group<sup>[383]</sup> (see figure B17 in appendix B) for stretchable applications in electronics which is a desirable property also for batteries. The designs either connect the walls of two hexagons or the corners of three hexagons. As these structures have not yet been tested for their functionality and required growth parameters, it is not clear yet which of these connections will work best in practice or how they need to be adapted. This is part of the future work on stress relief features.

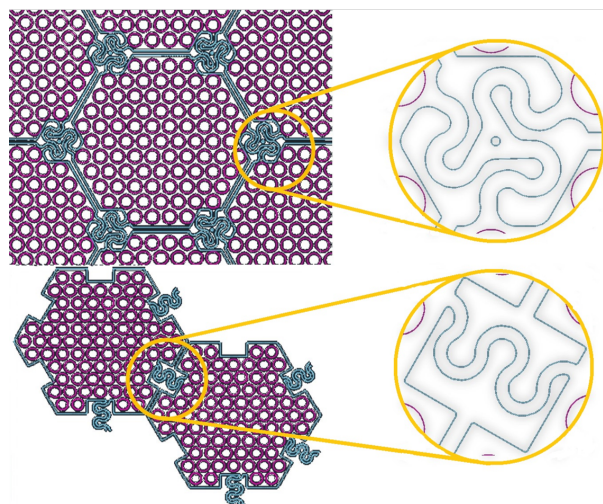


**Fig. 6.2** A controlled way to connect the hexagonal honeycomb patches is by introducing serpentine shaped connections either between two sides of the hexagons or connecting the corners of three hexagons, as the design on our lithography mask shows here.

### Sensing platform

A CNT honeycomb based platform for heavy metal sensing was developed in the next project. Sensitive, fast and selective sensors are needed that can detect impurities, e.g. heavy metals, such as lead, arsenic and mercury, easily. This project was done in collaboration with L. Nucara, Istituto Italiano di Tecnologia, during his research stay in our group for 6 months. There are many reports of CNTs as electrochemical sensors for chemical and biological sensing due to their excellent electrochemical transduction.<sup>[422]</sup> Balasubramanian et al.<sup>[27,423]</sup> gave a good overview of CNTs for chemical sensors and biosensors. CNT have been widely used as chemical sensors of metal ions in water solutions.<sup>[424]</sup> Liu et al.<sup>[425]</sup> reported a vertically aligned CNT sensor for ultrasensitive voltammetric detection of trace heavy metal ions, such as lead and cadmium.

Sensors relying on the swelling of their components in the presence of the analyte have been reported by Wei et al.<sup>[426]</sup> for vertically aligned CNT forests and De Volder<sup>[188]</sup> for vertically aligned CNT bridges. The electrical resistance changes when the distance between the CNTs changes, thus providing a mechanism that can be very sensitive to the analyte concentration. This principle was used for the fabrication of the CNT honeycomb sensor. A paper by Strelow et al.<sup>[427]</sup> indicated shrinking of polystyrene sulfonate (PSS) in the presence of heavy metal ions. L. Nucara found evidence of the shrinkage of PSS, expelling water in the presence of heavy metal ions, during his PhD thesis work and thus proposed this polymer as a coating for the CNT honeycomb structures. Hence, the goal for the project was to fabricate a working device with a PSS-coating on the CNT structure. The layers of the sensing device are shown in figure 6.3A. It is crucial to avoid conduction through the Si-wafer which is why SiN is used as a thick insulating layer that does not become conductive over the temperature treatment steps necessary for the CNT growth. Molybdenum electrodes and the patterned catalyst were added onto the structure. An optical microscopy image of the device (figure 6.3B) and an SEM image (figure 6.3C) show the final design after CNT growth, but before the densification of the structure into CNT honeycombs. The interface between the SiN and Mo layer did not cause a large gap in the CNT structure, indicating that the growth speeds on both underlayers are similar (figure 6.3 C1 and C2). Those design steps were done by L. Nucara in collaboration with N. Chiodarelli.

Subsequent modification was done by dropcasting of the PSS-solution onto the undensified CNT structure. As  $\pi$ - $\pi$ -stacking of  $sp^2$  hybridized carbon rings has been shown to provide strong interactions, this might be the most straightforward way of functionalization. Coating with a 30 wt.% PSS-solution did not only lead to a coating, but also filled the pores, which is undesirable, as the change in resistance can only be detected from the CNTs surrounded by PSS (figure 6.3D). Any excess PSS leads to an uptake of heavy metal ions without a measured change in resistance and thus a lower sensitivity of the final sensor. The concentration was lowered to 2 wt.% next but still led to filling of the pores and introduced cracking in the CNT structure (figure 6.3E). Also no densification could be seen in both cases. Densification brings the CNTs in closer contact making changes in their distance easier to detect.

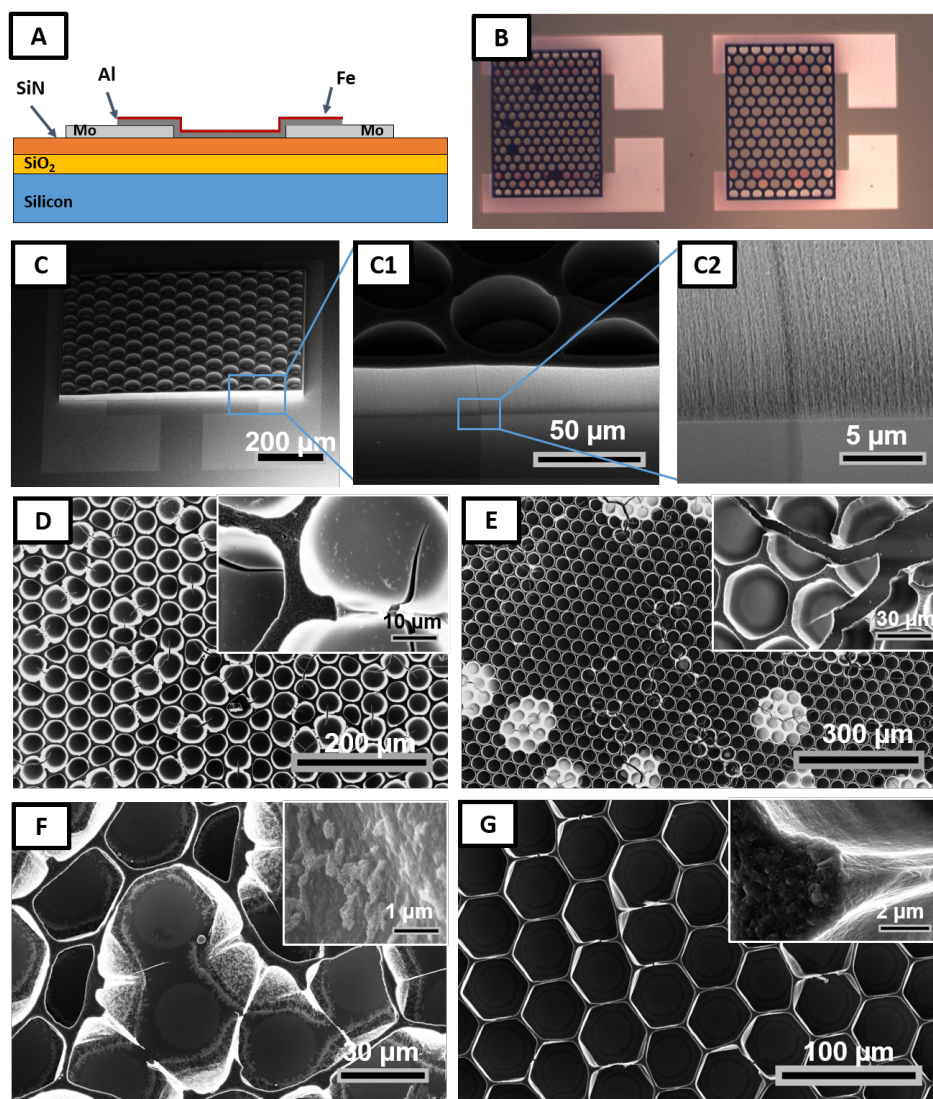


**Fig. 6.3** A schematic of the device is shown in (A). An optical microscopy (B) and SEM image (C) show the device after CNT growth and before modification and densification of the CNT structures. The interface between the two underlayers (SiN and Mo) shows no cracks, indicating similar growth rates on the two different substrates. Images (B-D) were taken by L. Nucara. A coating with a 30 wt.% (D) and 2 wt.% (E) PSS-solution led to filling of the pores, cracking of the structure during drying and no densification. Adding isopropanol to the solution to enhanced the densification of the structure resulted in small agglomerates of PSS particles on the CNT walls (F) instead of a coating due to the changed solubility of PSS in the solution. A washing step after the dropcasting of the 2 wt.% PSS solution removed the excess polymer and enabled densification (G).

Thus, for the next experiment a 50:50 v/v mixture of water and isopropanol was used, as isopropanol has been shown to introduce better densification than water on CNT structures. However, PSS is not soluble enough in isopropanol, leading to the formation of island with PSS on the CNT structure (figure 6.3F). Thus, the PSS-solution was kept in water but washed afterwards multiple times to get rid of the excess PSS. This procedure worked perfectly and the lower amount of PSS also enabled densification and thus the formation of CNT honeycombs coated with a thin layer of PSS (figure 6.3G).

## 6 Summary

---

During the electrical characterization after coating (done by L. Nucara), no resistance change in the presence of heavy metal ions could be detected. This might be due to insufficient coating, not enough interaction or a too small effect of shrinking, compared to the water-induced swelling of the structure. Reversible addition fragmentation chain transfer (RAFT) polymerization for the grafting of polystyrene onto CNTs has been reported<sup>[192]</sup> and Menzel et al.<sup>[417]</sup> have shown a temperature activated polymerization on CNTs. Both methods might lead to a better interface between the CNTs and the active material and could be tried on the structure.

The same principle can be applied for infra-red sensors if the CNT structure is coated with temperature sensitive polymers. Those polymers should have a reversible upper critical solution temperature (UCST) phase transition rather than lower critical solution temperature (LCST) phase transition, meaning they should swell above a certain temperature, not shrink. This eliminates poly(N-isopropylacrylamide) as the obvious choice of a temperature sensitive polymer. A suitable other polymer needs to be found. This will be part of S. Mahdi's PhD project.

### 3D CNT structures for bone tissue engineering

Another interesting area for the application of 3D CNT structures is bone tissue engineering. This project was done in collaboration with Laurien Van den Broeck, KU Leuven, during her 6 months research stay in our group. Hydrogels are used in bone tissue engineering as a matrix for the cells to grow, providing an environment that closely resembles the physiological environment of the cells due to their high water content and structural similarity with macromolecules in the body. However, these fail in giving proper support as bone scaffolds due to their low stiffness. Bone tissue itself is composed of two components: collagen fibres with hydroxyapatite (HAp,  $\text{Ca}_{10}(\text{PO}_4)_6(\text{OH})_2$ ) along them, providing an environment made from soft and hard tissue.<sup>[428,429]</sup> Mimicking this environment is crucial for regenerative osteogenesis, thus a novel hybrid structure is needed. The goal of the project was to use HAp-coated CNT structures as growth promoter and reinforcement in the hydrogel, mimicking the anisotropic bone structure. Cell growth has been shown before to be favored on 3D CNT networks.<sup>[430]</sup> Our 3D CNT structure provides the possibility to tune the pore sizes and achieve large scale uniform structures. The HAp coating is added to additionally support the preosteoblast differentiation.

Initially a range of protocols for the formation of HAp<sup>[431-434]</sup> was adapted in a microwave-assisted, hydrothermal synthesis for the coating of CNTs. Once a uniform coating of HAp on CNT powders could be achieved (figure 6.4A), the synthesis method was applied to CNT honeycomb structures, grown on a Si-wafer. A nice and uniform coating could be achieved on the CNT honeycombs (figure 6.4B), the EDX showed (in addition the carbon) calcium, phosphorous and oxygen, indicating that the desired elements are coating the structure (figure 6.4D) and the XRD showed the desired phase (figure 6.4E). Additionally, hydrogel coating experiments on the CNT honeycombs with polyethylene glycol hydrogel were done. The CNT honeycomb structure remained intact (figure 6.4C) but did not seem to be encapsulated in the hydrogel. Only a small layer of the hydrogel was visible on the CNT structure (inset in figure 6.4C). This might have been due to the drying conditions which have to be adjusted.

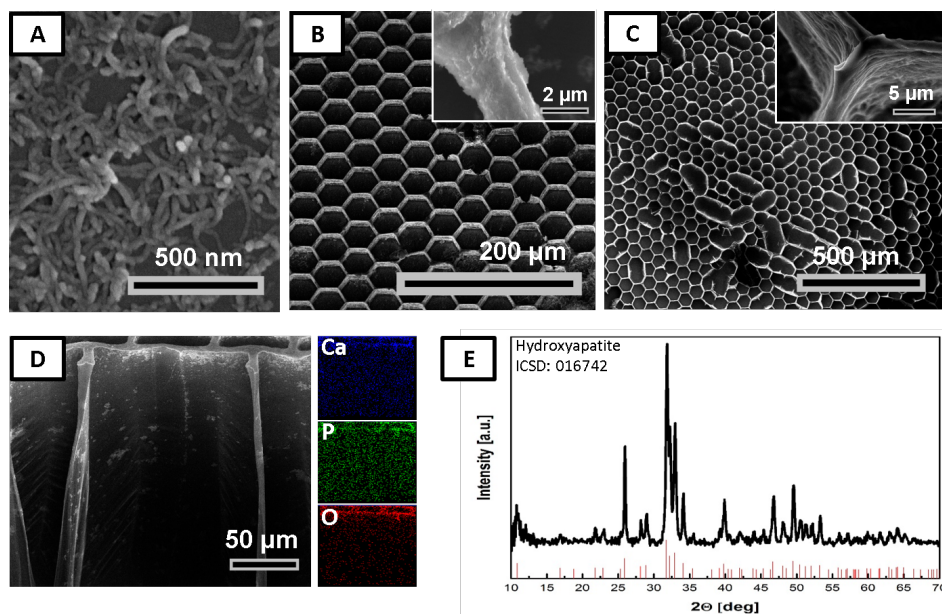


**Fig. 6.4** The microwave-assisted, hydrothermal coating of CNT powders was successful (A) and thus transferred to the coating of CNT honeycomb structures (B) which could be coated uniformly. The coating was analyzed using EDX (D) which showed the desired elements Ca, P and O in addition to carbon, and XRD (E) which confirmed the phase as hydroxyapatite. The encapsulation of the CNT honeycomb structure was not yet successful. Even though it did not damage the overall structure (C), it only left a very thin hydrogel film on the CNT structure instead of completely encapsulating it in a hydrogel.

Thus, the hydrogel encapsulation of the honeycomb structures needs to be improved, so it can be adapted to the HAp coated honeycomb structures. Cell growth experiments, as well nano-indentation and dynamic mechanical analysis to determine the improvement of the mechanical properties of the hydrogel-CNT hybrid structure will then be done by L. Van den Broeck. Higher 3D CNT structures and a change in cell sizes would be very desirable and thus the project can be further optimized to provide the best conditions for cell growth with adjusted pore sizes and heights.

A further application not explored within the work or side projects of this thesis is in catalysis to provide scaffold with a high surface area for heterogeneous catalysis and water filtration as mechanical filter membranes.



## **Chapter 7**

# **Experimental Section**

### 7.1 3D CNT structure preparation

#### 7.1.1 Catalyst patterning

The catalyst is prepared on a silicon wafers in two different ways - by UV-lithography up to the resolution limit of the employed slide mask (1.8  $\mu\text{m}$ ) and by colloidal lithography to achieve smaller patterns in a less expensive way.

##### 7.1.1.1 UV-lithography

After rinsing with acetone and isopropanol (IPA), the Si-wafer (100) is cleaned by exposure to Oxygen ( $\text{O}_2$ ) plasma for 360 s. The Si-wafer is then heated to 200  $^\circ\text{C}$  for 5 minutes for complete dehydration. Subsequently, the adhesion promotor Ti-prime is spincoated onto the wafer (4000 rpm for 40 s), followed by a 2 min bake at 115  $^\circ\text{C}$ . Photoresist (AZ 5214E) is spin-coated on the wafer (3000 rpm for 30 s) and is pre-baked for 1 minute at 115  $^\circ\text{C}$ . Afterward, the coated wafer is exposed to UV-light in the mask aligner for 6 s (incident light intensity of 10  $\text{W}/\text{cm}^2$ ) with a hard contact time of 5 s. Subsequently the patterned wafer is developed for 2 min with in diluted AZ351B (20% v/v in  $\text{H}_2\text{O}$ ), rinsed with DI-water, and dried.

##### 7.1.1.2 Colloidal lithography

Hexagonally ordered monolayers of polystyrene (PS) particles (Polybead® Microspheres 0.8  $\mu\text{m}$  and 0.3  $\mu\text{m}$ ) were produced using a Langmuir-Blodgett-trough method, adapting a protocol by Vogel et al.<sup>[169]</sup> A 0.1 mM solution of sodium dodecyl sulfate in DI-water is prepared and the pH is adjusted to 10-11 using ammonia solution. This water subphase is used as the liquid phase in the LB trough. A Si-wafer piece is immersed into the water, then 100  $\mu\text{L}$  of the PS sphere solution (1/1 v/v% water/ethanol) are slowly deposited onto the water/ air interface using an Eppendorf pipette combined with a micromanipulator. The tip is in direct contact with the water phase and the PS sphere solution is very slowly deposited onto the interface, trying to not disturb it too much (figure 7.1). When the entire solution is deposited, the barriers of the LB trough are slowly closed until a large area monolayer of the spheres is formed. This can be seen by the iridescent color of the interface without any white areas, as these indicate multilayer formation. The surface tension is not measured during these experiments. The Si-wafer is slowly, manually pulled through the surface (at a 45° angle), capturing the PS monolayers, and dried inclined (45°).

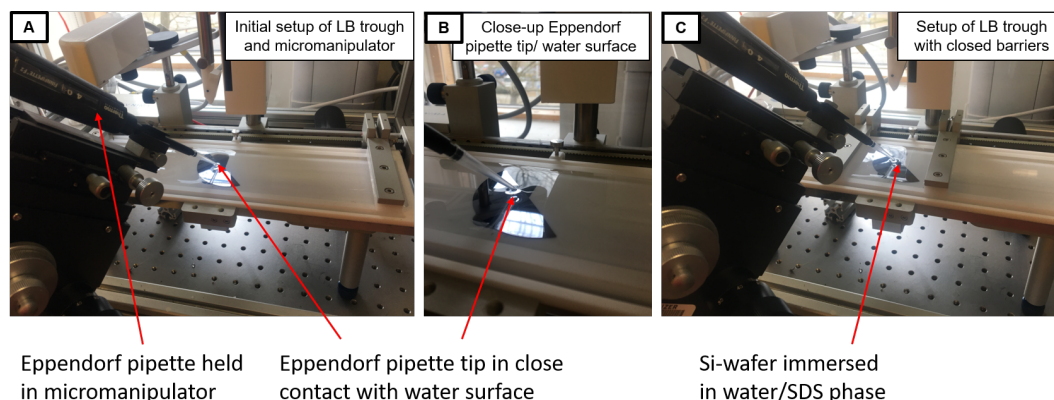


**Fig. 7.1** The setup for the monolayer deposition with the Eppendorf pipette in the micromanipulator for stability (A) and the tip in direct contact with the water subphase for PS sphere deposition (B). The barriers closing is shown in (C).

These monolayers are etched for increasing times (1 min, 2 min, 5 min, 10 min, 20 min) with  $O_2$  plasma at 50% -power and a pressure 0.8 mbar in a Diener plasma etcher to control the spacings between the circular patterns.

### 7.1.1.3 Catalyst deposition

After templating the Si-wafer with either photoresist or PS-particle monolayers, the catalyst is deposited onto the wafer using an e-beam physical vapor deposition (PVD) system. The catalyst typically deposited is a 10 nm alumina ( $Al_2O_3$ ,  $1 \text{ \AA s}^{-1}$ ), followed by a 1 nm iron-layer (Fe,  $0.25 \text{ \AA s}^{-1}$ ). For some experiments a layer of Molybdenum (40 nm,  $1 \text{ \AA s}^{-1}$ ) is deposited first before the standard catalyst.

### 7.1.1.4 Template lift-off

After catalyst deposition, the template needs to be removed; this step is called lift-off. For the UV-lithography, the photoresist is removed by sonicating the patterned wafer for 8 min in acetone, then 3 min in isopropanol (IPA) and then another 3 min in IPA. For colloidal lithography, the PS-spheres are dissolved in tetrahydrofuran (THF) by sonicating the Si wafer in THF for 20 min.

## 7.1.2 CNT forest growth

For the growth of vertically aligned CNTs (CNT "forests"), an ambient pressure tube furnace is used. The standard procedure for the growth is an annealing time of 14 minutes in a helium (100 sccm) and hydrogen (400 sccm) gas stream, followed by 1 minute adjustment time for the gas flow (helium to 400 sccm and hydrogen to 100 sccm) before ethylene (100 sccm) is introduced. Those are the standard flow rates. For some experiments a reduction in these flow rates to 20 sccm ethylene, 20 sccm hydrogen and 560 sccm helium is used to slow down the growth. Mostly, the growth time and the temperature is used to control the forest height. To improve adherence to the substrate,

## 7 Experimental Section

---

after the growth time the tube is pulled out of the furnace allowing the substrates to cool down while the helium-hydrogen-ethylene gas stream is still flowing. The typically used reaction parameters and their resulting forest heights are shown in table 7.1.

**Table 7.1** This table shows the used growth temperatures, times and flow rates and the resulting CNT structure heights.

Growth temperature [°C]	Growth time [min]	Flow rate	Growth height [ $\mu\text{m}$ ]	Used for
750	1	lowered	~2	Colloidal etching experiments
700	2	standard	~20	Crust etching experiments
720	16	standard	~100	Colloidal structures with Si
720	5	standard	~30	CNT honeycomb structures
720	2	standard	~15	Study of crack formation
720	4	standard	~27	Study of crack formation
720	6	standard	~46	Study of crack formation
720	8	standard	~86	Stress relieve features
800	30	standard	~330	High colloidal structures
750	60	standard	~500	High microscale CNT structures
800	1	standard	~100	Low microscale CNT structures

### 7.1.3 Crust removal by plasma or UV-ozone treatment

To enable good densification of the circular patterns, the crust needs to be etched away first. This is partly done by etching for 10 minutes in a Diener plasma cleaner with air plasma and partly using another Diener plasma cleaner with 50 % power and  $\text{O}_2$ -plasma for increasing times (see results). The standard etching time for air plasma to remove most of the crust is 10 minutes, in  $\text{O}_2$ -plasma it is 1 minute, and in UV-ozone 60 minutes. The methods are varied due to accessibility of the devices.

### 7.1.4 CNT honeycomb formation by densification

After etching of the crust the microscale circular patterns are densified using immersion densification. This is done by putting a drop of acetone on the structures and letting it evaporate. Densification of the colloidal structures is attempted by using a condensation method. Acetone is heated in a beaker on a hot plate at 180 °C. When a stable vapor front is achieved, the substrate is put into the resulting acetone vapor for ~3 s.

## 7.2 Honeycomb transfer onto polymer films and copper tape

### 7.2.1 PVA film fabrication and transfer

The PVA-film is prepared by depositing 500  $\mu\text{L}$  of a 10 wt% Polyvinyl alcohol (PVA, Mw 13,000-23,000  $\frac{\text{g}}{\text{mol}}$ , Sigma Aldrich) in DI-water solution on a clean Si-wafer at 60 °C. It is then heated up to 95 °C for 10 minutes. Then the temperature is increased to 180 °C for another 10 minutes to create a viscous PVA film and evaporate the solvent. The substrate with the CNT-structure is then placed on

the film, with the top of the structure in contact with the film. Approximately 2 g (Si-wafer piece) is placed on top of the wafer. This structure is then left for 5 minutes. The sample is removed from the hot plate and allowed to cool for 5 minutes. The upper wafer can be carefully lifted off with tweezers and the CNT-structure will be left in the PVA film.

### 7.2.2 PCP film fabrication and transfer

The PCP film was prepared following a protocol our group published previously.<sup>[65]</sup> In short, a solution of methanofullerene phenyl C61 butyric acid methyl ester (PCBM, 15 mg), poly(vinylidene fluoride) (PVDF, 300 mg) and CNTs (15 mg) in 6 ml dimethylformamide (DMF) is prepared, ballmilled for 2 hours at 300 rpm changing the rotation direction every 2 minutes with a 30 seconds break inbetween. The solution is then drop-casted onto a glass slide and slowly dried at 65 °C with a glass petri-dish covering it. After drying, the temperature is increased to 175 °C to soften the PVDF. The grown 3D CNT structures are then transferred onto the PCP film using microcontact printing. The structures are slightly pushed into the film with the tweezers but no additional weight is added on top of the structures for the standard transfer.

### 7.2.3 Transfer onto copper tape and annealing

The uncoated or Si-coated 3D CNT structure is transferred onto a sticky one-sided copper tape by microcontact printing. Similar to the transfer onto the polymer films, the structure is out onto the substrate and softly pushed onto it with tweezers. Then the Si-wafer is removed in a vertical upward motion. The structure remains on the Cu-tape. After the transfer the Cu-tape with the structure is annealed for 2 hours at 250 °C and 2 hours at 500 °C to carbonize the adhesive on the tape in inert atmosphere (helium, 250 sccm).

## 7.3 Inorganic modification of 3D CNT structures

### 7.3.1 Fe<sub>2</sub>O<sub>3</sub> by Li et al.<sup>[370]</sup>

For this synthesis, a published protocol<sup>[370]</sup> was slightly modified. 2 mM of iron(III) sulfate hydrate (Fe<sub>2</sub>(SO<sub>4</sub>)<sub>3</sub>·H<sub>2</sub>O, 244.98  $\frac{\text{g}}{\text{mol}}$ , Fisher) and 8 mM of urea (NH<sub>2</sub>CONH<sub>2</sub>, 60.06  $\frac{\text{g}}{\text{mol}}$ , Sigma-Aldrich) are dissolved in 50 mL of ethylene glycol (EG, 62.07  $\frac{\text{g}}{\text{mol}}$ , Fluka). 0.1 g of polyvinylpyrrolidone (PVP, K30, 40,000  $\frac{\text{g}}{\text{mol}}$ , Fluka) is added to the solution. After stirring for 10 minutes the solution is filled into teflon liners for the microwave reactor. The honeycomb structures on the Si-wafer chips are treated with air plasma for 10 minutes to increase the number of oxygen-containing surface groups and then slowly put into the solution. The liners are put into the microwave and heated to 160 °C for 5 hours. Afterwards the solution is filtered using vacuum filtration and the CNT structure is washed multiple times with DI-water. The filtered particles and the coated structure are dried at 80 °C overnight.

## 7 Experimental Section

---

### 7.3.2 Fe<sub>2</sub>O<sub>3</sub>-nanoflakes by Reddy et al.<sup>[280]</sup>

For this synthesis, a protocol by Reddy et al.<sup>[280]</sup> is slightly adapted. The CNT structures are coated with an iron film (Fe, 1 Å s<sup>-1</sup>) of about 100 nm by e-beam PVD. This is followed by a temperature treatment step of 5h at 300°C in air on a hotplate.

### 7.3.3 Fe<sub>2</sub>O<sub>3</sub> with Fe<sup>3+</sup> precursor

For the synthesis of iron oxide (Fe<sub>2</sub>O<sub>3</sub>), a published protocol by Wang et al.<sup>[320]</sup> is modified for the use as a microwave assisted synthesis.<sup>[320]</sup> The solution is prepared by dissolving 120 mg of iron(III) sulfate hydrate (Fe<sub>2</sub>(SO<sub>4</sub>)<sub>3</sub>·5H<sub>2</sub>O, 489.96  $\frac{\text{g}}{\text{mol}}$ , Acros) in 35 mL of DI-water and 5 mL of glycerol (92.09  $\frac{\text{g}}{\text{mol}}$ , Atom Scientific). After stirring for 10 minutes the solution is filled into two teflon liners (20 mL each) for the microwave reactor. The 3D CNT structures on the PCP film are treated with UV-ozone for 60 minutes on glass slides and then slowly put into the solution. For the modification of the CNT powder, 10 mg of oxidized CNTs are mixed with 20 mL of the above mentioned solution, sonicated for 30 minutes and then shaken overnight to ensure a uniform dispersion. Then the solution is filled into a teflon liner. The liners are put into the microwave and heated to 175 °C for 6 hours using the temperature sensor. Afterwards the solution is filtered using vacuum filtration and the CNT structure is washed multiple times with DI-water. The filtered particles and the coated structure are dried at 80 °C overnight.

### 7.3.4 Fe<sub>2</sub>O<sub>3</sub> with Fe<sup>2+</sup> precursor

For the synthesis of iron oxide (Fe<sub>2</sub>O<sub>3</sub>), a published protocol by Wang et al.<sup>[320]</sup> is modified for the use as a microwave assisted synthesis.<sup>[320]</sup> The solution is prepared by dissolving 120 mg of Iron(II) sulfate hydrate (Fe<sub>2</sub>SO<sub>4</sub>·7H<sub>2</sub>O, 278.01  $\frac{\text{g}}{\text{mol}}$ , Acros) in 35 mL of DI-water and 5 mL of Glycerol (92.09  $\frac{\text{g}}{\text{mol}}$ , Atom Scientific). After stirring for 10 minutes the solution is filled into two teflon liners (20 mL each) for the microwave reactor. For the VA-CNT structure modification, the structures on the PCP film are treated with UV-ozone for 60 minutes on glass slides and then slowly put into the solution. The liners are put into the microwave and heated to 175 °C for 6 hours using the temperature sensor. Afterwards the solution is filtered using vacuum filtration and the CNT structure is washed multiple times with DI-water. The filtered particles and the coated structure are dried at 80 °C overnight.

For the temperature screen of both reactions, the reaction temperature is 130, 145, 160, 175 and 190 °C for each reaction. For the different reaction times, the synthesis with Fe<sup>2+</sup> precursor is stopped after 10 min, 30 min, 1 hour, 2, 3, 4 and 5 hours.

### 7.3.5 Si-CVD

A thermal CVD process using SiH<sub>4</sub> as a precursor in an argon atmosphere is used to achieve the modification of 3D CNT structures fabricated by colloidal lithography. The coating of the samples is done with the help of Yanting Jin, a PhD student in the Department of Chemistry who used a

process initially reported by Ogata et al.<sup>[231]</sup> from their group and then by Y. Jin herself<sup>[232]</sup> for the formation of Si-nanowires. The deposition is run at 550 °C for 15 and 30 minutes with the colloidal structure on a Si-wafer inside the chamber at 15 mbar.

### 7.3.6 Si-PVD

For the deposition of Si onto the colloidal honeycomb structures at imec, Belgium, an e-beam evaporation with a deposition rate of  $4.9 \text{ \AA s}^{-1}$  is used.

### 7.3.7 Microwave-assisted synthesis of BiVO<sub>4</sub>

**Protocol by Zhang et al.**<sup>[416]</sup> Following a published protocol for monoclinic bismuth vanadate (BiVO<sub>4</sub>) nanostructures,<sup>[235]</sup> an aqueous solutions of 1 mmol bismuth nitrate pentahydrate (Bi(NO<sub>3</sub>)<sub>3</sub>, 485.07  $\frac{\text{g}}{\text{mol}}$ , Sigma Aldrich) and 1 mmol ammonium metavanadate (NH<sub>4</sub>VO<sub>3</sub>, 116.98  $\frac{\text{g}}{\text{mol}}$ , Sigma Aldrich) in 40 mL DI water is prepared. After stirring for 30 minutes at room temperature, the solution is filled into two teflon liners (20 mL each) for the microwave reactor. The CNT honeycomb structures on Si-wafers are treated with UV-ozone for 30 minutes and then slowly put into the solution. The liners are put into the microwave and heated to 180 °C for 6 hours using the temperature sensor. Afterwards the solution is filtered using vacuum filtration and the CNT structure is washed multiple times with DI-water. The filtered particles and the coated structure are dried at 80 °C overnight.

**Protocol by Shang et al.**<sup>[256]</sup> Following a published protocol for hierarchical bismuth vanadate (BiVO<sub>4</sub>) nanostructures,<sup>[256]</sup> a solution of 0.5 mmol bismuth nitrate pentahydrate (Bi(NO<sub>3</sub>)<sub>3</sub>, 485.07  $\frac{\text{g}}{\text{mol}}$ , Sigma Aldrich) and 0.5 mmol ammonium metavanadate (NH<sub>4</sub>VO<sub>3</sub>, 116.98  $\frac{\text{g}}{\text{mol}}$ , Sigma Aldrich) in 40 mL ethylene glycol (EG, 62.06  $\frac{\text{g}}{\text{mol}}$ , Acros Organics) is prepared and stirred for 10 minutes. Then 20 mL each of the solution are filled into two teflon liners for the microwave reactor. To introduce hydrophilicity and reactive groups, the honeycomb structures on the Si-wafer chips are treated with UV-ozone for 30 minutes and then slowly put into the solution. The liners are put into the microwave and heated to 140 °C for one hour. Afterwards the solution is filtered using vacuum filtration and the CNT structure is washed multiple times with DI-water. The filtered particles and the coated structure are dried at 80 °C overnight.

For some reactions the 3D CNT structure is soaked overnight in the vanadium precursor, and then put into the bismuth precursor right before the reaction start.

For the thermal treatment before the BiVO<sub>4</sub> modification, the protocol described by Menzel et al.<sup>[417]</sup> is adapted. The 3D CNT structure is put into a glass tube in the CVD furnace. The furnace is heated to 500 °C and then the tube is pushed into the furnace four times for 5 minutes with 2 minutes cooling time in between. The next step is a 2 hour temperature treatment in helium at 500 °C. Immediately after the sample is put into the prepared precursor solution in the teflon liner.

## 7 Experimental Section

---

**Protocol by Ma et al.**<sup>[415]</sup> Following a published protocol for olive-like bismuth vanadate ( $\text{BiVO}_4$ ) nanostructures,<sup>[415]</sup> solutions of 1 mmol bismuth nitrate pentahydrate ( $\text{Bi}(\text{NO}_3)_3$ ,  $485.07 \frac{\text{g}}{\text{mol}}$ , Sigma Aldrich) in 30 mL EG and 1 mmol ammonium metavanadate ( $\text{NH}_4\text{VO}_3$ ,  $116.98 \frac{\text{g}}{\text{mol}}$ , Sigma Aldrich) in 10 mL DI-water are prepared and stirred for 30 minutes. Then 5 mL of the vanadium precursor and 15 mL of the bismuth precursor are filled into a teflon liner for the microwave reactor. To introduce hydrophilicity and reactive groups, the CNT honeycomb structures on the Si-wafer chips are treated with air plasma for 10 minutes or UV-ozone for 30 minutes and then slowly put into the solution. The liners are put into the microwave and heated to 140 °C for 4 hours. Afterwards the solution is filtered using vacuum filtration and the CNT structure is washed multiple times with DI-water. The filtered particles and the coated structure are dried at 80 °C overnight.

For some reactions the 3D CNT structure is soaked overnight in the vanadium precursor, and then put into the bismuth precursor right before the reaction start.

**Protocol by Liu et al.**<sup>[413]</sup> Adapting the first published, hydrothermal protocol for bismuth vanadate ( $\text{BiVO}_4$ ),<sup>[413]</sup> solutions of 1 mmol bismuth nitrate pentahydrate ( $\text{Bi}(\text{NO}_3)_3$ ,  $485.07 \frac{\text{g}}{\text{mol}}$ , Sigma Aldrich) in 20 mL DI-water and 1 mmol sodium vanadium oxide ( $\text{NaVO}_3$ ) are prepared.  $\text{NaVO}_3$  is prepared by dissolving 39.997 mg NaOH in 20 mL DI-water and adding 9.09 mg vanadium(V)oxide ( $\text{V}_2\text{O}_5$ ,  $181.88 \frac{\text{g}}{\text{mol}}$ , Sigma Aldrich). All solutions are stirred for 30 minutes and then mixed together. The pH is adjusted to 7 using NaOH. Then 20 mL of the mixed precursor solution is filled into a teflon liner for the microwave reactor. To introduce hydrophilicity and reactive groups, the CNT honeycomb structures on the Si-wafer chips are treated with UV-ozone for 30 minutes (or with a thermal treatment as described before) and then slowly put into the solution. The liners are put into the microwave and heated to 140 °C for 3 hours. Afterwards the solution is filtered using vacuum filtration and the CNT structure is washed multiple times with DI-water. The filtered particles and the coated structure are dried at 80 °C overnight.

The concentration is lowered to  $1/10$  for some experiments. Additionally, an experiment is also conducted using the stirred reactor. Exactly the same conditions as described for the microwave-assisted, hydrothermal method are used, apart from the reaction time which is increased to the initially reported 12 hours.

### 7.3.8 Hotcasting of $\text{BiVO}_4$

The hotcasting protocols with the specific chemicals and concentrations are shown in the table 7.2. In the standard protocol, the precursor solution are either subsequently or together put onto the sample on a hotplate. Then the hotplate is heated to 350 °C (if not otherwise specified) and the solvent is removed. To finalize the  $\text{BiVO}_4$  crystallization, the sample is annealed at 500 °C for 2 hours with helium flowing at 350 sccm with a ramp rate of 10 °C/min.

**Table 7.2** An overview of BiVO<sub>4</sub> hotcasting experiments with changes in precursor, concentration, solvent and reaction temperature is given here.

Bismuth Source	Solvent	Vanadium Source	Solvent	Concentration	Pre-mixed?	Volume (μl)	Repetitions	Pre-densified?	Hot-Plate Temperature (°C)	Uniform Coating?	Correct Phase?
Bi(NO <sub>3</sub> ) <sub>3</sub> ·5H <sub>2</sub> O	Acetic Acid	VO(acac) <sub>2</sub>	Acetylacetone	0.303	y	10	0	n	350	y	n
Bi(NO <sub>3</sub> ) <sub>3</sub> ·5H <sub>2</sub> O	Acetic Acid	VO(acac) <sub>2</sub>	Acetylacetone	0.303	y	10	2	n	350	y	n
Bi(NO <sub>3</sub> ) <sub>3</sub> ·5H <sub>2</sub> O	Acetic Acid	VO(acac) <sub>2</sub>	Acetylacetone	0.1515	y	10	0	n	350	y	n
Bi(NO <sub>3</sub> ) <sub>3</sub> ·5H <sub>2</sub> O	Acetic Acid	VO(acac) <sub>2</sub>	Acetylacetone	0.1515	y	10	2	n	350	y	n
Bi(NO <sub>3</sub> ) <sub>3</sub> ·5H <sub>2</sub> O	Acetic Acid	VO(acac) <sub>2</sub>	Acetylacetone	0.1667	y	10	0	n	350	y	n
Bi(NO <sub>3</sub> ) <sub>3</sub> ·5H <sub>2</sub> O	Acetic Acid	VO(acac) <sub>2</sub>	Acetylacetone	0.08335	y	10	0	n	350	y	n
Bi(NO <sub>3</sub> ) <sub>3</sub> ·5H <sub>2</sub> O	Acetic Acid	VO(acac) <sub>2</sub>	Acetylacetone	0.041675	y	10	0	n	350	y	n
Bi(NO <sub>3</sub> ) <sub>3</sub> ·5H <sub>2</sub> O	Acetic Acid	VO(acac) <sub>2</sub>	Acetylacetone	0.08335	y	10	0	y	350	y	n
Bi(NO <sub>3</sub> ) <sub>3</sub> ·5H <sub>2</sub> O	Acetic Acid	VO(acac) <sub>2</sub>	Acetylacetone	0.041675	y	10	0	y	350	y	n
Bi(NO <sub>3</sub> ) <sub>3</sub> ·5H <sub>2</sub> O	Ethylene Glycol	NH <sub>4</sub> VO <sub>3</sub>	Ethylene Glycol	0.025	y	10	0	y	350	y	n
Bi(NO <sub>3</sub> ) <sub>3</sub> ·5H <sub>2</sub> O	Ethylene Glycol	NH <sub>4</sub> VO <sub>3</sub>	Ethylene Glycol	0.025	y	10	0	n	350	y	n
Bi(NO <sub>3</sub> ) <sub>3</sub> ·5H <sub>2</sub> O	Ethylene Glycol & Acetone	NH <sub>4</sub> VO <sub>3</sub>	Ethylene Glycol & Acetone	0.0125	y	10	0	n	350	y	n
Bi(NO <sub>3</sub> ) <sub>3</sub> ·5H <sub>2</sub> O	Ethylene Glycol	NH <sub>4</sub> VO <sub>3</sub>	Ethylene Glycol	0.0125	y	10	0	n	350	y	n
Bi(NO <sub>3</sub> ) <sub>3</sub> ·5H <sub>2</sub> O	Ethylene Glycol & IPA	NH <sub>4</sub> VO <sub>3</sub>	Ethylene Glycol & IPA	0.0125	y	10	0	n	350	y	n
Bi(NO <sub>3</sub> ) <sub>3</sub> ·5H <sub>2</sub> O	Ethylene Glycol & H <sub>2</sub> O	NH <sub>4</sub> VO <sub>3</sub>	Ethylene Glycol & H <sub>2</sub> O	0.0125	y	10	0	n	350	y	n
Bi(NO <sub>3</sub> ) <sub>3</sub> ·5H <sub>2</sub> O	Ethylene Glycol	NH <sub>4</sub> VO <sub>3</sub>	H <sub>2</sub> O	0.025	y	20	0	y	350	y	n
Bi(NO <sub>3</sub> ) <sub>3</sub> ·5H <sub>2</sub> O	Ethylene Glycol	NH <sub>4</sub> VO <sub>3</sub>	H <sub>2</sub> O	0.025	y	20	0	y	350	y	n
Bi(NO <sub>3</sub> ) <sub>3</sub> ·5H <sub>2</sub> O	Ethylene Glycol	NH <sub>4</sub> VO <sub>3</sub>	H <sub>2</sub> O	0.025	n	40	0	y	350	y	n
Bi(NO <sub>3</sub> ) <sub>3</sub> ·5H <sub>2</sub> O	Ethylene Glycol	NH <sub>4</sub> VO <sub>3</sub>	H <sub>2</sub> O	0.025	n	40	0	y	350	y	n
Bi(NO <sub>3</sub> ) <sub>3</sub> ·5H <sub>2</sub> O	Ethylene Glycol	NH <sub>4</sub> VO <sub>3</sub>	H <sub>2</sub> O	0.025	n	40	0	y	200	y	n
Bi(NO <sub>3</sub> ) <sub>3</sub> ·5H <sub>2</sub> O	Ethylene Glycol	NH <sub>4</sub> VO <sub>3</sub>	H <sub>2</sub> O	0.025	n	40	0	y	100	y	n
Bi(NO <sub>3</sub> ) <sub>3</sub> ·5H <sub>2</sub> O	Ethylene Glycol	NH <sub>4</sub> VO <sub>3</sub>	H <sub>2</sub> O	0.025	n	40	0	y	25	y	n
Bi(NO <sub>3</sub> ) <sub>3</sub> ·5H <sub>2</sub> O	2M HNO <sub>3</sub> in H <sub>2</sub> O	V <sub>2</sub> O <sub>5</sub>	2M HNO <sub>3</sub> in H <sub>2</sub> O	0.05	y	20	0	n	350	y	n
Bi(NO <sub>3</sub> ) <sub>3</sub> ·5H <sub>2</sub> O	2M HNO <sub>3</sub> in H <sub>2</sub> O	V <sub>2</sub> O <sub>5</sub>	2M HNO <sub>3</sub> in H <sub>2</sub> O	0.05	y	20	0	y	350	y	n
Bi(NO <sub>3</sub> ) <sub>3</sub> ·5H <sub>2</sub> O	2M HNO <sub>3</sub> in H <sub>2</sub> O	V <sub>2</sub> O <sub>5</sub>	2M HNO <sub>3</sub> in H <sub>2</sub> O	0.05	n	20	0	n	350	y	y
Bi(NO <sub>3</sub> ) <sub>3</sub> ·5H <sub>2</sub> O	2M HNO <sub>3</sub> in H <sub>2</sub> O	V <sub>2</sub> O <sub>5</sub>	2M HNO <sub>3</sub> in H <sub>2</sub> O	0.05	n	20	0	y	350	y	y
Bi(NO <sub>3</sub> ) <sub>3</sub> ·5H <sub>2</sub> O	2M HNO <sub>3</sub> in H <sub>2</sub> O	V <sub>2</sub> O <sub>5</sub>	2M HNO <sub>3</sub> in H <sub>2</sub> O	0.05	n	40	0	y	350	y	y

The Au/Pd deposition before some of the hotcasting is done for 30 s with a sputtering system at a 60 mA current.

## 7.4 Further modification of 3D CNT structures

### 7.4.1 PSS-coating

20 μL of a poly(sodium 4-styrenesulfonate) solution (PSS, M<sub>w</sub> 70,000, 30 wt.% in water, Sigma Aldrich) is dropcasted onto the CNT honeycomb structure and dried on a hotplate at 100 °C. For further experiments the solution is diluted to 2 wt.% in DI-water or 1 wt.% 50:50 v/v % H<sub>2</sub>O: IPA, dropcasted and dried at 100 °C. The samples with 2 wt.% in DI-water is washed overnight in DI-water and afterwards again dried on a hotplate.

### 7.4.2 HAp-coating

A microwave-assisted, hydrothermal protocol is adapted<sup>[432,434]</sup> to synthesize hydroxyapatite. A ratio of 2:1 EG and DI-water is prepared and the pH is adjusted to 11 using ammonium hydroxide (NH<sub>3</sub>, Sigma Aldrich). 0.1 M Calcium nitrate tetrahydrate (Ca(NO<sub>3</sub>)<sub>2</sub>·4H<sub>2</sub>O, 236.15  $\frac{\text{g}}{\text{mol}}$ , Alfa Aesar) and 0.1 M ammonium phosphate dibasic ((NH<sub>4</sub>)<sub>2</sub>HPO<sub>4</sub>, 132.06  $\frac{\text{g}}{\text{mol}}$ , Sigma Aldrich) are dissolved in the EG/water mixture. The calcium nitrate tetrahydrate reactants are added to the ammonium phosphate dibasic reactants to reach a molecular Ca/P ratio of 1.67. The final solution is put into a teflon liner for the microwave reactor. To introduce hydrophilicity and reactive groups, the CNT honeycomb

## 7 Experimental Section

structures on the Si-wafer chips are treated with UV-ozone for 60 minutes and then slowly put into the solution. The liners are put into the microwave and heated to 180 °C for 10 minutes. Afterwards the solution is filtered using vacuum filtration and the CNT structure is washed multiple times with DI-water. The filtered particles and the coated structure are dried at 80 °C overnight.

### 7.5 Electrochemical measurements

#### 7.5.1 Battery electrode fabrication

CR 2032 type cells were assembled in Ar filled glove box in a half-cell configuration. The 3D CNT structures coated with iron oxide or silicon and a pure Li metal foil were used as electrodes with  $\text{LiPF}_6$  in EMC and DEC as electrolyte and a glass fibre (Whatman) disc as separator. The electrochemical measurements were carried out using a VMP3 Biologics multi-channel potentiostat/battery cycler. These measurements were done by S. Engelke.

#### 7.5.2 Photoelectrode measurements

The electrochemical characterization of the  $\text{BiVO}_4$  coated CNT structures was done by J. Rongé at KU Leuven. A three-electrode configuration with graphite as a counter electrode and  $\text{Ag}/\text{AgCl}$  as a reference electrode was used with 1 M sodium sulfite ( $\text{Na}_2\text{SO}_3$ ) and 0.1 M KPi buffer (pH 7), with a 400 W Xe lamp with an AM 1.5 filter. The cell was stirred but not purged with gas. The experimental setup is shown in figure 7.2. These measurements were done by J. Rongé.

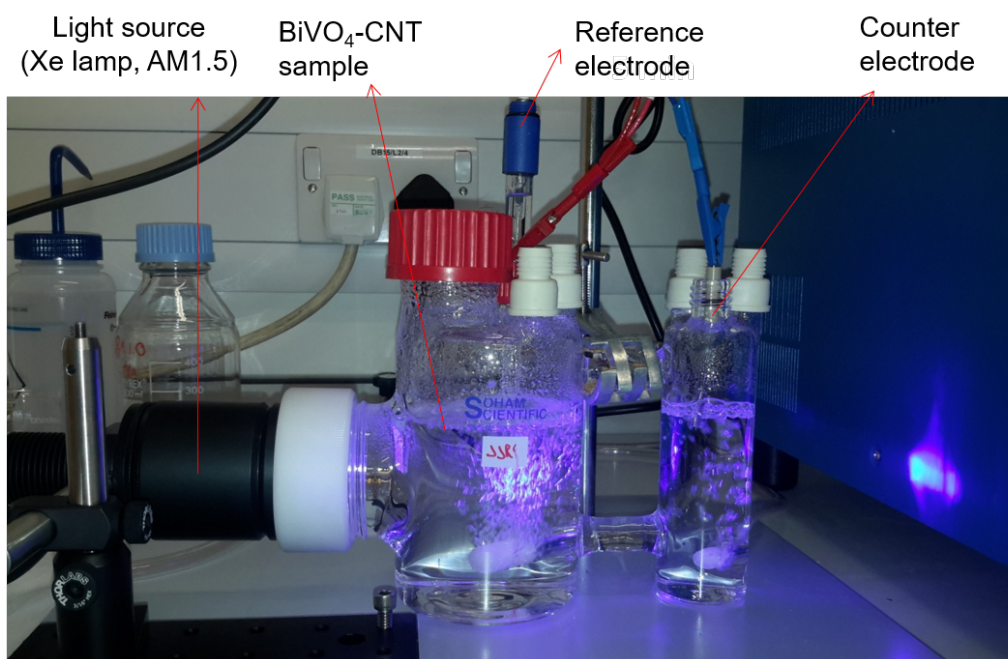


**Fig. 7.2** Set-up for electrochemical measurements for the advanced  $\text{BiVO}_4$  photoelectrode structure (image taken by J. Rongé).

## 7.6 Equipment

**Mask-aligner** A contact Mask Aligner MJB-4 from Karl Suss is used for the exposure of the photoresist to UV-light. The exposure time is regularly adjusted to the power of the lamp in the system.

**e-beam PVD** An e-beam PVD-system from Lesker (LEV-Lesker, PVD 75, four-crucible e-beam evaporator) is used to evaporate alumina ( $\text{Al}_2\text{O}_3$ ), aluminium (Al), molybdenum and iron (Fe) at a pressure of approximately 6  $\mu\text{Torr}$ . An e-beam PVD-system from Pfeiffer (PLS-B) is used at imec to evaporate silicon (Si) onto the CNT structures.

**SEM** The SEM measurements are performed with a Leo 1530VP Gemini from Zeiss operating at an accelerating voltage of 8 kV and using the InLens-detector. The working distance is varied between 3-10 mm. Samples are not sputtered with a metal layer.

**XRD** The XRD-system used is a D8- B1- Gen10 Bruker XRD. Measurements are done with a stepsize of  $0.05^\circ(2\theta)$ , and a step time of 0.5 s, if not otherwise indicated. The time-scan measurements for  $\text{Fe}_2\text{O}_3$  are done with a stepsize of  $0.025^\circ(2\theta)$ , and a step time of 0.1 s with a D8-B3-Gen9 Bruker D8 DAVINCI XRD. The software X-Pert Highscore Plus is used for the data evaluation.

**Microwave reactor** A microwave reaction system (Multiwave PRO) by Anton Paar with a pressure and temperature sensor is used for the microwave synthesis.

**Plasma cleaner** Two different plasma cleaners are used. A small Diener Femto plasma cleaner (40kHz/100W) is used with air plasma. A Diener Femto plasma etcher (60 Hz/ 3680W) is used with  $\text{O}_2$ -plasma in the clean room.

**UV-ozone** A UV-ozone generating system from Bioforce nanoscience is used for the etching of the crust and activation of the CNT structures.

**Stirred reactor** A stirred reactor system by Parr is used for one  $\text{BiVO}_4$  synthesis.



# Bibliography

- [1] Kroto, H. W.; Heath, J. R.; O'Brien, S. C.; Curl, R. F.; Smalley, R. E. *Nature* **1985**, *318*, 162–163.
- [2] Harris, P. J. F., Ed. *Carbon Nanotube Science - Synthesis, properties and applications*; Cambridge University Press: Cambridge, 2009.
- [3] Novoselov, K. S.; Geim, A. K.; Morozov, S. V.; Jiang, D.; Zhang, Y.; Dubonos, S. V.; Grigorieva, I. V.; Firsov, A. A. *Science* **2004**, *306*, 666–669.
- [4] Iijima, S. *Nature* **1991**, *354*, 56–58.
- [5] De Volder, M. F. L.; Tawfick, S. H.; Baughman, R. H.; Hart, A. J. *Science* **2013**, *339*, 535–539.
- [6] Prasek, J.; Drbohlavova, J.; Chomoucka, J.; Hubalek, J.; Jasek, O.; Adam, V.; Kizek, R. *Journal of Materials Chemistry* **2011**, *21*, 15872.
- [7] Peng, B.; Locascio, M.; Zapol, P.; Li, S.; Mielke, S. L.; Schatz, G. C.; Espinosa, H. D. *Nature Nanotechnology* **2008**, *3*, 626–631.
- [8] Wei, B. Q.; Vajtai, R.; Ajayan, P. M. *Applied Physics Letters* **2001**, *79*, 1172–1174.
- [9] Pop, E.; Mann, D.; Wang, Q.; Goodson, K.; Dai, H. *Nano Letters* **2006**, *6*, 96–100.
- [10] Pilgrim, G. a.; Leadbetter, J. W.; Qiu, F.; Siitonen, A. J.; Pilgrim, S. M.; Krauss, T. D. *Nano Letters* **2014**, *14*, 1728–1733.
- [11] Kar, S.; Bindal, R.; Tewari, P. *Nano Today* **2012**, *7*, 385–389.
- [12] Wang, Y.; Zhu, J.; Huang, H.; Cho, H.-H. *Journal of Membrane Science* **2015**, *479*, 165–174.
- [13] Gupta, V. K.; Agarwal, S.; Saleh, T. A. *Water research* **2011**, *45*, 2207–12.
- [14] Zardini, H. Z.; Amiri, A.; Shanbedi, M.; Maghrebi, M.; Baniadam, M. *Colloids and Surfaces B: Biointerfaces* **2012**, *92*, 196–202.
- [15] El Badawi, N.; Ramadan, A. R.; Esawi, A. M. K.; El-Morsi, M. *Desalination* **2014**, *344*, 79–85.
- [16] Chen, J.; Yan, L. *Advances in Materials* **2017**, *6*, 129.
- [17] Arash, B.; Wang, Q.; Varadan, V. K. *Scientific Reports* **2014**, *4*, 1–8.
- [18] Peng, H. *Journal of the American Chemical Society* **2008**, *130*, 42–43.
- [19] Si, J.; Zhong, D.; Xu, H.; Xiao, M.-M.; Yu, C.; Zhang, Z.; Peng, L. *ACS Nano* **2018**, acsnano.7b07665.
- [20] Brady, G. J.; Way, A. J.; Safron, N. S.; Evensen, H. T.; Gopalan, P.; Arnold, M. S. *Science Advances* **2016**, *2*, e1601240–e1601240.

- [21] Franklin, A. D. *Nature* **2013**, *498*, 443–444.
- [22] Choi, W. B.; Chu, J. U.; Jeong, K. S.; Bae, E. J.; Lee, J. W.; Kim, J. J.; Lee, J. O. *Applied Physics Letters* **2001**, *79*, 3696–3698.
- [23] Tans, S.; Verschueren, A.; Dekker, C. *Nature* **1998**, *672*, 669–672.
- [24] Eichler, A.; Moser, J.; Chaste, J.; Zdrojek, M.; Wilson-Rae, I.; Bachtold, A. *Nature Nanotechnology* **2011**, *6*, 339–342.
- [25] Eom, K.; Park, H. S.; Yoon, D. S.; Kwon, T. *Physics Reports* **2011**, *503*, 115–163.
- [26] Kis, A.; Zettl, A. *Philosophical transactions. Series A, Mathematical, physical, and engineering sciences* **2008**, *366*, 1591–1611.
- [27] Balasubramanian, K.; Kern, K. *Advanced Materials* **2014**, *26*, 1154–1175.
- [28] Shim, M. *Nano Letters* **2002**, *2*, 285–288.
- [29] Balasubramanian, K.; Kurkina, T.; Ahmad, A.; Burghard, M.; Kern, K. *Journal of Materials Research* **2012**, *27*, 391–402.
- [30] Lahiff, E.; Lynam, C.; Gilmartin, N.; O’Kennedy, R.; Diamond, D. *Analytical and Bioanalytical Chemistry* **2010**, *398*, 1575–1589.
- [31] Yang, W.; Ratinac, K. R.; Ringer, S. R.; Thordarson, P.; Gooding, J. J.; Braet, F. *Angewandte Chemie - International Edition* **2010**, *49*, 2114–2138.
- [32] Jiang, Y.; Wang, P.; Zang, X.; Yang, Y.; Kozinda, A.; Lin, L. *Nano Letters* **2013**, *13*, 3524–3530.
- [33] Hecht, D. S.; Hu, L.; Irvin, G. *Advanced Materials* **2011**, *23*, 1482–513.
- [34] Lee, S. W.; Kim, J.; Chen, S.; Hammond, P. T.; Shao-Horn, Y. *ACS Nano* **2010**, *4*, 3889–3896.
- [35] Kreupl, F. *Nature* **2012**, *484*, 321–322.
- [36] Wen, L.; Li, F.; Cheng, H.-M. *Advanced Materials* **2016**, *28*, 4306–4337.
- [37] Chen, J.; Liu, Y.; Minett, A. I.; Lynam, C.; Wang, J.; Wallace, G. G. *Chemistry of Materials* **2007**, *19*, 3595–3597.
- [38] Yamada, T.; Hayamizu, Y.; Yamamoto, Y.; Yomogida, Y.; Izadi-Najafabadi, A.; Futaba, D. N.; Hata, K. *Nature Nanotechnology* **2011**, *6*, 296–301.
- [39] Lipomi, D. J.; Vosgueritchian, M.; Tee, B. C.-K.; Hellstrom, S. L.; Lee, J. A.; Fox, C. H.; Bao, Z. *Nature nanotechnology* **2011**, *6*, 788–92.
- [40] Zhang, R.; Zhang, Y.; Zhang, Q.; Xie, H.; Qian, W.; Wei, F. *ACS Nano* **2013**, *7*, 6156–6161.
- [41] Shaffer, M.; Fan, X.; Windle, A. H. *Carbon* **1998**, *36*, 1603–1612.
- [42] Wu, J.; Antaris, A.; Gong, M.; Dai, H. *Advanced Materials* **2014**, 6151–6156.
- [43] Kumar, M. K.; Jayanisha, V.; Manjari, R.; Prabu, S. B.; Padmanabhan, K. A. *Materials Letters* **2014**, *114*, 68–71.
- [44] Baughman, R. H.; Zakhidov, A. A.; de Heer, W. A. *Science* **2002**, *297*, 787–792.
- [45] Li, Y.-L.; Kinloch, I. A.; Windle, A. H. *Science* **2004**, *304*, 276–278.
- [46] Zhang, M.; Atkinson, K. R.; Baughman, R. H. *Science* **2004**, *306*, 1358–1361.

- [47] Vigolo, B.; Pénicaud, A.; Coulon, C.; Sauder, C.; Pailler, R.; Journet, C.; Bernier, P.; Poulin, P. *Science* **2000**, *290*, 1331–1334.
- [48] Ericson, L. M. et al. *Science* **2004**, *305*, 1447–1450.
- [49] Hata, K.; Futaba, D. N.; Mizuno, K.; Namai, T.; Yumura, M.; Iijima, S. *Science* **2004**, *306*, 1362–1364.
- [50] Yasuda, S.; Futaba, D.; Yamada, T.; Satou, J. *ACS Nano* **2009**, *3*, 4164–4170.
- [51] Li, W. Z.; Xie, S. S.; Qian, L. X.; Chang, B. H.; Zou, B. S.; Zhou, W. Y.; Zhao, R. A.; Wang, G. *Science* **1996**, *274*, 1701–1703.
- [52] Chen, G.; Futaba, D. N.; Sakurai, S.; Yumura, M.; Hata, K. *Carbon* **2014**, *67*, 318–325.
- [53] De Volder, M.; Hart, A. J. *Angewandte Chemie - International Edition* **2013**, *52*, 2412–2425.
- [54] Futaba, D. N.; Hata, K.; Yamada, T.; Hiraoka, T.; Hayamizu, Y.; Kakudate, Y.; Tanaike, O.; Hatori, H.; Yumura, M.; Iijima, S. *Nature Materials* **2006**, *5*, 987–994.
- [55] Lu, W.; Qu, L.; Henry, K.; Dai, L. *Journal of Power Sources* **2009**, *189*, 1270–1277.
- [56] Hayamizu, Y.; Yamada, T.; Mizuno, K.; Davis, R. C.; Futaba, D. N.; Yumura, M.; Hata, K. *Nature Nanotechnology* **2008**, *3*, 289–294.
- [57] Yamada, T.; Makiomoto, N.; Sekiguchi, A.; Yamamoto, Y.; Kobashi, K.; Hayamizu, Y.; Yomogida, Y.; Tanaka, H.; Shima, H.; Akinaga, H.; Futaba, D. N.; Hata, K. *Nano Letters* **2012**, *12*, 4540–4545.
- [58] Wood, D. L.; Li, J.; Daniel, C. *Journal of Power Sources* **2015**, *275*, 234–242.
- [59] Huang, X.; Yu, H.; Chen, J.; Lu, Z.; Yazami, R.; Hng, H. H. *Advanced Materials* **2014**, *26*, 1296–1303.
- [60] Li, Y. Q.; Li, J. C.; Lang, X. Y.; Wen, Z.; Zheng, W. T.; Jiang, Q. *Advanced Functional Materials* **2017**, *27*, 1–8.
- [61] Shen, F.; Luo, W.; Dai, J.; Yao, Y.; Zhu, M.; Hitz, E.; Tang, Y.; Chen, Y.; Sprenkle, V. L.; Li, X.; Hu, L. *Advanced Energy Materials* **2016**, *6*, 1–7.
- [62] Zhang, H.; Cao, G.; Wang, Z.; Yang, Y.; Shi, Z.; Gu, Z. *Nano Letters* **2008**, *8*, 2664–2668.
- [63] Lu, W.; Goering, A.; Qu, L.; Dai, L. *Physical Chemistry Chemical Physics* **2012**, *14*, 12099.
- [64] Gohier, A.; Laik, B.; Kim, K. H.; Maurice, J. L.; Pereira-Ramos, J. P.; Cojocar, C. S.; Van, P. T. *Advanced Materials* **2012**, *24*, 2592–2597.
- [65] Ahmad, S.; Copic, D.; George, C.; De Volder, M. *Advanced Materials* **2016**, *28*, 6705–6710.
- [66] Ma, Y.; Wang, X.; Jia, Y.; Chen, X.; Han, H.; Li, C. *Chemical Reviews* **2014**, *114*, 9987–10043.
- [67] Huang, Z.-f.; Pan, L.; Zou, J.-j.; Wang, L. *Nanoscale* **2014**, *5*, 14044–14063.
- [68] Wang, H.; Robinson, J. T.; Diankov, G.; Dai, H. *Journal of the American Chemical Society* **2010**, 3270–3271.
- [69] Wang, H.; Yang, Y.; Liang, Y.; Cui, L. F.; Sanchez Casalongue, H.; Li, Y.; Hong, G.; Cui, Y.; Dai, H. *Angewandte Chemie - International Edition* **2011**, *50*, 7364–7368.
- [70] Wang, H.; Liang, Y.; Gong, M.; Li, Y.; Chang, W.; Mefford, T.; Zhou, J.; Wang, J.; Regier, T.; Wei, F.; Dai, H. *Nature Communications* **2012**, *3*, 917–918.

- [71] Wang, Hailiang; Dai, H. *Chem Soc Rev* **2013**, *42*, 3088–3113.
- [72] Saito, R.; Fujita, M.; Dresselhaus, G.; Dresselhaus, M. S. *Physical Review B* **1992**, *46*, 1804–1811.
- [73] Scarselli, M.; Castrucci, P.; De Crescenzi, M. *Journal of Physics: Condensed Matter* **2012**, *24*, 313202.
- [74] Hashimoto, A.; Suenaga, K.; Gloter, A.; Urita, K.; Iijima, S. *Nature* **2004**, *430*, 870–873.
- [75] Jorio, A., Dresselhaus, G., Dresselhaus, M. S., Eds. *Carbon Nanotubes*; Springer-Verlag Berlin Heidelberg: Berlin, 2008.
- [76] Avouris, P.; Chen, Z.; Perebeinos, V. *Nature Nanotechnology* **2007**, *2*, 605–615.
- [77] Subramaniam, C.; Yamada, T.; Kobashi, K.; Sekiguchi, A.; Futaba, D. N.; Yumura, M.; Hata, K. *Nature communications* **2013**, *4*, 2202.
- [78] Ando, Y.; Zhao, X.; Shimoyama, H.; Sakai, G.; Kaneto, K. *International Journal of Inorganic Materials* **1999**, *1*, 77–82.
- [79] Kaneto, K.; Tsuruta, M.; Sakaia, G.; Chob, W. Y.; Andob, Y. *Synthetic Metals* **1999**, *103*, 2543–2546.
- [80] Wei, B. Q.; Vajtai, R.; Ajayan, P. M. *Applied Physics Letters* **2001**, *79*, 1172–1174.
- [81] Samani, M. K.; Khosravian, N.; Chen, G. C. K.; Shakerzadeh, M.; Baillargeat, D.; Tay, B. K. *International Journal of Thermal Sciences* **2012**, *62*, 40–43.
- [82] Iijima, S. *Nature* **1991**, *354*, 56–58.
- [83] de Heer, W. A. *Science* **2005**, *307*, 907–910.
- [84] Harris, P. J. F.; Tsang, S. C.; Claridge, J. B.; Green, M. L. H. *Journal of the Chemical Society, Faraday Transactions* **1994**, *90*, 2799.
- [85] Bethune, D. S.; Klang, C. H.; de Vries, M. S.; Gorman, G.; Savoy, R.; Vazquez, J.; Beyers, R. *Nature* **1993**, *363*, 605–607.
- [86] Li, Y.; Mann, D.; Rolandi, M.; Kim, W.; Ural, A.; Hung, S.; Javey, A.; Cao, J.; Wang, D.; Yenilmez, E.; Wang, Q.; Gibbons, J. F.; Nishi, Y.; Dai, H. *Nano Letters* **2004**, *4*, 317–321.
- [87] Zhang, Q.; Huang, J. Q.; Qian, W. Z.; Zhang, Y. Y.; Wei, F. *Small* **2013**, *9*, 1237–1265.
- [88] Li, Y.; Kim, W.; Zhang, Y.; Rolandi, M.; Wang, D.; Dai, H. *Journal of Physical Chemistry B* **2001**, *105*, 11424–11431.
- [89] Deck, C. P.; Vecchio, K. *Carbon* **2006**, *44*, 267–275.
- [90] Li, Y.; Mann, D.; Rolandi, M.; Kim, W.; Ural, A.; Hung, S.; Javey, A.; Cao, J.; Wang, D.; Yenilmez, E.; Wang, Q.; Gibbons, J. F.; Nishi, Y.; Dai, H. *Nano Letters* **2004**, *4*, 317–321.
- [91] Omachi, H.; Nakayama, T.; Takahashi, E.; Segawa, Y.; Itami, K. *Nature Chemistry* **2013**, *5*, 572–576.
- [92] Sanchez-Valencia, J. R.; Dienel, T.; Gröning, O.; Shorubalko, I.; Mueller, A.; Jansen, M.; Amsharov, K.; Ruffieux, P.; Fasel, R. *Nature* **2014**, *512*, 61–64.
- [93] Fort, E. H.; Scott, L. T. *Tetrahedron Letters* **2011**, *52*, 2051–2053.
- [94] De Volder, M. F. L.; Tawfick, S. H.; Baughman, R. H.; Hart, A. J. *Science* **2013**, *339*, 535–539.

- [95] Yu, G.; Cao, A.; Lieber, C. M. *Nature Nanotechnology* **2007**, *2*, 372–377.
- [96] Liu, K.; Sun, Y.; Chen, L.; Feng, C.; Feng, X.; Jiang, K.; Zhao, Y.; Fan, S. *Nano Letters* **2008**, *8*, 700–705.
- [97] Zhang, M.; Fang, S.; Zakhidov, A. A.; Lee, S. B.; Aliev, A.; Williams, C.; Atkinson, K.; Baughman, R. H. *Science* **2005**, 1215–1220.
- [98] Imaizumi, S.; Matsumoto, H.; Konosu, Y.; Tsuboi, K.; Minagawa, M.; Tanioka, A.; Koziol, K.; Windle, A. *ACS Applied Materials and Interfaces* **2011**, *3*, 469–475.
- [99] Terranova, M. L.; Sessa, V.; Rossi, M. *Chemical Vapor Deposition* **2006**, *12*, 315–325.
- [100] Khalilov, U.; Bogaerts, A.; Hussain, S.; Kovacevic, E.; Brault, P.; Boulmer-Leborgne, C.; Neyts, E. C. *Journal of Physics D: Applied Physics* **2017**, *50*, 184001.
- [101] Nessim, G. D.; Seita, M.; Plata, D. L.; O'Brien, K. P.; Hart, A. J.; Meshot, E. R.; Reddy, C. M.; Gschwend, P. M.; Thompson, C. V. *Carbon* **2011**, *49*, 804–810.
- [102] Awano, Y.; Sato, S.; Kondo, D.; Ohfuti, M.; Kawabata, A.; Nihei, M.; Yokoyama, N. *Physica Status Solidi (A) Applications and Materials Science* **2006**, *203*, 3611–3616.
- [103] Nessim, G. D. *Nanoscale* **2010**, *2*, 1306–1323.
- [104] Yang, F. et al. *Nature* **2014**, *510*, 522–4.
- [105] Hofmann, S.; Csányi, G.; Ferrari, A. C.; Payne, M. C.; Robertson, J. *Physical Review Letters* **2005**, *95*, 1–4.
- [106] Puzos, A. A.; Geohegan, D.; Jesse, S.; Ivanov, I.; Eres, G. *Applied Physics A* **2005**, *81*, 223–240.
- [107] Chhowalla, M.; Teo, K. B. K.; Ducati, C.; Rupasinghe, N. L.; Amaratunga, G. A. J.; Ferrari, A. C.; Roy, D.; Robertson, J.; Milne, W. I. *Journal of Applied Physics* **2001**, *90*, 5308–5317.
- [108] Bower, C.; Zhou, O.; Zhu, W.; Werder, D. J.; Jin, S. *Appl. Phys. Lett.* **2000**, *77*, 2767–2769.
- [109] Bedewy, M.; Meshot, E. R.; Reinker, M. J.; Hart, J. A. *ACS Nano* **2011**, *5*, 8974 – 8989.
- [110] Wei, Y. Y.; Eres, G.; Merkulov, V. I.; Lowndes, D. H. *Applied Physics Letters* **2001**, *78*, 1394–1396.
- [111] Thess, A.; Lee, R.; Nikolaev, P.; Dai, H.; Petit, P.; Robert, J.; Xu, C.; Lee, Y. H.; Kim, S. G.; Rinzler, A. G.; Colbert, D. T.; Scuseria, G. E.; Tomanek, D.; Fischer, J. E.; Smalley, R. E. *Science* **1996**, *273*, 483–487.
- [112] Yudasaka, M.; Kokai, F.; Takahashi, K.; Yamada, R.; Sensui, N.; Ichihashi, T.; Iijima, S. *The Journal of Physical Chemistry B* **1999**, *103*, 3576–3581.
- [113] Dai, H.; Rinzler, A. G.; Nikolaev, P.; Thess, A.; Colbert, D. T.; Smalley, R. E. *Chemical Physics Letters* **1996**, *260*, 471–475.
- [114] Elliott, J. A.; Shibuta, Y.; Amara, H.; Bichara, C.; Neyts, E. C. *Nanoscale* **2013**, *5*, 6662.
- [115] Wagner, R. S.; Ellis, W. C. *Applied Physics Letters* **1964**, *4*, 89–90.
- [116] Yoshida, H.; Takeda, S.; Uchiyama, T.; Kohno, H.; Homma, Y. *Nano Letters* **2008**, *8*, 2–6.
- [117] Hofmann, S. et al. *Nano Letters* **2007**, *7*, 602–608.
- [118] Ohta, Y.; Okamoto, Y.; Page, A. J.; Irle, S.; Morokuma, K. *ACS Nano* **2009**, *3*, 3413–3420.

- [119] Page, A. J.; Chandrakumar, K. R. S.; Irle, S.; Morokuma, K. *Journal of the American Chemical Society* **2011**, *133*, 621–628.
- [120] Hofmann, S.; Ducati, C.; Kleinsorge, B.; Robertson, J. *Applied Physics Letters* **2003**, *83*, 4661–4663.
- [121] Wirth, C. T.; Zhang, C.; Zhong, G.; Hofmann, S.; Robertson, J. *ACS nano* **2009**, *3*, 3560–6.
- [122] Bedewy, M.; Meshot, E. R.; Guo, H.; Verploegen, E. A.; Lu, W.; Hart, J. A. *Journal of Physical Chemistry C* **2009**, *113*, 20576–20582.
- [123] Bedewy, M.; Meshot, E. R.; Hart, J. A. *Carbon* **2012**, *50*, 5106–5116.
- [124] Bedewy, M.; Hart, J. A. *Nanoscale* **2013**, *5*, 2928–2937.
- [125] Xu, M.; Futaba, D. N.; Yumura, M.; Hata, K. *ACS Nano* **2012**, *6*, 5837–5844.
- [126] Fan, S.; Chapline, M. G.; Franklin, N. R.; Tomblor, T. W.; Cassell, A. M.; Dai, H. *Science* **1999**, *283*, 512–514.
- [127] Balakrishnan, V.; Bedewy, M.; Meshot, E. R.; Pattinson, S. W.; Polsen, E. S.; Laye, F.; Zakharov, D. N.; Stach, E. A.; Hart, A. J. *ACS Nano* **2016**, *10*, 11496–11504.
- [128] De Volder, M. F. L.; Vidaud, D. O.; Meshot, E. R.; Tawfick, S.; Hart, A. J. *Microelectronic Engineering* **2010**, *87*, 1233–1238.
- [129] Amama, P. B.; Pint, C. L.; McJilton, L.; Kim, S. M.; Stach, E. A.; Murray, P. T.; Hauge, R. H.; Maruyama, B. *Nano Letters* **2009**, *9*, 44–49.
- [130] Wirth, C. T.; Bayer, B. C.; Gamalski, A. D.; Esconjauregui, S.; Weatherup, R. S.; Ducati, C.; Baetz, C.; Robertson, J.; Hofmann, S. *Chemistry of Materials* **2012**, *24*, 4633–4640.
- [131] Park, S. J.; Schmidt, A. J.; Bedewy, M.; Hart, A. J. *Physical Chemistry Chemical Physics* **2013**, *15*, 11511–9.
- [132] Jeong, S.; Lee, J.; Kim, H.-C.; Hwang, J. Y.; Ku, B.-C.; Zakharov, D. N.; Maruyama, B.; Stach, E. A.; Kim, S. M. *Nanoscale* **2016**, *8*, 2055–2062.
- [133] Sinnott, S. B.; Andrews, R.; Qian, D.; Rao, A. M.; Mao, Z.; Dickey, E. C.; Derbyshire, F. *Chemical Physics Letters* **1999**, *315*, 25–30.
- [134] Tessonier, J.-P.; Su, D. S. *ChemSusChem* **2011**, *4*, 824–847.
- [135] Meshot, E. R.; Verploegen, E.; Bedewy, M.; Tawfick, S.; Woll, A. R.; Green, K. S.; Hromalik, M.; Koerner, L. J.; Philipp, H. T.; Tate, M. W.; Gruner, S. M.; Hart, J. A. *ACS Nano* **2012**, *6*, 5091–5101.
- [136] Delzeit, L.; Nguyen, C. V.; Chen, B.; Stevens, R.; Cassell, A.; Han, J.; Meyyappan, M. *The Journal of Physical Chemistry B* **2002**, *106*, 5629–5635.
- [137] Cantoro, M.; Hofmann, S.; Pisana, S.; Scardaci, V.; Parvez, A.; Ducati, C.; Ferrari, A. C.; Blackburn, A. M.; Wang, K. Y.; Robertson, J. *Nano Letters* **2006**, *6*, 1107–1112.
- [138] Mattevi, C.; Wirth, C. T.; Hofmann, S.; Blume, R.; Cantoro, M.; Ducati, C.; Cepek, C.; Knop-Gericke, A.; Milne, S.; Castellarin-Cudia, C.; Dolafi, S.; Goldoni, A.; Schlögl, R.; Robertson, J. *The Journal of Physical Chemistry C* **2008**, *112*, 12207–12213.
- [139] De Volder, M.; Park, S.; Tawfick, S.; Hart, J. A. *Nature Communications* **2014**, *5*, 4512.
- [140] Hata, K.; Futaba, D. N.; Mizuno, K.; Namai, T.; Yumura, M.; Iijima, S. *Science* **2004**, *306*, 1362–1364.

- [141] Li, J.; Bedewy, M.; White, A. O.; Polsen, E. S.; Tawfick, S.; John Hart, A. *Journal of Physical Chemistry C* **2016**, *120*, 11277–11287.
- [142] Nessim, G. D.; Al-Obeidi, A.; Grisaru, H.; Polsen, E. S.; Ryan Oliver, C.; Zimrin, T.; Hart, A. J.; Aurbach, D.; Thompson, C. V. *Carbon* **2012**, *50*, 4002–4009.
- [143] Nessim, G.; Seita, M.; O'Brien, K. *Nano Letters* **2009**, *9*, 3398–3405.
- [144] Shi, W.; Li, J.; Polsen, E. S.; Oliver, C. R.; Zhao, Y.; Meshot, E. R.; Barclay, M.; Fairbrother, D. H.; Hart, A. J.; Plata, D. L. *Nanoscale* **2017**, *9*, 5222–5233.
- [145] Magrez, A.; Seo, J. W.; Smajda, R.; Korbely, B.; Andresen, J. C.; Mionic, M.; Casimirius, S.; Forro, L. *ACS Nano* **2010**, *4*, 3702–3708.
- [146] Su, H. C.; Chen, C. H.; Chen, Y. C.; Yao, D. J.; Chen, H.; Chang, Y. C.; Yew, T. R. *Carbon* **2010**, *48*, 805–812.
- [147] Jeong, D.-W.; Shin, U.-H.; Kim, J. H.; Kim, S.-H.; Lee, H. W.; Kim, J.-M. *Carbon* **2014**, *79*, 442–449.
- [148] Cheong, F. C.; Lim, K. Y.; Sow, C. H.; Lin, J.; Ong, C. K. *Nanotechnology* **2003**, *14*, 433–437.
- [149] Saurakhiya, N.; Zhu, Y. W.; Cheong, F. C.; Ong, C. K.; Wee, A. T. S.; Lin, J. Y.; Sow, C. H. *Carbon* **2005**, *43*, 2128–2133.
- [150] Rajabifar, B.; Kim, S.; Slinker, K.; Ehlert, G. J.; Hart, A. J.; Maschmann, M. R. *Applied Physics Letters* **2015**, *107*, 3–7.
- [151] Madou, M. J. *Fundamentals of Microfabrication: The Science of Miniaturization*, 2nd ed.; CRC Press, 2002.
- [152] Kern, W.; A., P. D. *RCA Rev.* **1970**, *31*, 187–206.
- [153] Senturia, S. D. *Microsystem Design*, 1st ed.; Springer US: Springer Science+Business Media New York, 2001.
- [154] Deckman, H. W.; Dunsmuir, J. H. *Applied Physics Letters* **1982**, *41*, 377–379.
- [155] Hulteen, J. C. *Journal of Vacuum Science & Technology A: Vacuum, Surfaces, and Films* **1995**, *13*, 1553.
- [156] Ai, B.; Yu, Y.; Möhwald, H.; Zhang, G.; Yang, B. *Advances in Colloid and Interface Science* **2014**, *206*, 5–16.
- [157] Ye, X.; Qi, L. *Science China Chemistry* **2014**, *57*, 58–69.
- [158] Gao, P.; He, J.; Zhou, S.; Yang, X.; Li, S.; Sheng, J.; Wang, D.; Yu, T.; Ye, J.; Cui, Y. *Nano Letters* **2015**, *15*, 4591–4598.
- [159] Tawfick, S.; De Volder, M.; Copic, D.; Park, S. J.; Oliver, C. R.; Polsen, E. S.; Roberts, M. J.; Hart, A. J. *Advanced Materials* **2012**, *24*, 1628–1674.
- [160] Plettl, A.; Enderle, F.; Saitner, M.; Manzke, A.; Pfahler, C.; Wiedemann, S.; Ziemann, P. *Advanced Functional Materials* **2009**, *19*, 3279–3284.
- [161] Hulteen, J. C.; Treichel, D. A.; Smith, M. T.; Duval, M. L.; Jensen, T. R.; Van Duyne, R. P. *Journal of Physical Chemistry B* **1999**, *103*, 3854–3863.
- [162] Fischer, U. C. *Journal of Vacuum Science and Technology* **1981**, *19*, 881.
- [163] Ye, X.; Qi, L. *Nano Today* **2011**, *6*, 608–631.

- [164] Vogel, N.; Weiss, C. K.; Landfester, K. *Soft Matter* **2012**, *8*, 4044.
- [165] Vogel, N.; Retsch, M.; Fustin, C.-A.; del Campo, A.; Jonas, U. *Chemical Reviews* **2015**, *115*, 6265–6311.
- [166] Majumder, M.; Rendall, C. S.; Eukel, J. A.; Wang, J. Y. L.; Behabtu, N.; Pint, C. L.; Liu, T. Y.; Orbaek, A. W.; Mirri, F.; Nam, J.; Barron, A. R.; Hauge, R. H.; Schmidt, H. K.; Pasquali, M. *Journal of Physical Chemistry B* **2012**, *116*, 6536–6542.
- [167] Yu, Y.; Zhang, G. *Updates in Advanced Lithography* **2013**, 3–34.
- [168] Retsch, M.; Zhou, Z.; Rivera, S.; Kappl, M.; Zhao, X. S.; Jonas, U.; Qin, L. *Macromolecular Chemistry and Physics* **2009**, *210*, 230–241.
- [169] Vogel, N.; Goerres, S.; Landfester, K.; Weiss, C. K. *Macromolecular Chemistry and Physics* **2011**, *212*, 1719–1734.
- [170] Zhang, J. T.; Wang, L.; Lamont, D. N.; Velankar, S. S.; Asher, S. A. *Angewandte Chemie - International Edition* **2012**, *51*, 6117–6120.
- [171] Hanarp, P.; Sutherland, D. S.; Gold, J.; Kasemo, B. *Colloids and Surfaces A: Physicochemical and Engineering Aspects* **2003**, *214*, 23–36.
- [172] De Volder, M.; Park, S. J.; Tawfick, S. H.; Vidaud, D. O.; Hart, A. J. *J. Micromech. Microeng.* **2010**, *21*, 045033.
- [173] De Volder, M.; Tawfick, S. H.; Park, S. J.; Copic, D.; Zhao, Z.; Lu, W.; Hart, A. J. *Advanced Materials* **2010**, *22*, 4384–4389.
- [174] Chakrapani, N.; Wei, B.; Carrillo, A.; Ajayan, P. M.; Kane, R. S. *Proceedings of the National Academy of Sciences of the United States of America* **2004**, *101*, 4009–4012.
- [175] Kaur, S.; Sahoo, S.; Ajayan, P.; Kane, R. S. *Advanced Materials* **2007**, *19*, 2984–2987.
- [176] Chandra, D.; Yang, S. *Accounts of Chemical Research* **2010**, *43*, 1080–1091.
- [177] Tawfick, S.; De Volder, M. F. L.; Hart, A. J. *Langmuir* **2011**, *27*, 6389–6394.
- [178] Járαι-Szabó, F.; Horvát, E. Á.; Vajtai, R.; Néda, Z. *Chemical Physics Letters* **2011**, *511*, 378–383.
- [179] Lim, X.; Gary Foo, H. W.; Chia, G. H.; Sow, C. H. *ACS Nano* **2010**, *4*, 1067–1075.
- [180] Wang, X. X.; Wang, J. N.; Chang, H.; Zhang, Y. F. *Advanced Functional Materials* **2007**, *17*, 3613–3618.
- [181] Zhang, Y.; Chen, T.; Wang, J.; Min, G.; Pan, L.; Song, Z.; Sun, Z.; Zhou, W.; Zhang, J. *Applied Surface Science* **2012**, *258*, 4729–4732.
- [182] Tasis, D.; Tagmatarchis, N.; Bianco, A.; Prato, M. *Chemical reviews* **2006**, *106*, 1105–1136.
- [183] Karousis, N.; Tagmatarchis, N.; Tasis, D. *Chemical reviews* **2010**, *110*, 5366–97.
- [184] Khlobystov, A. N.; Britz, D. A.; Briggs, G. A. D. *Accounts of Chemical Research* **2005**, *38*, 901–909.
- [185] Wu, H. B.; Lou, X. W.; Hng, H. H. *Chemistry - A European Journal* **2012**, *18*, 3132–3135.
- [186] Pourfayaz, F.; Mortazavi, Y.; Khodadadi, A.-a.; Jafari, S. H.; Boroun, S.; Naseh, M. V. *Applied Surface Science* **2014**, *295*, 66–70.

- [187] Lin, Y.; Lu, F.; Tu, Y.; Ren, Z. *Nano Letters* **2004**, *4*, 191–195.
- [188] De Volder, M.; Tawfick, S. H.; Copic, D.; Hart, A. J. *Soft Matter* **2011**, *7*, 9844–9847.
- [189] Pan, Y.; Wu, Q.; Weng, Y.; Zhang, X.; Yang, Z.; Meng, J.; Tsui, O. K. C. *J. Mater. Chem. A* **2015**, *3*, 11111–11116.
- [190] Zhang, H.; Cao, G.; Yang, Y. *Energy & Environmental Science* **2009**, *2*, 932.
- [191] Ravavikar, N. R.; Schadler, L. S.; Vijayaraghavan, A.; Zhao, Y.; Wei, B.; Ajayan, P. M. *Chemistry of Materials* **2005**, *17*, 974–983.
- [192] MacDonald, T.; Gibson, C. T.; Constantopoulos, K.; Shapter, J. G.; Ellis, A. V. *Applied Surface Science* **2012**, *258*, 2836–2843.
- [193] Ozden, S.; Ge, L.; Narayanan, T. N.; Hart, A. H. C.; Yang, H.; Sridhar, S.; Vajtai, R.; Ajayan, P. M. *ACS Applied Materials and Interfaces* **2014**, *6*, 10608–13.
- [194] Isrealachvili, J. N. *Intermolecular and Surface Forces*, third edit ed.; Academic Press, 2011; p 674.
- [195] Porter, D.; Easterling, K. E. *Phase Transformations in Metals and Alloys*, second edi ed.; Chapman&Hall, 1992.
- [196] Anumol, E. A.; Kundu, P.; Deshpande, P. A.; Madras, G.; Ravishankar, N. *ACS Nano* **2011**, *5*, 8049–8061.
- [197] Sun, Y. *National Science Review* **2015**, *2*, 329–348.
- [198] Lamer, V. K.; Dinegar, R. H. *Journal of the American Chemical Society* **1950**, *72*, 4847–4854.
- [199] Pound, G. M.; Mer, V. K. *Journal of the American Chemical Society* **1952**, *74*, 2323–2332.
- [200] Schwenke, A. M.; Hoepfener, S.; Schubert, U. S. *Advanced Materials* **2015**, 1–29.
- [201] Hu, H.; Zhao, B.; Itkis, M. E.; Haddon, R. C. *The Journal of Physical Chemistry B* **2003**, *107*, 13838–13842.
- [202] Hou, Z.; Cai, B.; Liu, H.; Xu, D. *Carbon* **2008**, *46*, 405–413.
- [203] Felten, A.; Bittencourt, C.; Pireaux, J. J.; Van Lier, G.; Charlier, J. C. *Journal of Applied Physics* **2005**, *98*.
- [204] Wang, W.-H.; Huang, B.-C.; Wang, L.-S.; Ye, D.-Q. *Surface & Coatings Technology* **2011**, *205*, 4896–4901.
- [205] Naseh, M. V.; Khodadadi, A. A.; Mortazavi, Y.; Pourfayaz, F.; Alizadeh, O.; Maghrebi, M. *Carbon* **2010**, *48*, 1369–1379.
- [206] Kolacyak, D.; Ihde, J.; Merten, C.; Hartwig, A.; Lommatzsch, U. *Journal of Colloid and Interface Science* **2011**, *359*, 311–317.
- [207] Chen, C.; Ogino, A.; Wang, X.; Nagatsu, M. *Applied Physics Letters* **2010**, *96*, 2008–2011.
- [208] Ago, H.; Kugler, T.; Cacialli, F.; Salaneck, W. R.; Shaffer, M. S. P.; Windle, A. H.; Friend, R. H. *The Journal of Physical Chemistry B* **1999**, *103*, 8116–8121.
- [209] Manoilova, O. V.; Lavalley, J. C.; Tsyganenko, N. M.; Tsyganenko, A. A. *Langmuir* **1998**, *14*, 5813–5820.
- [210] Neeb, P.; Horie, O.; Moortgat, G. K. *The Journal of Physical Chemistry A* **1998**, *102*, 6778–6785.

- [211] Simmons, J. M.; Nichols, B. M.; Baker, S. E.; Marcus, M. S.; Castellini, O. M.; Lee, C. S.; Hamers, R. J.; Eriksson, M. A. *Journal of Physical Chemistry B* **2006**, *110*, 7113–7118.
- [212] Mawhinney, D. B.; Naumenko, V.; Kuznetsova, A.; Yates, J. T.; Liu, J.; Smalley, R. E. *Journal of the American Chemical Society* **2000**, *122*, 2383–2384.
- [213] Ramos, S. C.; Vasconcelos, G.; Antunes, E. F.; Lobo, A. O.; Trava-Airoldi, V. J.; Corat, E. J. *Diamond and Related Materials* **2010**, *19*, 752–755.
- [214] Lobo, A. O.; Ramos, S. C.; Antunes, E. F.; Marciano, F. R.; Trava-Airoldi, V. J.; Corat, E. J. *Materials Letters* **2012**, *70*, 89–93.
- [215] Van Hooijdonk, E.; Bittencourt, C.; Snyders, R.; Colomer, J. F. *Beilstein Journal of Nanotechnology* **2013**, *4*, 129–152.
- [216] Kim, S.; Kim, H.-J.; Lee, H. R.; Song, J.-H.; Yi, S. N.; Ha, D. H. *Journal of Physics D: Applied Physics* **2010**, *43*, 305402.
- [217] Tawfick, S.; Hart, J. A.; De Volder, M. *Nanoscale* **2012**, *4*, 3852.
- [218] Kwak, M. K.; Jeong, H.-E.; Kim, T.-I.; Yoon, H.; Suh, K. Y. *Soft Matter* **2010**, *6*, 1849.
- [219] Ritala, M. et al. In *Chemical Vapour Deposition*; Jones, A. C., Hitchman, M. L., Eds.; The Royal Society of Chemistry, 2009; pp P001–P582.
- [220] Hsueh, Y.-C.; Wang, C.-C.; Liu, C.; Kei, C.-C.; Perng, T.-P. *Nanotechnology* **2012**, *23*, 405603.
- [221] Min, Y.-S.; Bae, E.; Jeong, K.; Cho, Y.; Lee, J.-H.; Choi, W.; Park, G.-S. *Advanced Materials* **2003**, *15*, 1019–1022.
- [222] Gomathi, A.; Vivekchand, S. R.; Govindaraj, A.; Rao, C. N. *Advanced Materials* **2005**, *17*, 2757–2761.
- [223] Boukhalifa, S.; Evanoff, K.; Yushin, G. *Energy & Environmental Science* **2012**, *5*, 6872.
- [224] Herrmann, C. F.; Fabreguette, F. H.; Finch, D. S.; Geiss, R.; George, S. M. *Applied Physics Letters* **2005**, *87*, 1–3.
- [225] Lahiri, I.; Oh, S.-M.; Hwang, J. Y.; Kang, C.; Choi, M.; Jeon, H.; Banerjee, R.; Sun, Y.-K.; Choi, W. *Journal of Materials Chemistry* **2011**, *21*, 13621.
- [226] Stano, K. L.; Carroll, M.; Padbury, R.; Mccord, M.; Jur, J. S.; Bradford, P. D. *ACS Applied Materials and Interfaces* **2014**, *6*, 19135 – 19143.
- [227] Hu, C. J.; Lin, Y. H.; Tang, C. W.; Tsai, M. Y.; Hsu, W. K.; Kuo, H. F. *Advanced Materials* **2011**, *23*, 2941–2945.
- [228] Dameron, A. A.; Pylypenko, S.; Bult, J. B.; Neyerlin, K. C.; Engtrakul, C.; Bochert, C.; Leong, G. J.; Frisco, S. L.; Simpson, L.; Dinh, H. N.; Pivovar, B. *Applied Surface Science* **2012**, *258*, 5212–5221.
- [229] Yazdani, N.; Chawla, V.; Edwards, E.; Wood, V.; Park, H. G.; Utke, I. *Beilstein Journal of Nanotechnology* **2014**, *5*, 234–244.
- [230] Hutchison, D. N.; Morrill, N. B.; Aten, Q.; Turner, B. W.; Jensen, B. D.; Howell, L. L.; Vanfleet, R. R.; Davis, R. C. *Journal of Microelectromechanical Systems* **2010**, *19*, 75–82.
- [231] Ogata, K.; Salager, E.; Kerr, C. J.; Fraser, A. E.; Ducati, C.; Morris, A. J.; Hofmann, S.; Grey, C. P. *Nature Communications* **2014**, *5*, 1–11.

- [232] Jin, Y.; Kneusels, N. J. H.; Magusin, P. C.; Kim, G.; Castillo-Martínez, E.; Marbella, L. E.; Kerber, R. N.; Howe, D. J.; Paul, S.; Liu, T.; Grey, C. P. *Journal of the American Chemical Society* **2017**, *139*, 14992–15004.
- [233] Xue, B.; Chen, P.; Hong, Q.; Lin, J.; Tan, K. L. *Journal of Materials Chemistry* **2001**, *11*, 2378–2381.
- [234] Fang, B.; Kim, M.-S.; Kim, J. H.; Song, M. Y.; Wang, Y.-J.; Wang, H.; Wilkinson, D. P.; Yu, J.-S. *Journal of Materials Chemistry* **2011**, *21*, 8066.
- [235] Zhang, S.; Shao, Y.; Yin, G.; Lin, Y. *Journal of Materials Chemistry* **2010**, *20*, 2826.
- [236] Cui, L.; Du, Z.; Zou, W.; Li, H.; Zhang, C. *RSC Advances* **2014**, *4*, 27591–27596.
- [237] Mohan, R.; Shanmugaraj, A. M.; Sung Hun, R. *Journal of Biomedical Materials Research - Part B Applied Biomaterials* **2011**, *96 B*, 119–126.
- [238] Raney, J. R.; Zhang, H.-L.; Morse, D. E.; Daraio, C. *Carbon* **2012**, *50*, 4432–4440.
- [239] Stano, K. L.; Chapla, R.; Carroll, M.; Nowak, J.; McCord, M.; Bradford, P. D. *ACS Applied Materials and Interfaces* **2013**, *5*, 10774–81.
- [240] Lee, S.-W.; Sigmund, W. M. *Chemical Communications* **2003**, 780–781.
- [241] Marr, K. M.; Chen, B.; Mootz, E. J.; Geder, J.; Pruessner, M.; Melde, B. J.; Vanfleet, R. R.; Medintz, I. L.; Iverson, B. D.; Claussen, J. C. *ACS Nano* **2015**, *9*, 7791–7803.
- [242] Lu, W.; Goering, A.; Qu, L.; Dai, L. *Physical Chemistry Chemical Physics* **2012**, *14*, 12099–104.
- [243] Yang, Y.; Qu, L.; Dai, L.; Kang, T. S.; Durstock, M. *Advanced Materials* **2007**, *19*, 1239–1243.
- [244] Lim, S. X.; Chang, S. L.; Cheong, F. C.; Tok, E. S.; Zhang, Z.; Lim, C. T.; Sow, C. H. *Journal of Physical Chemistry C* **2013**, *117*, 14408–14417.
- [245] Yang, Z.; Zhou, X.; Jin, Z.; Liu, Z.; Nie, H.; Chen, X.; Huang, S. *Advanced Materials* **2014**, *26*, 3156–3161.
- [246] Ajayan, P. M.; Stephan, O.; Redlich, P.; Colliex, C. *Nature* **1995**, *375*, 564–567.
- [247] Wang, H.; Cui, L.-f.; Yang, Y.; Casalongue, H. S. *Journal of the American Chemical Society* **2010**, *132*, 13978–13980.
- [248] Byrappa, K.; Yoshimura, M. In *Handbook of Hydrothermal Technology (Second Edition)*, second ed. ed.; Byrappa, K., Yoshimura, M., Eds.; William Andrew Publishing: Oxford, 2013; pp 177–267.
- [249] Wiltshire, J. G.; Khlobystov, A. N.; Li, L. J.; Lyapin, S. G.; Briggs, G. A.; Nicholas, R. J. *Chemical Physics Letters* **2004**, *386*, 239–243.
- [250] Liu, J.; Rinzler, A. G.; Dai, H.; Hafner, J. H.; Bradley, R. K.; Boul, P. J.; Lu, A.; Iverson, T.; Shelimov, K.; Huffman, C. B.; Rodriguez-Macias, F.; Shon, Y.-S.; Lee, T. R.; Colbert, D. T.; Smalley, R. E. *Science* **1998**, *280*, 1253–6.
- [251] Shulga, E.; Pohako, K.; Treshchalov, A.; Joost, U.; Kisand, V.; Kink, I. *Micro & Nano Letters* **2011**, *6*, 704–708.
- [252] Brunner, G. In *Hydrothermal and Supercritical Water Processes, Volume 5*; Kiran, E., Ed.; Elsevier B.V: Weinheim, 2014; p 604.
- [253] Yoshimura, M.; Byrappa, K. *Journal of Materials Science* **2008**, *43*, 2085–2103.

- [254] Li, L.; Wu, H. B.; Yu, L.; Madhavi, S.; Lou, X. W. D. *Advanced Materials Interfaces* **2014**, *1*.
- [255] Ma, F.-X.; Hu, H.; Wu, H. B.; Xu, C.-Y.; Xu, Z.; Zhen, L.; David Lou, X. W. *Advanced Materials* **2015**, 4097 – 4101.
- [256] Shang, M.; Wang, W.; Ren, J.; Sun, S.; Zhang, L. *CrystEngComm* **2010**, *12*, 1754.
- [257] Shearer, C. J.; Cherevan, A.; Eder, D. *Advanced Materials* **2014**, *26*, 2295–2318.
- [258] Wang, B.; Hu, C.; Dai, L. *Chem. Commun.* **2016**, *52*, 14350–14360.
- [259] Wang, Z.; Luan, D.; Madhavi, S.; Hu, Y.; Lou, X. W. D. *Energy & Environmental Science* **2012**, *5*, 5252.
- [260] Wu, H. B.; Chen, J. S.; Hng, H. H.; Lou, X. W. D. *Nanoscale* **2012**, *4*, 2526–42.
- [261] Wu, H. B.; Zhang, G.; Yu, L.; Lou, X. W. D. *Nanoscale Horizons* **2016**, 27–40.
- [262] Xia, H.; Lai, M.; Lu, L. *Journal of Materials Chemistry* **2010**, *20*, 6896–6902.
- [263] Horikoshi, S., Serpone, N., Eds. *Microwaves in Nanoparticle Synthesis*; WILEY-VCH Verlag GmbH & Co. KGaA: Weinheim, 2013.
- [264] Schwenke, A. M.; Hoepfener, S.; Schubert, U. S. *Advanced Materials* **2015**, 1–29.
- [265] Hu, X.; Yu, J. C. *Advanced Functional Materials* **2008**, *18*, 880–887.
- [266] Mazloumi, M.; Shadmehr, S.; Rangom, Y.; Nazar, L. F.; Tang, X. *ACS Nano* **2013**, *7*, 4281–4288.
- [267] Liu, H.; Li, S.; Zhai, J.; Li, H.; Zheng, Q.; Jiang, L.; Zhu, D. *Angewandte Chemie - International Edition* **2004**, *43*, 1146–1149.
- [268] Lee, C. J.; Park, J.; Huh, Y.; Yong Lee, J. *Chemical Physics Letters* **2001**, *343*, 33–38.
- [269] Lee, Y. T.; Park, J.; Choi, Y. S.; Ryu, H.; Lee, H. J. *Journal of Physical Chemistry B* **2002**, *106*, 7614–7618.
- [270] Cools, J.; Copic, D.; Luo, Z.; Callewaert, G.; Braeken, D.; De Volder, M. *Advanced Functional Materials* **2017**, *27*, 1–9.
- [271] Pint, C. L.; Nicholas, N.; Pheasant, S. T.; Duque, J. G.; Parra-Vasquez, N. G.; Eres, G.; Pasquali, M.; Hauge, R. H. *Journal of Physical Chemistry C* **2008**, *112*, 14041–14051.
- [272] Park, S. J.; Ok, J. G.; Park, H. J.; Lee, K. T.; Lee, J. H.; Kim, J. D.; Cho, E.; Baac, H. W.; Kang, S.; Guo, L. J.; Hart, J. A. *Carbon* **2018**, *129*, 8–14.
- [273] Lu, J.; Chen, Z.; Ma, Z.; Pan, F.; Curtiss, L. A.; Amine, K. *Nature Nanotechnology* **2016**, *11*, 1031 – 1039.
- [274] Cherian, C. T.; Sundaramurthy, J.; Kalaivani, M.; Ragupathy, P.; Kumar, P. S.; Thavasi, V.; Reddy, M. V.; Sow, C. H.; Mhaisalkar, S. G.; Ramakrishna, S.; Chowdari, B. V. R. *Journal of Materials Chemistry* **2012**, *22*, 12198–12204.
- [275] Spinner, N.; Zhang, L.; Mustain, W. E. *J. Mater. Chem. A* **2014**, *2*, 1627–1630.
- [276] Hadjipaschalis, I.; Poullikkas, A.; Efthimiou, V. *Renewable and Sustainable Energy Reviews* **2009**, *13*, 1513–1522.
- [277] Etacheri, V.; Marom, R.; Elazari, R.; Salitra, G.; Aurbach, D. *International Journal of Electrochemical Science* **2011**, *4*, 3243–3262.

- [278] Liu, C.; Neale, Z. G.; Cao, G. *Materials Today* **2016**, *19*, 109–123.
- [279] ICGM-AIME research. <https://www.icgm.fr/en/recherche-aime-en/ion-and-electron-transfer-materials-for-energy-storage>.
- [280] Reddy, M. V.; Yu, T.; Sow, C. H.; Shen, Z. X.; Lim, C. T.; Subba Rao, G. V.; Chowdari, B. V. R. *Advanced Functional Materials* **2007**, *17*, 2792–2799.
- [281] Poizot, P.; Laruelle, S.; Grugeon, S.; Dupont, L.; Tarascon, J.-m. *Nature* **2000**, *407*, 496 – 499.
- [282] Wang, Q.; Ping, P.; Zhao, X.; Chu, G.; Sun, J.; Chen, C. *Journal of Power Sources* **2012**, *208*, 210–224.
- [283] Liu, H.; Nishide, D.; Tanaka, T.; Kataura, H. *Nature Communications* **2011**, *2*, 309.
- [284] Hu, L.; Wu, H.; La Mantia, F.; Yang, Y.; Cui, Y. *ACS Nano* **2010**, *4*, 5843–5848.
- [285] Chen, X.; Mao, S. S. *Chemical Reviews* **2007**, *107*, 2891–2959.
- [286] Kong, D.; Li, X.; Zhang, Y.; Hai, X.; Wang, B.; Qiu, X.; Song, Q.; Yang, Q.-H.; Zhi, L. *Energy Environ. Sci.* **2016**, *9*, 906–911.
- [287] Che, G.; Lakshmi, B. B.; Fisher, E. R.; Martin, C. R. *Nature* **1998**, *393*, 346–349.
- [288] Garau, C.; Frontera, A.; Quiñonero, D.; Costa, A.; Ballester, P.; Deyà, P. M. *Chemical Physics* **2004**, *297*, 85–91.
- [289] Ishihara, T.; Kawahara, A.; Nishiguchi, H.; Yoshio, M.; Takita, Y. *Journal of Power Sources* **2001**, *97-98*, 129–132.
- [290] Claye, A. S.; Fischer, J. E.; Huffman, C. B.; Rinzler, A. G.; Smalley, R. E. *Journal of The Electrochemical Society* **2000**, *147*, 2845.
- [291] Yang, Z.-H.; Wu, H.-Q. *Solid State Ionics* **2001**, *143*, 173–180.
- [292] Wang, X.; Liu, H.; Jin, Y.; Chen, C. *Journal of Physical Chemistry B* **2006**, *110*, 10236–10240.
- [293] Yang, S.; Huo, J.; Song, H.; Chen, X. *Electrochimica Acta* **2008**, *53*, 2238–2244.
- [294] Eom, J.; Kim, D.; Kwon, H. *Journal of Power Sources* **2006**, *157*, 507–514.
- [295] Danner, T.; Singh, M.; Hein, S.; Kaiser, J.; Hahn, H.; Latz, A. *Journal of Power Sources* **2016**, *334*, 191–201.
- [296] Izadi-Najafabadi, A.; Futaba, D. N.; Iijima, S.; Hata, K. *Journal of the American Chemical Society* **2010**, *132*, 18017–18019.
- [297] Taberna, P. L.; Mitra, S.; Poizot, P.; Simon, P.; Tarascon, J.-M. *Nature Materials* **2006**, *5*, 567–573.
- [298] Li, J.-Y.; Xu, Q.; Li, G.; Yin, Y.-X.; Wan, L.-J.; Guo, Y.-G. *Mater. Chem. Front.* **2017**, 1691–1708.
- [299] Aguiló-Aguayo, N.; Pena Espiñeira, P.; Manian, A. P.; Bechtold, T. *RSC Advances* **2016**, *6*, 69685–69690.
- [300] Ji, J.; Ji, H.; Zhang, L. L.; Zhao, X.; Bai, X.; Fan, X.; Zhang, F.; Ruoff, R. S. *Advanced Materials* **2013**, *25*, 4673–4677.
- [301] Liu, H.; Zuo, K.; Vecitis, C. D. *Environmental Science and Technology* **2014**, *48*, 13871–13879.

- [302] Reddy, A. L. M.; Gowda, S. R.; Shaijumon, M. M.; Ajayan, P. M. *Advanced Materials* **2012**, *24*, 5045–5064.
- [303] Li, H.; Wang, Z.; Chen, L.; Huang, X. *Advanced Materials* **2009**, *21*, 4593–4607.
- [304] Jiang, Y.; Lin, L. *Sensors and Actuators, A: Physical* **2012**, *188*, 261–267.
- [305] Zhang, L.; Wu, H. B.; Lou, X. W. D. *Advanced Energy Materials* **2014**, *4*, 1300958.
- [306] Cheng, J.; Gu, G.; Guan, Q.; Razal, J.; Wang, Z.; Li, X.; Wang, B. *Journal of Materials Chemistry A* **2016**, *4*, 2729–2737.
- [307] Fan, Y.; Zhang, Q.; Xiao, Q.; Wang, X.; Huang, K. *Carbon* **2013**, *59*, 264–269.
- [308] Lv, X.; Deng, J.; Wang, B.; Zhong, J.; Sham, T.-K.; Sun, X.; Sun, X. *Chemistry of Materials* **2017**, *29*, 3499–3506.
- [309] Kang, E.; Jung, Y. S.; Cavanagh, A. S.; Kim, G. H.; George, S. M.; Dillon, A. C.; Kim, J. K.; Lee, J. *Advanced Functional Materials* **2011**, *21*, 2430–2438.
- [310] Reddy, M. V.; Rao, G. V. S.; Chowdari, B. V. R. *Chemical Reviews* **2013**, *113*, 5364–5457.
- [311] Wu, W.; Wu, Z.; Yu, T.; Jiang, C.; Kim, W. S. *Science and Technology of Advanced Materials* **2015**, *16*.
- [312] Pascu, O.; Carenza, E.; Gich, M.; Estradé, S.; Peiró, F.; Herranz, G.; Roig, A. *The Journal of Physical Chemistry C* **2012**, *116*, 15108–15116.
- [313] Hu, L.; Percheron, A.; Chaumont, D.; Brachais, C. H. *Journal of Sol-Gel Science and Technology* **2011**, *60*, 198–205.
- [314] Chen, J. S.; Zhu, T.; Yang, X. H.; Yang, H. G.; Lou, X. W. **2010**, 13162–13164.
- [315] Wang, X.; Chen, X.; Gao, L.; Zheng, H.; Ji, M. *J. Mater. Chem.* **2004**, *14*, 905–907.
- [316] Liu, H.; Wang, G.; Park, J.; Wang, J.; Liu, H.; Zhang, C. *Electrochimica Acta* **2009**, *54*, 1733–1736.
- [317] Kang, G.-D.; Cao, Y.-M. *Water Research* **2012**, *46*, 584–600.
- [318] Chen, J. Y.; Kutana, A.; Collier, C. P.; Giapis, K. P. *Science* **2005**, *310*, 1480–1483.
- [319] Koo, B.; Xiong, H.; Slater, M. D.; Prakapenka, V. B.; Balasubramanian, M.; Podsiadlo, P.; Johnson, C. S.; Rajh, T.; Shevchenko, E. V. *Nano Letters* **2012**, *12*, 2429–2435.
- [320] Wang, B.; Chen, J. S.; Wu, H. B.; Wang, Z. *Journal of the American Ceramic Society* **2011**, *133*, 17146–17148.
- [321] Xu, S.; Hessel, C. M.; Ren, H.; Yu, R.; Jin, Q.; Yang, M.; Zhao, H.; Wang, D. *Energy & Environmental Science* **2014**, *7*, 632.
- [322] NuLi, Y.; Zeng, R.; Zhang, P.; Guo, Z.; Liu, H. *Journal of Power Sources* **2008**, *184*, 456–461.
- [323] Lei, D.; Zhang, M.; Qu, B.; Chen, L.; Wang, Y.; Zhang, E.; Xu, Z.; Li, Q.; Wang, T. *Nanoscale* **2012**, *4*, 3422.
- [324] Zhou, J.; Song, H.; Ma, L.; Chen, X. *RSC Advances* **2011**, *1*, 782.
- [325] Liu, H.; Wang, G.; Wang, J.; Wexler, D. *Electrochemistry Communications* **2008**, *10*, 1879–1882.

- [326] Bruce, P. G.; Scrosati, B.; Tarascon, J.-M. *Angewandte Chemie - International Edition* **2008**, *47*, 2930–2946.
- [327] Kim, T. W.; Choi, K.-S. *Science* **2014**, *343*, 990–994.
- [328] Zhu, X.; Zhu, Y.; Murali, S.; Stoller, M. D.; Ruoff, R. S. *ACS Nano* **2011**, *5*, 3333–3338.
- [329] He, C.; Wu, S.; Zhao, N.; Shi, C.; Liu, E.; Science, M.; Materials, F. *ACS Nano* **2013**, 4459–4469.
- [330] Wei, W.; Yang, S.; Zhou, H.; Lieberwirth, I.; Feng, X.; Müllen, K. *Advanced Materials* **2013**, *25*, 2909–2914.
- [331] Cheng, X.; Gui, X.; Lin, Z.; Zheng, Y.; Liu, M.; Zhan, R.; Zhu, Y.; Tang, Z. *Journal of Materials Chemistry A: Materials for Energy and Sustainability* **2015**, *3*, 20927–20934.
- [332] Sun, Y.; Zhang, J.; Huang, T. *International Journal of ...* **2013**, *8*, 2918–2931.
- [333] Huang, Y.; Lin, J.; Ding, X. X.; Tang, C.; Gu, C. Z.; Qi, S. R. *Materials Letters* **2007**, *61*, 697–700.
- [334] He, Y.; Huang, L.; Cai, J.-S.; Zheng, X.-M.; Sun, S.-G. *Electrochimica Acta* **2010**, *55*, 1140–1144.
- [335] Su, J.; Cao, M.; Ren, L.; Hu, C. *Journal of Physical Chemistry C* **2011**, *115*, 14469–14477.
- [336] Wang, Z.; Luan, D.; Madhavi, S.; Hu, Y.; Lou, X. W. D. *Energy & Environmental Science* **2012**, *5*, 5252.
- [337] Liang, B.; Liu, Y.; Xu, Y. *Journal of Power Sources* **2014**, *267*, 469–490.
- [338] McDowell, M. T.; Lee, S. W.; Nix, W. D.; Cui, Y. *Advanced Materials* **2013**, *25*, 4966–4985.
- [339] He, Y.; Yu, X.; Wang, Y.; Li, H.; Huang, X. *Advanced Materials* **2011**, *23*, 4938–4941.
- [340] Maranchi, J. P.; Hepp, A. F.; Kumta, P. N. *Electrochemical and Solid-State Letters* **2003**, *6*, A198.
- [341] Aricò, A. S.; Bruce, P.; Scrosati, B.; Tarascon, J.-M.; van Schalkwijk, W. *Nature materials* **2005**, *4*, 366–377.
- [342] Kasavajjula, U.; Wang, C.; Appleby, A. J. *Journal of Power Sources* **2007**, *163*, 1003–1039.
- [343] Wu, H.; Cui, Y. *Nano Today* **2012**, *7*, 414–429.
- [344] Chan, C. K.; Peng, H.; Liu, G.; Mcllwraith, K.; Zhang, X. F.; Huggins, R. A.; Cui, Y. *Nature Nanotechnology* **2008**, *3*, 31–35.
- [345] Wu, H.; Chan, G.; Choi, J. W.; Ryu, I.; Yao, Y.; McDowell, M. T.; Lee, S. W.; Jackson, A.; Yang, Y.; Hu, L.; Cui, Y. *Nature Nanotechnology* **2012**, *7*, 310–315.
- [346] Park, M.-H.; Kim, M. G.; Joo, J.; Kim, K.; Kim, J.; Ahn, S.; Cui, Y.; Cho, J. *Nano Letters* **2009**, *9*, 3844–3847.
- [347] Xu, Q.; Li, J. Y.; Sun, J. K.; Yin, Y. X.; Wan, L. J.; Guo, Y. G. *Advanced Energy Materials* **2017**, *7*, 1–6.
- [348] Ng, S. H.; Wang, J.; Wexler, D.; Konstantinov, K.; Guo, Z. P.; Liu, H. K. *Angewandte Chemie - International Edition* **2006**, *45*, 6896–6899.
- [349] Zhou, R.; Fan, R.; Tian, Z.; Zhou, Y.; Guo, H.; Kou, L.; Zhang, D. *Journal of Alloys and Compounds* **2016**, *658*, 91–97.

- [350] Sohn, M.; Kim, D. S.; Park, H. I.; Kim, J. H.; Kim, H. *Electrochimica Acta* **2016**, *196*, 197–205.
- [351] Liu, N.; Lu, Z.; Zhao, J.; McDowell, M. T.; Lee, H.-W.; Zhao, W.; Cui, Y. *Nature Nanotechnology* **2014**, *9*, 187–192.
- [352] Fang, S.; Tong, Z.; Nie, P.; Liu, G.; Zhang, X. *ACS Applied Materials & Interfaces* **2017**, *9*, 18766–18773.
- [353] Gao, X.; Li, J.; Xie, Y.; Guan, D.; Yuan, C. *ACS Applied Materials & Interfaces* **2015**, *7*, 7855–7862.
- [354] Han, X.; Chen, H.; Zhang, Z.; Huang, D.; Xu, J.; Li, C.; Chen, S.; Yang, Y. *Journal of Materials Chemistry A* **2016**, *4*, 17757–17763.
- [355] Cui, L.-F.; Hu, L.; Wook, J.; Cui, Y. *ACS Nano* **2010**, *4*, 3671–3678.
- [356] Zhou, J. et al. *Nanoscale* **2016**, *8*, 4903–4907.
- [357] Feng, X.; Yang, J.; Bie, Y.; Wang, J.; Nuli, Y.; Lu, W. *Nanoscale* **2014**, *6*, 12532–12539.
- [358] Fu, K.; Yildiz, O.; Bhanushali, H.; Wang, Y.; Stano, K.; Xue, L.; Zhang, X.; Bradford, P. D. *Advanced Materials* **2013**, *25*, 5109–5114.
- [359] Cui, L.-F.; Ruffo, R.; Chan, C. K.; Peng, H.; Cui, Y. *Nano Letters* **2008**, *9*, 491–495.
- [360] Cui, L.-f.; Yang, Y.; Hsu, C.-m.; Cui, Y. *Nano Letters* **2009**, *9*, 1–5.
- [361] Ji, L.; Zhang, X. *Carbon* **2009**, *47*, 3219–3226.
- [362] Wu, J.; Qin, X.; Miao, C.; He, Y. B.; Liang, G.; Zhou, D.; Liu, M.; Han, C.; Li, B.; Kang, F. *Carbon* **2016**, *98*, 582–591.
- [363] Jung, D. S.; Hwang, T. H.; Park, S. B.; Choi, J. W. *Nano Letters* **2013**, *13*, 2092–2097.
- [364] Pring, J. N.; Fielding, W. *J. Chem. Soc.* **1909**, *95*, 1497–1506.
- [365] Hoelbling, R. *Angewandte Chemie* **1927**, *40*, 655–659.
- [366] Zuo, X.; Zhu, J.; Müller-Buschbaum, P.; Cheng, Y. J. *Nano Energy* **2017**, *31*, 113–143.
- [367] Jin, Y.; Zhu, B.; Lu, Z.; Liu, N.; Zhu, J. *Advanced Energy Materials* **2017**, *1700715*, 1–17.
- [368] Wang, W.; Kumta, P. N. *ACS Nano* **2010**, *4*, 2233–2241.
- [369] Liang, Y.; Li, Y.; Wang, H.; Dai, H. *Journal of the American Chemical Society* **2013**, *135*, 2013–2036.
- [370] Li, L.; Wu, H. B.; Yu, L.; Madhavi, S.; Lou, X. W. D. *Advanced Materials Interfaces* **2014**, *1*, 1400050.
- [371] Yu, T.; Zhu, Y.; Xu, X.; Yeong, K.-S.; Shen, Z.; Chen, P.; Lim, C.-T.; Thong, J. T.-L.; Sow, C.-H. *Small* **2006**, *2*, 80–84.
- [372] Rong, Z.; Zhou, Y.; Chen, B.; Robertson, J.; Federle, W.; Hofmann, S.; Steiner, U.; Goldberg-Oppenheimer, P. *Advanced Materials* **2014**, *26*, 1456–1461.
- [373] Cao, A.; Dickrell, P. L.; Sawyer, W. G.; Ghasemi-Nejhad, M. N.; Ajayan, P. M. *Science* **2005**, *310*, 1307–1310.
- [374] Maschmann, M. R.; Ehlert, G. J.; Tawfick, S.; Hart, A. J.; Baur, J. W. *Carbon* **2014**, *66*, 377–386.

- [375] Maschmann, M. R. *Carbon* **2015**, *86*, 26–37.
- [376] Ou, X.; Xu, S.; Liang, G.; Wang, L.; Zhao, X. *Science in China Series E: Technological Sciences* **2009**, *52*, 264–268.
- [377] Bersani, D.; Lottici, P. P.; Montenero, A. *Journal of Raman Spectroscopy* **1999**, *30*, 355–360.
- [378] Baettie, I. R.; Gilson, T. R. *J. Chem. Soc. A* **1970**, 980–986.
- [379] Obrovac, M. N.; Krause, L. J. *Journal of The Electrochemical Society* **2007**, *154*, A103.
- [380] Favors, Z.; Wang, W.; Bay, H. H.; George, A.; Ozkan, M.; Ozkan, C. S. *Scientific Reports* **2014**, *4*, 4605.
- [381] Chang, W.-S. et al. *Energy & Environmental Science* **2012**, *5*, 6895.
- [382] Yan, N.; Wang, F.; Zhong, H.; Li, Y.; Wang, Y.; Hu, L.; Chen, Q. *Scientific reports* **2013**, *3*, 1568.
- [383] Fan, J. A. et al. *Nature Communications* **2014**, *5*, 3266.
- [384] Rongé, J.; Bosserez, T.; Martel, D.; Nervi, C.; Boarino, L.; Taulelle, F.; Decher, G.; Bordiga, S.; Martens, J. A. *Chemical Society reviews* **2014**, *43*, 7963.
- [385] Winter, M.; Brodd, R. J. *Chemical Reviews* **2004**, *104*, 4245–4269.
- [386] Cox, N.; Retegan, M.; Neese, F.; Pantazis, D. A.; Boussac, A.; Lubitz, W. *Science* **2014**, *345*, 804–808.
- [387] Pinaud, B. A.; Benck, J. D.; Seitz, L. C.; Forman, A. J.; Chen, Z.; Deutsch, T. G.; James, B. D.; Baum, K. N.; Baum, G. N.; Ardo, S.; Wang, H.; Miller, E.; Jaramillo, T. F. *Energy & Environmental Science* **2013**, *6*, 1983.
- [388] Fujishima, A.; Honda, K. *Nature* **1972**, *238*, 37–38.
- [389] Gan, J.; Lu, X.; Tong, Y. *Nanoscale* **2014**, *6*, 7142.
- [390] Rao, P. M.; Cai, L.; Liu, C.; Cho, I. S.; Lee, C. H.; Weisse, J. M.; Yang, P.; Zheng, X. *Nano Letters* **2014**, *14*, 1099–1105.
- [391] Zhou, L.; Wang, W.; Liu, S.; Zhang, L.; Xu, H.; Zhu, W. *Journal of Molecular Catalysis A: Chemical* **2006**, *252*, 120–124.
- [392] Sayama, K.; Nomura, A.; Arai, T.; Sugita, T.; Abe, R.; Oi, T.; Iwasaki, Y.; Abe, Y.; Sugihara, H. *The Journal of Physical Chemistry B* **2006**, *3*, 11352–11360.
- [393] Kudo, A.; Omori, K.; Kato, H. *Journal of the American Chemical Society* **1999**, *121*, 11459–11467.
- [394] Luo, H.; Mueller, A. H.; McCleskey, T. M.; Burrell, A. K.; Bauer, E.; Jia, Q. X. *Journal of Physical Chemistry C* **2008**, *112*, 6099–6102.
- [395] Ma, Y.; Pendlebury, S. R.; Reynal, A.; Le Formal, F.; Durrant, J. R. *Chem. Sci.* **2014**, *5*, 2964–2973.
- [396] Long, M.; Cai, W.; Kisch, H. *Journal of Physical Chemistry C* **2008**, *112*, 548–554.
- [397] Borno, P.; Abdi, F. F.; Tilley, S. D.; Dam, B.; Van De Krol, R.; Graetzel, M.; Sivula, K. *Journal of Physical Chemistry C* **2014**, *118*, 16959–16966.
- [398] Kweon, K. E.; Hwang, G. S. *Applied Physics Letters* **2013**, *131603*, 1–5.

- [399] Tokunaga, S.; Kato, H.; Kudo, A. *Chemistry of Materials* **2001**, *13*, 4624–4628.
- [400] Vinke, I. C.; Diepgrond, J.; Boukamp, B. A.; De Vries, K. J.; Burggraaf, A. J. *Solid State Ionics* **1992**, *57*, 83–89.
- [401] Venkatesan, R.; Velumani, S.; Kassiba, A. *Materials Chemistry and Physics* **2012**, *135*, 842–848.
- [402] Xi, G.; Ye, J. *Chemical Communications* **2010**, *46*, 1893.
- [403] Zhao, Y.; Xie, Y.; Zhu, X.; Yan, S.; Wang, S. *Chemistry - A European Journal* **2008**, *14*, 1601–1606.
- [404] Eda, S. I.; Fujishima, M.; Tada, H. *Applied Catalysis B: Environmental* **2012**, *125*, 288–293.
- [405] Rettie, A. J.; Lee, H. C.; Marshall, L. G.; Lin, J. F.; Capan, C.; Lindemuth, J.; McCloy, J. S.; Zhou, J.; Bard, A. J.; Mullins, C. B. *Journal of the American Chemical Society* **2013**, *135*, 11389–11396.
- [406] Wang, D.; Jiang, H.; Zong, X.; Xu, Q.; Ma, Y.; Li, G.; Li, C. *Chemistry - A European Journal* **2011**, *17*, 1275–1282.
- [407] Nishikawa, M.; Hiura, S.; Mitani, Y.; Nosaka, Y. *Journal of Photochemistry and Photobiology A: Chemistry* **2013**, *262*, 52–56.
- [408] Li, G.; Zhang, D.; Yu, J. C. *Chem Mater* **2008**, *20*, 3983–3992.
- [409] Su, J.; Guo, L.; Bao, N.; Grimes, C. A. *Nano Letters* **2011**, *11*, 1928–1933.
- [410] Sun, T.; Cui, D.; Ma, Q.; Peng, X.; Yuan, L. *Journal of Physics and Chemistry of Solids* **2017**, *111*, 190–198.
- [411] Zhao, D.; Zong, W.; Fan, Z.; Xiong, S.; Du, M.; Wu, T.; Fang, Y.-W.; Ji, F.; Xu, X. *CrystEngComm* **2016**, *18*, 9007–9015.
- [412] Zhao, D.; Wang, W.; Sun, Y.; Fan, Z.; Du, M.; Zhang, Q.; Ji, F.; Xu, X. *RSC Adv.* **2017**, *7*, 33671–33679.
- [413] Liu, J. B.; Wang, H.; Wang, S.; Yan, H. *Materials Science and Engineering B: Solid-State Materials for Advanced Technology* **2003**, *104*, 36–39.
- [414] Reece, S. Y.; Hamel, J. A.; Sung, S.; Jarvi, T. D.; Esswein, A. J.; Pijpers, J. J. H.; Nocera, D. G. *Science* **2011**, *1*, 3.
- [415] Ma, L.; Li, W.-H.; Luo, J.-H. *Materials Letters* **2013**, *102-103*, 65–67.
- [416] Zhang, X.; Ai, Z.; Jia, F.; Zhang, L.; Fan, X.; Zou, Z. *Materials Chemistry and Physics* **2007**, *103*, 162–167.
- [417] Menzel, R.; Tran, M. Q.; Menner, A.; Kay, C. W. M.; Bismarck, A.; Shaffer, M. S. P. *Chemical Science* **2010**, *1*, 603–608.
- [418] Balamurugan, K.; Baskar, P.; Mahesh Kumar, R.; Das, S.; Subramanian, V. *The Journal of Physical Chemistry C* **2012**, *116*, 4365–4373.
- [419] Ma, Y.; Pendlebury, S. R.; Reynal, A.; Le Formal, F.; Durrant, J. R. *Chem. Sci.* **2014**, *5*, 2964–2973.
- [420] Luo, W.; Yang, Z.; Li, Z.; Zhang, J.; Liu, J.; Zhao, Z.; Wang, Z.; Yan, S.; Yu, T.; Zou, Z. *Energy & Environmental Science* **2011**, *4*, 4046.
- [421] Galembeck, A.; Alves, O. L. *Thin Solid Films* **2000**, *365*, 90–93.

- [422] Lan, Y.; Wang, Y.; Ren, Z. F. *Advances in Physics* **2011**, *60*, 553–678.
- [423] Balasubramanian, K.; Kurkina, T.; Ahmad, A.; Burghard, M.; Kern, K. *Journal of Materials Research* **2012**, *27*, 391–402.
- [424] Musameh, M. M.; Hickey, M.; Kyratzis, I. L. *Research on Chemical Intermediates* **2011**, *37*, 675–689.
- [425] Liu, G.; Lin, Y.; Tu, Y.; Ren, Z. *The Analyst* **2005**, *130*, 1098.
- [426] Wei, C.; Dai, L.; Roy, A.; Tolle, T. B. *Journal of the American Chemical Society* **2006**, *128*, 1412–1413.
- [427] Strelow, F. W. E.; Rethermeyer, R.; Bothma, C. J. C. *Analytical Chemistry* **1965**, *37*, 106–111.
- [428] Glimcher, M. J. *Reviews in Mineralogy and Geochemistry* **2006**, *64*, 223–282.
- [429] Holmgren, S. K.; Taylor, K. M.; Bretscher, L. E.; Raines, R. T. *Nature* **1998**, *392*, 666–667.
- [430] Correa-Duarte, M. A.; Wagner, N.; Rojas-Chapana, J.; Morscheck, C.; Thie, M.; Giersig, M. *Nano Letters* **2004**, *4*, 2233–6.
- [431] Zhang, Y. G.; Zhu, Y. J.; Chen, F.; Wu, J. *Materials Letters* **2015**, *144*, 135–137.
- [432] Chen, F.; Zhu, Y.-J.; Zhao, X.-Y.; Lu, B.-Q.; Wu, J. *CrystEngComm* **2013**, *15*, 4527.
- [433] Smolen, D.; Chudoba, T.; Malka, I.; Kedzierska, A.; Lojkowski, W.; Swieszkowski, W.; Kurzydowski, K. J.; Kolodziejczyk-Mierzynska, M.; Lewandowska-Szumiel, M. *International Journal of Nanomedicine* **2013**, *8*, 653–668.
- [434] Wang, Y. J.; Lai, C.; Wei, K.; Chen, X.; Ding, Y.; Wang, Z. L. *Nanotechnology* **2006**, *17*, 4405–4412.



## Appendix A

# Theoretical Background Carbon Nanotubes

**Table A1** A comparison between evaporation and sputtering as two techniques for physical vapor deposition.<sup>[151]</sup>

	Evaporation	Sputtering
Rate	Thousand atomic layers per second (e.g., 0.5 $\mu\text{m}/\text{min}$ for Al)	One atomic layer per second
Choice of materials	Limited	Almost unlimited
Purity	Better (no gas inclusions, very high vacuum)	Possibility of incorporating impurities (low-medium vacuum range)
Substrate heating	Very low	Unless magnetron is used substrate heating can be substantial
Surface damage	Very low, with e-beam x-ray damage is possible	Ionic bombardment damage
<i>In situ</i> cleaning	Not an option	Easily done with a sputter etch
Alloy compositions, stoichiometry	Little or no control	Alloy composition can be tightly controlled
X-ray damage	Only with e-beam evaporation	Radiation and particle damage is possible
Changes in source material	Easy	Expensive
Decomposition of material	High	Low
Scaling-up	Difficult	Good
Uniformity	Difficult	Easy over large areas
Capital equipment	Low cost	More expensive
Number of depositions	Only one deposition per charge	Many depositions can be carried out per target
Thickness control	Not easy to control	Several controls possible
Adhesion	Often poor	Excellent
Shadowing effect	Large	Small
Film properties (e.g., grain size and step coverage)	Difficult to control	Control by bias, pressure, substrate heat

## A Theoretical Background Carbon Nanotubes

**Table A2** A comparison is shown here for several powder synthesis and their advantages and disadvantages for a range of parameters. [253]

Parameter	Solid state reactions	Co-precipitation	Sol-Gel	Polymerizable complex	Hydrothermal
Cost	Low to moderate	Moderate	High	High	Moderate
State of development	Commercial	Demonstration/commercial	R & D	R & D	R & D/demonstration
Compositional control	Poor	Good	Excellent	Excellent	Good/excellent
Morphology control	Poor	Moderate	Moderate	Moderate	Good
Powder reactivity	Poor	Good	Good	Good	Good
Purity (%)	<99.5	>99.5	>99.9	>99.9	>99.5
Calcination step	Yes (multiple)	Yes	Yes	Yes	No
Milling step	Yes (multiple)	Yes	Yes	Yes	No

<u>Environmental</u>	<u>Medical uses</u>	<u>Films and paper</u>
✓ Sintering of asbestos	✓ Hyperthermia	✓ Dryness of book cover
✓ Decomposition of dioxin and PCB	✓ Sterilization	✓ Selective heating of pastes
✓ Oil recovery from plastics	✓ Muscular warming	✓ Sintering of electronic wiring
✓ Process treatment of waste oil	✓ Cutting of blood vessels	✓ Film curating
✓ Processing of medical wastes	<u>Usage for foodstuffs</u>	<u>Agriculture</u>
✓ Processing of radioactive contaminated substances	✓ Sterilization	✓ Sterilization of soil
✓ Degradation of chlorofluorocarbons	✓ Processing	✓ Drying of wood
✓ Decomposition of VOCs	✓ Defrosting	✓ Extermination of noxious insects in wood
✓ Exhaust gas treatment	✓ High-speed cooking	✓ Extraction and degradation of contaminants
✓ Incineration of garbage	✓ Reduced-pressure drying	
✓ Electrodeless lamps	✓ Activation of enzyme and yeast	<u>Usage in Wood treatments</u>
✓ Biomass	<u>Ink and paint</u>	✓ Adhesion processing
✓ Oxidization of soot	✓ Drying of printing ink	✓ Bending
✓ Enhancement of activity of photocatalysts	✓ Drying of paints	✓ Drying of wood
✓ Recycling of scrap tires		
✓ Solidification of waste plastics		

**Microwave chemistry**

<u>Organic chemistry</u> ✓ Rapid syntheses ✓ Solid-phase syntheses ✓ Non-solvent and non-catalytic processes ✓ Organometallic complexes ✓ Combinatorial chemistry <u>Analytical chemistry</u> ✓ Carbonization processing ✓ Acid and alkali treatment ✓ High-speed concentration, extraction and degradation <u>Biochemistry</u> ✓ Enzyme reactions ✓ PCR ✓ Heating brain of rat ✓ DNA dyeing <u>Polymer</u> ✓ Vulcanization and firing of rubber ✓ Higher selectivity in polymer syntheses ✓ Heat processing of plastics ✓ Size control of polymers <u>Catalytic chemistry</u> ✓ Heterogeneous catalysis (reduction reactions, etc...) ✓ Homogeneous catalysis (Suzuki coupling, & others) ✓ Syntheses of catalysts and catalyst supports (e.g., zeolites)	<u>Inorganic materials and metal chemistry</u> ✓ Functional material composition ✓ Composition of quality nanomaterials ✓ Hydrothermal syntheses ✓ Particulate coatings ✓ Control of crystallinity ✓ Syntheses of nitrides ✓ Drying of refractory products ✓ Calcination of ceramics & formation of interfacial junctions ✓ Microwave-assisted iron manufacturing ✓ Metallic powder metallurgy ✓ Carbonization ✓ High-speed treatments of lightweight fire-resistant building materials ✓ Heat treatments of specially glasses ✓ Syntheses of artificial zeolites ✓ Drying of extruded molding ceramics ✓ Syntheses of artificial bones <u>Photochemistry</u> ✓ Electrodeless lamps ✓ UV hardening of transparent coatings ✓ Photochemical syntheses
---	--

**Fig. A1** This figure shows the fields of applications for microwave radiation and microwave chemistry. [263]

# Appendix B

## Results

### B1 Formation of 3D CNT Structures

**Table B1** The characteristics of positive and negative photoresists are shown here. [151]

Characteristic	Resist type	
	Positive	Negative
Adhesion to Si	Fair	Excellent
Available compositions	Many	Vast
Contrast $\gamma$	Higher, e.g., 2.2	Lower, e.g., 1.5
Cost	More expensive	Less expensive
Developer	Aqueous based (ecologically sound)	Organic solvent
Developer process window	Small	Very wide, insensitive to overdeveloping
Influence of oxygen	No	Yes
Lift-off	Yes [usually with multiple-layer resist (MLR)]	Yes, with new types of negative resists [single-layer resist (SLR)]
Minimum feature	0.5 $\mu\text{m}$ and below	$\pm 2 \mu\text{m}$
Opaque dirt on clear portion of mask	Not very sensitive to it	Causes printing of pinholes
Photospeed	Slower	Faster
Pinhole count	Higher	Lower
Pinholes in mask	Prints mask pinholes	Not so sensitive to mask pinholes
Plasma etch resistance	Very good	Not very good
Proximity effect	Prints isolated holes or trenches better	Prints isolated lines better
Residue after development	Mostly at $<1 \mu\text{m}$ and high aspect ratio	Often a problem
Sensitizer quantum yield $\Phi$	0.2 to 0.3	0.5 to 1
Step coverage	Better	Lower
Strippers of resist over		
Oxide steps	Acid	Acid
Metal steps	Simple solvents	Chlorinated solvent compounds
Swelling in developer	No	Yes
Thermal stability	Good	Fair
Wet chemical resistance	Fair	Excellent

\*Never resist systems are discussed under *Photolithography Resolution Enhancement Technology*, page 32.

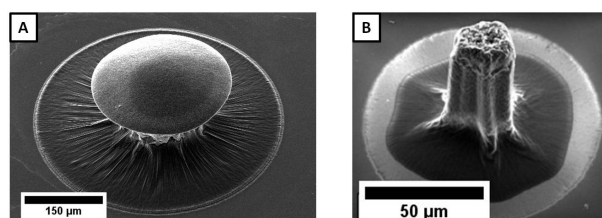


**Fig. B1** The influence of the crust on the densification of a CNT structure. (A) the densification is incomplete due to the influence of a too thick crust (courtesy of M. De Volder), whereas in (B) the densification into CNT pillar structures worked very well due to previous etching of the crust. [172]

## B Results

**Table B2** List of experimental parameters used to determine the influence of various factors during 3D honeycomb formation.

	Diameter	Spacing	Aspect ratio	Growth	Growth time	positions furnace	f
sj_hc_dim_01	5	5	1	1	4	9	
sj_hc_dim_02	10	5	2	1	4	3	
sj_hc_dim_03	5	10	0.5	1	4	5	
sj_hc_dim_04	10	10	1	1	4	2	
sj_hc_dim_05	15	10	1.5	1	4	8	
sj_hc_dim_06	20	10	2	1	4	1	
sj_hc_dim_07	20	5	4	1	4	4	
sj_hc_dim_08	15	5	3	1	4	7	
sj_hc_dim_10	5	5	1	2	4	1	
sj_hc_dim_12	10	10	1	2	4	3	
sj_hc_dim_13	15	5	3	2	4	4	
sj_hc_dim_14	20	5	4	2	4	5	
sj_hc_dim_15	5	10	0.5	2	4	6	
sj_hc_dim_16	15	10	1.5	2	4	7	
sj_hc_dim_17	10	5	2	2	4	8	
sj_hc_dim_18	20	10	2	2	4	9	
sj_hc_dim_19	5	10	0.5	3	2	1	
sj_hc_dim_20	20	10	2	3	2	2	
sj_hc_dim_21	10	5	2	3	2	3	
sj_hc_dim_22	15	10	1.5	3	2	4	
sj_hc_dim_23	15	5	3	3	2	5	
sj_hc_dim_24	5	5	1	3	2	6	
sj_hc_dim_26	10	10	1	3	2	8	
sj_hc_dim_27	20	5	4	3	2	9	
sj_hc_dim_29	10	10	1	4	2	2	
sj_hc_dim_30	20	5	4	4	2	3	
sj_hc_dim_31	10	5	2	4	2	4	
sj_hc_dim_32	5	5	1	4	2	5	
sj_hc_dim_33	15	5	3	4	2	6	
sj_hc_dim_34	20	10	2	4	2	7	
sj_hc_dim_35	15	10	1.5	4	2	8	
sj_hc_dim_36	5	10	0.5	4	2	9	
sj_hc_dim_37	15	5	3	5	6	1	
sj_hc_dim_38	10	5	2	5	6	2	
sj_hc_dim_39	20	10	2	5	6	3	
sj_hc_dim_40	15	10	1.5	5	6	4	
sj_hc_dim_41	5	10	0.5	5	6	5	
sj_hc_dim_42	20	5	4	5	6	6	
sj_hc_dim_43	5	5	1	5	6	7	
sj_hc_dim_45	10	10	1	5	6	9	
sj_hc_dim_46	5	5	1	6	6	1	
sj_hc_dim_47	10	10	1	6	6	2	
sj_hc_dim_48	15	5	3	6	6	3	
sj_hc_dim_50	5	10	0.5	6	6	5	
sj_hc_dim_51	20	5	4	6	6	6	
sj_hc_dim_52	15	10	1.5	6	6	7	
sj_hc_dim_53	10	5	2	6	6	8	
sj_hc_dim_54	20	10	2	6	6	9	

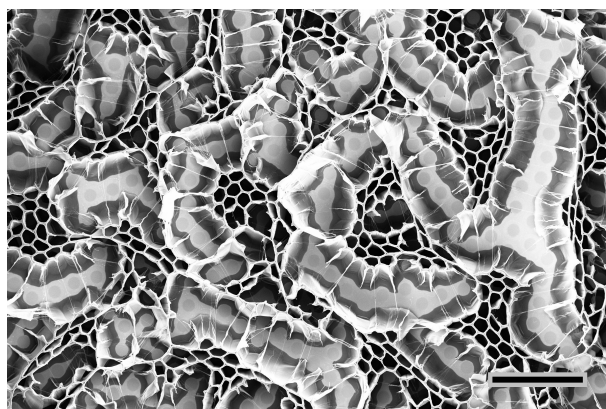


**Fig. B2** The SEM shows many cracks in the honeycomb formation for a sample grown to a height of  $\sim 90 \mu\text{m}$  before densification. Scale bar is  $200 \mu\text{m}$ .

**Table B3** Data for the calculations for the area change before and after densification of the honeycombs in the stress relief features.

Before densification			After densification			Percentage of initial area
hexagon side length [ $\mu\text{m}$ ]	Calculated area [ $\mu\text{m}^2$ ]	Shape	diameter circle [ $\mu\text{m}$ ]	hexagon side length [ $\mu\text{m}$ ]	Calculated area [ $\mu\text{m}^2$ ]	
103	27563	circle	52		8495	31
155	62419	circle	105		34636	55
230	137438	hexagon		150	58457	43
375	365354	hexagon		320	266043	73

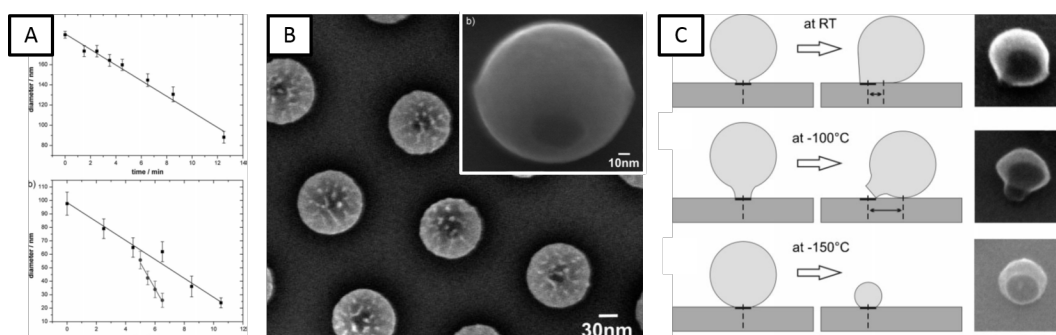


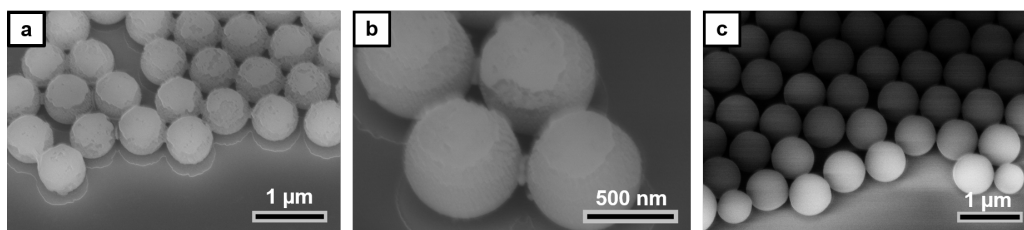
**Fig. B3** The linear relationship between the particle size and the etching time is shown in (A). The influence of pure isotropic etching (inset) and the addition of an anisotropic component is shown in the SEM in (B). The temperature influence on the shape is shown in (C).<sup>[160]</sup>

## B Results

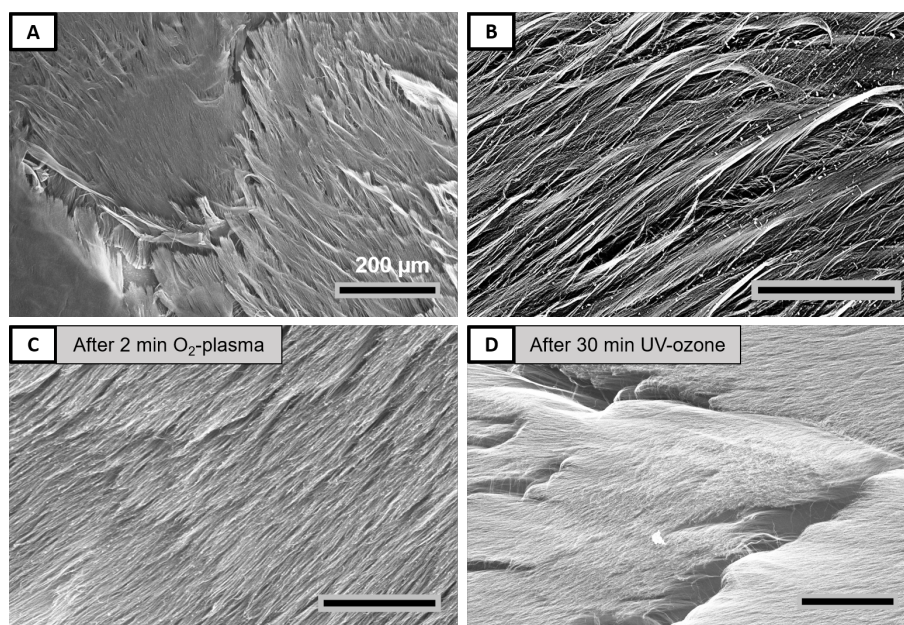
**Table B4** A study of the etching rates for different particles sizes and substrates.<sup>[169]</sup>

Initial colloid size <sup>a)</sup> [nm]	Plasma gas <sup>b)</sup>	Flow rate [sccm]	Substrate	Substrate temperature [°C]	Etch rate [nm · min <sup>-1</sup> ]
408	O <sub>2</sub> (50W)	3	Si	20	44 ± 5.0
246	O <sub>2</sub>	3	Si	20	37 ± 1.1
408	O <sub>2</sub>	3	Si	20	23 ± 0.8
246	O <sub>2</sub>	3	Si	20	22 ± 1.2
408	O <sub>2</sub>	10	Si	20	16 ± 1.8
246	O <sub>2</sub>	10	Si	20	18 ± 2.1
408	Ar	3	Si	20	10 ± 1.3
246	Ar	3	Si	20	11 ± 1.0
408	O <sub>2</sub>	3	Si	0	19 ± 2.0
246	O <sub>2</sub>	3	Si	0	21 ± 1.3
408	Ar	3	Si	0	7 ± 0.9
246	Ar	3	Si	0	10 ± 0.6
408	O <sub>2</sub> /Ar	2/1	Si	20	21 ± 1.0
408	O <sub>2</sub> /Ar	1.5/1.5	Si	20	20 ± 0.9
408	O <sub>2</sub> /Ar	1/2	Si	20	20 ± 0.8
408	O <sub>2</sub>	10	SiO <sub>2</sub>	20	7 ± 0.4
408	O <sub>2</sub>	10	Au@Si	20	15 ± 2.0
408	O <sub>2</sub>	10	Au@SiO <sub>2</sub>	20	5 ± 0.5
408	O <sub>2</sub>	10	SU-8@Si	20	11 ± 1.4
239 (PMMA)	O <sub>2</sub>	3	Si	20	71 ± 13.0
239 (PMMA)	O <sub>2</sub>	10	Si	20	50 ± 4.4
239 (PMMA)	Ar	3	Si	20	34 ± 0.8

<sup>a)</sup>Unless otherwise stated, the polymer material was polystyrene; <sup>b)</sup>the plasma power was 15W unless specified.

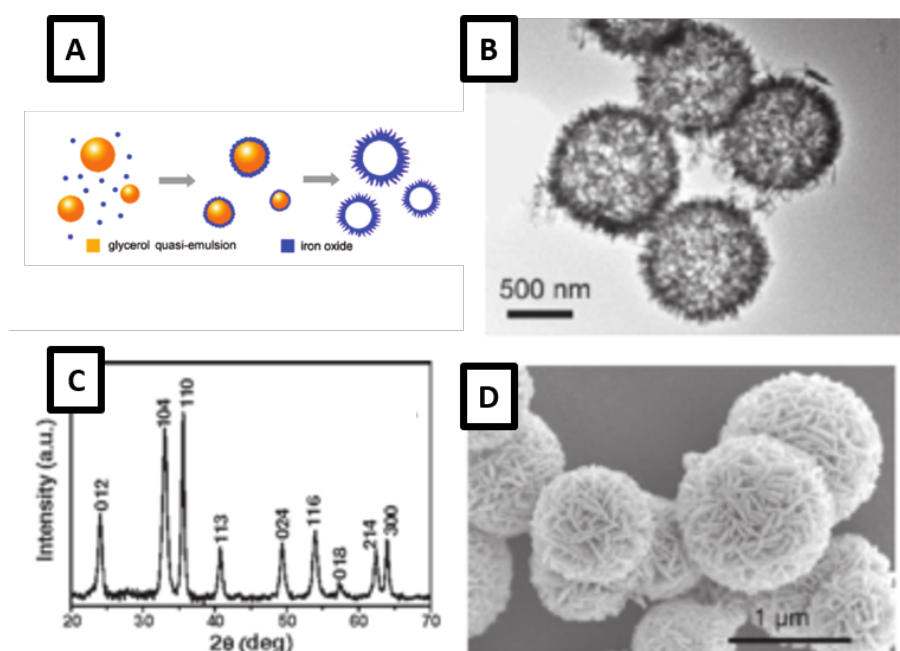


**Fig. B4** Colloidal PS-spheres (800 nm) shown with a 35° tilt after etching for 2 minutes (a) with the bridges between them clearly visible (b), and after 10 minutes (c).



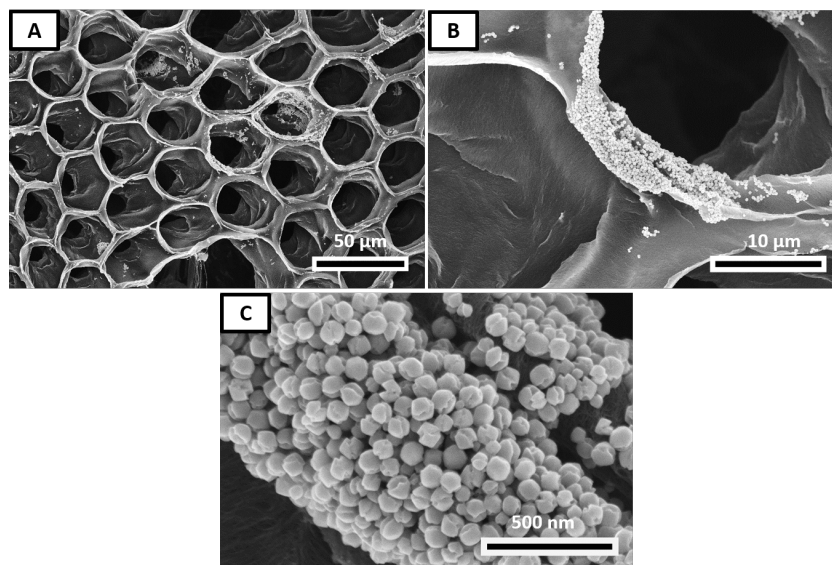
**Fig. B5** The SEM shows the effect of too much external stresses and shear forces during the transfer of a 3D CNT structure. The nanometer-sized holes are no longer visible and closed by horizontally aligned CNTs. Scale bar is 50  $\mu\text{m}$  if not otherwise indicated.

## B2 Modification with Iron Oxide

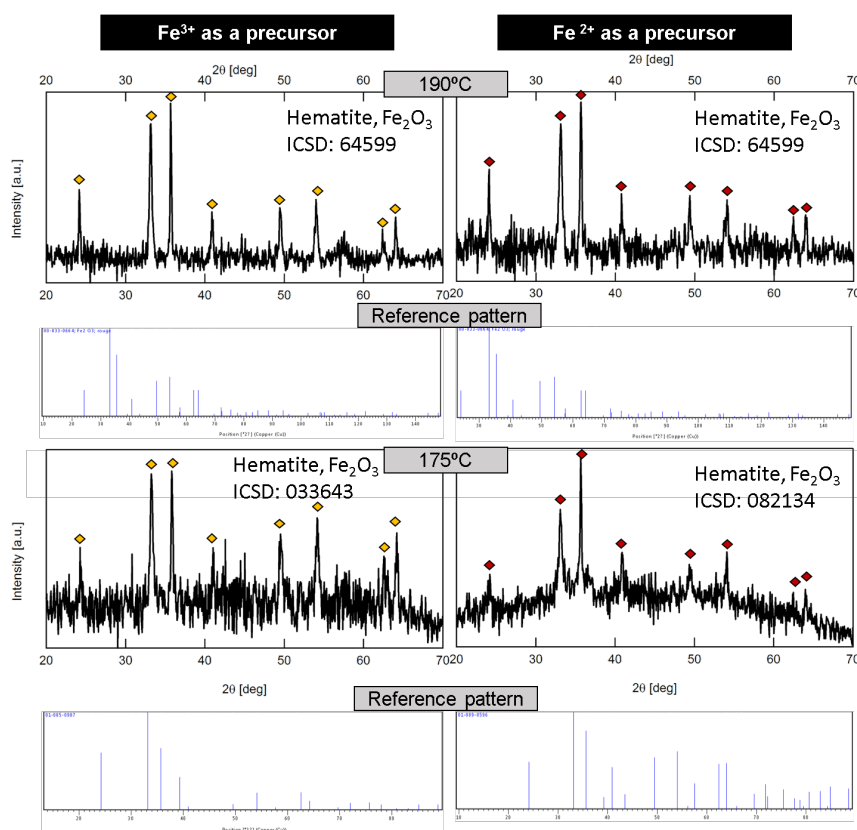


**Fig. B6** The process for the preparation of hollow  $\text{Fe}_2\text{O}_3$  nanospheres can be seen in (A), a TEM image of the produced spheres in (B) and an SEM image in (D). The XRD in (C) confirm that the phase is hematite.<sup>[320]</sup>

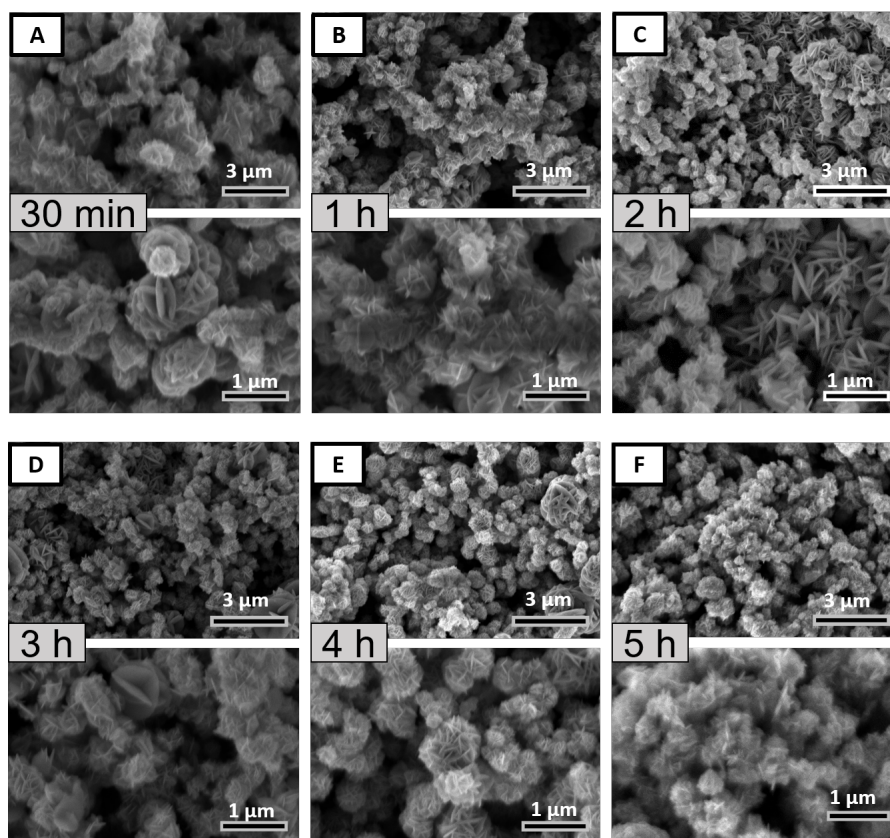
## B Results



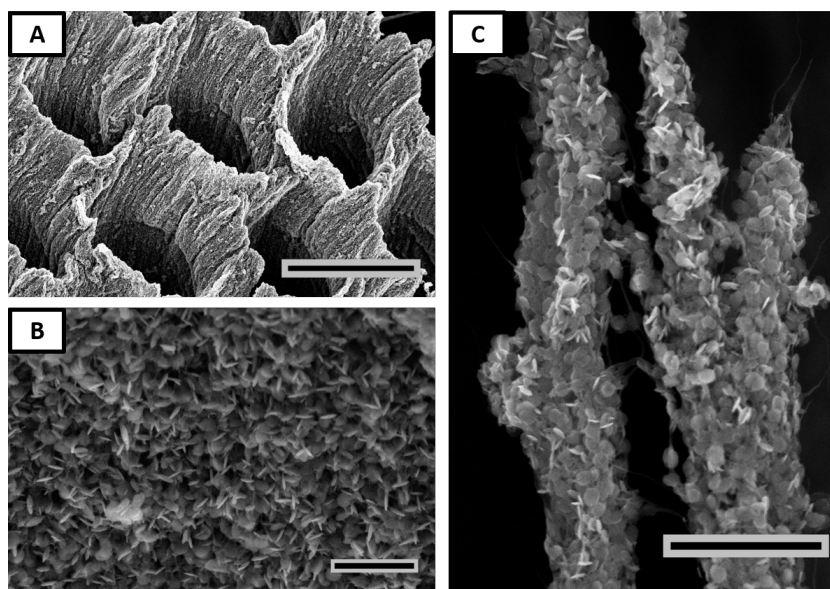
**Fig. B7** During the synthesis of Fe<sub>2</sub>O<sub>3</sub>-cubes, following a protocol by Zhu et al.,<sup>[328]</sup> on a CNT structure the nucleation did not take place on the CNTs themselves but mostly in solution.



**Fig. B8** Reference patterns for the hematite patterns used for the analysis.

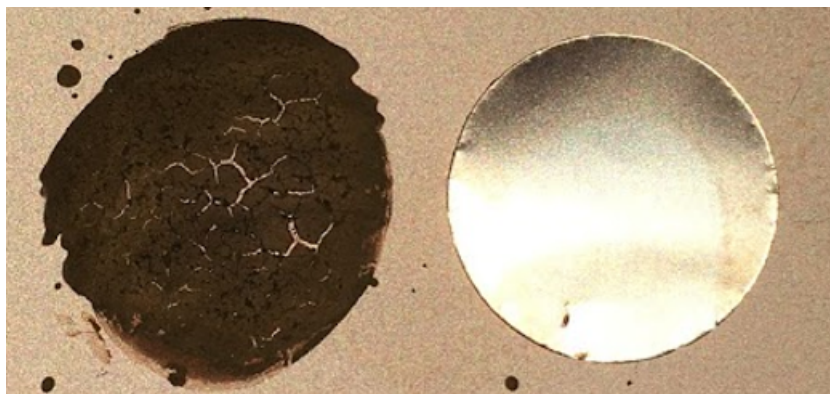


**Fig. B9** The SEM images show an overview of the particles created by a synthesis adapted from Wang et al.<sup>[320]</sup> at 175 °C for different reaction times. All of them are polydisperse, suggesting ongoing nucleation in the solution.



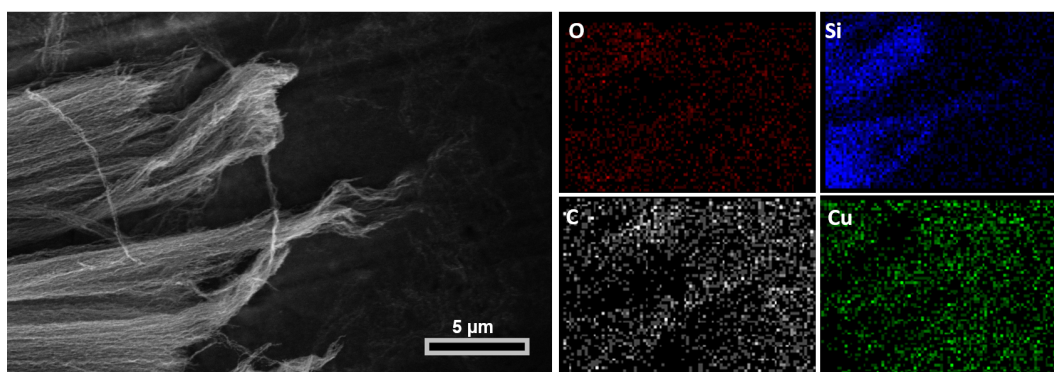
**Fig. B10** These images show the coating of the 3D CNT structures on a PCP film with Fe<sup>3+</sup> as a precursor. Scale bars are 30 μm in (A), 1 μm in (B) and 2 μm in (C).

## B Results



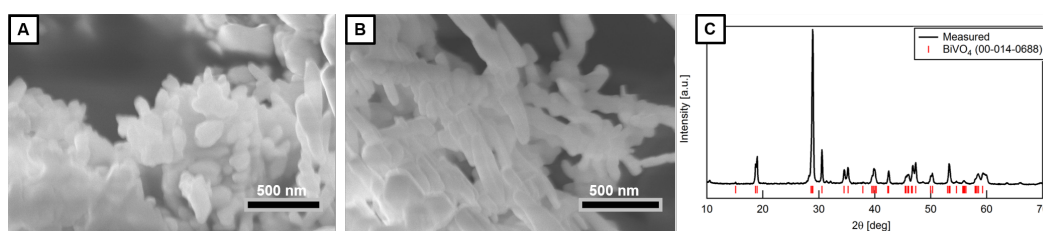
**Fig. B11** A thick standard film of  $\sim 300\mu\text{m}$  was cast with  $\text{Fe}_2\text{O}_3$ -particles and then dried. The cracking during drying can clearly be seen here.

### B3 Modification with Silicon

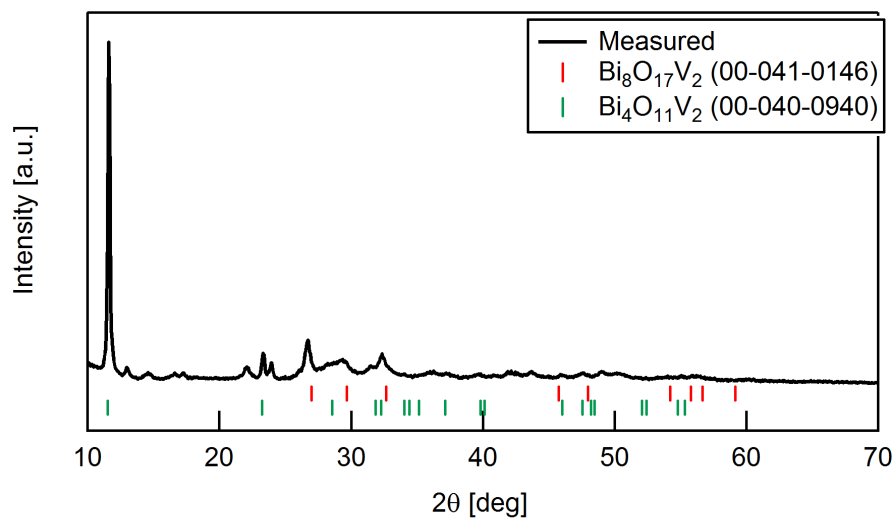


**Fig. B12** These images show the EDX mapping of the bottom of the Si-coated CNT sample after the transfer onto a copper tape. The found elements are oxygen, silicon (coating), carbon (CNTs) and copper (tape).

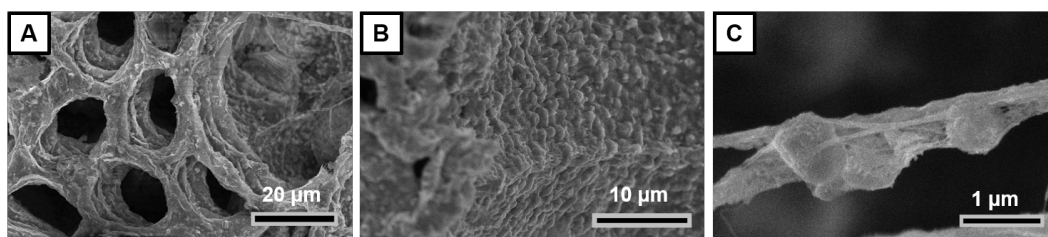
### B4 Modification with Bismuth Vanadate



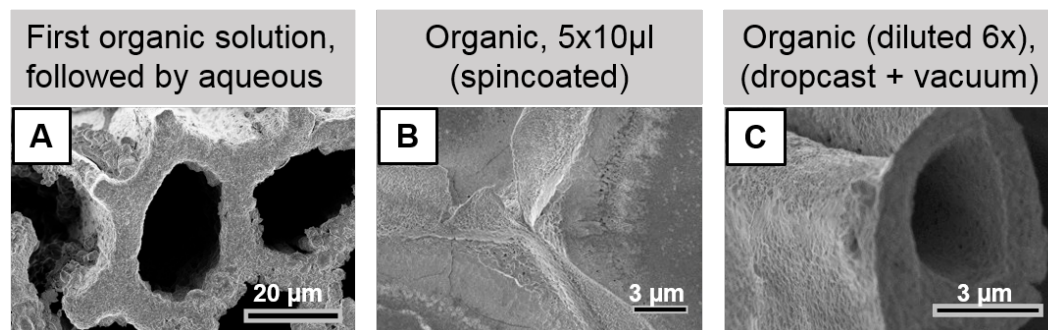
**Fig. B13** These SEMs (A) and (B) show  $\text{BiVO}_4$  particles made by a hydrothermal synthesis reported by Zhang et al.<sup>[416]</sup> The XRD shows that it is the desired phase (monoclinic  $\text{BiVO}_4$ ) and has no impurities.



**Fig. B14** A larger image of the XRD pattern of the coating with dumbbell shaped  $\text{BiVO}_4$ .



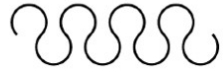
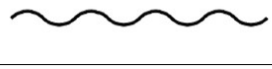
**Fig. B15** Soaking the 3D CNT structure in the vanadium precursor and drying it before the reaction with the bismuth precursor leads to a coverage of the overall structure with nanoparticles (A). Those spherical particles are spread all over the CNT side walls (B) and are emerging from the CNT strands (C). However, they don't show the right color and thus not the right composition.



**Fig. B16** An overview of the parameters tried for hotcasting by the visiting PhD student J. Rongé on a range of structures is shown here.

## B Results

---

Serpentine Patterns	Arc Angle 	Elastic Stretchability
	270°	61%
	235°	60%
	180°	36%
	135°	18%
	90°	6%

**Fig. B17** A controlled way to connect the hexagonal honeycomb patches is by introducing serpentine shaped connections either between two sides of the hexagons, as they were originally reported by J. A. Rogers' group for stretchable electronics.<sup>[383]</sup>